The Structure of Dark Matter Haloes in Cosmological Simulations

BETT, PHILIP, EDWARD

The Structure of Dark Matter Haloes in Cosmological Simulations

Philip Edward Bett

Abstract

We study the angular momentum, shape and density structures of dark matter haloes using very large dark matter simulations, and use smaller, higher-resolution simulations to investigate how the distributions of these properties are changed by the physical processes associated with baryons and galaxy formation.

We begin with a brief review of the necessary background theory, including the growth of cosmic structures, the origin of their angular momenta, and the techniques used to simulate galaxies, haloes and the large scale structure.

In Chapter 2, we use the *Millennium Simulation* (MS) to investigate the distributions of the spin and shape parameters of millions of dark matter haloes. We compare results for haloes identified using three different algorithms, including one based on the branches of the halo merger trees. In addition to characterising the relationships between halo spin, shape and mass, we also study their impact on halo clustering and bias.

We go on in Chapter 3 to investigate the internal angular momentum structure of dark matter haloes. We look at the radial profiles of the dark matter angular momentum in terms of both magnitude and direction, again using large-volume dark matter simulations including the MS. We then directly compare dark matter haloes simulated both with and without baryonic physics, studying how this changes the dark matter angular momentum. After relating the spin orientation of galaxies to their haloes, we consider the shape of the projected, stacked mass distribution of haloes oriented according to their central galaxy, mimicking attempts to measure halo ellipticity by weak gravitational lensing.

We consider the density structure of dark matter haloes in Chapter 4. For the dark matter simulations, we focus our interest on the source of the scatter in the distribution of concentration parameters, correlating it with both the halo spin and formation time. We compare different algorithms for predicting the concentration distribution using different aspects of the merger histories. We again go on to directly compare high-resolution haloes in simulations run with and without baryons and galaxy formation, looking at how these additional physical processes transform the density profiles. Finally, we compare the circular velocity curves of the haloes simulated with galaxies to the rotation curves of observed galaxies, using the *Universal Rotation Curve* model.

The Structure of Dark Matter Haloes in Cosmological Simulations

by Philip Edward Bett

A thesis submitted to the University of Durham
in accordance with the regulations for
admittance to the Degree of Doctor of Philosophy.

Institute for Computational Cosmology
Department of Physics

September 2008

Contents

List of Figures

List of Tables

Declaration

The work described in this thesis was undertaken between 2004 and 2008 while the author was a research student under the supervision of Professor Carlos Frenk & Dr Vince Eke in the Department of Physics at the University of Durham. This work has not been submitted for any other degree at the University of Durham or any other University.

Chapter 2 of this thesis has been published in the form of a paper,

- P. Bett, V. Eke, C. Frenk, A. Jenkins, J. Helly, & J. Navarro, "The spin and shape of dark matter haloes in the Millennium simulation of a Λ cold dark matter universe", 2007, *MNRAS*, 376, 215–232.

Parts of Chapter 4 were published as part of the following paper:

- A. F. Neto, L. Gao, P. Bett, S. Cole, J. F. Navarro, C. S. Frenk, S. D. M. White, V. Springel, A. Jenkins, "The statistics of ΛCDM halo concentrations", 2007, *MNRAS*, 381, 1450–1462.

Chapter 3 is to be submitted in the form of a paper as

- P. Bett, V. Eke, C. S. Frenk, A. Jenkins, T. Okamoto, "Cold dark matter haloes with and without baryons: angular momentum and internal alignment"

The author was supported through a PPARC/STFC studentship.

Acknowledgements

I must first of all thank Carlos Frenk, Vince Eke and Adrian Jenkins, who have supervised and encouraged, taught, motivated and even entertained me, with unending patience and support, for the past four years.

Thank you also to my other collaborators, John Helly, Julio Navarro, Takashi Okamoto, Liang Gao and Angelo Fausti Neto in particular, for providing code, data, help and advice, without which this thesis would have been impossible. Alan Lotts and Lydia Heck deserve special credit for their work constantly maintaining and improving the various computer systems at the ICC.

A large part of what has made the last four years so enjoyable is the open and friendly working environment at the ICC. Thanks to everyone there, past and present, but in particular those who I've had the privilege to share office OC319 with: Cesario Almeida, Raul Angulo, Rob Crain, Greg Davies, and Milan Raičević.

It is the people from outside work that make life complete. Particular thanks go to Helen and Tim (from other corners of physics), for their advice and support through the Thesis Adventure; and to Becca and Kat, who have shown me that 'Arts' students can do Real PhDs too. You've borne my ramblings about physics, haloes, and the toy & comic book industry with great patience, as well as providing amazing food (brownies are a food group, it turns out). Particular thanks must go to the Thursday Ustinov/Botanic Lunch Posse, and the IPPPeople for always making me glad I do astrophysics (and, again, for the brownies).

Special thanks must go to Karina for her unwavering encouragement, support and patience, and for making sure I don't lose sight of the things that really matter.

Finally, this thesis dedicated to the most inspirational teachers in my life: my parents. You taught me all the important bits first.

> Beyond the top of the sky was the place the Thing had called the universe. It contained – according to the Thing – everything and nothing. And there was very little everything and more nothing than anyone could imagine.

Pratchett (1990)

Chapter 1 | *Introduction*

People have always looked into the night sky and wondered how the various patterns of lights they saw came to be, and how they related to their lives on Earth. In ancient times, the writings of Greek philosophers such as Plato and Aristotle (4th century BCE) promoted models of a geocentric universe, which were later expanded in great detail by Ptolemy in his *Almagest* (mid-2nd century CE). This Ptolemaic system was the dominant cosmological model for over a thousand years, amongst astronomers from both Islamic and Christian cultures. However, in 1543, Copernicus published *De Revolutionibus Orbium Cœlestium*, using observational evidence to propose a detailed heliocentric model. In 1610, Galileo published *Sidereus Nuncius*, describing discoveries made using his telescope: there were mountains on the Moon; some of the nebulous patches of light, including the Milky Way itself, were made up of stars; and there were four moons orbiting the planet Jupiter. Around the same time, Kepler was formulating his three Laws of Planetary Motion, describing planets orbiting the Sun in elliptical orbits. Finally, in 1687, Newton published his laws of motion and theory of Universal Gravitation, in the *Philosophiæ Naturalis Principia Mathematica*. The motions of the heavenly bodies were described, and a reason for their motions proposed, in terms of a physical force that applied as much to them as it did to life on Earth.

In the early 20th century, two scientific developments further revolutionised our view of the cosmos. The first was the General Theory of Relativity, upon which all modern cosmology is based (Einstein, 1916). The second was the build-up of observational evidence that some of the nebulae in the sky were in fact other galaxies, similar in scale to the Milky Way itself but at a far greater distance. This was a rapid paradigm shift that vastly increased the scale of the Universe as people knew it: in 1920 it was still a matter of debate[1], but the middle of the decade saw it well-established (e.g. Hubble, 1926). These two discoveries set the scene for the standard cosmological models of the late 20th and

[1]The "Great Debate", in fact (Shapley and Curtis, 1921). A further example of the conceptual difficulties involved with questions of distance and perceived scale, for a static observer, can be seen in Linehan and Mathews (1996).

early 21st centuries, on which this thesis is based.

In this chapter, we describe the modern cosmological paradigm, and the techniques used to study it. In section 1.1 we briefly review the physics of the expanding Universe, providing the basic expressions and definitions necessary to discuss cosmology. Section 1.2 describes the mass and energy content of the Universe, in terms of the ΛCDM model. The growth of cosmic structure is followed in section 1.3, from perturbations to the formation of the haloes that are the focus of this thesis. Section 1.5 describes the methods used to simulate structures in the Universe, and describes in detail the particular simulations used in this thesis. Finally, in section 1.6, we outline the contents of the remaining chapters.

A note on notation: we shall denote scalars, vectors and matrices using the styles of p, $\boldsymbol{p}$ and p respectively. Logarithms are written as $\log x \equiv \log_{10} x$, and $\ln x \equiv \log_e x$. Quantities will generally be given in SI units (except where noted), supplemented by the standard astronomical units for convenience: masses are given in terms of the solar mass ($1\,\mathrm{M}_\odot \approx 2 \times 10^{30}\,\mathrm{kg}$), distances in terms of the parsec ($1\,\mathrm{pc} \approx 3.086 \times 10^{16}\,\mathrm{m}$), and times in terms of Gigayears ($1\,\mathrm{Gyr} \approx 3.16 \times 10^{16}\,\mathrm{s}$).

1.1 The expanding universe

The standard paradigm of modern cosmology has its basis in a particular solution of the Field Equations of general relativity: the Robertson–Walker metric for a homogeneous, isotropic spacetime, which can vary with time (i.e. expand or contract), and is assumed to apply to the Universe as a whole. In terms of the spacetime element $\mathrm{d}s$, this is

$$\mathrm{d}s^2 = -c^2\mathrm{d}t^2 + a^2(t)\left[\frac{\mathrm{d}x^2}{1-\frac{kx^2}{R_\mathrm{u}^2}} + x^2\left(\mathrm{d}\theta^2 + \sin^2\theta\mathrm{d}\phi^2\right)\right]. \tag{1.1}$$

Here, θ and ϕ are angles in standard spherical polar coordinates, and x is a radial coordinate that follows the expansion of the Universe (a *comoving* coordinate). These are related to *physical* coordinates $\boldsymbol{r}$ via the expansion factor $a(t)$, by $\boldsymbol{r} = a(t)\boldsymbol{x}$. The curvature of space is defined through the dimensionless constant k, which can take values of -1, 0 or $+1$, and the 'radius of curvature', R_u, a constant with dimensions of length. If $k = 1$, the Universe is spatially closed, and therefore finite in volume. The Universe is open if $k = -1$, and if $k = 0$ then it is flat: the metric then corresponds to Euclidian geometry for the comoving coordinates. The constant c is the speed of light.

The assumptions of homogeneity and isotropy (the "Cosmological Principle") were originally introduced as a simplifying first step in studying the dynamics of the Universe.

However, they have since been found to be a good description of the real Universe on sufficiently large scales: on scales larger than $\sim 100\,h^{-1}$Mpc (e.g. Yadav et al., 2005), the Universe really does look the same regardless of location or orientation.

The evolution of the expansion factor in such a universe is given by the Friedmann Equations,

$$\left(\frac{\dot{a}}{a}\right)^2 = \frac{8}{3}\pi G\rho(t) - \frac{kc^2}{a^2 R_{\rm u}^2} \tag{1.2}$$

$$\frac{\ddot{a}}{a} = -\frac{4}{3}\pi G\left(\rho + \frac{3P}{c^2}\right). \tag{1.3}$$

In these equations, the dots denote derivatives with respect to time, G is the gravitational constant, and P and ρ are the pressure and density respectively of the content of the Universe. Consider an observer at time $t_{\rm o}$, measuring an object at a distance r, which is receding with the expansion of the Universe at a velocity $v = {\rm d}r/{\rm d}t$ (the light from this object was of course emitted at a time earlier than $t_{\rm o}$). The relationship between physical and comoving distances leads to the Hubble Law, $v = H(t_{\rm o})r$, where the Hubble Parameter $H(t) \equiv \dot{a}/a$ is known as the Hubble Constant when the observation is made in the present time[2], $H_0 = H(t_0)$. Throughout this thesis, we shall parameterise the Hubble Constant as $H_0 = 100h\,{\rm km\,s^{-1}\,Mpc^{-1}}$, where h is dimensionless.

The wavelengths of photons are also affected by the expansion of the Universe, such that if a photon was emitted with wavelength $\lambda_{\rm e}$ when the expansion factor was a, then the wavelength observed in the present is $\lambda_0 = \lambda_{\rm e}/a$. We define the redshift, z, to be the ratio of the change in wavelength to the emitted wavelength. This means that

$$\frac{\lambda_0}{\lambda_{\rm e}} = \frac{1}{a} = 1 + z. \tag{1.4}$$

In the case that the velocity due to the expansion of the Universe $v \ll c$, we can say $z = \Delta\lambda/\lambda_{\rm e} \simeq v/c$.

In the Friedmann Equations, the average (mass) density ρ and pressure P of the Universe are commonly separated into different components according to their equation of state, $P = w\rho c^2$:

- Non-relativistic matter: this has negligible pressure compared to its mass-density, so we can say $w = 0$, but $\rho_{\rm m} > 0$.
- Radiation and relativistic matter: $w = 1/3$, so $P_\gamma = \frac{1}{3}\rho_\gamma c^2$.

[2]Throughout this chapter, a subscript zero will denote functions evaluated at the present; note that we define $a_0 = a(t_0) = 1$.

- We can also allow for a positive vacuum energy density (which we shall take to be constant for simplicity). This has $w = -1$, i.e. a negative pressure $P_\Lambda = -\rho_\Lambda c^2$.

This last component can be identified with the *Cosmological Constant* term that can be added to the Field Equations. The constant itself, Λ, has units of inverse length squared, and is related to its equivalent mass-density through $\Lambda = 8\pi G\rho_\Lambda/c^2$.

It is convenient to define a critical density from equation 1.2 to separate the three possible values of k. Taking $k = 0$ in the first Friedmann Equation, we get:

$$\rho_{\rm crit}(t) = \frac{3H^2(t)}{8\pi G}. \tag{1.5}$$

We can then refer densities to this value, resulting in the cosmological density parameters $\Omega_i = \rho_i/\rho_{\rm crit}$, where i refers to any of the components described above, or the total density $\Omega_{\rm tot}$. We can therefore rewrite the first Friedmann Equation as

$$\Omega_{\rm tot} - 1 = \frac{kc^2}{\dot{a}^2 R_{\rm u}^2}. \tag{1.6}$$

This shows how the density $\Omega_{\rm tot}$ and curvature k are tied together: If the Universe is closed ($k = +1$), then $\Omega_{\rm tot} > 1$ always; an open universe ($k = -1$) means $\Omega_{\rm tot} < 1$, and a flat universe $k = 0$ is always at the critical density ($\Omega_{\rm tot} = 1$). This expression can also be used to give a value for the radius of curvature, $R_{\rm u}^2 = kc^2/\left[H_0^2\left(\Omega_{\rm tot,0} - 1\right)\right]$

Using the First Law of Thermodynamics ($\mathrm{d}U + P\mathrm{d}V = \mathrm{d}Q$), with the internal energy $U = \rho c^2 V$, and the heat flow into/out of the Universe $\mathrm{d}Q = 0$, we get the Fluid Equation

$$\mathrm{d}\rho + \left(\rho + \frac{P}{c^2}\right)\frac{\mathrm{d}V}{V} = 0. \tag{1.7}$$

Using the equation of state above, and integrating, we get that $\rho \propto V^{-(1+w)}$. Since volume grows like $V \propto a^3$, we have an expression that relates density to the expansion factor:

$$\rho \propto a^{-3(1+w)}. \tag{1.8}$$

If we consider the three components described above, we find that the matter density ($\rho_{\rm m} \propto a^{-3}$) decreases slower than the radiation density ($\rho_\gamma \propto a^{-4}$), and ρ_Λ is constant. Knowing these relations, we can write the Friedmann equation just in terms of the Hubble parameter and the expansion factor, and the components' cosmological densities in the present:

$$H^2(t) = H_0^2\left[\Omega_{\rm m,0}a^{-3} + \Omega_{\gamma,0}a^{-4} + \Omega_{\Lambda,0} - \frac{kc^2}{a^2 H_0^2 R_{\rm u}^2}\right]. \tag{1.9}$$

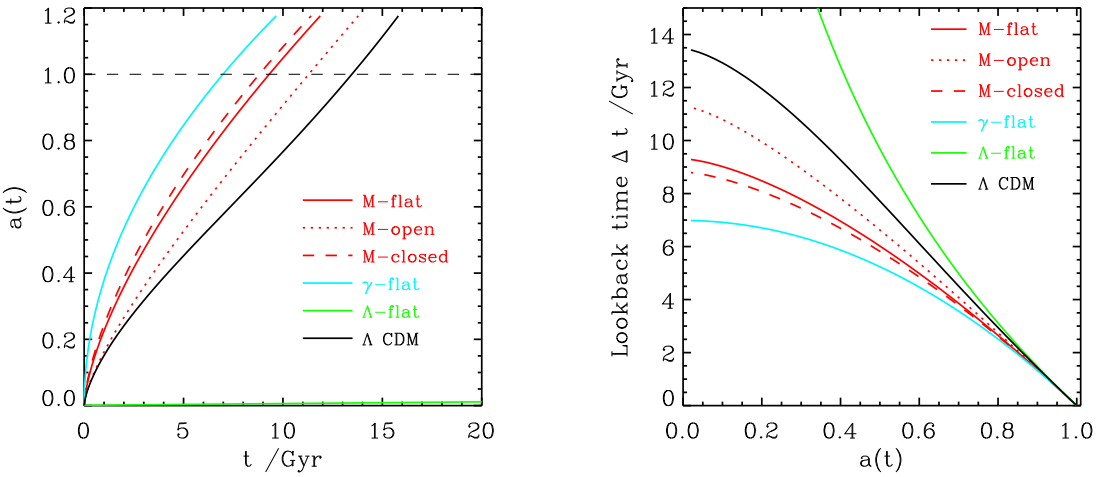

Figure 1.1: The growth of the Universe. The left panel shows the expansion of the Universe as a function of time for the different cosmologies described in table 1.1. We take $H_0 = 70\,\mathrm{km\,s^{-1}\,Mpc^{-1}}$. The lines are normalised such that $t(a = 10^{-3}) = 0$. The ΛCDM universe in the present is older than the flat matter-dominated universe, and has also started accelerating. The radiation-dominated universe grows faster than the other models. The Λ-dominated massless universe starts growing at a much slower rate, reaching $a = 1$ only after about 95 Gyr (not shown). The right-hand panel shows the lookback time for the same models, i.e. the normalisation is such that $\Delta t(a = 1) = 0$.

This can then be integrated to find how the expansion factor behaves as a function of time:

$$H_0 \int_{t(a_1)}^{t(a_2)} \mathrm{d}t = \int_{a_1}^{a_2} \left(\Omega_{\mathrm{m},0} a^{-1} + \Omega_{\gamma,0} a^{-2} + \Omega_{\Lambda,0} a^2 - \frac{kc^2}{H_0^2 R_{\mathrm{u}}^2} \right)^{-1/2} \mathrm{d}a \tag{1.10}$$

One can easily find $a(t)$ in the case of dominance by any one of the components in a flat universe: if it is matter-dominated (an *Einstein–de Sitter*, EdS, universe), then $a \propto t^{2/3}$; if it is radiation dominated, then $a \propto t^{1/2}$; and it grows exponentially if it is dominated by the cosmological constant ($a \propto e^{H_0 t}$). Figure 1.1 shows both the degree of expansion *after* a given time, and the *lookback time*, $\Delta t(a) = t(a_0) - t(a)$ for a given expansion factor $a \leq 1$, for a selection of cosmological models (see table 1.1).

Cosmology	$\Omega_{\Lambda,0}$	$\Omega_{\mathrm{m},0}$	$\Omega_{\gamma,0}$	$\Omega_{\mathrm{tot},0}$	k
M-flat (EdS)	0.0	1.0	0.0	1.0	0
M-open	0.0	0.3	0.0	0.3	-1
M-closed	0.0	1.3	0.0	1.3	$+1$
γ-flat	0.0	0.0	1.0	1.0	0
Λ-flat	1.0	0.0	0.0	1.0	0
ΛCDM	0.7	0.3	0.0	1.0	0

Table 1.1: A selection of simple cosmologies, used in figure 1.1. There are three matter-dominated examples (the flat one corresponding to an EdS universe), and three other flat cosmologies: radiation (γ) dominated, vacuum energy (Λ) dominated, and the 'concordance' ΛCDM model (believed to be similar to the real Universe).

1.2 The ΛCDM model and the content of the Universe

The ΛCDM model is of particular interest, not least because it is the one favoured by the majority of researchers in the field. It describes a flat universe ($\Omega_{\mathrm{tot}} = 1$), with the majority of the energy density budget taken by the cosmological constant ($\Omega_\Lambda \approx 0.7$ to 0.8), the simplest possible form of "dark energy". This causes the expansion of the Universe to be accelerating in the present, an effect that was first measured through the use of distant Type Ia supernovae as standard candles, in the late 1990s (Riess et al., 1998; Goldhaber and Perlmutter, 1998). Although using the cosmological constant to produce a flat universe with a low mass density was not unheard of before these results (e.g. Peebles, 1984; Lahav et al., 1991; Carroll et al., 1992), the measurement of the acceleration allowed models of dark energy to be taken seriously, and has motivated a great deal of further research. Although many models of dark energy have been hypothesized in the past decade, current data are consistent with the equation of state being a constant $w = -1$. Falsifying any of the more complex models (i.e. measuring any deviation from a constant energy density across space and time) will be an immense technical challenge (see Frieman et al. 2008 for a recent review).

The rest of the ΛCDM Universe is made of matter, $\Omega_{\mathrm{m},0} \approx 0.2$ to 0.3, distinguishable from dark energy by clustering under gravity (radiation makes a negligible contribution in the present). The matter content is divided into baryonic[3], $\Omega_{\mathrm{b},0} \approx 0.04$, and non-baryonic.

[3]Baryonic refers to matter made from three quarks, i.e. protons and neutrons in practice. Leptons such

"Dark matter" can refer to part of either of these: in the case of baryonic dark matter, it refers to objects that do not emit a measurable amount of electromagnetic radiation, although this can simply mean that we do not yet have the technical capability to measure it. For example, one can compute the mass density in stars alone, using the galaxy luminosity function to compute the total stellar luminosity density, and making reasonable assumptions about stellar mass-to-light ratios: the value comes out at $\Omega_{*,0} \sim 10^{-3} \ll \Omega_{\mathrm{b},0}$ (e.g. Eke et al., 2005). The "missing" baryonic mass can be termed dark matter, although it all radiates to some extent: some is the hot gas in clusters (dark in optical light, but bright in X-rays), some is the mass of people and planets (which emit a tiny amount of thermal radiation, which will be swamped by reflected light from their parent star, which in most cases will also be swamped by direct light from the star); the majority however is believed to reside in the Warm/Hot Intergalactic Medium (WHIM), gas that is cooler than that in galactic haloes and the intracluster medium, and which is spread thinly between the galaxies. The problem of the missing baryons and the WHIM is reviewed in Bregman (2007), Nicastro et al. (2008), and Prochaska and Tumlinson (2008).

For the purposes of this thesis however, we shall use "dark matter" to refer to the non-baryonic kind, which is dark simply because it does not interact with photons[4]: it only feels the gravitational force (although it may also be able to decay through Weak interactions). This means that it behaves in a fundamentally different way to baryonic matter, since it cannot dissipate its energy by heating or cooling in the normal sense, but only exchange it through gravitational interactions.

In principle, this dissipationless matter could be "hot", i.e. relativistic until after it decouples from the radiation field (see the next section); the neutrino is an obvious candidate particle. However, it has long been known that hot dark matter prevents structures forming in the manner observed (e.g. White et al., 1983, 1984): the high velocities of the neutrinos cause any small-scale structures to be erased in the early Universe, such that objects form first on the largest scales (e.g. superclusters). However, the largest structures we observe are seen to be still in the process of formation (they are not yet necessarily self-bound or virialised), and individual protogalaxies have been observed at high redshift. Furthermore, simulations using the neutrino as the dominant matter component result

as electrons and the neutrinos will also be present, but can be assumed to make a negligible contribution to the cosmic density.

[4]Whereas planets are literally dark, and intergalactic gas glows only at certain wavelengths, the non-baryonic dark matter is actually transparent rather than dark.

in clustering behaviour that is inconsistent with the observed galaxy distribution. So although neutrinos definitely exist, and have been measured to have mass, they cannot be the dominant component during structure formation.

So we resort to the dark matter being "cold", i.e. non-relativistic when structure formation begins. No such particle is currently known to exist. It is hoped that future particle physics experiments such as the LHC will provide viable possibilities, by revealing evidence for extensions to the Standard Model of particle physics, such as supersymmetry (Baer and Tata, 2008; Kane and Watson, 2008). Bertone et al. (2005) review the evidence and constraints for different dark matter particle candidates; see also the overview in the appendix to Weinberg (1997).

It has been the measurements of the cosmic microwave background (CMB) radiation by the WMAP satellite (Dunkley et al., 2008), in conjunction with measurements of galaxy clustering from two large-scale surveys (2dFGRS and SDSS, see Sánchez et al. 2006 and Tegmark et al. 2004 respectively) and the distant supernovae data, which have provided the strongest evidence in favour of the ΛCDM model. Komatsu et al. (2008) gives the currently-favoured parameters from the 5-year WMAP data, together with supernova and galaxy clustering constraints.

So, most of the baryons in the Universe are (at least) hard to detect, most of the mass in the Universe is made of some substance we have yet to detect directly (although its physical behaviour on astronomical scales is reasonably well-understood), and most of the energy density in the Universe is something else entirely, about which we know almost nothing. This may sound problematic at best, but the simplicity of the major constituents—a constant dark energy component, with dissipationless cold dark matter—actually make the Universe significantly easier to model than if was dominated by baryonic gas, at least on large scales. Future discoveries, from both particle physics and astronomy, are certain to make things more complicated.

1.3 The growth of cosmic structures

Although the background theory of section 1.1 assumes a homogeneous and isotropic universe, there is clearly structure on all but the largest scales. These structures are believed to originate as random quantum fluctuations in the very early Universe, which were expanded to physical scales during a period of exponential growth called Inflation. Their post-Inflation growth in the early Universe is usually understood through Linear Theory,

which follows perturbations in the otherwise-homogeneous background (with mean density $\bar{\rho}(t)$). The perturbations are usually described by their amplitude $\delta \ll 1$, in terms of their density $\rho = \bar{\rho}(t)\,(1 + \delta(\boldsymbol{x}, t))$. They can be considered to be a combination of plane waves, $\delta(\boldsymbol{x}, t) \propto \int \delta_{\boldsymbol{k}}(\boldsymbol{k}, t) e^{i\boldsymbol{k}\cdot\boldsymbol{x}} \mathrm{d}^3k$, where $\delta_{\boldsymbol{k}}$ is the Fourier transform of the density fluctuations δ, and $\boldsymbol{k}$ is the (comoving) wavevector. The fluctuations are usually assumed to be a Gaussian random field, specified entirely by its power spectrum $P(\boldsymbol{k}) = |\delta_{\boldsymbol{k}}|^2$.

Most models of Inflation predict the primordial power spectrum to have the form $P(k) \propto k^n$, with the simplest case being $n = 1$ (the Harrison–Zeldovich power spectrum; more complex models allow n to vary with scale). After Inflation, the power spectrum is modified by the growth of structures from Linear Theory. This is usually parameterised by a *transfer function*, $T(k)$, such that the power spectrum from Linear Theory is given by $P(k) \propto k^n\,|T(k)|^2$. The precise form of the transfer function is determined by the different matter components in the cosmological model, and is usually specified by fitting formulae or computed numerically (e.g. Bardeen et al., 1986; Seljak and Zaldarriaga, 1996; Eisenstein and Hu, 1999, and references therein).

The power spectrum is normalised using the variance, σ_8^2, of density fluctuations within an $8\,h^{-1}$Mpc sphere at $z = 0$, extrapolated from linear theory. Since they are needed to fully determine the fluctuation power spectrum, the spectral index n and the normalisation σ_8 are treated as parameters of the cosmological model, and are measured alongside the cosmological densities Ω_i. The current preferred values are $n \approx 0.95$ and $\sigma_8 \approx 0.8$ to 0.9 (e.g. Komatsu et al., 2008).

One can consider a physical length scale for the perturbations using the wavelength $\lambda = 2\pi a/k$. While matter perturbations are larger than the horizon scale ($R_\mathrm{H} \approx c/H$, the Hubble Radius), they grow like $\delta \propto a^2$ in the radiation-dominated regime, and $\delta \propto a$ if the Universe has passed into the matter-dominated regime (matter-radiation equality occurs at $z_\mathrm{eq} \approx 3100$). Once the horizon has grown larger than the perturbation, the growth changes. While $a < a_\mathrm{eq}$, growth of cold dark matter fluctuations is suppressed by the Mészáros Effect (Mészáros, 1974): the expansion of the radiation-dominated Universe is fast enough that the dark matter cannot respond in time, effectively freezing δ. Fluctuations in the baryons are coupled to the radiation field, and are prevented from growth by pressure. Instead, the fluctuations oscillate as acoustic waves with constant amplitude.

After a_eq, matter is the dominant component, and perturbations in the the dark matter are free to grow again, following $\delta \propto a$. The baryons are still coupled to the

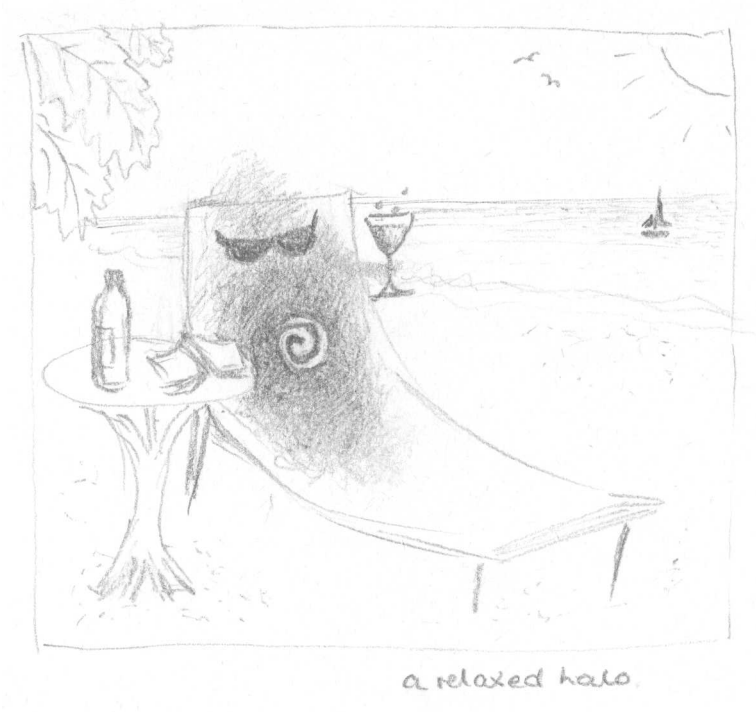

Figure 1.2: A relaxed halo (Williams, 2007). Note that it is located a comfortable distance from disruptive tidal fields.

photons however, until *recombination* occurs ($z_{\rm rec} \approx 1100$): the temperature and radiation density become low enough for electrons to bind to protons as atoms, and the Universe becomes transparent[5]. The pressure on the baryons plummets, and they rapidly fall into the enhanced potential wells made by the dark matter since $a_{\rm eq}$, afterwards slowing to match the dark matter growth rate.

At some point, the perturbations become non-linear ($\delta \gtrsim 1$), so a different theoretical approach is required. The *spherical collapse* model follows the evolution of a spherical overdense region containing a given mass, initially expanding with the Hubble flow. As the radius of the perturbation grows, the mass within it causes it to decelerate, and eventually it turns around and starts collapsing under gravity. In an idealised model, the collapse is a time-reversal of the expansion, but in reality the object will not be perfectly smooth: small irregularities will grow, and the matter in the object becomes virialised

[5]This description is, of course, a simplification. If an atom forms in an excited state, it can emit a photon. This can excite another atom, making it more easily reionised by other photons. Furthermore, the density fluctuations mean that some regions remain ionised, and coupled to the radiation, longer than others. A significant amount of residual ionisation remains well into redshifts of $\sim 10^2$ (see Peebles 1993 p165-175 for details).

(i.e. relaxed; see figure 1.2). The object is now referred to as a *halo*. In the EdS model, virialised haloes have an overdensity of $\Delta_c = \rho/\rho_{crit} = 18\pi^2 \approx 200$. This basic prediction was extended to the case of an open, low mass-density universe in Lacey and Cole (1993), and the flat ΛCDM universe in Eke et al. (1996). Bryan and Norman (1998) provided a simple quadratic fit to the results for the latter case. This overdensity can be used to define an outer boundary for the halo: the radius which encloses that overdensity is usually referred to as the virial radius, R_{vir}, and halo mass can be identified with the mass within that radius:

$$M_{vir} = \frac{4}{3}\pi\Delta_c\rho_{crit}R_{vir}^3 \tag{1.11}$$

Measurements from simulations however have shown that haloes do not usually exhibit any special features at R_{vir}, for example in their density or radial velocity profiles (e.g. Prada et al., 2006). Instead, the transition between the virialised matter of the halo and the surrounding infalling material appears to occur at ~ 1–$2R_{vir}$ (although this depends on the mass of the halo, and how isolated it is). Furthermore, haloes are rarely spherical (for example, in terms of isodensity or isopotential contours: Jing and Suto 2002; Hayashi et al. 2007), instead forming irregular but roughly triaxial shapes, with a tendency for prolateness.

The form of the CDM power spectrum is such that the power per logarithmic interval in k-space is greatest at small scales. This means that the smallest scale perturbations are the first to collapse to form haloes. Structures then form hierarchically, with larger perturbations collapsing later. In the non-linear regime, haloes grow by the accretion of surrounding matter, and through mergers with other haloes. This builds up ever larger objects. The structure on large scales becomes the Cosmic Web: matter flows out of voids into surrounding sheets of matter; these collapse into long filaments, which drain into nodes. Haloes exist at all levels in this structure: small ones like beads along the filaments, with massive haloes at the nodes. These remarkable structures exist in both simulations and observations of the large-scale structure (see figure 1.3).

1.4 The origin of angular momentum

Since the angular momentum of dark matter haloes is such a central quantity in this thesis, it is worth discussing its origin in a cosmological context.

Any primordial rotation decays away rapidly due to the expansion of the Universe (see e.g. Schäfer, 2008, and references therein), so the angular momentum must come

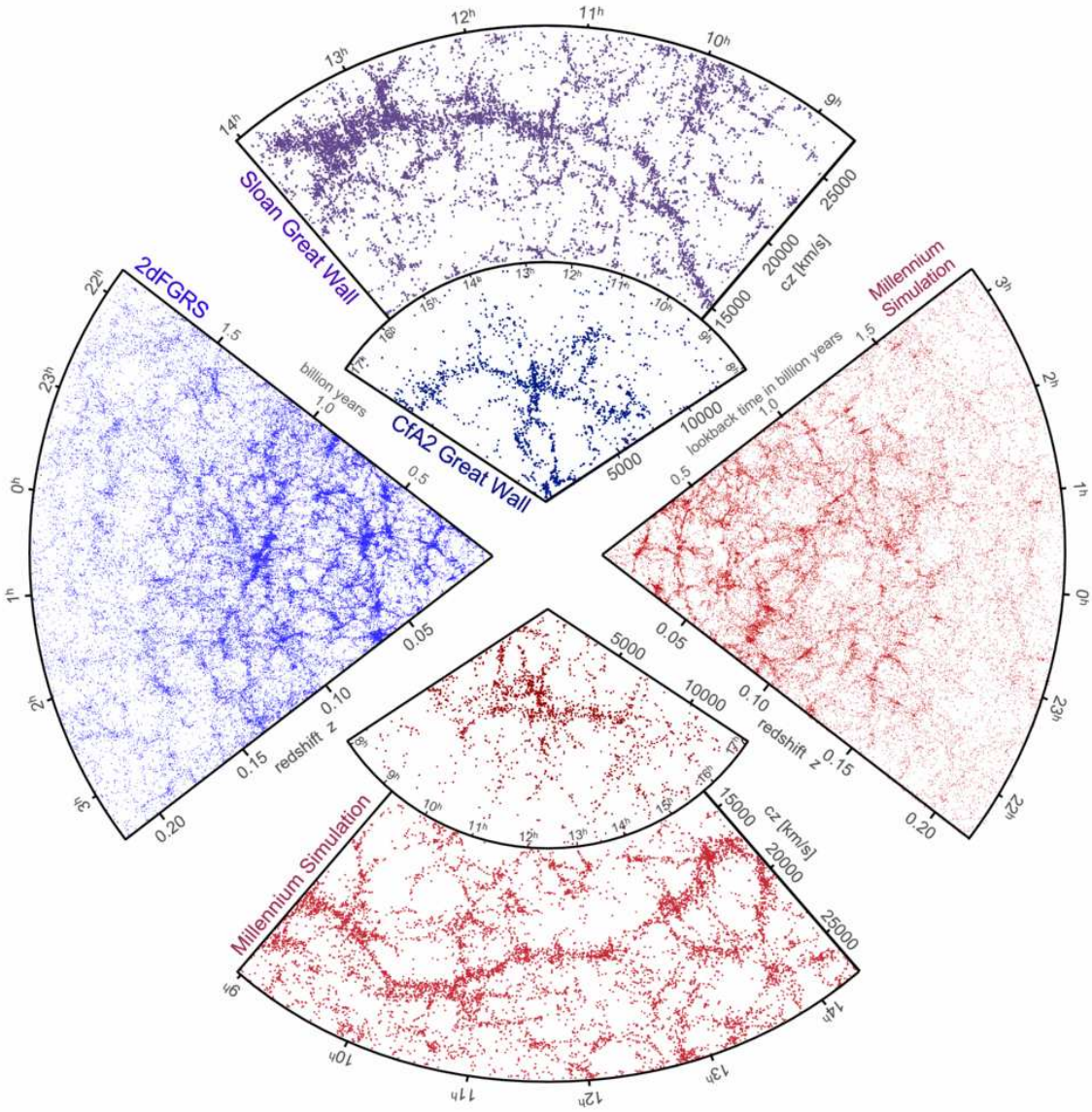

Figure 1.3: Illustration of the large-scale structure of the universe, from observations (blues shades) and simulations (red shades). The two top panels show very large "Great Wall" superstructures from the SDSS (Gott et al., 2005) and CfA2 (Geller and Huchra, 1989) galaxy redshift surveys. The left panel shows half of the 2dF Galaxy Redshift Survey (Colless et al., 2003), showing the filamentary structure of the cosmic web. The bottom and right panels show mock galaxy surveys made using semi-analytic modelling to produce galaxies in the Millennium Simulation (Springel et al., 2005b). The mock galaxies have been selected using the same survey geometries and magnitude limits as the corresponding observational plot in each case. *This figure has been reproduced from Springel et al. (2006).*

from another source. The work of Hoyle (1951), Peebles (1969), Doroshkevich (1970), White (1984) and Catelan and Theuns (1996) developed the *tidal torque theory* (TTT), which describes the growth of angular momentum for density perturbations in the linear (mass-dominated) regime. Although a full description of TTT is beyond the scope of this thesis, we shall outline the main results here (see also Porciani et al., 2002a; Schäfer, 2008).

We consider the matter in the Lagrangian volume that is destined to become a virialised halo in the present (the protohalo). Angular momentum is transferred to this pre-collapse protohalo by torques, caused by its mass distribution coupling to the tidal field due to neighbouring fluctuations. The angular momentum vector $\boldsymbol{L}(t)$ of this object can be written in terms of its components as (White, 1984):

$$L_i(t) = a^2(t)\dot{D}(t)\epsilon_{ijk}\mathcal{D}_{jl}\mathcal{I}_{lk}, \tag{1.12}$$

where we use the Einstein summation convention on the indices, and ϵ_{ijk} is the Levi-Civita symbol. The linear growth factor $D(t)$, here appearing in terms of its time derivative $\dot{D}(t)$, gives the temporal evolution of density perturbations from Linear Theory; i.e. in the matter-dominated regime, $D(t) \propto a(t)$, and since $a(t) \propto t^{2/3}$, we have that $\dot{D}(t) \propto t^{-1/3}$. Therefore, the angular momentum of the protohalo grows as $L(t) \propto a^{3/2}$.

The magnitude of the angular momentum is also governed by the two tensors $\mathcal{D}_{ij}$ and $\mathcal{I}_{ij}$. The external gravitational field enters through the deformation tensor,

$$\mathcal{D}_{ij} = -\left.\frac{\partial^2\Phi}{\partial q_i \partial q_j}\right|_{\boldsymbol{q}=0} \tag{1.13}$$

where Lagrangian coordinates are given by $\boldsymbol{q}$ and the derivative is evaluated at the centre of mass of the protohalo. The potential $\Phi(\boldsymbol{q})$ has units of area and is proportional to the gravitational potential (approximated by a Taylor expansion to second order). The shape of the protohalo is given by the inertia tensor,

$$\mathcal{I}_{ij} = \bar{\rho}_0 a_0^3 \int_{V_\mathrm{L}} q_i q_j \mathrm{d}^3 q \tag{1.14}$$

where the integral is over the Lagrangian volume V_L, and $\bar{\rho}_0$ is the mean density of the Universe in the present.

The tensor product in equation 1.12 means that L correlates with the *mis*alignment between the shape and the tidal field. For example, in the principle axis frame of the inertia tensor, we have $L_1 \propto \mathcal{D}_{23}\,(\mathcal{I}_{33} - \mathcal{I}_{22})$, with similar expressions for L_2 and L_3.

Only the off-diagonal terms of the deformation tensor are involved[6]. This means that if the tidal field and the protohalo's axes are perfectly aligned then the angular momentum vanishes (and hence cannot grow). It also vanishes if the protohalo is spherical[7].

If we assume that the tidal field and protohalo shape are uncorrelated, then the direction of the angular momentum from TTT is dictated by the shape of the halo at turnaround, when the inertia tensor is greatest. The angular momentum would tend to align with the intermediate axis of the inertia tensor (Navarro et al., 2004a). However, tests with N-body simulations find that the inertia and tidal tensors are actually highly correlated, with their directions well-aligned (Porciani et al., 2002a,b; Navarro et al., 2004a). This means that the angular momentum is reduced to being a residual effect, caused by deviations away from the alignment of the tidal field and protohalo shape. In addition to being much smaller, the angular momentum now tends to be aligned perpendicular to the direction of maximum compression due to the tidal field (i.e. the smallest eigenvector of $\mathcal{D}_{ij}$), which itself tends to be aligned with the minor axis of inertia.

It is worth recalling that these predictions for the magnitude and direction of the angular momentum are for the linear system at turnaround. After turnaround, the protohalo decouples from the expanding background and collapses, becoming a halo. The lever arm for torquing shrinks due to the collapse, and the angular momentum growth is effectively stopped. The angular momentum of that Lagrangian volume is conserved however, and for isolated systems the predictions from TTT can be preserved (Navarro et al., 2004a; Zavala et al., 2008). However, in general, non-linear effects cause scatter in the predicted angular momentum. Porciani et al. (2002a) found that the predicted magnitude was accurate to within an order of magnitude, and the direction had a mean error of $\sim 50°$.

[6]This means that in general the $\mathcal{D}_{ij}$ and $\mathcal{I}_{ij}$ tensors can be replaced by their traceless counterparts: the tidal or shear tensor $\mathcal{T}_{ij} = \mathcal{D}_{ij} - \frac{1}{3}\mathcal{D}_{kk}\delta_{ij}$, and the traceless quadrupole moment tensor $\mathcal{Q}_{ij} = \mathcal{I}_{ij} - \frac{1}{3}\mathcal{I}_{kk}\delta_{ij}$, where δ_{ij} is the Kroneker delta. Note that the "usual" inertia tensor that we use in later chapters, which relates angular momentum to angular velocity through $L_i = \mathcal{I}'_{ij}\omega_j$, is given by $\mathcal{I}'_{ij} = \mathcal{I}_{kk}\delta_{ij} - \mathcal{I}_{ij}$ (Binney and Tremaine, 2008, p796)

[7]Peebles (1969) originally considered a spherical *Eulerian* volume, and found that its angular momentum does grow. White (1984) showed that this was due to surface effects, and that an initially spherical *Lagrangian* volume has no angular momentum growth.

1.5 Simulations of cosmic structures

The non-linear nature of structure formation means that precise and accurate studies of the predictions of particular models can only be done numerically. On astrophysical scales, the physical dark matter and baryonic particles behave as continuous fluids, which we can describe using a probability density in 6-dimensional phase-space, $f(\boldsymbol{x}, \boldsymbol{u}, t)$.[8] The evolution of a fluid f_i is described by the Boltzmann equation:

$$\frac{\partial f_i}{\partial t} + \boldsymbol{u}\cdot\frac{\partial f_i}{\partial \boldsymbol{x}} + \dot{\boldsymbol{u}}\cdot\frac{\partial f_i}{\partial \boldsymbol{u}} = \sum_j C[f_i, f_j], \tag{1.15}$$

where the collision integral, C, describes the physical processes of the interaction between particles of the fluids f_i and f_j, such as scattering, creation and annihilation. For dark matter and stars, the fluid is collisionless and $C = 0$; equation 1.15 is then known as the Vlasov equation. Its solutions are found using characteristic equations, which look like particle equations of motion. This leads us to approximate the continuous mass density field into discrete "particles" (much larger than the physical particles). Following their characteristic equations yields an approximation to the evolution of the continuous system. The particles in this N-body approach are Monte-Carlo samplings of the probability-density distribution in position and velocity.

1.5.1 Collisionless matter

In the case of the collisionless fluids (dark matter and stars), the equations we have to solve for the N-body system are then:

$$\frac{\mathrm{d}\boldsymbol{x}_i}{\mathrm{d}t} = \boldsymbol{u}_i; \qquad \frac{\mathrm{d}\boldsymbol{u}_i}{\mathrm{d}t} = -\boldsymbol{\nabla}\Phi(\boldsymbol{x}_i, t), \tag{1.16}$$

where the variables and derivatives here refer to *physical* (not comoving) coordinates. The gravitational potential Φ is given by Poisson's equation:

$$\nabla^2\Phi(\boldsymbol{x}_i, t) = 4\pi G\rho_{\mathrm{tot}}(\boldsymbol{x}_i, t), \tag{1.17}$$

where $\rho_{\mathrm{tot}}(\boldsymbol{x}_i, t)$ is the total mass density field visible to particle i (located at position $\boldsymbol{x}_i$ at time t). Once Poisson's equation has been solved for a given distribution of particles, the equations of motion can be 'integrated', by approximating the differentials as finite differences: the particle positions and velocities are computed for the next time step, the clock is advanced, and we again solve Poisson's equation for the new positions.

[8] This is defined such that $f(\boldsymbol{x}, \boldsymbol{u}, t)\mathrm{d}^3\boldsymbol{x}\mathrm{d}^3\boldsymbol{u}$ is the probability that at time t a given particle is in the volume of phase space centred on the position $\boldsymbol{x}$ and velocity $\boldsymbol{u} \equiv \dot{\boldsymbol{x}}$.

The naïve way of progressing is to construct the potential for each particle i (although in practice one would go directly to the acceleration $\boldsymbol{\nabla}\Phi$) using simple direct summation, over each of the remaining $N-1$ particles:

$$\Phi(\boldsymbol{x}_i) = -G\sum_{j\neq i}\frac{m_j}{\sqrt{|\boldsymbol{x}_i-\boldsymbol{x}_j|^2+\epsilon^2}}, \tag{1.18}$$

where we have introduced a gravitational softening length ϵ to reflect the fact that an astrophysical object of mass m_i such as our particles will not have zero volume. Its inclusion prevents unphysical two-body effects such as scattering to large angles, or forming a bound pair (the softened potential shown here is just a simple example; a detailed study of different choices is given in Dehnen 2001). Since we always want to use as many particles as possible, to maximise the number of well-resolved objects in the simulation, this method is clearly not appropriate: the number of operations scales like N^2. More efficient solutions than this Particle–Particle (PP) method must be sought.

The Particle–Mesh (PM) technique (e.g. Klypin and Shandarin, 1983; Hockney and Eastwood, 1988; Klypin and Holtzman, 1997, and references therein) works by assigning the particle masses to grid cells, according to a given interpolation scheme. This is used to calculate a discretised density field ρ_{ijk} (where the subscripts label the grid cells). We then use the fact that the potential can be represented as the convolution of the density field and an appropriate Green's function, $\mathcal{G}$: in Fourier space, the convolution becomes a straightforward product, $\hat{\Phi}(\boldsymbol{k}) = \hat{\mathcal{G}}(\boldsymbol{k})\hat{\rho}(\boldsymbol{k})$ (where the circumflex indicates the Fourier-transform of a quantity). Therefore, we transform the density field $\rho_{ijk} \rightarrow \hat{\rho}_{lmn}$ (where l, m and n index the cell in $\boldsymbol{k}$-space), solve for $\hat{\Phi}_{lmn}$, and transform it back into the potential in real space, Φ_{ijk}. The acceleration of each particle can now be computed by interpolating the potential onto the particle's position (with the same scheme used for the particle-cell density assignment) and using the finite-difference method to compute $\boldsymbol{\nabla}\Phi$. The accelerations are then used to compute the new particle positions and velocities; these are typically output as a "snapshot" file, and the simulation can then advance to the next time-step.

While the PM method is efficient both in terms of operations and memory requirements, it can suffer from the resolution limit imposed by the grid size. One way to avoid this is to use direct-summation on small scales, and reserve the particle-mesh for larger scales: the Particle–Particle, Particle–Mesh scheme, $\mathrm{P^3M}$ (e.g. Efstathiou and Eastwood, 1981; Hockney and Eastwood, 1988). Although this does provide an improvement over each of the PP and PM techniques alone, the highly-clustered nature of matter at late

times can result in the PP part becoming dominant. For well-resolved systems (large N), the simulation will slow dramatically, and could make it impractical to complete. The Adaptive P^{3}M method (AP^{3}M, Couchman 1991) attempts to overcome this problem by introducing sub-grids in high-density regions. This reduces the PP load by instead performing more PM steps on a finer mesh. (We describe other adaptive methods later.)

A rather different method involves organising the particles into a hierarchical 'Tree' structure. A commonly-used system is the octree (Barnes and Hut, 1986): if a cubic node contains more than one particle, it is divided into eight equal-sized child-nodes. The process starts with a cube containing the entire simulation, and is performed recursively in each child-node. The resulting tree structure is then used to produce an approximation to the gravitational force felt by each particle in turn. For a given particle, the force experienced due to the other particles is computed as follows. Starting with the largest node, the following criterion is tested:

$$r > \frac{l}{\theta} \tag{1.19}$$

where r is the distance between the particle and the node in question, l is the size of the node, and θ is the *tree opening angle*, a simulation parameter that governs the force accuracy. If the criterion is true, the force from that node is added onto the accumulating force felt by the particle. If it is false, then the node is "opened", and equation 1.19 is evaluated for each child-node in turn. This continues recursively until all the particles have contributed. This criterion means that distant particles contribute collectively through larger-scale nodes. For nearby particles though, the tree is "walked" to greater depth, resulting in a more accurate force contribution.

A decision has to be made regarding the accuracy of the force contribution from a given node. An obvious first choice is simply to use the node's total mass, located at its centre of mass. In practice, a multipole expansion of the gravitational potential is often used; the simple choice just described is the monopole term in such an expansion. There is a compromise between evaluating the force from a given node to greater accuracy using higher-order terms, and walking the tree to greater depth to improve the force resolution. The GADGET-1 code of Springel et al. (2001b) evaluates up to the quadrupole moment, whereas the GASOLINE code of Wadsley et al. (2004) continues to the hexadecapole moment, while using fewer tree nodes. The GADGET-2 code (Springel, 2005) however just uses the monopole[9], and walks deeper into the tree.

[9]The dipole term just gives the centre of mass of the node. Since the particle coordinates in the

In fact, GADGET-2 can be used as a hybrid TreePM code: it evaluates the potential at large-scales in Fourier space using the PM method, while the Tree is used for the potential at smaller-scales. The simulations analysed in this paper all use variants of GADGET-2.

1.5.2 Gas dynamics

Baryonic gas behaves differently to the dark matter fluid, and requires solving the standard equations of hydrodynamics in addition to Poisson's equation. If we discretise the gas into particles in the same way as the dark matter and stars, we can use the same method for dealing with gravity in both cases. However, the gas particles carry more information than just their position, velocity and mass; they also have an intrinsic internal energy for example, which can be converted to a temperature if we know, or assume, its composition (e.g. hydrogen).

The most commonly-used method for dealing with gas particles is through Smoothed Particle Hydrodynamics (SPH, Gingold and Monaghan 1977; Lucy 1977; Monaghan 1988, 1992). The key aspect of this formalism is that quantities (such as densities, velocities, energies, etc) are computed by smoothing over neighbouring particles. This is done using a smoothing kernel function, $W(\boldsymbol{x}, h)$, where h is the *smoothing length*; in combination with the functional form of W, it governs the volume over which to smooth, and can vary between particles. In general, for some property A at position $\boldsymbol{x}$, we compute the smoothed average

$$\langle A(\boldsymbol{x})\rangle = \int A(\boldsymbol{x}')W(\boldsymbol{x}-\boldsymbol{x}', h)\mathrm{d}^3\boldsymbol{x}'. \tag{1.20}$$

Discretising to a set of particles (with $\mathrm{d}^3\boldsymbol{x}' \to m_j/\rho_j$), we can estimate the value of A at particle i by

$$A_i = A(\boldsymbol{x}_i) = \sum_{j=1}^{N} \frac{m_j}{\rho_j} A(\boldsymbol{x}_j)W(\boldsymbol{x}_i - \boldsymbol{x}_j, h). \tag{1.21}$$

For example, the density around particle i can be estimated by $\rho_i = \sum_j m_j W(\boldsymbol{x}_{ij}, h)$, and the velocity field by $\boldsymbol{v}_i = \sum_j (m_j/\rho_j)\boldsymbol{v}_j W(\boldsymbol{x}_{ij}, h)$ (where we have written $\boldsymbol{x}_{ij} \equiv \boldsymbol{x}_i - \boldsymbol{x}_j$). These quantities can be easily differentiated, since for a particular sum element it is only the smoothing kernel that depends explicitly on the coordinates, e.g. $(\boldsymbol{\nabla}\cdot\boldsymbol{v})_i = \sum_j (m_j/\rho_j)\boldsymbol{v}_j \boldsymbol{\nabla} W(\boldsymbol{x}_{ij}, h)$.

In practice, the particular expressions used to derive quantities, and the form of the hydrodynamic equations used, are not unique: different choices have consequences for the numerical accuracy of the resulting code, and relate to which quantities are explicitly

multipole expansion are computed relative to the centre of mass, the dipole term does not contribute.

conserved. Springel and Hernquist (2002) investigate different formulations, and derived a form of SPH that manifestly conserves both energy and entropy. They found that it produced significantly better results, in terms of reducing numerical artefacts. It also allows the particle equations of motion to be written in a form that can easily be integrated forward in time. This entropy-based formulation of SPH replaced the standard form in the subsequent release of the GADGET-2 code (Springel, 2005).

SPH implementations also require the addition of terms describing an artificial viscosity. This allows the SPH method to produce physical shocks, which would otherwise be smoothed away due to W (although SPH shocks are usually still not strong enough compared to analytic results). The original form of the artificial viscosity term (Monaghan and Gingold, 1983) was found to also add viscosity unphysically to pure shear flows (i.e. where the velocity field has zero divergence but non-zero curl), and caused additional angular momentum transport (e.g. during disc formation; Hernquist and Katz, 1989; Katz and Gunn, 1991). The alternative form of Balsara (1991, 1995) removes the shear-flow viscosity, and was found to vastly reduce the spurious angular momentum transport (Steinmetz, 1996). This form of the artificial viscosity was used in GADGET-1, with a slightly modified version used in GADGET-2 (Monaghan, 1997; Springel, 2005).

1.5.3 Adaptive grid methods

There is another set of methods for astrophysical simulations that we have not yet discussed, which make use of *adaptive mesh refinement* (AMR): i.e. an adaptive grid is used in the N-body gravity solver, with Eulerian[10] hydrodynamics on the grid for the gas. The resolution limitations of the PM method are overcome by adaptively refining (and de-refining) the grid in regions requiring higher (or lower) resolution, for example in high density regions. AMR codes are typically more difficult than Lagrangian codes to parallelise effectively, and often do not scale as well. However, they are able to accurately simulate systems with a much greater dynamic range than their Lagrangian competitors; for example shocks are much better-resolved. Currently popular AMR codes include ART (Kravtsov et al., 1997, 2002), ENZO (Bryan and Norman, 1997; Norman and Bryan, 1999; O'Shea et al., 2004), FLASH (Fryxell et al., 2000) and MLAPM/AMIGA (Knebe et al., 2001). A detailed description of the methods used in AMR codes is beyond the scope

[10]The SPH method previously discussed is Lagrangian, as it describes the properties of individual mass elements that move with the fluid flow. Eulerian methods do not use particles, instead tracking the properties of the flow through discrete volume elements.

of this thesis; a recent comparison between Lagrangian and Eulerian hydrodynamics was done in O'Shea et al. (2005).

1.5.4 Additional physics for galaxy formation

In order to fully simulate the processes of galaxy formation, a great deal more physics has to be modelled. These processes typically involve adding or removing heat and/or mass from the gas, and enter the hydrodynamics equations through sink or source terms. Although a detailed discussion of the modelling of these processes is beyond the scope of this thesis, we shall outline them in brief here (see Okamoto, 2008, for a recent review).

The gas as described above is often known as 'adiabatic', although 'non-radiative' is a more accurate term: it has no provision for transferring energy to or from the gas itself other than through pressure ('$P\mathrm{d}V$' work). Giving the gas the ability to cool radiatively is a common first step in proceeding towards more realistic simulations. The gas radiative cooling rate depends on its composition, in terms of the abundance of different elements (its metallicity). The net cooling functions for gas of a range of metallicities is usually tabulated (e.g. Sutherland and Dopita, 1993), since it is very memory-intensive to track each element individually, and needlessly processor-intensive to compute the cooling rates for each gas particle from scratch at each timestep. In addition, there is often assumed to be photoionising UV background radiation, acting as a heat source (Haardt and Madau, 1996). Because efficient computation of radiative transfer is difficult (due, in part, to the high propagation speed compared to the sound speed of the gas; see e.g. Iliev et al. 2006), the UV background is often assumed to be spatially uniform, although it can evolve with time. Other heat sources that can be included are those more directly related to star formation processes, such as stellar winds and supernovae.

A difficulty in implementing these heating/cooling processes in simulations is that the timescales for the energy transfer (e.g. the cooling time) are typically much shorter than the dynamic timescales for the hydrodynamic processes. A commonly-used solution is to perform the heating/cooling integration in-between hydrodynamics timesteps. The gas is assumed to be static over that period, and the net internal energy change due to heating and cooling is computed and applied to the particles, ready for the next hydrodynamic timestep.

Clearly, one cannot simulate galaxy formation without star formation. Gas particles can be converted into collisionless 'star' particles if they satisfy certain conditions, such as being above a certain density and below a certain temperature. Star formation occurs

according to a probability distribution, designed such that the result mimics an observed star formation rate. The star particles, which carry additional properties such as their formation time and metallicity, represent a stellar population that is a Monte Carlo sample of the distribution of stellar properties. The task of computing the details of the stellar population is known as Stellar Population Synthesis (SPS), and can be part of the simulation code itself, or a separate program for post-processing. The SPS code takes a star particle's age and metallicity, and assumes a particular initial mass function (IMF, the number of stars produced in bins of initial stellar mass, e.g. $\mathrm{d}N/\mathrm{d}m$). It can work out how the corresponding stellar population would evolve, by considering individual stellar evolution tracks. It also needs to estimate how much energy, metals, and mass are fed back into the gas due to processes such as stellar winds and supernova explosions. Codes can also generate spectral and photometric properties of the stellar populations, for more direct comparisons with observations. Commonly-used population synthesis codes include GALAXEV (Bruzual and Charlot, 2003) and PEGASE (Le Borgne et al., 2004), although procedures can also be written directly into the simulation codes.

The constraints of processor-time and memory usage in simulations mean that many processes in the interstellar medium (ISM), such as instabilities in cooling gas, nebulae such as molecular clouds that form stars, and winds from stellar evolution, are well below any practical resolution limit. Therefore, a multiphase ISM is usually implemented through 'sub-grid' (or sub-particle) modelling, treating processes statistically rather than following individual instances. This will usually include models for the growth and evaporation of cool clouds, which can have a significant influence on the star formation rate, as well as the hot gas and stars already discussed. Implementations are commonly based on the early work of McKee and Ostriker (1977), and include those of Yepes et al. (1997), Springel and Hernquist (2003), Springel et al. (2005a) and Booth et al. (2007).

A relatively recent addition to the physics included in galaxy-formation simulations is the tracking of central black holes. Heating due to radiation from active galactic nuclei (AGN) can generate bubbles of hot gas in the ISM, as well as help regulate star formation and gas cooling. Black hole sink particles can be placed in the centres of galaxies or clusters, and their mass accretion rate tracked. The black hole particle consumes local gas particles stochastically, to match the accretion rate; the use of gas from the neighbourhood of the black hole means that the ISM model will have a role in determining the mass accretion rate. The black hole can then inject energy back into the surrounding gas through a luminosity proportional to the accretion rate. Mergers of black holes can also

Simulation	$L_{\rm box}$	$N_{\rm part}$	$m_{\rm p}$	η
	h^{-1}Mpc		$10^7\,h^{-1}{\rm M}_\odot$	h^{-1}kpc
MS	500	10 077 696 000	86.066	5.0
HR1	100	729 000 000	9.518	2.4
DMO	35.325	3 397 215	1.933	0.7
DMG:	35.325			
–DM		3 397 215	1.650	0.7
–Gas		2 985 242	0.2845	0.35
–Stars		1 668 836	0.06683	0.35
GDMO	35.325	207 605	1.955	0.7
GDMG:	35.325			
–DM		161 009	1.694	0.7
–Gas		141 946	0.2607	0.35
–Stars		130 873	0.06138	0.35

Table 1.2: Parameters for the simulations used in this thesis: periodic box size, numbers and masses of particles, and gravitational softening η (see equations 2.5 and 3.4). For (G)DMG and (G)DMO, we analyse the high-resolution region in the centre of the $L_{\rm box}$ cube (see text). Note that in (G)DMG, the number of gas and star particles, and their masses, vary over the course of the simulation according to the star formation algorithm. The values presented here are the numbers and median masses at $z = 0$.

be tracked. Recent simulations that include models of black holes and AGN include Sijacki and Springel (2006), Sijacki et al. (2007), and Okamoto et al. (2008).

1.5.5 Simulations used in this thesis

We use a particular set of simulations throughout this thesis. To avoid repetition in subsequent chapters, we describe their main features here. Important simulation parameters are shown in table 1.2, and their cosmological parameters are shown in table 1.3.

Simulations	$\Omega_{\Lambda,0}$	$\Omega_{\mathrm{m},0}$	$\Omega_{\mathrm{b},0}$	h	n	σ_8
MS & HR1	0.75	0.25	0.045	0.73	1.0	0.9
G/DMG & G/DMO	0.70	0.30	0.044	0.70	1.0	0.9

Table 1.3: Cosmological parameters for the simulations used in this thesis: The cosmological density parameters, the dimensionless Hubble constant, the spectral index and the power spectrum normalisation (see sections 1.1 and 1.3).

Simulations of the large scale structure

We use two main simulations that provide very large numbers of well-resolved dark matter haloes, over a broad range of masses.

The *Millennium Simulation* (MS) is a major project of the Virgo Consortium, and was run in the summer of 2004. It uses over ten billion dark matter particles (2160^3), in a periodic box of length $500\,h^{-1}$Mpc (described fully in Springel et al., 2005b). It simulates the large scale structure of a ΛCDM universe, with cosmological parameters chosen to be consistent with the results of the *Two-degree Field Galaxy Redshift Survey* (2dFGRS, Colless et al., 2001; Percival et al., 2002) and the first-year results from the *Wilkinson Microwave Anisotropy Probe* (WMAP, Spergel et al. 2003; see also Sánchez et al. 2006).

More recent data from the WMAP satellite, in combination with other data sources such as the 2dFGRS (Spergel et al., 2007; Dunkley et al., 2008; Komatsu et al., 2008), now favour a slightly different cosmology. The most significant difference is a slight tilt in the power spectrum ($n = 0.960^{+0.014}_{-0.013}$), and a lower value of $\sigma_8 = 0.817 \pm 0.026$ (Komatsu et al., 2008). A universe with a smaller n would have less power at small scales, which would delay the formation of small haloes. Although this would be significant at early times, there will be very little difference at $z = 0$. The lower σ_8 means there is less power overall, so that that rare objects (such as high-mass haloes) are made significantly rarer.

The second large-scale simulation used here we shall refer to as HR1. It uses the same cosmology as the MS, but with higher spatial resolution, fewer particles (900^3), and a smaller box size ($100\,h^{-1}$Mpc). In addition to the work presented here, this simulation has also been used in Gao et al. (2008). The HR1 simulation allows studies of the ΛCDM halo population to be extended down to lower masses, improving the dynamic range of the analyses. This is particularly important for studies of the internal structure of haloes (such as the angular momentum and density profiles), as each halo selected for study

must be well resolved down to a very small distance from the centre.

Both the MS and HR1 simulations were performed using L-GADGET-2, a 'lean' version of the GADGET-2 code that had been optimised for massively parallel computation and low memory consumption (Springel, 2005; Springel et al., 2005b).

Simulations of galaxy formation

The use of the HR1 simulation allows us to push the mass of well-resolved haloes down to the scale of individual galaxies. However, these haloes are simulated using only dissipationless dark matter particles: in the real world, we expect the structure of the inner regions of haloes (at least) to be substantially modified by the action of baryonic processes. To investigate these effects, we have made use of the simulations described in Okamoto et al. (2005)[11]. The code used was the modified version of GADGET-2, which includes a sophisticated implementation of the physical processes required for forming galaxies. Although we briefly review the details of these processes here, the reader is referred to the original paper for the full details.

The main galaxy-formation simulation consists of a periodic box of length $35.325\,h^{-1}$Mpc, initially containing an arrangement of dissipationless particles of various masses, and SPH gas particles co-incident with the highest resolution (lowest mass) dissipationless particles. This evolves over cosmic time, such that at $z = 0$ there is a population of dark matter haloes and galaxies in a roughly spherical high-resolution region in the centre of the box, with a diameter of about $12.5\,h^{-1}$Mpc. This is surrounded by progressively lower-resolution boundary particles.

The modelling of the interstellar medium (ISM) mostly follows the method of Springel and Hernquist (2003): the ISM is a two-phase gas, consisting of an ambient hot phase and cool clouds, in pressure equilibrium with each other. The heating and cooling of gas is done under the assumptions of collisional ionisation equilibrium and the presence of a uniform ultraviolet background that evolves with time (Haardt and Madau, 1996). Cooling depends explicitly on the gas metallicity, using the cooling tables from Sutherland and Dopita (1993). Molecular cooling and metal cooling for temperatures below $10^4\,$K are not included.

Energy to heat the gas is supplied from both Type II and Type Ia supernovae, and provides a feedback mechanism from the stellar population. Stars form from the cool gas in either a 'quiescent' or 'burst' mode. In quiescent star formation, stars form according

[11] Libeskind et al. (2007) also used them, to investigate satellite galaxy alignments

to a given probability once the cold gas density goes above a certain threshold. Stars are formed with an initial mass function (IMF) following Salpeter (1955). For the burst mode, star formation occurs with a top-heavy IMF (Baugh et al., 2005) and a shorter star-formation timescale. This causes stronger feedback due to the increased number of subsequent supernovae; the resultant heating is greater than the local cooling, and the heated gas gets blown out of the galaxy. The starbursts are triggered by the presence of shocks, which are typically caused by galaxy mergers.

These prescriptions for star formation and feedback ensure that much gas remains hot during the early stages of the galaxy-formation process, and that once the merger-rate has reduced at later times the gas can cool and form stars stably, resulting in realistic galaxies. We shall refer to the simulation ran with this code as "DMG" (dark matter plus galaxies; this was the 'SR' simulation of Libeskind et al. 2007).

In addition, we re-ran the DMG simulation without baryons, redistributing the baryonic mass to the dark matter in the initial conditions to conserve the overall mass. Using this dark-matter only ("DMO") simulation allows us to link the complex physics but relatively few objects of the DMG simulation with the simpler physics of the MS and HR1, which contain many orders of magnitude more objects. Furthermore, since both DMO and DMG use the same mass distribution in the initial conditions, individual haloes from the two simulations can be compared directly, allowing the effects of baryonic physics to be seen in detail.

In Chapter 4, we also use the single-halo simulation described in Okamoto et al. (2005) and Libeskind et al. (2007) (referred to there as 'SD'), which uses the same physical model and is at approximately the same resolution. It provides a single additional well-resolved galaxy–halo system, which is very welcome given the strenuous resolution constraints required for the analysis of density profiles. The high-resolution region at $z = 0$ is roughly spherical with a diameter of $1.8\,h^{-1}$Mpc. We shall refer to this simulation as 'GDMG', and its corresponding dark matter-only version as 'GDMO'.

The cosmological parameters used for these galaxy-formation simulations are slightly different to those of the MS and HR1, but this is not expected to significantly affect the results.

1.6 Structure of this thesis

In this thesis, we analyse the properties of haloes identified at $z = 0$ in the simulations described above, with a focus on their angular momentum and density profiles. These properties are not only fundamental to our understanding of the growth and structure of dark matter haloes, but they are also essential to current and future observational tests of the ΛCDM model. The distribution of halo angular momentum is a key parameter in models of the growth of galactic discs, and the mass density profile is now able to be measured through gravitational lensing.

Chapter 2 focuses on the dimensionless spin parameter, λ, which is a measure of the amount of coherent rotation in an isolated system. We characterise the spin parameter distribution, and its dependence on halo mass. We also measure the shapes of the haloes, and relate the shape distribution to that of both the spin magnitudes and directions. These distributions can depend sensitively on the halo definition used, and we test this by comparing the results from different halo finders. Finally, we relate the spin and shape of the haloes to their spatial clustering, and measure how these properties bias the halo population with respect to the mean dark matter distribution.

In Chapter 3, we extend the study of halo spin to look at the direction and magnitude of the angular momentum vector itself, as a function of halo radius. However, we expect the inner regions of real haloes to be influenced by baryonic processes, so in addition to the large-scale dark matter simulations, we use the DMO and DMG simulations to measure the effect of the baryons. This also lets me compare the orientation of galaxies with respect to their parent haloes, which leads to consequences for possible tests of ΛCDM using weak gravitational lensing.

Chapter 4 studies the density profiles of haloes. Using the Millennium Simulation halo concentration parameters derived in Neto et al. (2007), we investigated the source of the scatter in the concentration-mass relation. This involves investigating correlations between concentration, the spin parameter, and the halo formation time (measured using the merger trees). Since the definition of 'formation time" is somewhat arbitrary, we compare the measured concentrations with those predicted by three models, which take into account different aspects of the halo merger history. As with the angular momentum, we then move on to analyse the density profiles of haloes with baryons, comparing individual haloes in the DMO and DMG simulations. Finally, we look at the haloes' corresponding circular velocity profiles, and compare them to the Universal Rotation Curve (URC)

model, which is calibrated to match observational data.

We bring together the conclusions of the thesis in Chapter 5. Appendix A contains a gallery of haloes. The first set illustrate various important aspects of the groupfinder algorithms tested in Chapter 2. These are followed by images of the four best-resolved haloes from the DMO/DMG simulations used in Chapters 3 and 4. Finally, Appendix B gives details of the bootstrap tests of the angular momentum profile orientation, used in Chapter 3.

Chapter 2

The spin and shape of dark matter haloes

2.1 Introduction

The formation of galaxies is intimately linked to the acquisition and distribution of angular momentum. In the current cosmological paradigm, the inflationary ΛCDM model, cosmic structures grow hierarchically. Dark matter haloes form by the dissipationless gravitational collapse of material associated with peaks in the primordial density fluctuation field, growing, through mergers and smooth accretion, into objects with a wide range of masses at the present day. Galaxies form when baryons cool and condense near the centre of these haloes (White and Rees 1978, White and Frenk 1991). They undergo mergers and tidal interactions along with their haloes, giving rise to the rich spectrum of galaxy types and environments that we see today.

Understanding the generation and evolution of the angular momentum of dark matter haloes is a prerequisite for understanding the angular momentum and morphology of galaxies. For example, the distribution of halo spins is a basic input to models of galaxy formation (e.g. Mo et al. 1998, van den Bosch 1998, Cole et al. 2000). The early evolution of the angular momentum of a density perturbation is adequately described by the linear tidal torque theory (see section 1.4, and e.g. Hoyle 1951, Peebles 1969, Doroshkevich 1970, White 1984, Catelan and Theuns 1996, Lee and Pen 2000). However, as work such as that of White (1984) and Porciani et al. (2002a) has shown, the non-linear effects inherent in the formation of large-scale structure lead to large quantitative disagreements between the predictions of the tidal torque theory and the angular momenta found in N-body simulations of dark matter haloes.

N-body simulations provide the way to progress beyond the linear regime. As computing power has improved, so has the scale and resolution of simulations. Very early numerical studies of the angular momentum of "proto-galaxies" were performed by Pee-

bles (1971) (with $N_{\rm p} \sim 100$ particles) and Efstathiou and Jones (1979) ($N_{\rm p} = 1000$), and led the way to the analysis of the spins and shapes of CDM haloes in more sophisticated simulations (Davis et al. 1985; Barnes and Efstathiou 1987; Frenk et al. 1988; all with $N_{\rm p} = 32\,768$). Warren et al. (1992) used a much larger simulation ($N_{\rm p} \sim 10^6$) and focused particularly on the details of the distributions of halo spins and shapes, and their relationship through the alignment of the halo angular momentum vector. Cole and Lacey (1996) also investigated the shapes and spins of dark matter haloes, in addition to various other aspects of halo structure.

An early study by Barnes and Efstathiou (1987) examined the relationship between spin and the spatial clustering of haloes, as measured by the two-point correlation function. Later, Lemson and Kauffmann (1999) examined the environmental dependence of halo properties, and found no correlations with halo spin. More recently, Faltenbacher et al. (2002) carried out a mark correlation function analysis to investigate how spin varies with halo pair-separation. They found that neighbouring cluster pairs tend to have higher spins than the average.

Recent years have seen a large amount of work on the analysis of haloes in ΛCDM simulations. Halo shapes and their variation with mass were investigated by Bullock (2002), Kasun and Evrard (2005), Shaw et al. (2006) and Allgood et al. (2006). In agreement with previous studies, halo spin was found to vary little, if at all, with halo mass. The relationship between halo shape and spin was investigated by Bailin and Steinmetz (2005), Avila-Reese et al. (2005), Shaw et al. (2006) and Gottlöber and Turchaninov (2006). While the work presented here was being completed an independent analysis of halo properties, investigating halo concentrations, spins and shapes in a series of simulations, was published by Macciò et al. (2007).

Using the the 10-billion particle Millennium Simulation of the evolution of dark matter in the ΛCDM cosmology (Springel et al. 2005b, see section 1.5.5), we re-examine, in this chapter, some of the shape and spin properties of dark matter haloes previously considered. Our analysis improves upon earlier work because the millions of haloes that formed in this simulation provide unprecedented statistical power. This allows us, for example, to quantify the distribution of halo spins and the relationship between spin, halo mass and shape with a precision that has not hitherto been possible. Unlike previous work, we consider different ways to identify haloes in the simulations; it turns out that the details of halo definition and selection can have a strong impact on the results. Finally we investigate how halo clustering depends on spin and shape for haloes of different masses.

This chapter is structured as follows. Section 2.2 provides a description of the Millennium Simulation itself, and the various halo properties we shall be investigating. Section 2.3 describes the construction of the catalogues whose haloes we investigate, including the group-finding algorithms and halo selection criteria. These we use to remove haloes whose properties are unreliable or biased, due to both numerical effects and the group-finding algorithms themselves. The main results of this chapter are presented in section 2.4, where we describe the distribution of halo spins as a function of mass and shape, and examine its effect on halo clustering. Our conclusions are presented in section 2.5. In addition, Appendix A shows various examples of haloes that illustrate the effects of the group-finders.

2.2 Dark matter halo properties

The Millennium Simulation is described in section 1.5.5. It followed the evolution of 10 billion dark matter particles in the ΛCDM model, which cluster under gravity to form 'haloes', groups of particles selected according to a particular algorithm. For each halo-finding algorithm we consider in this chapter, we compute a range of halo properties. We shall discuss these quantities here, and defer the details of the halo-finding and halo-selection procedures to the next section.

Much of this work concentrates on the dimensionless spin parameter λ, introduced by Peebles (1969, 1971). This is defined as:

$$\lambda \equiv \frac{J|E|^{1/2}}{GM_{\rm h}^{5/2}} \equiv \frac{j|E|^{1/2}}{GM_{\rm h}^{3/2}}, \tag{2.1}$$

where $M_{\rm h}$ is the halo mass, J is the magnitude of the angular momentum vector $\boldsymbol{J}$ (and j is the specific angular momentum), E is the total energy, and G is Newton's gravitational constant. It is important to note that λ is defined for any object which has a well-defined j, E and $M_{\rm h}$; all these quantities are conserved for an isolated system, virialised or not. In reality, none of the haloes in cosmological simulations are completely isolated, leading to ambiguities in the definition. This means that for the λ of a halo to be useful, it is the definition of *halo* that requires the most care (and conditions such as virialisation; see section 2.3.2), not the definition of λ.

The meaning of λ is therefore best understood by considering an isolated, virialised, spherical system. The spin parameter can be seen to be a measure of the amount of coherent rotation in a system compared to random motions. For a spherical object, it is

approximately the ratio of its own angular velocity to the angular velocity needed for it to be supported against gravity solely by rotation (see e.g. Padmanabhan, 1993).

The specific angular momentum $\boldsymbol{j}$ and kinetic energy T of each halo containing N_p particles are given by[1]:

$$\boldsymbol{j} = \frac{1}{N_\mathrm{p}} \sum_{i=1}^{N_\mathrm{p}} \boldsymbol{r}_i \times \boldsymbol{v}_i \tag{2.2}$$

$$T = \frac{1}{2} m_\mathrm{p} \sum_{i=1}^{N_\mathrm{p}} \boldsymbol{v}_i^2 \tag{2.3}$$

where $\boldsymbol{r}_i$ is the position vector of particle i relative to the halo centre, and $\boldsymbol{v}_i$ is its velocity relative to the halo centre of momentum.

The halo potential energy, U, is calculated using all halo particles if $M_\mathrm{h} \leq 1000 m_\mathrm{p}$, and is rescaled up from that of 1000 randomly-sampled particles otherwise. The potential is that used in the simulation itself:

$$U = \left(\frac{N_\mathrm{p}^2 - N_\mathrm{p}}{N_\mathrm{sel}^2 - N_\mathrm{sel}} \right) \left(\frac{-G m_\mathrm{p}^2}{\eta} \right) \sum_{i=1}^{N_\mathrm{sel}-1} \sum_{j=i+1}^{N_\mathrm{sel}} -W_2(r_{ij}/\eta) \tag{2.4}$$

where N_sel is the number of selected particles ($N_\mathrm{sel} \leq 1000$), η is the softening length (see table 1.2), r_{ij} is the magnitude of the separation vector between the ith and jth particles in the halo, and the softening kernel (see Springel et al., 2001b) is:

$$W_2(u) = \begin{cases} \frac{16}{3}u^2 - \frac{48}{5}u^4 + \frac{32}{5}u^5 - \frac{14}{5}, & 0 \leq u \leq \frac{1}{2}, \\ \frac{1}{15u} + \frac{32}{3}u^2 - 16u^3 + \frac{48}{5}u^4 - \frac{32}{15}u^5 - \frac{16}{5}, & \frac{1}{2} \leq u \leq 1, \\ -\frac{1}{u}, & u \geq 1 \end{cases} \tag{2.5}$$

A halo's shape is derived from its mass distribution, which we characterise using the inertia tensor, I. This relates angular momentum $\boldsymbol{J}$ and angular velocity $\boldsymbol{\omega}$ through $\boldsymbol{J} = \mathsf{I}\boldsymbol{\omega}$, and is formed from the following components:

$$I_{\alpha\beta} \equiv \sum_{i=1}^{N_\mathrm{p}} m_i \left(\boldsymbol{r}_i^2 \delta_{\alpha\beta} - r_{i,\alpha} r_{i,\beta} \right), \tag{2.6}$$

where $\boldsymbol{r}_i$ is the position vector of the ith particle, α and β are are the tensor indices with values of 1, 2 or 3, and $\delta_{\alpha\beta}$ is the Kronecker delta. The process of diagonalising I is equivalent to rotating the coordinate system to find a set of axes in which a torque about one does not induce a rotation about another; i.e. such that $\boldsymbol{J}$ is parallel to $\boldsymbol{\omega}$. These

[1]Note that in the original paper of Bett et al. (2007), the expression for T had an error, with M_h written instead of m_p. The correct version had been used in the code, so this did not affect any results.

axes then describe a hypothetical uniform ellipsoid whose axes $a \geq b \geq c$ are those of the halo itself:

$$\mathsf{I} = \frac{1}{5} M_{\rm h} \begin{pmatrix} b^2 + c^2 & 0 & 0 \\ 0 & a^2 + c^2 & 0 \\ 0 & 0 & a^2 + b^2 \end{pmatrix}. \tag{2.7}$$

The eigenvalues are the moments of inertia $\mathcal{I}$ for rotation about that axis. For example, rotation about the semi-major axis $\boldsymbol{a}$ has the moment of inertia $\mathcal{I}_a = \frac{1}{5} M_{\rm h}(b^2 + c^2)$; note that $\mathcal{I}_a \leq \mathcal{I}_b \leq \mathcal{I}_c$. These eigenvalues can then be combined to find the relative axis lengths, e.g.

$$a = \sqrt{\frac{5}{2M_{\rm h}} (-\mathcal{I}_a + \mathcal{I}_b + \mathcal{I}_c)}. \tag{2.8}$$

The axis vectors are given directly by the corresponding eigenvectors, so that, for example, rotation about the $\boldsymbol{a}$-axis of the ellipsoid (with the longest length a) has the smallest moment of inertia, $\mathcal{I}_a$.

Much of the literature on halo shapes uses the following description of the mass distribution, confusingly also calling it the inertia tensor (e.g. Cole and Lacey 1996, Hopkins et al. 2005, Bailin and Steinmetz 2005, Shaw et al. 2006):

$$\mathcal{M}_{\alpha\beta} = \frac{1}{N_{\rm p}} \sum_{i=1}^{N_{\rm p}} r_{i,\alpha} r_{i,\beta}. \tag{2.9}$$

Since $I_{\alpha\beta} = \mathcal{M}_{\gamma\gamma}\delta_{\alpha\beta} - \mathcal{M}_{\alpha\beta}$, the results are entirely equivalent: if one diagonalises this matrix, then a, b and c can be found as just the square roots of the eigenvalues, and the eigenvectors again give the axis vectors (see also the discussion in section 1.4).

Once the halo's principal axes have been found, relationships between the axes and between the shape and other properties such as spin can be examined in terms of the axis ratios $p \equiv c/b$, $q \equiv b/a$ and $s \equiv c/a$. The minor-to-major axis ratio s is a useful measure of the sphericity of the system, but does not specify in what way a halo might be aspherical. For this, we can use the triaxiality parameter introduced by Franx et al. (1991):

$$\mathcal{T} = \frac{a^2 - b^2}{a^2 - c^2} \tag{2.10}$$

This measures whether a halo is prolate ($\mathcal{T} = 1$) or oblate ($\mathcal{T} = 0$), but it does not quantify how aspherical a halo is.

2.3 The halo catalogues

2.3.1 Groupfinder algorithms

The problem of how best to identify groups of particles within N-body simulations is a ubiquitous feature in studies of dark-matter halo properties. Many solutions have been found to this problem, typically involving first finding candidate-halo centres, followed by an iterative scheme to shrink or grow the halo according to criteria involving the binding energy or overdensity. Such algorithms include Bound Density Maxima (BDM, Klypin et al. 1999), Spline Kernel Interpolative DENMAX (SKID, Weinberg et al. 1997), the AMIGA Halo Finder (AHF, Gill et al. 2004), and SUBFIND (Springel et al., 2001a), which we use below.

The very simple 'friends-of-friends' group-finder (FOF, Davis et al. 1985) was run on-the-fly, during the Millennium Simulation run, with a linking length of $s_0 = b(L^3_{\rm box}/N_{\rm part})^{1/3}$ where $b = 0.2$, to attempt to select virialised structures in the particle distribution. As is often the case (e.g. Porciani et al. 2002a, Shaw et al. 2006, Macciò et al. 2007), this simple FOF catalogue forms the basis for the more sophisticated halo definitions we use.

An enhanced version of the SUBFIND program (Springel et al., 2005b) was run on the data to identify self-bound substructures within each FOF halo, which we then use to construct the different group catalogues we investigate. The SUBFIND algorithm is essentially a two-step process. The first task is to identify subhalo candidates within each FOF halo. This is done using an adaptively-smoothed dark matter density field, effectively lowering a density threshold and identifying the peaks that grow out of it. The second stage consists of performing an iterative gravitational unbinding procedure on the candidates, successively removing particles that are not bound to the subhalo candidate. For this purpose, the potential energies are computed using a tree algorithm similar to that used for the simulation itself. The candidates that are left with at least 20 particles after this procedure are then subhaloes of the parent halo. The algorithm can and does identify subhaloes within subhaloes. It results in the FOF haloes typically consisting of a hierarchy of self-bound structures (which are not necessarily bound to each other), and a set of particles (referred to as "fuzz") that are spatially linked to the halo but not part of any self-bound (sub)structure. The most massive "subhalo" (MMSH) typically contains most of the mass of the corresponding FOF object, and so is best regarded as the self-bound background halo itself, with the remaining subhaloes as its substructure.

In addition to finding the bound structures within haloes, SUBFIND also computes

Halo catalogue	Number of haloes	
FOF (without SUBFIND)	17 709 121	('raw' catalogue)
FOFall	15 494 624	(87.5% of FOF raw)
FOFclean	1 332 239	(8.60% of FOFall)
SOall	15 458 379	(99.8% of FOFall)
SOclean	1 239 494	(8.02% of SOall)
TREEall	17 041 498	(110.0% of FOFall)
TREEclean	1 503 922	(8.83% of TREEall)

Table 2.1: Numbers of haloes in the halo catalogues defined in this chapter. The "all" catalogues are the unfiltered results of the groupfinder algorithms described in sections 2.3.1, 2.3.1 and 2.3.2. The "clean" catalogues have been filtered as discussed in sections 2.3.2 and 2.3.2, with the quasi-equilibrium parameter $Q = 0.5$ and the particle-number limit $N_{\rm p} \geq 300$.

certain subhalo properties, which are then stored in the subhalo catalogue files. These include the location of the potential minimum, the ID number of the most bound particle, the mass (number of particles), and the half-mass radius. SUBFIND also computes and stores additional data related to each parent halo. Starting at the potential minimum of the MMSH of a halo, three radii are found: the first two are those where the density within them drops below $200\rho_{\rm crit}$ and $200\bar{\rho}$, to aid comparison with other work. The third is the virial radius proper, which uses the fitting formula of Bryan and Norman (1998) for spherical top-hat collapse in a flat ($\Omega_\Lambda + \Omega_{\rm m} = 1$) cosmology (see also Eke et al. 1996):

$$\frac{\rho}{\rho_{\rm crit}} = 18\pi^2 + 82(\Omega_{\rm m}(z) - 1) - 39(\Omega_{\rm m}(z) - 1)^2 \tag{2.11}$$

This gives $\rho/\rho_{\rm crit} \approx 94$ at $z = 0$. Although these properties are associated with sets of grouped particles, SUBFIND does not restrict itself to these particles when computing them.

We will now describe the group catalogues whose halo properties we have investigated, and how they are built from the results of the FOF and SUBFIND algorithms. A key point that is used for each halo definition is that we take the halo centre to be at the potential minimum of the MMSH. For reference, table 2.1 gives a list of each halo catalogue we will discuss, and the number of haloes they contain.

FOF haloes

The basic FOF algorithm, run as already described, results in 17 709 121 groups containing at least 20 particles, i.e. of mass $\gtrsim 1.7 \times 10^{10}\, h^{-1}\mathrm{M}_{\odot}$, at redshift $z = 0$. The most massive group contained 4 386 162 particles ($\approx 3.8 \times 10^{15}\, h^{-1}\mathrm{M}_{\odot}$). Using this catalogue we can therefore identify dark matter haloes over a range of more than 5 orders of magnitude in mass, ranging from subgalactic clumps to the most massive clusters.

In practice, since we use the centre (potential minimum) of the MMSHs as the centres of the haloes themselves, we only use FOF haloes for which SUBFIND has found bound substructures. Haloes without substructure (and hence without an MMSH) are excluded from our base FOF catalogue. This has the effect of reducing the catalogue size by 12.5%, preferentially at lower masses. We shall refer to this catalogue as FOFall, and we will not discuss the larger raw FOF catalogue further.

SO haloes

The properties calculated by SUBFIND make it possible to construct a second halo catalogue, in which each halo consists of only the particles within R_{vir} of the centre of the MMSH of the corresponding FOF object (note that these particles do not have to be members of the FOF halo). Due to the way SUBFIND constructs the MMSH, this yields haloes whose definition is similar to those from a "spherical overdensity" algorithm (Lacey and Cole, 1994), so we will refer to them as the SO haloes. We do not impose a lower limit on the number of particles comprising these objects; as a result, haloes can be identified with masses $< 20m_{\mathrm{p}}$ when their virial radii encompass fewer particles than their original FOF halo. This is simply a consequence of the algorithm employed; later examination of halo spins reveals the need for a much higher particle-number limit, as discussed in full in section 2.3.2. This halo definition is similar, but not identical, to that used in Macciò et al. (2007).

2.3.2 Better halo catalogues

Groupfinder problems

The FOF and SO group-finding algorithms have various well-documented drawbacks. Groupfinders such as SO which use the overdensity contained within a spherical region tend to impose a more spherical geometry on the resulting systems. Although this is not a problem for many objects, the algorithm can sometimes result in very unnatural-looking

structures. An example is shown in figure A.4. This compares a massive FOF halo with the corresponding SO object. The centre of mass of the FOF system is well separated from the minimum of the potential, and the halo is significantly elongated. This results, when growing a sphere around the potential minimum to form the SO halo, in the virial overdensity being reached sooner in one direction than another. The SO halo contains particles in low-density regions outside the FOF halo, and has a sharp cutoff in another direction when the FOF halo continues. The more 'normal' haloes, in the background, are much less affected.

The problems associated with the FOF groupfinder can be more extreme, and can affect a greater proportion of the haloes. One of the most commonly-cited problems (e.g. Gelb and Bertschinger 1994, Governato et al. 1997) is that well-resolved objects identified using the FOF algorithm are often at risk of becoming linked with neighbouring objects via tenuous bridges of particles. Low-mass particle bridges are usually extremely transient structures, being just a chance grouping of particles at that instant in time. The joining of two (or more) otherwise unrelated objects of similar mass in this way results in a very large velocity dispersion. Examining the halo in velocity-space will clearly show the multiple-object nature of the system. An example of a halo formed from objects joined by a tenuous bridge can be seen in figure A.1.

Sometimes more massive haloes can be formed by the chaining together of somewhat smaller objects that are undergoing mergers or close flybys with their neighbours. Their multi-object composition can again be seen in velocity space as well as in real space, and although their connections are likely to be less transitory than in the case of a thin bridge, these objects are nevertheless well out of their equilibrium state, and so are unhelpful when trying to characterise the spins of typical dark matter haloes. See figure A.2 for an example of a larger multi-object halo.

A similar effect is that of velocity contamination of small objects due to their proximity to more massive ones (see figure A.3 for an example). Just as particles can form a bridge between passing haloes at the moment of the snapshot, so an individual particle orbit can take it within the linking length of a neighbouring halo, without forming enough of a bridge for the haloes themselves to be joined. The smaller halo will be contaminated by these interloper particles, which will have a quite different mean velocity to the halo's own particles. This causes the mean velocity to be shifted away from that of the 'original' halo, and the resulting halo to have a much larger velocity dispersion than expected for an object of that mass. The massive neighbouring object will have a much higher velocity

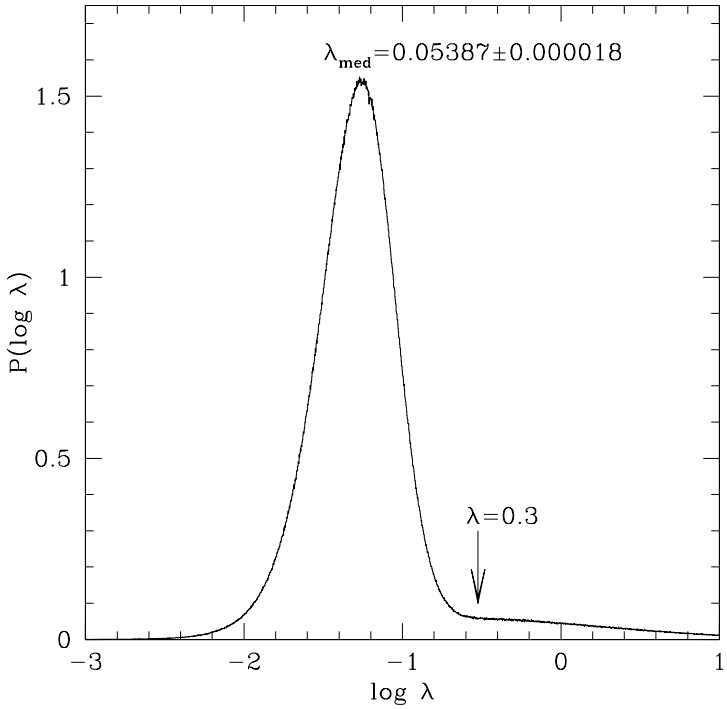

Figure 2.1: Histogram of the spin parameters from the basic FOFall halo catalogue of the Millennium Simulation, showing a long tail to high spins. The tail continues up to $\lambda \approx 680$, and there are over 900 000 objects with $\lambda \geq 0.3$ (marked on the graph). The median spin of the distribution, $\lambda_{\rm med}$, is displayed with the uncertainty given by equation 2.13. This demonstrates the need for more careful definition and selection of haloes.

dispersion anyway, so will be unaffected by such effects.

To illustrate the effect that these problems have on the physical properties we calculate, we show the spin distribution of the FOFall catalogue in figure 2.1. It shows a long tail at higher spins; there are 900 748 objects (6% of the catalogue) with spin $\lambda \geq 0.3$. Figure 2.2 shows the FOFall spin distribution as a function of halo mass, rescaled to show the fractional number of objects at each mass so the trend of the mass function is removed. It shows that the high-spin tail comes from objects over a large range of masses, and is therefore not due to under-resolving groups. These presumed-anomalous high spins come from objects with high velocity dispersions for their masses, caused by situations such as those described above. This increases the haloes' kinetic energies, T, leading to large values of λ.

These features are not usually seen in other published spin distributions (e.g. Gardner 2001, Vitvitska et al. 2002, Avila-Reese et al. 2005, Tonini et al. 2006, among many

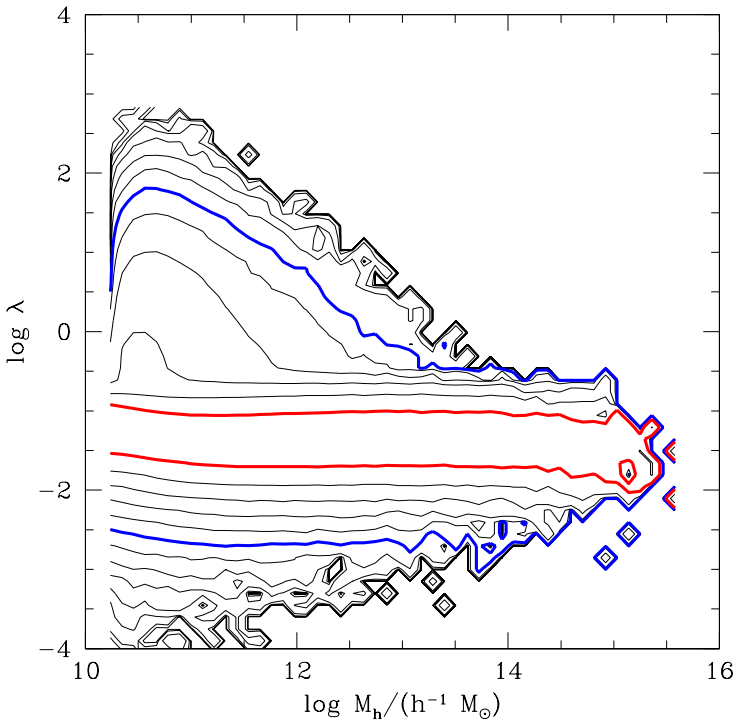

Figure 2.2: Halo spin as a function of halo mass for the FOFall halo catalogue. The contours indicate the relative number density of haloes with that value of $\lambda(M_{\rm h})$; that is, the haloes were binned onto a 50×50 grid between the maximum and minimum values in $\log M_{\rm h}$ and $\log \lambda$, and the number of haloes in each grid cell was normalised by the number of haloes in that mass-bin, thus removing the effects of the halo mass function from the plot. The contours are spaced logarithmically, with one contour for every factor of $10^{0.5}$ in halo number density. The innermost bold contour (red) represents 10^{-1} (i.e. a tenth of the haloes in each mass bin), and the outer bold contour (blue) represents $10^{-3.5}$. Notice the high-spin bulge, which extends over a large range of halo masses. The results for SO haloes show a very similar distribution.

others), partly because more advanced groupfinders and halo selection criteria are often used (as we do below). However, the fact that we can see these artifacts so clearly is because the Millennium Simulation gives us a vast number of objects, over a wide range of masses.

For convenience, we shall refer to haloes suffering from the problems described in this subsection as "mis-defined" haloes, as their anomalously-high spins originate in how the haloes are defined by the groupfinder algorithm in relation to their environment, rather than any physical or numerical effect.

A better groupfinder: The TREE haloes

As a third definition of halo, we use the 'merger-tree' haloes described by Harker et al. (2006). These are the $z = 0$ objects in a catalogue of halo merger trees constructed in the Millennium Simulation. These merger trees are similar to, but distinct from those of Springel et al. (2005b) and Gao et al. (2005), who used different criteria for identifying and tracking the haloes over time. The merger-tree-halo catalogue used here was designed with the needs of the N-body GALFORM semi-analytic models in mind (e.g. Helly et al. 2003, Bower et al. 2006).

The haloes in the TREE catalogue are formed from the SUBFIND subhalo catalogue (based on the FOF haloes) in the following way. Each halo is initially taken to consist solely of its constituent subhaloes (i.e., is equivalent to the corresponding FOF halo, but without the "fuzz"). Next, a "splitting" algorithm is applied, which attempts to account for the linking of distinct, bound objects that often occurs with FOF. A subhalo can be split off from its parent halo if it satisfies at least one of the following conditions: (1) The distance between the subhalo's centre and the parent's centre is more than twice the parent's half-mass radius; or (2) the subhalo has retained at least 75% of the mass it had at the last snapshot in which it was an independent halo. This second condition, which uses the merger-tree data, is based on the idea that if the subhalo was genuinely merging with the halo, it would be rapidly stripped of its mass. If however it was just a rapid encounter causing an artificial link, then its mass would be retained. If the subhalo is split off, any other subhaloes that reside within twice *its* half-mass radius are also split off to become part of the new halo. We shall refer to the catalogue of all haloes defined in this method as the TREEall catalogue.

This definition of the TREE-halo catalogue alleviates the groupfinder-based problems somewhat. The unbound particles excluded from the TREE haloes have, by definition,

higher velocities than the bound structures in the haloes. Their removal therefore reveals the more relaxed underlying haloes, with lower kinetic energies and hence λ. "Interloper particle" contamination, in particular, is reduced by this feature. The halo splitting algorithm also helps in many cases by separating objects that have been spuriously linked by bridges.

The spin-mass distribution of the TREEall catalogue can be seen in figure 2.3; although some of the high-spin objects remain, the majority are now gone (there are sufficiently few high-spin objects remaining that they are invisible in a plot of $P(\log \lambda)$ such as Fig 2.2). Investigating the remaining high-spin objects reveals them to be victims of velocity contamination from very massive neighbours. They are somewhat special cases however: for them not to have been rejected as fuzz, the contaminants must be self-bound bodies, with ≥ 20 particles each. They must also be built on density maxima independent of that of the host halo, in order for SUBFIND to have identified them as separate subhaloes. Furthermore, the interloping subhalo must be within twice the half-mass radius of the halo, so that the tree algorithm does not split it off. A consequence of this is that the resulting halo must consist of at least 40 particles (20 for the interloper subhalo and 20 for the main halo), and this can be seen in the offset low-mass cutoff for high-λ haloes in figure 2.3.

A better halo catalogue: The QE criterion

A relatively simple way of culling the remaining anomalous spin objects is to remove those that are clearly out of equilibrium at the moment of the snapshot. This is not quite the same as selecting only objects that are within a certain degree of true virialisation, since we do not have the necessary time-resolution to determine if the system properties are genuinely stationary: just as an object can appear to be linked to another by a bridge that may exist only fleetingly, so a halo could instantaneously have very similar energies to those of a stationary system. Therefore we will apply a cut in the instantaneous 'virial ratio' of halo energies, $2T/U+1$, and describe the objects that meet this criterion as haloes in a *quasi-equilibrium* (QE) state. This name avoids implying the zero time-derivative necessary for the true virial ratio.

The question of where to make the cut in 'virialisation' (i.e. applying a QE limit) is a difficult one, because the decision will always be somewhat arbitrary. Since it is desirable to minimise the effect of such arbitrariness, we concentrate on the effect of applying a QE limit to the TREE haloes, since the merger-tree algorithm has already removed many of

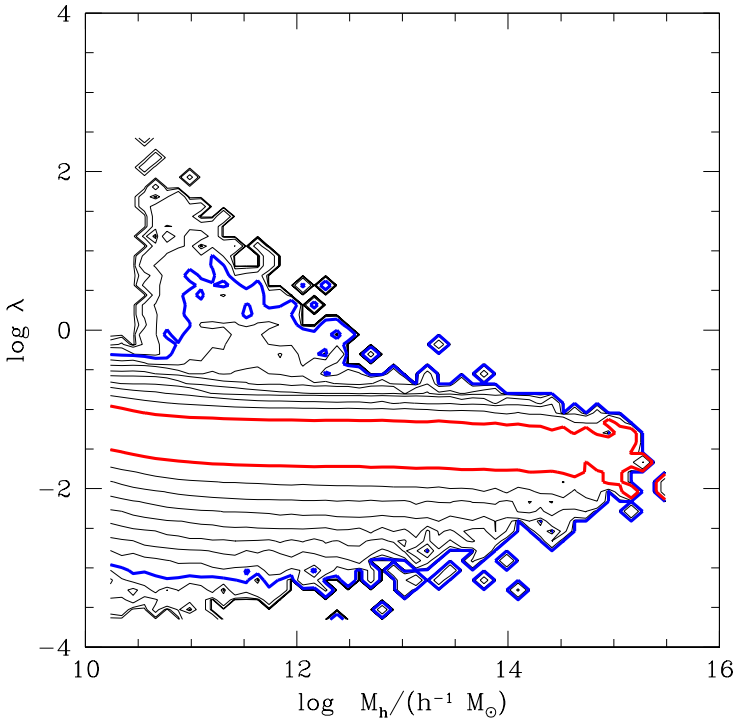

Figure 2.3: Spin as a function of halo mass for haloes in the TREEall catalogue. The contouring is as in figure 2.2, i.e. in equal logarithmic steps of $10^{0.5}$, normalised to remove the mass function. In this plot, the inner bold contour (red) represents 10^{-1} of the haloes at each mass, and the outer bold contour (blue) represents 10^{-5} of the haloes at each mass. The merger-tree halo definition has moved many of the high-spin haloes visible in figure 2.2 down into the main body of the distribution.

the mis-defined haloes.

The value of $2T/U + 1$ for the TREE haloes is plotted against their mass in figure 2.4. We applied a QE cut of the form

$$-Q \leq \frac{2T}{U} + 1 \leq Q \tag{2.12}$$

to the TREEall catalogue, examining the effect of a wide range of Q-values on the $P(\log\lambda)$ and $\lambda(M_{\rm h})$ distributions. Because of the relatively small numbers of objects with anomalously high spins, we find that the QE cut makes negligible difference to the shape of the spin distribution, $P(\log\lambda)$. A very small value, $Q \lesssim 0.3$, will act to shift the median spin lower by a few percent, due to the mass dependence seen in Fig 2.4. Through a detailed examination of the $\lambda(M_{\rm h})$ distribution, we find that a value of Q between 0.4 and 0.6 gives a good balance between removing the mis-defined haloes and reducing the overall sample size (adding noise and biasing it by mass). Higher values of Q allow some mis-defined haloes to creep in, with a significant impact for $Q \gtrsim 1.0$. We will use a value of $Q = 0.5$ for our cleaned halo catalogues. This cut is shown in the horizontal dashed lines of figure 2.4, and the resulting $\lambda(M_{\rm h})$ distribution is shown in figure 2.5. Applying this form of virialisation cut on the halo catalogue provides a useful tool with which to remove haloes with anomalous spins caused by mis-defined haloes.

A better halo catalogue: Numerical effects

A second peculiarity of the spin distributions is visible in figures 2.2, 2.3 and 2.5 (for the FOFall, TREEall and quasi-equilibrium TREE halo catalogues respectively): an upturn in the spin distribution at low masses. This can be seen clearer in the variation of the median spin over mass bins $\lambda_{\rm med}(M_{\rm h})$, plotted for the FOF haloes in figure 2.6. This effect is unrelated to the velocity contamination problems of the mis-defined haloes, and instead comes from the mass resolution of the simulation affecting the angular momenta. This effect has been seen before, for example by Reed et al. (2005) in the context of subhaloes. To understand the cause of this effect, consider a continuous object with angular momentum $\boldsymbol{J_{\rm true}}$. If we construct a realisation of this object using a sample of N discrete particles, the resulting angular momentum can be modelled as the vector sum of the 'true' angular momentum (from the continuous object) with a noise vector oriented in a random direction: $\boldsymbol{J} = \boldsymbol{J_{\rm true}} + \boldsymbol{J_{\rm noise}}$. This will act to push the measured magnitude J up above $J_{\rm true}$ because the random direction of $\boldsymbol{J_{\rm noise}}$ will mean it reaches outside the sphere of radius $|\boldsymbol{J_{\rm true}}|$ more than 50% of the time. Therefore, the random noise inherent

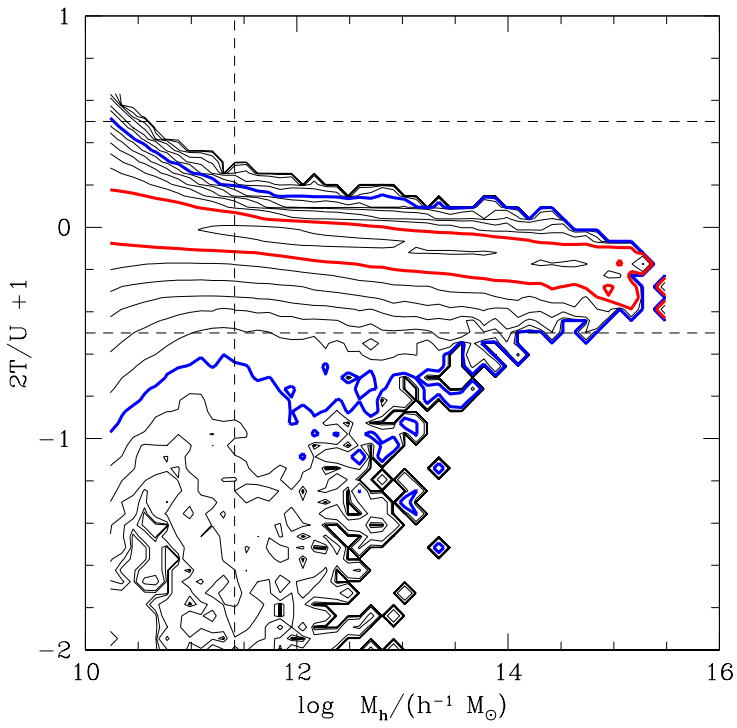

Figure 2.4: Contour plot of the instantaneous 'virial ratio', $2T/U + 1$, against halo mass for TREE haloes. A virialised object has a value around zero, and a gravitationally bound object has a value > -1. The tail at low values (large T) extends down to $2T/U + 1 \approx -960$; there are 3733 objects with $2T/U + 1 \leq -1$. The dashed lines show the QE limit of $Q = 0.5$, and the lower particle-number limit of $N_{\rm p} = 300$. The contouring is as in figure 2.2, i.e. relative halo number density in equal logarithmic steps of size $10^{0.5}$. The inner bold contour (red) represents 10^{-1} of the haloes at each mass, and the outer bold contour (blue) represents 10^{-4} of the haloes at each mass. The plots for FOF and SO groups are similar to this.

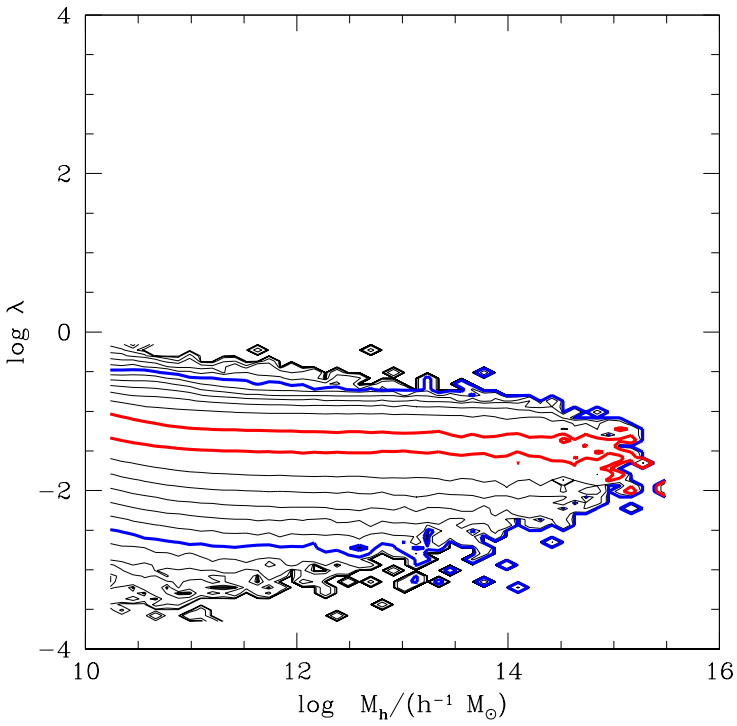

Figure 2.5: Spin parameter against halo mass for TREE haloes with a quasi-equilibrium (QE) limit of 0.5 applied; this can be compared with figures 2.2 and 2.3. The same contouring is used, i.e. relative halo number density in equal logarithmic steps of size $10^{0.5}$. The inner bold contour (red) represents 10^{-1} of the haloes at each mass, and the outer bold contour (blue) represents 10^{-4} of the haloes at each mass. The QE-limit has removed the vast majority of the high-spin haloes seen in figure 2.3.

in using discrete particles to sample a near-continuous object such as a dark matter halo would act to bias J upwards, and λ along with it.

Modern N-body codes such as the L-GADGET-2 code used for the Millennium Simulation are very good at conserving quantities such as energy and angular momentum, so for a well-resolved object there is negligible inaccuracy arising from particle discreteness. For a less well-resolved object however, the effect can nevertheless be relevant, even though the angular momentum of the particles making up the halo has been well conserved. Discreteness mainly affects the outer parts of a halo, making the effective surface more jagged than that of the continuous object it represents. We also expect the outer parts to harbour most of the angular momentum. For lower-mass haloes, a greater fraction of their particles make up these 'surface' regions, so this problem has a greater effect; the inclusion of a single particle can make a significant contribution to λ. Hence, the spin parameter rises for haloes with fewer particles because the discreteness of the haloes' surface layers adds noise to their 'true' angular momenta. (This is not the same effect as discussed in Shaw et al. (2006); there, a surface pressure term is added to the virial theorem to account for their halo truncation at $R_{\rm vir}$.)

The importance of the noise contribution to λ can be examined by determining the spin distribution of the same simulation (same code and same corresponding initial condition waves) but run at a different resolution. We performed a lower resolution resimulation of the Millennium Simulation, with $2160^3/64 = 540^3$ particles (so their mass is $m_{\rm p,low} = 64 m_{\rm p,Millen}$), which we will refer to as `milli_lowres`. The FOF and SUBFIND algorithms were implemented on `milli_lowres` in the same way as in the Millennium Simulation itself. (Although we do not have merger-tree data for `milli_lowres`, and hence cannot construct a TREE halo catalogue, the Millennium Simulation results show that the same effect is seen in FOF, SO and TREE haloes.) Figure 2.6 shows the median spin $\lambda_{\rm med}(N_{\rm p})$ for FOF haloes in the Millennium Simulation and `milli_lowres`, with vertical error bars showing a Gaussian-like estimate of the precision of the median given by:

$$\epsilon_{\rm med} \equiv \frac{(\lambda_{84} - \lambda_{16})}{\sqrt{N_{\rm halo}}} \tag{2.13}$$

where λ_i is the ith percentile of λ ($84\% - 16\% = 68\%$, the amount of data within $\pm 1\sigma$ of a Gaussian peak) and $N_{\rm halo}$ is the number of haloes in that mass bin. Note that the *spread* in λ is much greater than the uncertainty in $\lambda_{\rm med}$; compare the error bars in figure 2.6 with the data shown in figure 2.2.

Although the two curves show the same qualitative behaviour (the low-$N_{\rm p}$ upturn),

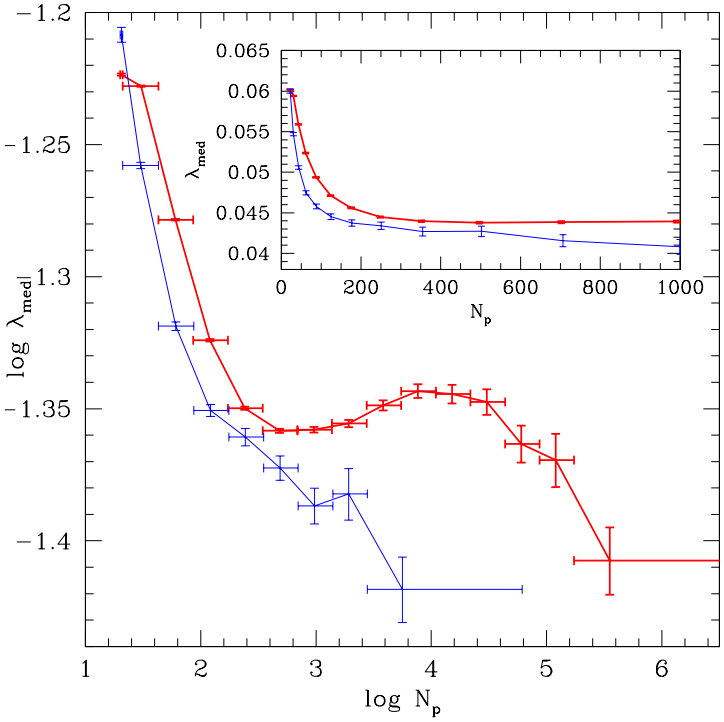

Figure 2.6: Median spins for all FOF haloes for the Millennium Simulation (thick red line) and the `milli_lowres` run (thin blue line). The most massive bin contains 2000 haloes, and the remaining bins are logarithmically spaced, with one bin every factor of 2 in halo mass (except for the leftmost bin which extends down to the cutoff limit of 20 particles.) Horizontal bars mark the bin widths, and vertical error bars give a measure of the precision of the median according to equation 2.13.

there is a vertical shift between them. This is due to `milli_lowres` containing fewer of the mis-defined objects described in section 2.3.2 than the Millennium Simulation itself. Decreasing the resolution effectively smooths the density field, so that small objects with more massive neighbours can disappear completely, whereas a more isolated object of the same mass may still survive (although containing fewer particles). This means that the "real" objects are retained (and there are still many under-resolved ones causing the upturn in $\lambda_{\rm med}(N_{\rm p})$), but there is a reduction in the number of mis-defined objects. The `milli_lowres` results seem to confirm the dominance of numerical effects at low-$N_{\rm p}$, above which the effect of noise is negligible.

If we apply the quasi-equilibrium cut described in section 2.3.2 to remove the mis-defined objects, we can examine the effect of discreteness on the median spins of just the 'real' haloes. Figure 2.7 shows $\lambda_{\rm med}(N_{\rm p})$ for QE-selected FOF haloes, compared with QE-

selected FOF haloes from `milli_lowres`. In contrast to figure 2.6, the two lines now lie on top of each other, exhibiting the same upturn in spin for haloes with the same number of particles. This demonstrates that the upturn is purely a numerical effect. We can exclude haloes that appear to be dominated by this effect by fixing a limit of $N_{\rm p} \geq 300$ on the halo catalogue.

Figure 2.4 shows how the QE and $N_{\rm p}$ cuts we use relate to one another for the TREE haloes. The low-$N_{\rm p}$ cut has a significantly stronger effect on the halo catalogue. Applying the QE cut on its own reduces the population of the TREEall catalogue by only 0.3%; applying the low-$N_{\rm p}$ limit as well means removing in total 91.17% of the original TREEall haloes (see table 2.1). We refer to the resulting cleaned TREE-halo catalogue as TREEclean, and it is these haloes whose properties we shall be examining in detail. In some cases, for completeness, we shall compare the results with those from the FOFclean and SOclean catalogues. These are cleaned using the same $Q = 0.5$ and $N_{\rm p} \geq 300$ cuts as the TREEclean catalogue.

It is important to note that the criteria we have adopted—the QE cut and low-$N_{\rm p}$ limit—are those appropriate to the quantities of interest in this work. For example, Neto et al. (2007) (see Chapter 4) use the substructure parameter $S = \Delta r/R_{\rm vir}$, where Δr is the distance between the potential minimum of the halo and its centre of mass (see section 4.2.2). Their final criteria for selecting haloes in the Millennium Simulation are $S < 0.07$ and $\frac{2T}{U} + 1 > -0.25$. They are concerned with fitting density profiles to haloes, and using the substructure parameter allows them to remove haloes with a large fraction of mass in substructures which would otherwise contaminate their results. Similarly, Macciò et al. (2007) define an "offset parameter" as $x_{\rm off} = \Delta r/R_{\rm vir}$, where Δr is measured from the most-bound particle rather than the potential minimum. They use this alongside the rms of their density profile fits, to assess the quality of their halo catalogues for estimates of halo concentration. Although we have examined the substructure/offset parameter and how it affects λ, we find that it is not useful in removing the mis-defined haloes, or those whose spins are dominated by the numerical effects discussed above.

Having successfully implemented an appropriate groupfinder and cleaned the resulting halo catalogues, we can now proceed to examine their spin properties. The FOF and TREE halo catalogues, including some halo properties and semi-analytic galaxy properties, are publicly available online[2] (Lemson and Virgo Consortium, 2006).

[2] `http://www.mpa-garching.mpg.de/millennium`

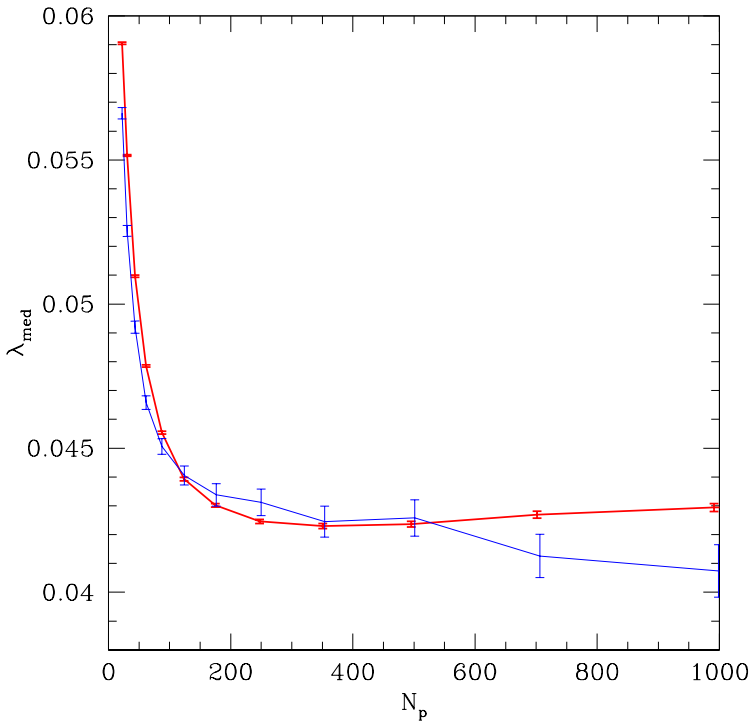

Figure 2.7: Median spins against number of particles in haloes, for FOF haloes with the QE cut applied. The thin blue line shows the `milli_lowres` haloes and the thick red line shows those from the Millennium Simulation itself. The error bars show the uncertainty on the median, using equation 2.13. The two lines show an identical trend at low $N_{\rm p}$, demonstrating that the upturn in $\lambda_{\rm med}$ is indeed a numerical effect, affecting the spins of haloes containing fewer than about 300 particles.

2.4 Results

2.4.1 The form of the spin distribution

The median spin of the TREEclean halo catalogue is $\lambda_{\rm med} = 0.0381$. The distribution of halo spins about the median, $P(\lambda)$, has been often fitted with a lognormal function (e.g. van den Bosch 1998; Gardner 2001; Bailin and Steinmetz 2005), i.e. a Gaussian in $\log\lambda$:

$$P(\log\lambda) = \frac{1}{\sigma_{\rm lg}\sqrt{2\pi}} \exp\left[-\frac{\log^2(\lambda/\lambda_0)}{2\sigma_{\rm lg}^2}\right] \tag{2.14}$$

While this fitting function has proved adequate for small numbers of objects, we find that for the $> 10^6$ haloes in the Millennium simulation, deviations from a Gaussian are clear and significant. The spin distribution drops faster than a Gaussian at high spins, and slower than a Gaussian at low spins. The best fit to the TREEclean catalogue is shown in figure 2.8, which fits equation 2.14 with peak location $\lambda_0 = 0.03687 \pm 0.000016$ and width $\sigma_{\rm lg} = 0.2216 \pm 0.00012$.[3] The corresponding lognormal function of λ has the same peak, and a width of $\sigma = \ln(10)\sigma_{\rm lg}$. The fit has a reduced-$\chi^2$ of 40.46.

Part of the reason why a lognormal is such a poor fit is that this function strongly avoids very low spin values, whereas the real distribution, based as it is on the three-dimensional vector $\boldsymbol{j}$, does not. The longer tail at low-λ is primarily due to the distribution of $\boldsymbol{j}$ being smooth and isotropic about $j = 0$, implying[4] that $P(\log\lambda) \propto \lambda^3$.

We have found that the following function provides a better description of the data:

$$P(\log\lambda) = A\left(\frac{\lambda}{\lambda_0}\right)^3 \exp\left[-\alpha\left(\frac{\lambda}{\lambda_0}\right)^{3/\alpha}\right]. \tag{2.15}$$

For the normalised spin distribution, we can express A in terms of the other free parameters, α and λ_0 (the peak location):

$$A = 3\ln(10)\frac{\alpha^{\alpha-1}}{\gamma(\alpha)}, \tag{2.16}$$

where the gamma function $\gamma(\alpha) = (\alpha-1)!$. The best fit to the data is shown in figure 2.9, and has parameters:

$$\lambda_0 = 0.04326 \pm 0.000020, \qquad \alpha = 2.509 \pm 0.0033,$$

[3] Throughout this chapter, the quoted uncertainties on best-fitting parameters are given by the square root of the diagonal of the covariance matrix for that fit.

[4] Macciò et al. (2007) claimed the low-λ tail is due to the higher uncertainty in λ at low values. However, by varying the minimum $N_{\rm p}$ for the halo catalogue, and hence the uncertainty in λ, we found that the low-λ side of the distribution consistently drops off slower than the high-λ end, confirming that this shape is not primarily due to uncertainties.

with a much-improved reduced-χ^2 of 2.58.

We have examined whether the deviations from lognormal depends on our choice of the quasi-equilibrium parameter Q when cleaning the halo catalogue. We found that the fit remains good over a wide range of Q. We have also found the best fit of equation 2.15 to the FOFclean and SOclean catalogues. The results for SOclean haloes are remarkably similar to those for the TREEclean haloes, with a reduced-χ^2 of 3.10:

$$\lambda_0 = 0.04174 \pm 0.000022, \qquad \alpha = 2.540 \pm 0.0036.$$

The median spin of the distribution is $\lambda_{\rm med} = 0.0367$. The haloes in the FOFclean catalogue, which have a median spin of $\lambda_{\rm med} = 0.04288$, are not as well fitted by equation2.15. The reduced-χ^2 is 15.0 and the parameter values are:

$$\lambda_0 = 0.04929 \pm 0.000027, \qquad \alpha = 3.220 \pm 0.0046.$$

This is, in fact, slightly worse than the best-fitting lognormal (equation 2.14), which yields a reduced-χ^2 of 12.5, with a peak location $\lambda_0 = 0.04222 \pm 0.000022$ and width $\sigma_{\rm lg} = 0.2611 \pm 0.00016$.

These tests show that the distribution of λ depends on the careful definition and selection of dark matter haloes. However, the fact that the distribution is non-lognormal is not a consequence of the particular choice of groupfinder or selection criteria used here—the form of the distribution is not peculiar to the TREEclean catalogue.

2.4.2 Correlation of spin and halo mass

The variation of median spin parameter with halo mass, for the cleaned catalogues from the three groupfinders, is shown in figure 2.10. It is interesting to note that the FOF haloes exhibit an upturn in spin for objects more massive than the low-$N_{\rm p}$ cut, an effect that is not present in the TREE or SO haloes. This can be attributed to the outer parts of the FOF haloes consisting mainly of unbound 'fuzz' particles. These will usually have higher velocities, which act to inflate the spin. These particles are not part of the TREE haloes, and most will be shaved off in SO haloes too. The SO and TREE haloes show a shallow downwards trend of $\lambda_{\rm med}$ up to $M_{\rm h} \sim 10^{13}\,h^{-1}{\rm M}_\odot \sim 12\,000 m_{\rm p}$ and a rapid decline at larger masses.

We fit a cubic polynomial to the TREEclean median spin data,

$$\log \lambda_{\rm med} = \alpha x^3 + \beta x^2 + \gamma x + \delta, \tag{2.17}$$

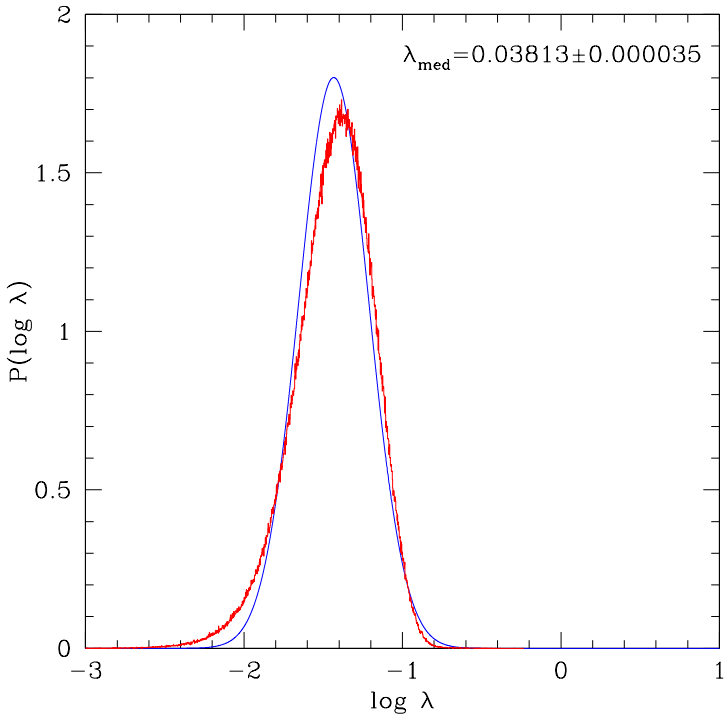

Figure 2.8: The normalised spin distribution (red histogram) for merger-tree haloes with $N_{\rm p} > 300$ and filtered using the QE criterion (the TREEclean catalogue). The best-fitting single Gaussian function is plotted as the smooth blue curve. The Gaussian drops too quickly at low spins, and too slowly at higher spins. To try to minimise these effects, the best fit has a peak location that is shifted away from that of the histogram data. The median spin of the distribution is also displayed.

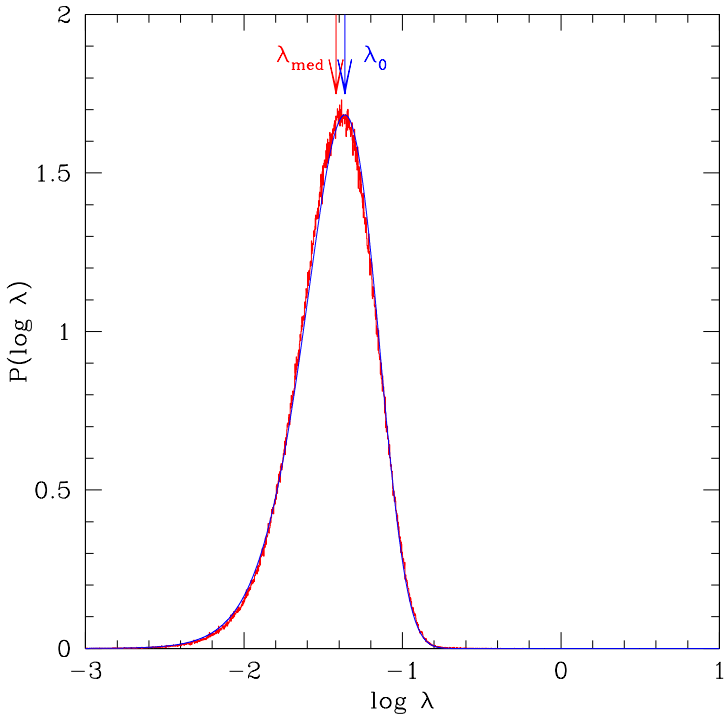

Figure 2.9: Histogram (red) of the normalised $\log\lambda$ distribution of TREEclean haloes, as in figure 2.8. The smooth solid curve (blue) is the best fit to the data using equation 2.15. The peak location of the fit (λ_0) and the median of the data ($\lambda_{\rm med}$) are marked with arrows.

where $x = \log M_{\rm h}/(\,h^{-1}{\rm M}_\odot)$. The best-fitting values of these parameters are:

$$\begin{aligned}
\alpha &= (-8.6 \pm 1.4) \times 10^{-3}, \\
\beta &= (3.2 \pm 0.54) \times 10^{-1}, \\
\gamma &= -4.1 \pm 0.68, \\
\delta &= 15.7 \pm 2.8,
\end{aligned}$$

with a reduced-χ^2 of 0.44.

While the trend of $\lambda_{\rm med}$ with mass is real, it is important to note that it is a small effect; the scatter around this median is large (compare with figure 2.5, which shows data from the same haloes but on a $\log\lambda$ scale). This is in qualitative agreement with previous results (e.g. Cole and Lacey 1996), but because of its weak nature, this trend has often not been visible (e.g. Warren et al. 1992; Lemson and Kauffmann 1999; Macciò et al. 2007).

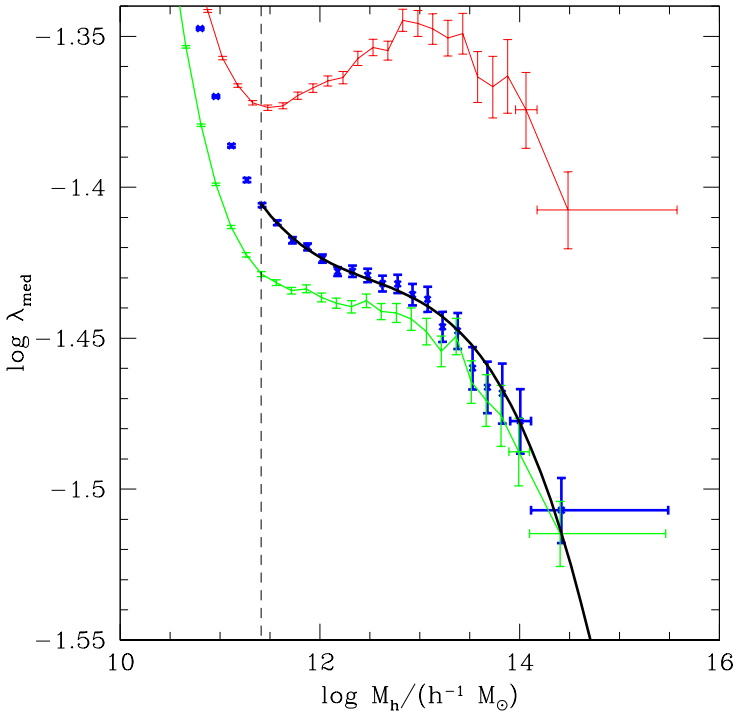

Figure 2.10: The median spins of halo mass bins, for TREEclean haloes (bold blue points), SOclean haloes (medium green line) and FOFclean haloes (thin red line). Data have also been calculated below the 300-particle low-mass limit (marked with a dashed line). The thick black curve is the best-fitting cubic polynomial to the TREEclean data. The vertical error bars are given by equation 2.13. The mass-binning scheme is similar to figure 2.6, but with bins every factor of $\sqrt{2}$ in mass. Only the widths of the most massive two bins are marked, for clarity.

2.4.3 The halo shape distribution

The shapes of the haloes are described by the axes, $a \geq b \geq c$, of the ellipsoid derived from the inertia tensor, as described in section 2.2. Figure 2.11 shows the distributions of $p = c/b$ and $q = b/a$ for the three cleaned halo catalogues. The haloes are generally triaxial, but they have a range of shapes, with a slight preference for prolateness over oblateness. The distribution agrees qualitatively with previous work such as that by Frenk et al. (1988), Warren et al. (1992), Cole and Lacey (1996), Faltenbacher et al. (2002) and Bailin and Steinmetz (2005). Unsurprisingly, SO haloes are more spherical than FOF or TREE haloes. FOF haloes show a much broader distribution of shapes (and a stronger preference for prolateness) than SO or TREE haloes.

Figure 2.12 shows how the median shape of haloes in the TREEclean catalogue changes with halo mass, using the minor-to-major axis ratio s and the triaxiality parameter $\mathcal{T} = (a^2 - b^2)/(a^2 - c^2)$. More massive haloes tend be less spherical and more prolate. Again, this is in qualitative agreement with previous results, such as those of Warren et al. (1992), Bullock (2002), Kasun and Evrard (2005), Shaw et al. (2006), Gottlöber and Turchaninov (2006), Allgood et al. (2006), and Macciò et al. (2007). This is also what one might expect in a hierarchical formation model in which haloes tend to form by matter collapsing along filaments, leading to prolateness, rather than onto sheets which would lead to oblateness. Furthermore, the more massive haloes form later, and have had less time to relax into more spherical configurations. Since we have deliberately tried to select the more relaxed objects, the remaining trend we see here is weak. Furthermore, although the medians follow well-defined trends, the spread of the distribution in halo shapes covers virtually the entire range in both s and $\mathcal{T}$, as can be seen from the percentile bars on the graph.

The two graphs in figure 2.12 both show a change in behaviour not seen in previous work, around the $N_\mathrm{p} = 300$ limit. Resolution tests similar to those described in section 2.3.2 were carried out using the `milli_lowres` simulation, to assess whether this change in behaviour was indeed a numerical effect similar to that seen in halo spins (in figures 2.6, 2.7 and 2.10). The results showed that these halo shape parameters do also require $N_\mathrm{p} \gtrsim 300$, reinforcing our previous choice. Indeed, one would expect haloes whose spins are affected by particle discreteness (i.e. with $N_\mathrm{p} \lesssim 300$) to be less spherical and more stringy (prolate).

We fit a broken line to both shape parameters for the TREEclean catalogue, of the

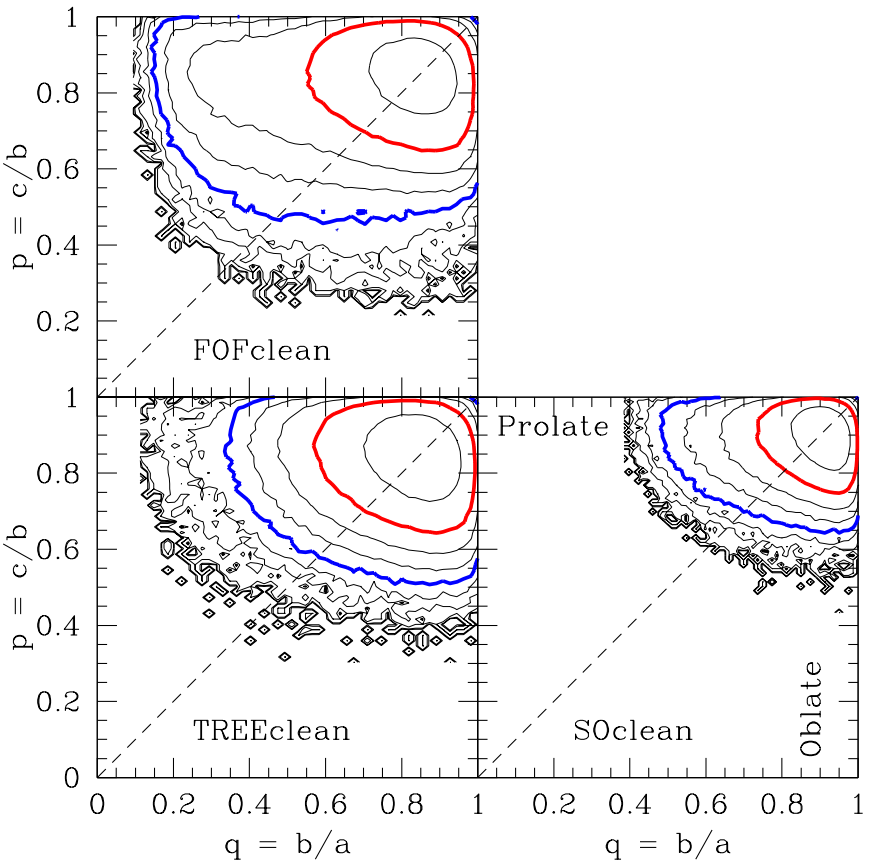

Figure 2.11: Axis ratios p and q for the cleaned TREE, FOF and SO halo catalogues. Prolate objects have $p = 1$, oblate objects have $q = 1$, and spherical objects have $p = q = 1$. The SO haloes are more spherical than the other two types. TREE and FOF objects exhibit a range of shapes, and all three catalogues show a preference for prolateness over oblateness. The contouring is by halo numbers, in equal logarithmic steps of $10^{0.5}$. In each plot, the red inner bold contour represents 10^3 haloes, and the blue outer bold contour represents $10^{1.5}$ haloes.

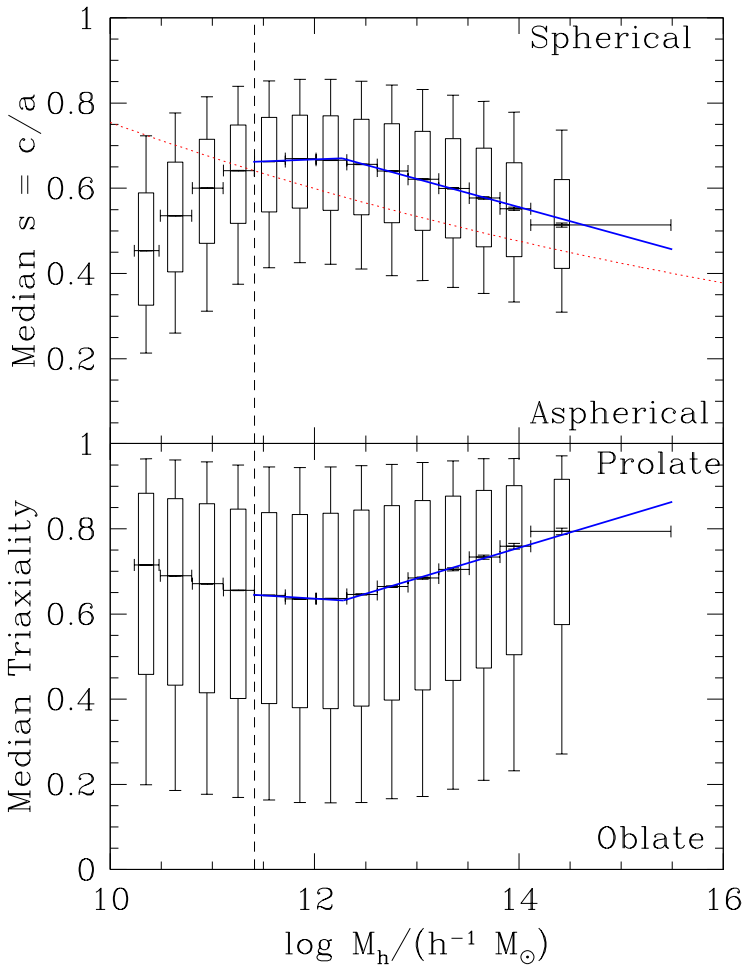

Figure 2.12: The median, in bins of halo mass, of the axis ratio s (top) and the triaxiality parameter $\mathcal{T}$ (bottom), for TREEclean haloes, using the same mass binning scheme as in figure 2.6. The low-$N_{\rm p}$ limit of 300 particles is marked with a dashed line, and data points have also been plotted below this limit. The medians for FOFclean and SOclean haloes follow the same behaviour as the TREEclean haloes, but with SO objects being more spherical and FOF objects less; FOF haloes are more prolate and SO haloes show a weaker preference for prolateness. Error bars on the medians (following equation 2.13) are plotted, but most are vanishingly small. The outer bars and boxes indicate percentiles, at the equivalent of 1σ (68% of haloes, boxes) and 2σ (95% of haloes, bars); from the bottom to the top of each graph, these show where approximately 2.5%, 16%, 84%, and 97.5% of the haloes have s (or $\mathcal{T}$) below these values. The thick blue lines show broken-line fits to the data; see the text for details. The dotted red line is the fit of Allgood et al. 2006, who used a different definition of a halo (see text).

form:

$$y_{\rm med}(x) = \begin{cases} m_1 x + c_1 & x \leq x_0 \\ m_2 x + c_2 & x \geq x_0, \end{cases} \tag{2.18}$$

where $x = \log M_{\rm h}/(\,h^{-1}{\rm M}_\odot)$. We fit with m_1, m_2, x_0 and c_2 as free parameters, with $c_1 \equiv c_2 + (m_2 - m_1)x_0$. The fitted parameters for $s_{\rm med}$ are:

$$\begin{aligned} m_{1,s} &= (9.2 \pm 0.87) \times 10^{-3}, \qquad & c_{1,s} &= 0.56 \pm 0.015, \\ m_{2,s} &= (-6.6 \pm 0.12) \times 10^{-2}, \qquad & c_{2,s} &= 1.48 \pm 0.015, \\ x_{0,s} &= 12.27 \pm 0.012, \end{aligned}$$

with a reduced-χ^2 of 29.9. The fitted parameters for $\mathcal{T}_{\rm med}$ are:

$$\begin{aligned} m_{1,\mathcal{T}} &= (-1.6 \pm 0.18) \times 10^{-2}, \qquad & c_{1,\mathcal{T}} &= 0.82 \pm 0.031, \\ m_{2,\mathcal{T}} &= (7.2 \pm 0.24) \times 10^{-2}, \qquad & c_{2,\mathcal{T}} &= -0.25 \pm 0.029, \\ x_{0,\mathcal{T}} &= 12.28 \pm 0.021, \end{aligned}$$

with a reduced-χ^2 of 4.27. The two mass breakpoints $x_{0,s}$ and $x_{0,\mathcal{T}}$ agree within their uncertainties.

Allgood et al. (2006) fit a power-law to $s_{\rm med}(M_{\rm h})$. This is plotted in figure 2.12, and indicates that that their haloes are significantly less spherical than ours. This is largely a result of different group definitions; although not plotted, we find that our SOclean and FOFclean catalogues differ from the TREEclean results by a similar amount. A power-law of the type used by Allgood et al. (2006) would not be a good fit to the data presented here which have a definite change in slope towards lower halo masses.

The overall distributions of s and $\mathcal{T}$ are shown in the upper plots of figures 2.13 and 2.15. These agree well with distributions seen previous work, e.g. Bailin and Steinmetz (2005) and Shaw et al. (2006). The drop-off in halo sphericity below about $s \sim 0.3$ can be explained by considering how flatter haloes would puff up due to bending instabilities (Merritt and Sellwood, 1994).

2.4.4 Spin and shape parameters

The relationship between spin parameter and halo shape is illustrated in figures 2.13, 2.14 and 2.15. Figure 2.14 emphasises the trend visible in figure 2.13 by plotting the median spin parameter as a function of s for different mass bins. There is a clear trend for more spherical haloes to exhibit less coherent rotation. Although this trend is in the

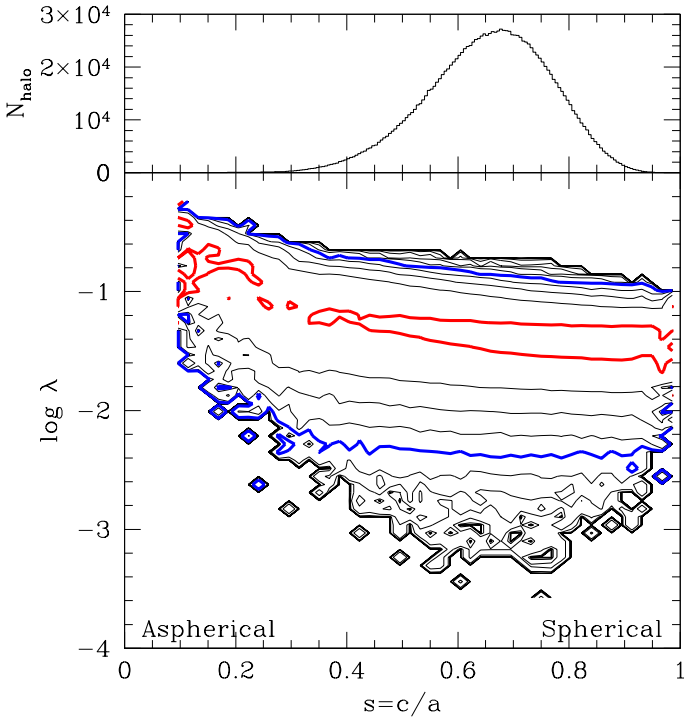

Figure 2.13: The main plot shows spin versus axis ratio $s = c/a$ for TREEclean haloes; contouring is similar to figure 2.2, showing the number density of haloes, normalised by the number of haloes in each s-bin. The red inner bold contour represents 10^{-1} of the haloes in each s-bin, the blue outer bold contour represents 10^{-3} of the haloes in each s-bin, and the contours are spaced in equal logarithmic steps of $10^{0.5}$. The upper plot is a histogram of s for TREEclean haloes, effectively showing the function by which the contour plot has been normalised.

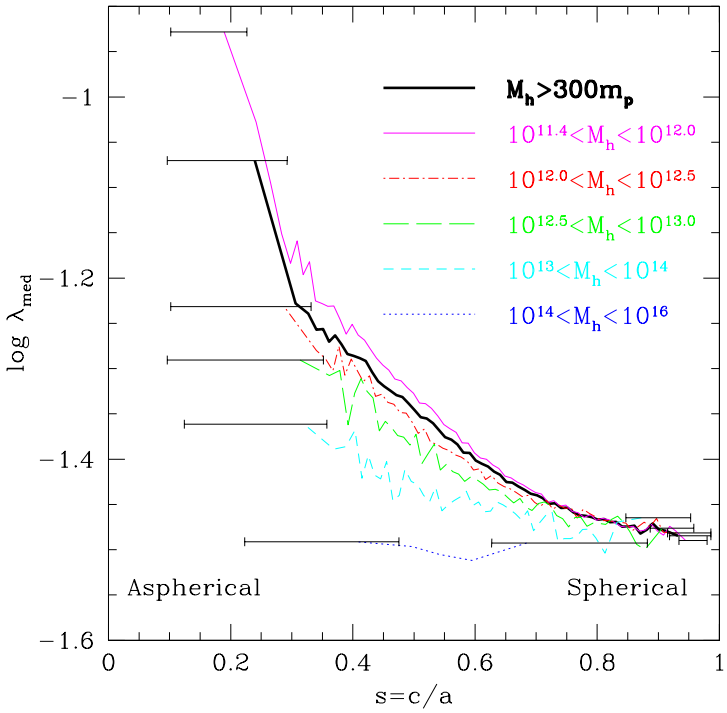

Figure 2.14: The median spin parameter in bins of axis ratio $s = c/a$, for haloes from the TREEclean catalogue. The heavy black line is for all haloes with more than 300 particles (the full TREEclean sample); the other lines show the trends for different halo mass bins. The horizontal bars show the widths of the first and last bins for each line. The trend is for more spherical haloes to have less coherent rotation in the median. This trend becomes very steep for the most aspherical haloes (although these are not present at higher masses because of the rapid drop in the halo mass function).

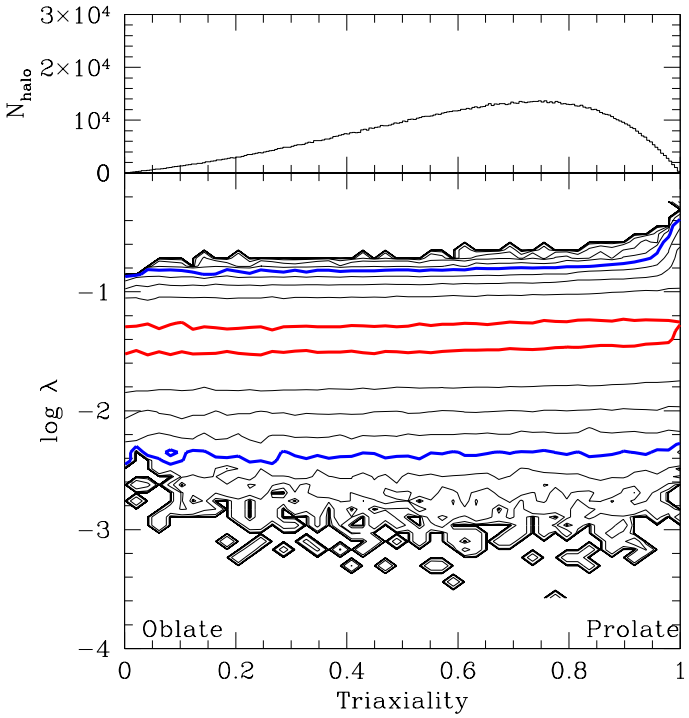

Figure 2.15: The main plot shows spin versus triaxiality parameter $\mathcal{T}$ for TREEclean haloes; contouring is as for figure 2.13, i.e. in equal logarithmic steps of $10^{0.5}$ haloes per $\mathcal{T}$-bin. The red inner bold contour represents 10^{-1} of the haloes in each $\mathcal{T}$-bin, and the blue outer bold contour represents 10^{-3} of the haloes in each $\mathcal{T}$-bin. The upper plot is a histogram of $\mathcal{T}$ for TREEclean haloes, effectively showing the function by which the contour plot has been normalised.

sense one might naïvely expect, the haloes, in fact, do not have very high spin, and are not rotationally supported. The origin of this trend is likely to lie instead in the effects of the tidal torques experienced by the haloes during their early phases of formation.

As seen previously in figure 2.10, the least massive objects have the most extreme spins, in the median. Figure 2.14 shows that the higher spin objects are also less spherical. The haloes which are closest to spherical have a spin parameter that is independent of halo mass, and has $\lambda_{\rm med} \approx 0.033$. (This does not apply to the most massive haloes, however, since their population lacks the more spherical objects) Furthermore, the median spins for the more massive haloes are independent of shape and have $\lambda_{\rm med} \approx 0.032$.

In contrast to the variation of $\lambda_{\rm med}$ with s, figure 2.15 shows that there is only a very weak trend of spin with halo triaxiality. Over the entire range of triaxiality, each $\mathcal{T}$-bin contains a very similar fraction of haloes at each value of $\log \lambda$.

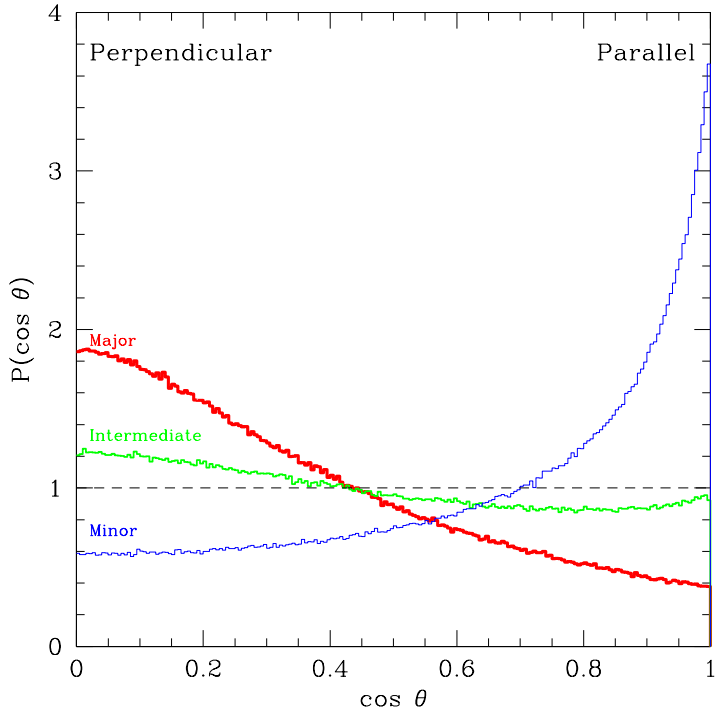

Figure 2.16: Normalised histograms of the cosines of the angle between the angular momentum vector and the major (thick red line), intermediate (medium green line) and minor (thin blue line) axes of haloes in the TREEclean catalogue, as defined in the text. A random distribution would be a flat line at $P(\cos\theta) = 1$.

2.4.5 Spin-shape alignment

Figure 2.16 shows the angle between the angular momentum vector and the three shape axis vectors, e.g.

$$\cos\theta_a = \frac{|\boldsymbol{j}\cdot\hat{\boldsymbol{a}}|}{j} \tag{2.19}$$

for alignment with the semi-major axis given by the unit vector $\hat{\boldsymbol{a}}$. Note that this definition does not distinguish between $\boldsymbol{j}$ lying parallel or antiparallel to the axis vectors.

Most haloes have their spin axis well aligned with their minor axis, and lying perpendicular to their major axis. However, the distribution of alignments with respect to all three axes is fairly broad. This agrees with previous results (e.g. Warren et al. 1992, Bailin and Steinmetz 2005, Allgood et al. 2006 and Shaw et al. 2006).

Extremely oblate objects have a degeneracy between the major and intermediate axes ($\frac{b}{a} \sim 1$), so there is an equal probability for the angular momentum vector to subtend a given angle with either axis This can be seen in the top-left panel of figure 2.17, which

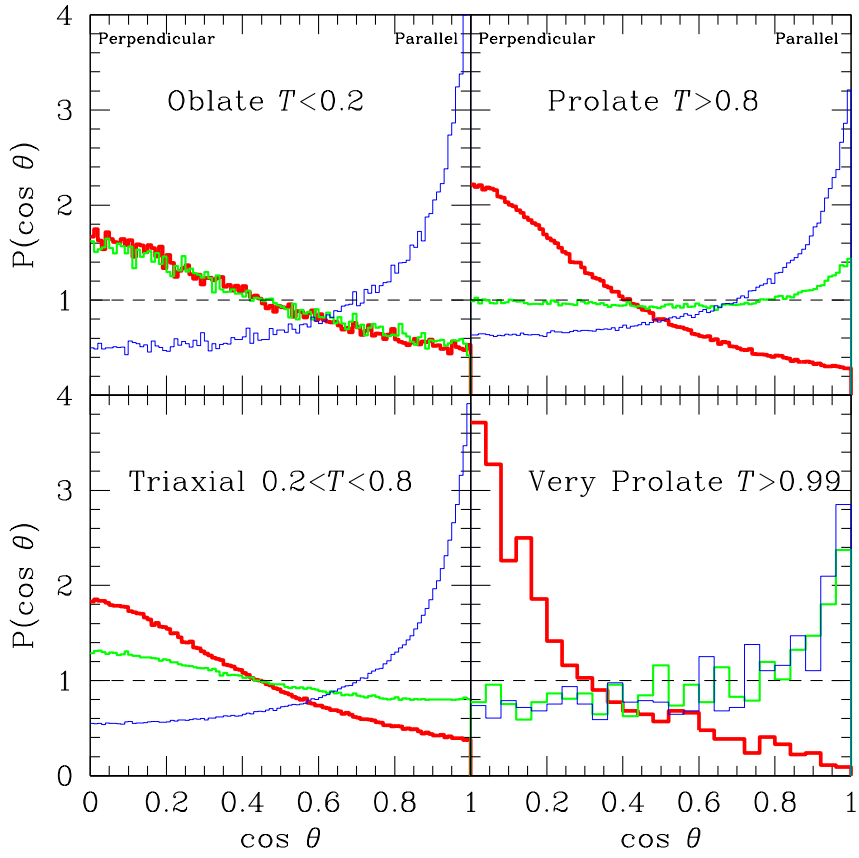

Figure 2.17: Normalised histograms of the cosine of the angle between the specific angular momentum vector and the major (thick red line), intermediate (medium green line) and minor (thin blue line) axes of the haloes. The TREEclean catalogue has been cut at the values of the triaxiality parameter shown. The most spherical haloes ($s > 0.8$) have been removed from each sample. The 'very prolate' selection only contains 1360 groups, giving rise to a noisier histogram.

shows the alignment distribution for the more oblate haloes, i.e. those with $\mathcal{T} < 0.2$ (and $s < 0.8$ in order to avoid an $a \sim b \sim c$ degeneracy). Since most haloes have $\boldsymbol{j}$ aligned with $\hat{\boldsymbol{c}}$, $\boldsymbol{j}$ has a preference for being at right angles to the two large axes.

For extremely prolate haloes, the degeneracy is between minor and intermediate axes ($\frac{c}{b} \sim 1$). In this case, the distribution of the alignment of the angular momentum vector with either of these axes is similar only for the tail of extremely prolate haloes, $\mathcal{T} > 0.99$ (bottom-right panel). For $\mathcal{T} > 0.8$, only a small number of haloes have their spin axis aligned with the intermediate axis (top-right panel); like the bulk of the population as a whole, most of these haloes rotate around their smallest axis.

The reason for the distinction between the major and intermediate axes present in figure 2.16 can now be seen to be a combination of various effects. The preference for prolateness over oblateness means that there is a tendency for the intermediate axis to be more similar to the minor than to the major axis. This increases the probability of $\boldsymbol{j}$ being aligned to the $\hat{\boldsymbol{b}}$ axis. However, since $\boldsymbol{j}$ can be aligned with only one axis (and when this happens it must be perpendicular to the other two), the preference for the spin axis to be the minor axis outweighs the preference for prolateness, and this results in the slight excess probability for $\boldsymbol{j}$ to be perpendicular to the intermediate axis seen in the figure.

2.4.6 Spin, shape and halo clustering

In this section, we investigate whether halo spin and shape has an environmental dependence. We quantify environment by means of the haloes' two-point correlation function, $\xi(r)$, and we explore whether the clustering amplitude differs for haloes with different spin. The three halo catalogues were divided into four bins in mass, and the haloes in each mass bin were then divided about the median spin for that mass; $\xi(r)$ was calculated for each set of haloes. The results are plotted in figures 2.18 and 2.19 for the TREEclean and FOFclean catalogues respectively. (The results for SOclean haloes are very similar to the FOF results.) The lines in figure 2.18 show power-law fits over the limited range of pair separations shown,

$$\xi(r) = \left(\frac{r}{r_0}\right)^{\gamma}. \tag{2.20}$$

The fitted values of r_0 and γ are given in table 2.2.

For the higher mass bins, the results from the different types of haloes are similar: higher spin haloes are more strongly clustered than lower spin haloes. This could

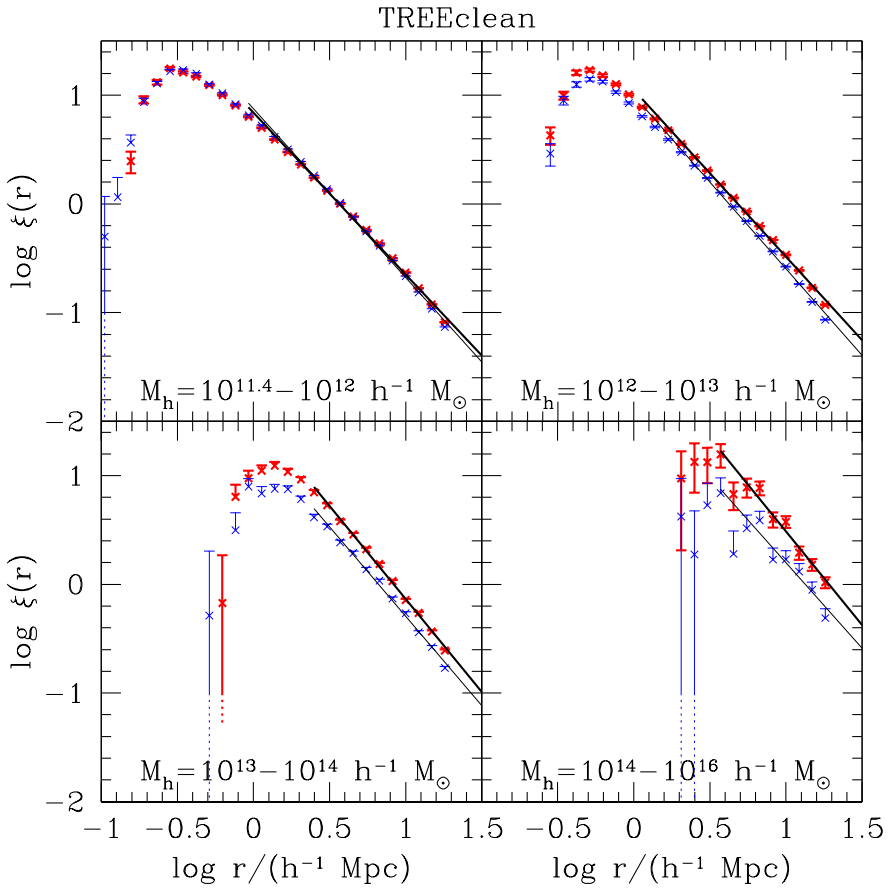

Figure 2.18: Two-point correlation function, $\xi(r)$, for TREEclean haloes in four mass bins. The lines represent power-law fits over the r-bins shown. The thick lines and red points are for haloes with $\lambda \geq \lambda_{\rm med}$ for that mass bin; the thin lines and blue points are for haloes with $\lambda < \lambda_{\rm med}$. The data are noisy in the higher mass bins which contain fewer haloes. The error bars are Poisson errors, i.e. the square-root of the number of pairs in each r-bin, divided by the mean number of pairs per r-bin.

Mass bin	$\lambda < \lambda_{\rm med}$		$\lambda \geq \lambda_{\rm med}$	
(h^{-1}M$_\odot$)	γ	$r_0/(h^{-1}$Mpc)	γ	$r_0/(h^{-1}$Mpc)
$10^{11.4}$–10^{12}	-1.553 ± 0.0013	3.670 ± 0.0070	-1.489 ± 0.0012	3.671 ± 0.0073
10^{12}–10^{13}	-1.591 ± 0.0031	4.22 ± 0.020	-1.537 ± 0.0026	4.82 ± 0.021
10^{13}–10^{14}	-1.64 ± 0.021	6.6 ± 0.24	-1.71 ± 0.016	8.3 ± 0.23
10^{14}–10^{16}	-1.6 ± 0.19	13 ± 5.8	-1.7 ± 0.12	19 ± 4.8

Table 2.2: Parameters for the power-law $\xi(r) = (r/r_o)^\gamma$ from fitting to the eight two-point correlation functions for TREEclean haloes.

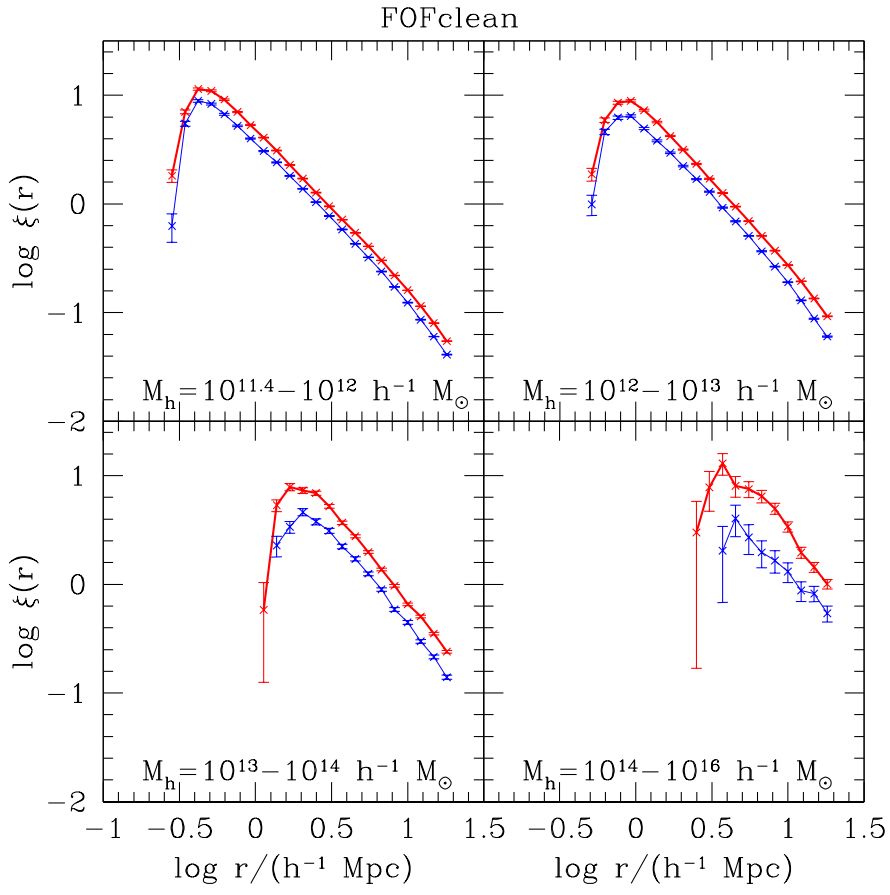

Figure 2.19: As figure 2.18, but for the FOFclean haloes. No fits were made to these data, and the lines merely join the points. For this catalogue, the higher spin haloes (thick red lines) are consistently and significantly more strongly clustered that the lower spin haloes (thin blue lines). The results for the SOclean haloes are very similar.

be because objects evolving in denser, more clustered environments are more likely to experience stronger tidal forces, leading to more coherent rotation. These results are consistent with the tentative earlier work of Barnes and Efstathiou (1987), as well as the mark correlation function analysis of Faltenbacher et al. (2002).

The difference in clustering strength between high and low spin haloes increases with halo mass. For the least massive TREE haloes, $M = 10^{11.4}$–$10^{12}\,h^{-1}\mathrm{M}_{\odot}$, there is virtually no difference in the correlation functions of the fast and slow rotators.

Note that haloes from the 'cleaner' groupfinder (TREE) exhibit stronger clustering at all scales, for all but the highest masses. This is due to the fact that the splitting algorithm applied during the construction of the merger trees results in a greater number of close halo neighbours (albeit with reduced masses) compared to the corresponding FOF haloes.

We have performed a similar analysis to that presented in figures 2.18 and 2.19 for the halo sphericity parameter, s. We found analogous results, in that the more spherical haloes are more clustered than the less spherical haloes.

To examine the effect of halo spin and shape on clustering in more detail, we consider the bias parameter, b, which describes how much more or less clustered a set of haloes is relative to the underlying dark matter distribution. We examine how the bias varies for haloes with different values of λ or s, at a fixed range of mass. Similar analyses have recently been performed by Gao et al. (2005), Wechsler et al. (2006) and Wetzel et al. (2007), who examined the effect of halo formation time, concentration, substructure content and time since last major merger on the bias.

The bias parameter is related to the correlation function through:

$$\xi_{\mathrm{hh}}(r|M_{\mathrm{h}},\lambda) = b^2(r|M_{\mathrm{h}},\lambda)\,\xi_{\mathrm{mm}}(r) \tag{2.21}$$

where $\xi_{\mathrm{hh}}(r|M_{\mathrm{h}},\lambda)$ denotes the halo-halo correlation function for haloes in a given range of mass and spin (in this example), and $\xi_{\mathrm{mm}}(r)$ is the dark matter correlation function. We compute the bias parameter as a function of mass, $b(M_{\mathrm{h}})$, using a similar method to that of Gao et al. (2005). Specifically, we compute $\xi_{\mathrm{hh}}(r|M_{\mathrm{h}},\lambda)$ in four r-bins in the range $6 \leq r \leq 25\,h^{-1}$Mpc, equally spaced in $\log r$. The bias parameter at each mass is then found as the normalisation constant that minimises:

$$\chi^2 = \sum_{i=1}^{n} \left(\frac{\xi_{\mathrm{hh}}(r_i) - b^2\xi_{\mathrm{mm}}(r_i)}{\sigma_{\mathrm{hh}}(r_i)} \right)^2 \tag{2.22}$$

where the $\sigma_{\mathrm{hh}}(r_i)$ are the Poisson errors on $\xi_{\mathrm{hh}}(r_i)$, and the sum is over all (> 1) r-bins where $\xi_{\mathrm{hh}}(r_i) > 0$ and $\xi_{\mathrm{hh}}(r_i)$ was computed using at least 100 objects. This procedure is

performed first for all the TREEclean and FOFclean haloes. It is then repeated for the haloes in the upper and lower 20th percentiles of the λ and s distributions, from both catalogues.

The results are shown in figure 2.20. This shows that higher spin haloes are more clustered than the average, and the lower spin haloes are less clustered. This trend is largest at higher masses, reaching a factor of ≈ 2.2 between the high-spin and low-spin bias at the largest mass, $\sim 2 \times 10^{14}\, h^{-1}\mathrm{M}_{\odot}$.

2.5 Conclusions

The huge size and high resolution of the Millennium Simulation (Springel et al., 2005b) makes it possible to determine the properties of dark matter haloes in the ΛCDM cosmology with unprecedented statistical power. In this chapter, we have concentrated on the spins and shapes of dark matter haloes, ranging in mass from those of dwarf galaxies to those of rich clusters. We have investigated the distribution of the spin parameter, λ, its dependence on mass, the distribution of shapes, the relationship between shape and spin, and the environmental dependence of spin and shape. We provide accurate fitting formulae for several quantities of interest.

While many of the properties we have investigated here have been studied in earlier simulations going back over twenty years, a novel aspect of our work is the analysis and comparison of haloes identified in different ways. Alongside the traditional "friends-of-friends" (FOF) algorithm of Davis et al. (1985) and the "spherical overdensity" (SO) algorithm of Lacey and Cole (1994), we have introduced a new halo definition, the TREE haloes, which are perhaps the most appropriate when carrying out comparisons of the simulation results with galaxy and cluster data. The TREE haloes are defined as branches of the halo merger trees, in which special care has been taken to identify physical haloes by separating objects that are artificially and transiently linked together. Each groupfinder results in more than 15 million haloes at $z = 0$.

The TREE halo catalogue was further 'cleaned' in two ways. Firstly, to remove any remaining spurious objects, we applied a cut in the instantaneous virial ratio, ($-0.5 \leq \frac{2T}{U} + 1 \leq 0.5$). Secondly, to remove objects whose angular momentum is biased due to particle discreteness, we considered only haloes with more than 300 particles, as indicated by convergence tests. Our final cleaned halo catalogues consist of $> 10^6$ haloes at $z = 0$.

We find that the distribution of the dimensionless spin parameter, $P(\lambda)$, is poorly fit by

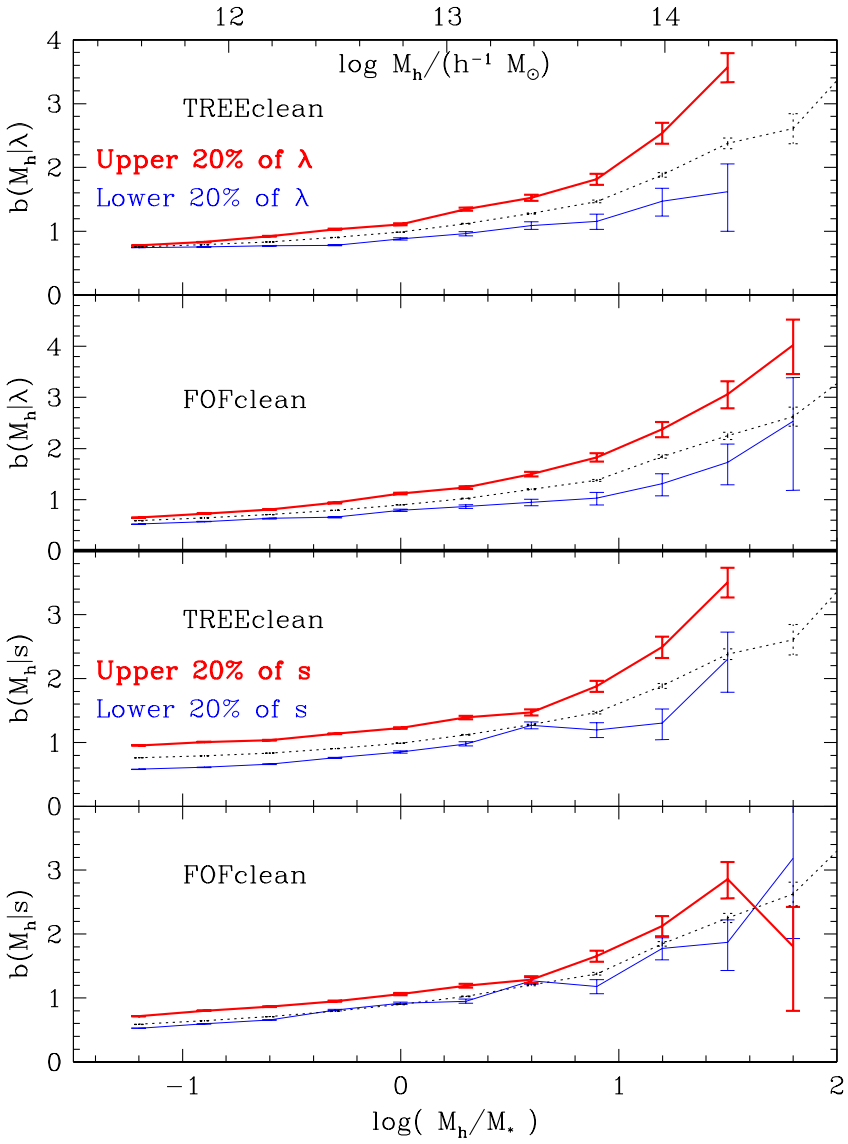

Figure 2.20: Bias parameter, $b(M_{\rm h})$, for the halo populations indicated in the legend. In each plot, the central dotted line marks the bias for the entire population at that mass. The thick red line is the bias for haloes in the upper 20 per cent of the distributions of λ (upper two plots) and s (lower two plots), and the thin blue line is for haloes in the lower 20 percent of the distributions. The error bars give the $\Delta\chi^2 = 1$ confidence interval. The lines stop either when the correlation function $\xi(r)$ for at least 3 of the 4 radial bins is non-positive, or if it was made using fewer than 100 objects.

a lognormal when this many objects are considered. The function given by equation 2.15 provides a much better description of the data. Although the distribution of $\lambda(M_{\rm h})$ is fairly broad, there is a clear trend of the median spin with halo mass, with more massive haloes spinning more slowly. However, the strength and shape of the trend is significantly different for different halo definitions. The cubic polynomial of equation 2.17 provides a very good fit to the median spin of the TREEclean halo catalogue, over a factor of $\sim 10^3$ in halo mass.

We analysed the shapes of the haloes, and found, as in previous studies, that there is a broad distribution of shapes with a slight preference for prolateness over oblateness. More massive haloes are less spherical and more prolate in the median, although the data span a large fraction of the available shape parameter space. We fit broken lines to the trends with $\log M_{\rm h}$ of the median sphericity axis ratio $s = c/a$ and the median triaxiality parameter $\mathcal{T}$ (equation 2.18). Both these quantities exhibit a change of behaviour at a galactic mass scale, $M_{\rm h} \approx 2 \times 10^{12}\, h^{-1}{\rm M}_{\odot}$, where the gradient of the fit changes sign, with haloes becoming increasingly aspherical and more prolate with increasing mass.

The rounder haloes have less coherent rotation, with a median spin that is independent of mass ($\lambda_{\rm med}(s \gtrsim 0.9) \approx 0.033$). The most massive haloes have a median spin that is independent of sphericity ($\lambda_{\rm med}(s) \approx 0.032$). However, there is significantly less correlation between the nature of halo triaxiality (prolateness *vs* oblateness) and the spin parameter. Although the haloes are far from being rotationally supported, there is a strong preference for the spin vector to be aligned parallel to the halo minor axis and to be perpendicular to the major axis. The tendency for the spin to be perpendicular to the intermediate axis is significantly weakened by the prevalence of prolate shapes for which there is a near degeneracy between the intermediate and minor axes.

We find a clear signal that the spins and shapes of haloes are sensitive to the cosmological environment: more rapidly rotating haloes of a given mass are more strongly clustered. The strength of this effect increases with halo mass. It is weak for subgalactic and galactic haloes, but can be larger than a factor of ~ 2 for galaxy cluster haloes. A similar effect is seen when examining halo shapes: more spherical haloes are more strongly clustered, with a greater signal at higher masses. Our result adds further evidence to the recent finding by Gao et al. (2005), also from analysis of the Millennium Simulation, that the internal properties of haloes depend not only upon their mass but also upon the environment in which they form.

The huge number of haloes in the ΛCDM Millennium Simulation enables us to charac-

terise the distribution of halo spins, and their relation to halo mass, shape and clustering, with unprecedented precision. However, we have also shown the significance of a careful halo definition. The properties of haloes defined and identified in different ways are noticeably different, and it is important to make the appropriate choice for a given application. For comparisons with real data, we recommend using the new class of "TREE" haloes which we have investigated in this work.

Chapter 3

Angular momentum profiles of dark matter haloes

3.1 Introduction

The formation of structures such as galaxies in the Universe we observe today is often understood in the context of the two-stage model of White and Rees (1978), within a ΛCDM cosmology: mass density perturbations (dominated by dark matter) collapse under gravity, hierarchically forming ever-larger 'haloes', with galaxies forming from the collapse of baryons that cool within them. While the relatively simple physics of the dark matter evolution has enabled the evolution of haloes to be studied in increasing detail over many years, the details of the galaxy-formation process, and the relationships between galaxies and their parent dark-matter structures, are still poorly understood. Modern computer simulations are however able to test different models to try and assess the relative importance of various physical processes, and can now produce well-resolved galaxies that match some observed relations (see Mayer et al. 2008, and Okamoto 2008 for reviews).

A difficulty that appeared when simulating the growth of galaxies was what became known as the 'angular momentum problem'—baryons cooled too fast as they collapsed, losing their energy and falling rapidly into the centres of small haloes early on. When these haloes then underwent mergers to form larger structures, the angular momentum of the baryons got transferred to the dark matter through tidal stripping and dynamical friction, resulting in galactic discs that were far too small. (see Maller and Dekel, 2002, for a review). It is generally accepted that the solution to this problem lies in preventing the premature cooling of baryons through 'feedback' mechanisms associated with the galactic evolution process, which can inject energy back into the baryons. Processes that could

provide this energy include winds from supernovae heating up gas and/or blowing it out of the galaxy (e.g. Governato et al., 2004, 2007), and radiating jets from AGN re-heating the gas (e.g. Sijacki et al., 2007; Di Matteo et al., 2008; Okamoto et al., 2008).

However, if we wish to understand the complex interplay of baryonic processes during galaxy formation, we must first also understand the much simpler physics of the underlying dark halo. There is a long history of studies of the angular momentum structure of dark matter haloes. Modern computational techniques enable us to combine the high resolution required to measure halo properties reliably, with the large volumes needed to measure the statistical distribution of those properties definitively (e.g. Hahn et al. 2007, Macciò et al. 2007, and Chapter 2 of this thesis).

An important gap in our knowledge of the angular momentum (and other) properties of extragalactic structures is the question of the link between the well-studied properties of the dark matter haloes, and the well-observed properties of the galaxies. The advent of simulations that can produce reasonably realistic galaxies means that we are now able to investigate that relationship meaningfully.

We expect the internal mass and velocity distribution of haloes to be transformed by the baryonic processes of galaxy formation, when compared to haloes in dark matter only ΛCDM simulations. This can be characterised in a variety of interrelated ways. We study the density profile itself in Chapter 4. The shape profile (i.e. sphericity of the mass distribution as a function of halo radius) and the angular momentum magnitude profile also contain information related to the merger history of the halo. The relative directions of the angular momentum and/or shape vectors at different radii within the halo are also expected to be changed by the galaxy; the degree of alignment with the galaxies themselves is of particular interest.

Kazantzidis et al. (2004) showed that haloes become much more spherical when gas cooling and star formation was allowed to occur, compared to haloes in which gas was not allowed to cool radiatively. The effect was strongest towards the halo centre, but was significant throughout the halo. In a similar vein, Bailin et al. (2005a) examined the *alignment* of galaxies with their parent haloes. They found that, although the dark matter at the virial radius was essentially uncorrelated with the orientation of the galactic disc, the presence of the disc had altered the mass distribution in the inner halo such that the halo minor axis tended to align with the disc axis. Sharma and Steinmetz (2005) and van den Bosch et al. (2002) looked at the relative orientations of dark matter and (non-radiative) gas in haloes (at $z = 0$ and $z = 3$ respectively), finding a broad distribution of

alignments; the former also found negligible evolution of misalignment with redshift, and the latter found significant mis-alignment between the inner and outer regions of the halo. Chen et al. (2003) also examined the angle between the halo and gas angular momentum vectors, comparing the results from simulations where the gas is and is not allowed to cool radiatively (although they did not have star formation). They found that the cold gas shows a broader range of orientations relative to the dark matter than either the hot or non-radiative gas.

Gustafsson et al. (2006) similarly analysed simulations of haloes run with and without galaxy-formation processes, examining the density profiles, shapes and shape-orientation profiles. Their found that the baryons made their haloes more spherical in shape, with a wide range of angles between the dark matter and the galaxies. Croft et al. (2008) used a model that included black hole feedback in the star formation process, and found a broad distribution of angles between galaxies and their parent haloes, as well as between the shape and angular momentum axes of each halo component (gas, stars, dark matter).

The limitations of studies such as these stem from the large amount of time and computational resources required to run such simulations. Simulations usually cover only a small volume, resolving just a handful of objects; or the galaxy formation recipe is incomplete, not including radiative cooling of gas, star formation or feedback; or the simulation is not run to the present day, biasing the nature of the galaxy population involved.

However, the relationship between the way the dark matter and galaxy are arranged in haloes, and how this differs from the purely-ΛCDM case, is highly important for future work in testing our theories of structure formation. Semi-analytic models provide a useful tool for this testing process. They allow us to assess the relative importance of different physical processes, without having to run a prohibitively expensive series of hydrodynamic simulations. However, despite many successes, there are many areas where the physical models used could be improved (see Baugh, 2006, for a review). One of these is the treatment of angular momentum. The size of galactic discs in semi-analytic models is directly related to the angular momentum of the halo, under the assumption that the baryons initially have the same angular momentum distribution as the dark matter, and that this is conserved as the baryons collapse within their haloes (see, e.g. Cole et al., 2000, for details). The halo angular momentum is usually generated by sampling a lognormal distribution of the spin parameter λ, although different groups have found that the λ distribution does not quite have this shape (see Chapter 2, and Macciò et al.

2007, 2008). The assumption that there is no transfer of angular momentum between the dark matter and gas is difficult to test, because of the angular momentum problem found in hydrodynamic simulations (discussed above); indeed, the conservation of baryonic angular momentum is one of the key features in semi-analytic models that leads to a realistic galaxy distribution compared to the hydrodynamic simulations. Furthermore, semi-analytic models do not yet model the orientation of the galaxies that form, which limits their ability to make mock observations, for example for studies of gravitational lensing.

Weak gravitational lensing is a potentially very powerful tool for performing observational tests of the ΛCDM paradigm (see Hoekstra and Jain, 2008, for a recent review). By probing the gravitational field around luminous objects, it is hoped that the predictions of ΛCDM and alternative-gravity theories such as TeVeS/MOND can be distinguished (Bekenstein 2004; Mortlock and Turner 2001 described gravitational lensing in MOND theories). In the absence of dark matter, the shape of the gravitational potential at large distances from galaxies is expected to be spherical, which contrasts with the prolate-triaxial shape of ΛCDM haloes (see Chapter 2, and Hayashi et al. 2007). In practice, while attempts have been made to measure potential shapes of galactic haloes using weak lensing (Hoekstra et al., 2004; Mandelbaum et al., 2006; Parker et al., 2007), the complexities of the systematic errors and weakness of the signal have made it difficult to provide definite conclusions. Hoekstra et al. (2004), using the Red-Sequence Cluster Survey (RCS), claimed to observe a definite halo-ellipticity signal; given their assumption of exact galaxy–halo alignment, this is a lower limit. Mandelbaum et al. (2006), using data from the Sloan Digital Sky Survey (SDSS), did not manage to make a definite detection of halo ellipticity, but their data suggested distinct galaxy–halo alignment distributions for spiral and elliptical galaxies. Parker et al. (2007) used the CFHT Legacy Survey to attempt to measure the halo ellipticity, again detecting a non-spherical signal but at relatively low significance. Evans and Bridle (2008) have recently used a similar method to measure the ellipticity of cluster haloes, reporting ruling out of spherical haloes. Rozo et al. (2006) and Minor and Kaplinghat (2007) also demonstrated the importance of considering the effects of baryons, looking at the impact of galaxy–halo alignment and halo contraction on the *strong*-lensing signal.

In this chapter, we use the statistical power given by the Millennium Simulation (Springel et al., 2005b) to determine the angular momentum profiles of dark matter haloes in a purely ΛCDM universe (that is, without baryons). We look at both the

magnitude and orientation of the angular momentum vectors as functions of halo radius and mass (section 3.2). In section 3.3, we use a pair of simulations of a smaller volume, one of which contains just dark matter and the other has a sophisticated implementation of the baryonic processes of galaxy formation. Using these simulations, we examine the angular momentum profiles of the haloes in detail, comparing the dark matter at different radii between the two simulations, and with the central galaxies. We also examine how the changes we see in the dark matter angular momentum are related to the different mass distributions in the haloes. Finally, we relate our results directly to the problem of weak gravitational lensing, by computing the 2-D projected mass distributions (individual and stacked), when each halo is aligned according to its galaxy's axes. We present our conclusions in section 3.4.

3.2 Dark matter haloes

We first examine the angular momentum structure of simulated dark matter haloes without baryons, using two cosmological simulations containing a large number of well-resolved objects.

3.2.1 The simulations

We use the two periodic-box dark-matter simulations of the ΛCDM large-scale structure described in section 1.5.5: the *Millennium Simulation* (MS), and the smaller higher-resolution HR1 simulation. These provide very precise statistics of dark matter halo properties over a wide range of mass. We perform all our analyses at redshift $z = 0$.

3.2.2 Halo definition

We shall be looking at various halo properties defined in spherical shells, so it is makes sense to use a Spherical Overdensity (SO, Lacey and Cole, 1994) algorithm to define haloes. We do this in the same way as in section 2.3.1, but we cover it again here for convenience. The halo definition algorithm starts by using Friends-of-Friends (FOF, see e.g. Davis et al., 1985) with a linking length of 0.2 to construct an initial set of particle groups. We then use the SUBFIND program (Springel et al., 2001a) to identify self-bound structures within each group (one of which will always be the main halo itself), as well as the location of the gravitational potential minimum. We consider the potential minimum of the main self-bound structure within each FOF group to be the centre of the

corresponding dark matter halo. We then grow a spherical boundary around each centre until the total enclosed mass density (not just the original FOF particles) matches that of a virialised halo in the spherical top hat model for a flat cosmology ($\Omega_{\rm tot} = \Omega_{\rm m} + \Omega_\Lambda = 1$; see section 1.3, and Bryan and Norman 1998; Eke et al. 1996):

$$\Delta_{\rm c} = \frac{\rho}{\rho_{\rm crit}} \approx 18\pi^2 + 82(\Omega_{\rm m}(z) - 1) - 39(\Omega_{\rm m}(z) - 1)^2. \tag{3.1}$$

This gives $\Delta_{\rm c} \approx 94$ for MS and HR1. We shall refer to this halo boundary as its virial radius, $R_{\rm vir}$, and the total mass within this radius as $M_{\rm vir}$.

3.2.3 Analysis of physical properties

After defining the sets of particles that make up the haloes in the two simulations, a series of physical properties of those objects is computed, in the same way as in section 2.2.

The kinetic energy of each halo, T, is computed by

$$T = \frac{1}{2}\sum_{i=1}^{N_{\rm p}} m_i \boldsymbol{v}_i^2, \tag{3.2}$$

where the halo consists of $N_{\rm p}$ particles. Each particle i has mass $m_i = m_{\rm p}$, and velocity vector $\boldsymbol{v}_i$ relative to the centre-of-mass velocity.

To calculate the potential energy of each halo, U, we use a random sample of up to $N_{\rm sel} = 1000$ particles from each halo, then scale the total back up according to

$$U = \left(\frac{N_{\rm p}^2 - N_{\rm p}}{N_{\rm sel}^2 - N_{\rm sel}}\right)\left(\frac{-Gm_{\rm p}}{\eta}\right)\sum_{i=1}^{N_{\rm sel}-1}\sum_{j=i+1}^{N_{\rm sel}} -W_2(r_{ij}/\eta). \tag{3.3}$$

This uses the form of the potential used in the simulation code itself, which incorporates the SPH smoothing kernel (Springel et al., 2001b):

$$W_2(x) = \begin{cases} \frac{16}{3}x^2 - \frac{48}{5}x^4 + \frac{32}{5}x^5 - \frac{14}{5}, & 0 \le x \le \frac{1}{2}, \\ \frac{1}{15x} + \frac{32}{3}x^2 - 16x^3 + \frac{48}{5}x^4 - \frac{32}{15}x^5 - \frac{16}{5}, & \frac{1}{2} \le x \le 1, \\ -\frac{1}{x}, & x \ge 1 \end{cases} \tag{3.4}$$

where the argument x is given by the ratio of the particle-pair separation r_{ij} to the spatial softening constant, η (see table 1.2).

For computing the specific angular momentum profiles, we divide each halo into a spherical 'inner' core region and a series of concentric spherical shells. The shells have an equal spacing of 0.2 in $\log_{10}(r/R_{\rm vir})$, where r is the radial distance from the halo centre. We use an inner region of radius $0.1R_{\rm vir}$ for the analysis of angular momentum magnitudes, and $10^{-0.6}R_{\rm vir} \approx 0.25R_{\rm vir}$ for the orientation analyses. This is because

angles between the angular momentum vectors are subject to different numerical errors, and require more particles within a given radius to ensure the results are reliable (see the discussion in Appendix B for full details).

The (cumulative) specific angular momentum[1] vector, $\boldsymbol{j}(\leq r)$, of the $N_{\rm p}(\leq r)$ dark matter particles within a given radius r (of total mass $M(\leq r)$) is then given by

$$\boldsymbol{j}(\leq r) = \frac{1}{M(\leq r)} \sum_{i=1}^{N_{\rm p}(\leq r)} m_i \boldsymbol{x}_i \times \boldsymbol{v}_i, \tag{3.5}$$

where $\boldsymbol{x}_i$ and $\boldsymbol{v}_i$ are the position and velocity vectors of particle i relative to the halo centre and centre-of-mass velocity. Since we use the SO algorithm to define our haloes, the total halo specific angular momentum is $\boldsymbol{j}_{\rm tot} = \boldsymbol{j}(\leq R_{\rm vir})$.

The shapes of the dark matter haloes are computed using the inertia tensor, I, which directly relates angular momentum $\boldsymbol{J}$ and angular velocity $\boldsymbol{\omega}$ (i.e. $\boldsymbol{J} = \mathsf{I} \cdot \boldsymbol{\omega}$). This has components

$$I_{\alpha\beta} = \sum_{i=1}^{N_{\rm p}} m_i \left(\boldsymbol{x}_i^2 \delta_{\alpha\beta} - x_{i,\alpha} x_{i,\beta} \right), \tag{3.6}$$

such that $J_\alpha = I_{\alpha\beta}\omega_\beta$ (i indexes particles, α and β are the tensor indices with values of 1, 2 or 3, and $\delta_{\alpha\beta}$ is the Kronecker delta). The eigenvectors of the diagonalised inertia tensor define an ellipsoid, which represents the equivalent homogeneous shape of the object, in terms of a semi-major axis $\boldsymbol{a}$, intermediate axis $\boldsymbol{b}$ and semi-minor axis $\boldsymbol{c}$ (see also the previous discussions on definitions of the inertia tensor, sections 1.4 and 2.2).

We also use the angular velocity magnitude profile, $\omega(r)$. This is defined from the angular velocity vector $\boldsymbol{\omega}(r)$, using the mass distribution within radius r, through the expression

$$\boldsymbol{\omega}(r) = \mathsf{I}^{-1}(\leq r) \cdot \boldsymbol{J}(\leq r). \tag{3.7}$$

3.2.4 Halo selection

In the analysis of the halo shapes and spin parameters in the MS (Chapter 2), we used a halo catalogue that removed haloes that were clearly out of equilibrium at the time of the simulation snapshot. This was done by restricting the selected haloes to a certain range in the instantaneous 'virial ratio' of halo energies:

$$Q \equiv \left| \frac{2T}{U} + 1 \right| \leq Q_{\rm lim} \tag{3.8}$$

[1]The rather verbose phrase 'specific angular momentum' occurs throughout this chapter. However, it was felt that the obvious acronym Sp.A.M. would have an adverse effect on the readability (see e.g. Chapman et al. 1970), so it was not used.

Here, we apply a cut of the same form, and adopt the same value of $Q_{\rm lim} = 0.5$ (see section 2.3.2 for a detailed discussion).

In Chapter 2, we also found that angular momentum and shape parameters of a halo were subject to numerical biases if it was realised with fewer than approximately 300 particles. For the analyses presented here, we apply the $N_{\rm p} \geq 300$ selection criterion either to the object in total (when profile information is not required), or to the innermost radial bin considered, e.g. $r \leq 0.1R_{\rm vir}$. This ensures that only reliable angular momentum profiles are considered, and is by far the most stringent criterion used in this chapter. The mass functions of haloes selected in this way are shown in figure 3.1.

We apply further selection criteria when studying the orientation of the angular momentum vectors, since the magnitude of the vector is related to the uncertainty in the direction. These are detailed in Appendix B.

3.2.5 Results

Angular momentum profiles

The cumulative specific angular momentum magnitude profiles, $j(\leq r)$, of haloes in the MS and HR1 are shown in figure 3.2. The vertical error bars (directly around the data points) give an estimate of the uncertainty in the median, by analogy to a Gaussian mean,

$$\epsilon_+ = \frac{X_{84} - X_{50}}{\sqrt{N}}, \qquad \epsilon_- = \frac{X_{50} - X_{16}}{\sqrt{N}}, \tag{3.9}$$

where X_i is the value at the ith percentile of the distribution in question, made up of N objects (X_{50} is the median; note that this is an asymmetric version of equation 2.13). These error bars are virtually invisible on the lines describing the simulations' full halo populations, but are quite significant in the higher-mass bin medians as they contain considerably fewer haloes. In contrast, the outer bars and boxes (only shown on the MS median line) indicate the spread of the data; the boxes enclose 68 percent of the data, and the outer bars enclose 95 percent.

Figure 3.2 shows the trend of $j(\leq r)$ with mass, as well as the trend with radius at a fixed halo mass. For comparison, we also show the scaling with radius from simple arguments from circular motion: if $j = vr$, and the circular velocity v is constant with radius (as for an isothermal density profile), then $j \propto r$.

A complementary measure of the angular momentum profile is the angular velocity profile, $\omega(r)$. We show this in figure 3.3. We also show the simple scaling consistent with

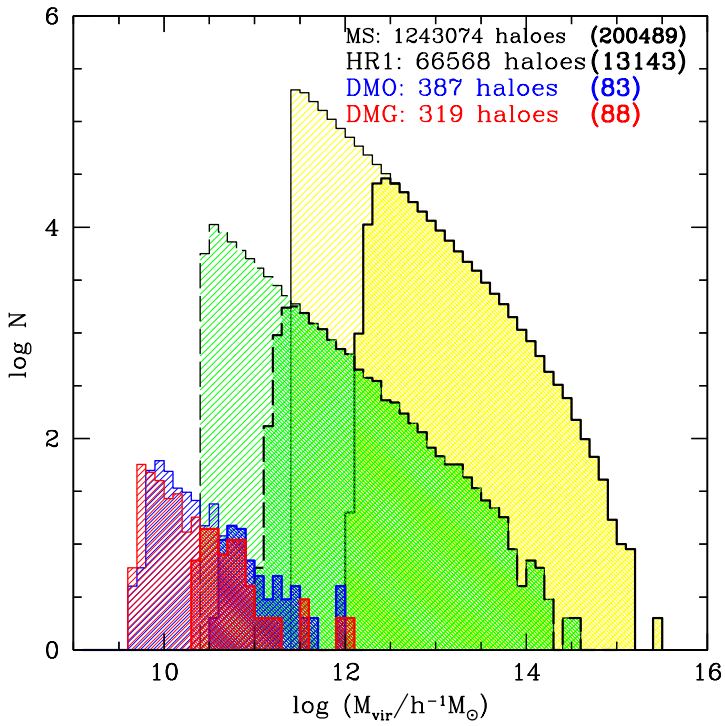

Figure 3.1: Mass functions (halo number histograms) for haloes from the four simulations we use in this chapter. The Millennium Simulation is shown in black with yellow shading, HR1 is in dashed-black with green shading, DMO is in blue and DMG is in red (the DMO and DMG simulations are used in section 3.3). For each simulation we show the histogram of mass within $R_{\rm vir}$ for each halo (for the DMG haloes this includes stars and gas). We show two selections for each simulation: objects that contain at least 300 dark matter particles within $R_{\rm vir}$ (thin lines, light shading), and within $r \leq 0.1R_{\rm vir}$ (heavy lines and shading). In both cases, selected haloes must also satisfy the 'virialisation' criterion, $Q \leq 0.5$.

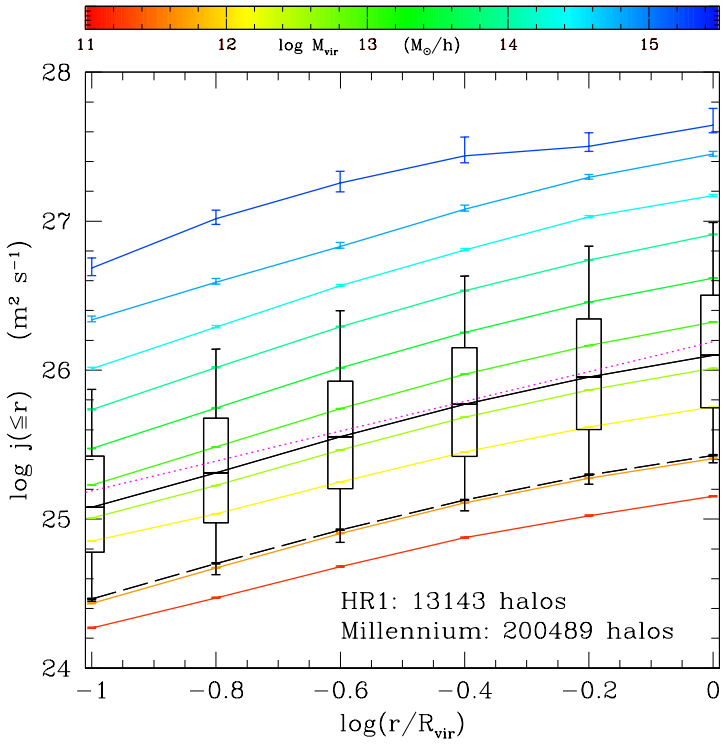

Figure 3.2: Dark matter halo cumulative specific angular momentum profiles, for objects in the MS and HR1 simulations. Coloured lines show the median profiles for haloes in different mass bins, and the black lines show the medians for the MS (solid) and HR1 (dashed) data together. The error bars on each line (nearly invisible for MS and HR1) are given by equation 3.9. The outer bars and boxes on the MS line indicate the spread of individual halo profiles around the median (the boxes enclose 68 percent of the data, the bars enclose 95 percent). The dotted magenta line shows the $j \propto r$ scaling (with arbitrary normalisation; see text).

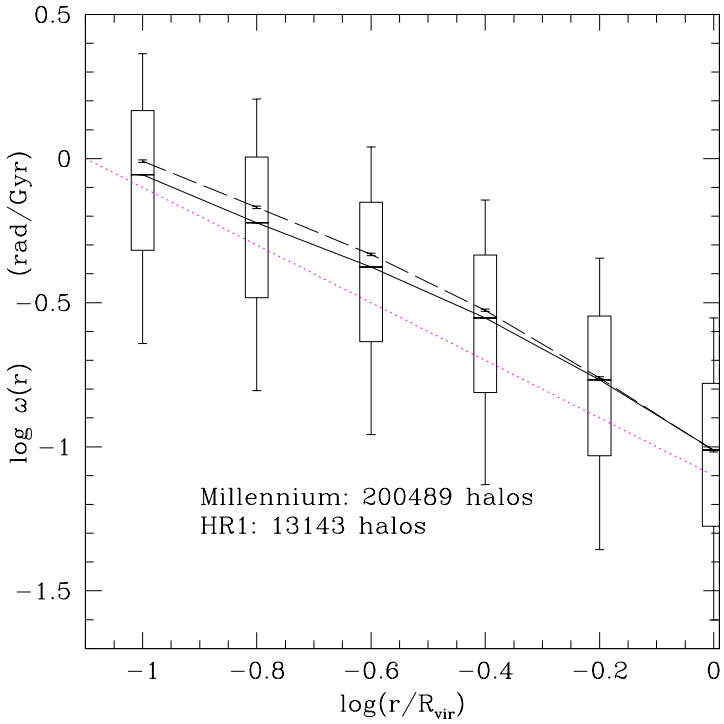

Figure 3.3: Angular velocity profiles $\omega(r)$ (see equation 3.7), for haloes in MS (solid black) and HR1 (dashed black). As with figure 3.2, we plot error bars on both lines, and indicate the the spread of the data by the outer bars and boxes on the MS line. The trend $\omega \propto r^{-1}$ is plotted as the magenta dotted line (with arbitrary normalisation, see text).

$j \propto r$, i.e. $\omega \propto r^{-1}$. Using ω instead of j removes the mass dependence, but we still find a similar amount of scatter about the median.

Spin orientation profiles

Having examined the magnitudes of the haloes' angular momentum vectors, we now consider the vector orientations. We compute the cumulative angular momentum orientation profile,

$$\cos\theta(\leq r) = \hat{\boldsymbol{j}}_{\rm inner} \cdot \hat{\boldsymbol{j}}(\leq r), \tag{3.10}$$

where the hat denotes a unit vector (e.g. $\hat{\boldsymbol{j}} = \boldsymbol{j}/|\boldsymbol{j}|$) and the 'inner' region is now defined as $r \leq 10^{-0.6} R_{\rm vir} \simeq 0.25 R_{\rm vir}$. The direction of the cumulative angular momentum vector is subject to significant uncertainty due to numerical effects. To ensure that our results are robust, we have applied a different, additional, set of selection criteria to the datasets used in this section. The net angular momentum of a halo, $\boldsymbol{j}(\leq r)$, is constructed by the 3-D

vector sum of its individual particles' angular momenta. But haloes in fact have very little coherent rotation, so the specific angular momentum of a halo is small compared to the typical specific angular momentum of an individual particle. A halo that has a particularly small j compared to those of its particles will have its direction information dominated by very few particles, which allows a significant amount of uncertainty. Therefore, restricting our halo sample to those whose j are not too small will reduce the scatter, leaving reliable angular momentum directions. We discuss the details of this process in Appendix B.

Figure 3.4 shows the orientation profiles of the haloes from the MS and HR1 simulations. The cumulative angular momentum becomes increasingly poorly aligned with the inner regions of the halo as one considers larger radii. Although the median alignment of the angular momentum at $R_{\rm vir}$ with that in the inner regions is always within 30°, there is a very large scatter between haloes. This scatter is much larger than that expected to remain due to the numerical issues discussed above, so we conclude that it comes from the intrinsic variation between haloes.

Furthermore, when the data is split into different mass bins, we can see that there is a clear trend, with more massive haloes tending to be less well aligned at large radius. Figure 3.5 examines the mass trend in more detail, by looking at how the angle between $\boldsymbol{j}_{\rm tot} = \boldsymbol{j}(\leq R_{\rm vir})$ and $\boldsymbol{j}_{\rm inner} = \boldsymbol{j}(\leq 0.25R_{\rm vir})$ varies as a function of halo mass. There is a clear decrease in alignment for the very highest-mass haloes, although the trend is weak over a wide range of mass at the lower end. The most massive haloes formed most recently, and are likely to have had a major merger more recently than haloes with less mass. Major mergers have been found to have a strong effect on a halo's angular momentum magnitude (see D'Onghia and Navarro, 2007, for a discussion); it is highly likely that a major merger would de-correlate the alignment profile of a halo, albeit in a way that could depend strongly on the details of the merger.

We have also examined how the halo inner angular momentum vector compares to the shape orientation, as measured by the halo major axis $\boldsymbol{a}$ (if we expect haloes to have a tendency towards prolateness, then the two smaller axis directions $\boldsymbol{b}$ and $\boldsymbol{c}$ are more likely to be degenerate). We find a slight trend with mass in the distribution of the angle between $\boldsymbol{a}$ and $\boldsymbol{j}_{\rm inner}$ (see figure 3.6). This is also likely to be due to the difference in halo merger histories, but with the added complication of using a halo's shape axis rather than its spin axis. The distribution of angles between the halo mass distribution and the angular momentum at $R_{\rm vir}$ was shown in Chapter 2 (figure 2.16), and is in fact very similar to the shape-$\boldsymbol{j}_{\rm inner}$ distribution we show here.

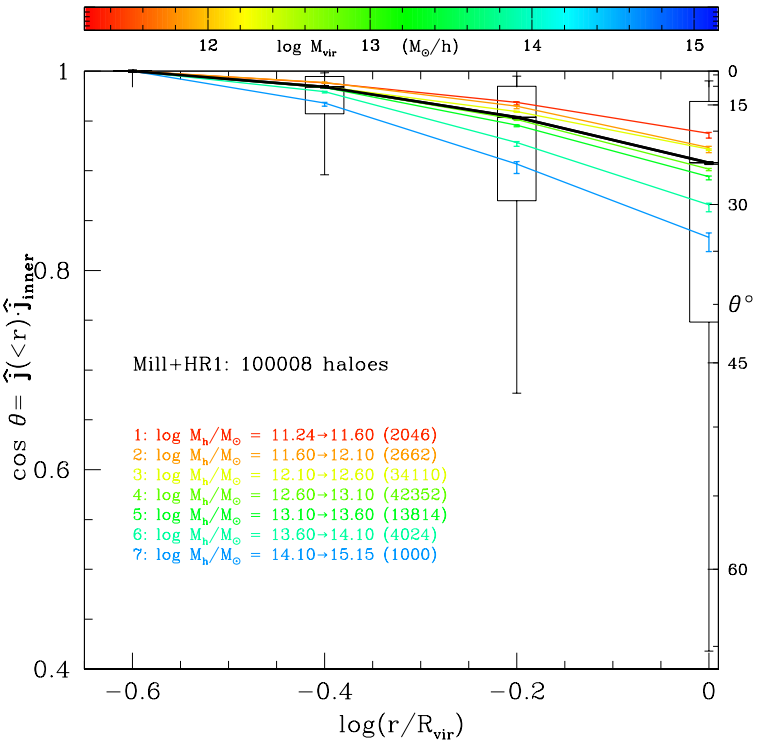

Figure 3.4: Cumulative specific angular momentum orientation profiles for haloes from the MS and HR1 simulations. The median profile for the entire halo population is shown in black, with error bars and percentile bars shown as in figure 3.2. There is an increasing likelihood of misalignment at larger radius, with a very large amount of scatter between haloes. The coloured lines show the results for the haloes in different mass bins, showing that the lower-mass haloes tend to remain better-aligned to a larger radius.

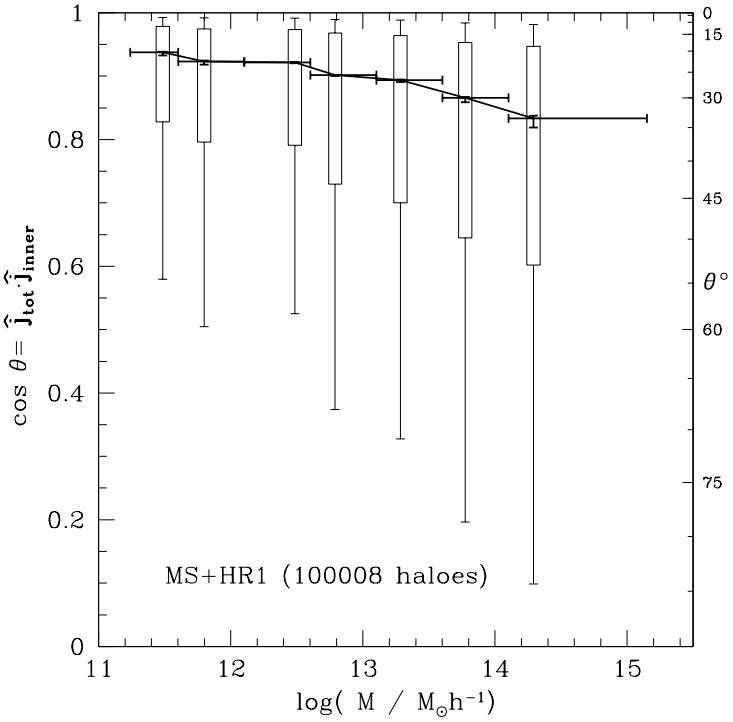

Figure 3.5: Angle between the specific angular momentum within $R_{\rm vir}$ and within the inner region ($\approx 0.25R_{\rm vir}$), as a function of halo mass $M_{\rm vir}$. There is very little trend for the majority of haloes, but the most massive ones show a clear tendency for increased mis-alignment. The error bars indicate the uncertainty on the median, and the outer bars and boxes show the spread of the data, as in figure 3.2.

We can compare our results to those found by Bailin and Steinmetz (2005). There, the authors compared both the angular momentum and shapes-axis vectors of haloes as a function of radius. Our results actually suggest better internal halo alignment than Bailin and Steinmetz (2005), but the difference in selection and analysis means that direct comparisons are difficult. Firstly, Bailin and Steinmetz (2005) used discrete radial shells, whereas we use cumulative radial bins. This allows us to retain more objects, as the particle-number limit for well-resolved objects does not have to be satisfied in each radial bin separately. Although Bailin and Steinmetz (2005) have slightly better mass resolution, our halo populations are actually over a very similar mass range, and we have used similar techniques to control errors due to numerical effects. These include limiting the minimum number of particles in the halo and using bootstrap resampling to test for and reject haloes whose vector directions are unreliable. However, we also explicitly remove haloes whose energies indicate that they are out of equilibrium. Although we do not find that this is as

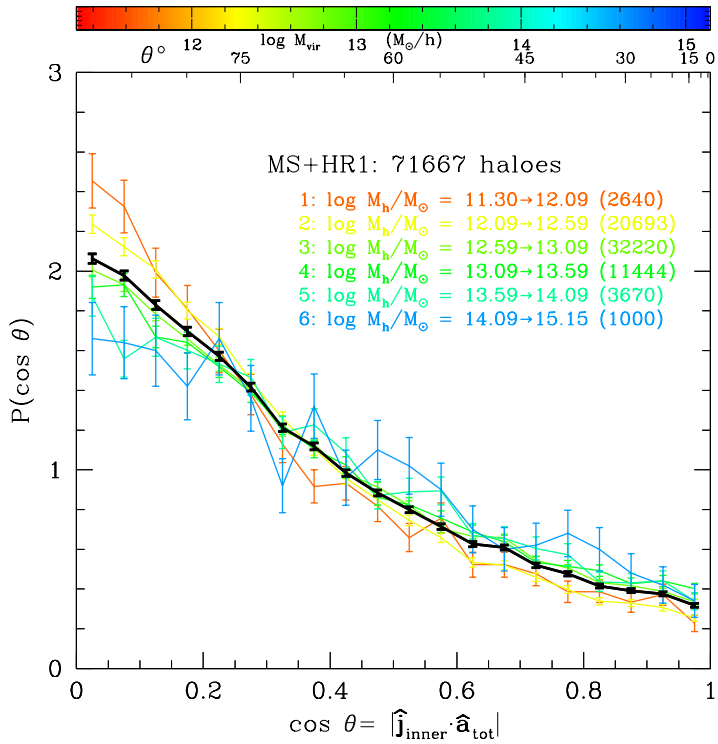

Figure 3.6: Normalised histogram of the angle between the halo major axis and the specific angular momentum of the halo inner region ($\approx 0.25R_{\rm vir}$). The overall median for the MS and HR1 simulations is plotted in black over the coloured lines representing the medians in different mass bins. The error bars show the Poissonian uncertainty ($\sqrt{N}$) in each bin.

strong a constraint as the limits on particle number and those derived from the bootstrap analysis of the vectors, it could still be a significant contributor in scattering the median $\boldsymbol{j}_{\rm inner} \cdot \boldsymbol{j}_{\rm tot}$ alignment to larger angles. This is especially the case given that Bailin and Steinmetz (2005) had relatively few haloes. The lack of a clear trend with halo mass seen in their results is consistent with the results we presented in figure 3.5, since the trend we see is quite weak and has a very large scatter. The similarity between the distribution of angles between the shape axes and angular momentum vectors at $R_{\rm vir}$ and $0.25R_{\rm vir}$ is also in good agreement with Bailin and Steinmetz (2005).

3.3 The effect of baryons

In order to extend our results down to galaxy-scale objects it becomes important to consider the effects of baryons and the galaxy-formation process on the dark matter structures. We wish to know both about the properties of 'realistic' dark matter haloes,

and also how the baryonic physics has transformed them in comparison to purely dark-matter-only structures, such as we see in the larger simulations like the MS.

3.3.1 The simulations

We use the DMG simulation of dark matter with galaxy-formation, described in section 1.5.5; we refer the reader to that section and to Okamoto et al. (2005) for the full details. Very briefly, the simulation consists initially of high-resolution dark matter and gas particles, surrounded in progressively higher-mass collisionless boundary particles. The gas can be transformed into star particles if it either exceeds a density threshold whilst cool (the quiescent mode), or if it is shocked, for example due to a galaxy merger (the burst mode). Stars formed in the quiescent mode have a Salpeter (1955) initial mass function (IMF), but those from the burst mode have a top-heavy IMF as used in Baugh et al. (2005). Stars from the burst mode result in more supernovae, which inject more energy back into the gas, heating it and blowing some of it outside its halo. We use the DMG simulation in conjunction with its dark matter-only counterpart, DMO. Using this allows us to compare the halo properties at the level of individual haloes. As in section 3.2, we analyse our simulations at $z = 0$.

We identify haloes in DMO and DMG in the same way as for MS and HR1 (see section 3.2.2). The spherical overdensity algorithm uses equation 3.1 to define the 'virial' radius of the haloes; for the DMO/DMG cosmology, the overdensity parameter has the value of $\Delta_c = 101$. We have to take account of the low-resolution (high-mass) boundary particles that surround the high-resolution central region in the DMO and DMG simulations. Haloes near the edge of the high-resolution region are at risk of contamination by boundary particles. To ensure that this does not bias our results, we retain haloes only if there are no boundary particles within a radius of $R_{\rm vir} + 100\,h^{-1}$kpc of their centre.

3.3.2 Galaxy identification

We identify galaxies as collections of gas and star particles within dark matter haloes. Each galaxy is identified as the most massive object found by a FOF algorithm performed on the baryonic particles (both stars and gas together) within the parent halo's virial radius, using a linking length of $1.07\,h^{-1}$kpc. This corresponds to $b = 0.02$ using the stellar particle number density at $z = 0$. This value of b was chosen to be an order of magnitude below the value used for dark matter, since baryons collapse by a factor of $\sim 1/(2\lambda)$, and $\lambda \sim 0.04$; see e.g. Fall and Efstathiou (1980), Pearce et al. (2001), Baugh

(2006). We have checked that this results in reasonable-looking galaxies: it does not include lots of hot halo gas, or satellite galaxies that would strongly bias measurements of shape and angular momentum.

The centre of each halo's galaxy is determined by first finding the centre of mass of the stellar particles within the halo, and the radius of the sphere encompassing them all. The radius is then shrunk by 5 percent, and the centre of mass of the particles remaining within the sphere is calculated. Using the new centre, the radius is shrunk again, and we continue to iterate until we have ≤ 50 particles remaining. The galaxy centre is then taken to be the last centre of mass calculated using at least 50 particles. The galaxy centres are found to correspond very well with the halo centres. We also define the galaxy outer radius to be the distance from the galaxy centre to the farthest baryonic particle included in the FOF group.

3.3.3 Physical properties

Just as for the MS and HR1 simulations, we compute a series of physical properties for the haloes identified in DMO and DMG. The inclusion of baryons in the DMG haloes means some definitions have to be made more carefully. The virial masses and radii of the DMG haloes are defined using all the mass (i.e. including baryons), as are the kinetic and potential energies. The smaller number of haloes in these simulations means that it is possible to compute the potential energies using *all* the particles within $R_{\rm vir}$ in a reasonable amount of time, rather than having to use 1000-particle samples as we did for the MS and HR1 data. We have to take into account the different gravitational softening lengths and individual masses of the baryonic particles, so the contribution to the potential energy from each particle pair i–j is the mean:

$$u_{ij} = \frac{1}{2}\left(\frac{-W_2(r_{ij}/\eta_i)}{\eta_i} + \frac{-W_2(r_{ij}/\eta_j)}{\eta_j}\right) \tag{3.11}$$

where $W_2(x)$ is the SPH smoothing kernel (see equations 3.3 and 3.4). The total potential energy of each halo system is therefore:

$$U = -G\sum_{i=1}^{N-1}\sum_{j=i+1}^{N} m_i m_j u_{ij} \tag{3.12}$$

We compute the cumulative specific angular momentum and angular velocity profiles of the halo dark matter only. We also compute the specific angular momentum of the baryonic components (gas and stars) of the galaxies.

Finally, we perform a dynamical decomposition on the star particles in our galaxies, computing the fraction of stars that are in a disc component, in terms of both the mass and B-band luminosity. We do this for galaxies containing at least 5000 star particles, in the same way as Okamoto et al. (2005), which is based on the method of Abadi et al. (2003). The stringent particle-number criterion ensures that we exclude galaxies whose morphologies are biased towards bulginess due to poor numerical resolution. We let the angular momentum of the stellar component of each galaxy define a 'z'-axis, and compute the component of the angular momentum of each star particle parallel to this direction. Half of the bulge is identified with the particles that have $j_z < 0$; the total bulge mass is defined as twice the mass of those particles. The disc mass is then given by the difference between the total stellar mass and the bulge mass. Using the same method, we also compute the disc-to-total ratio in terms of the star particles' B-band luminosity.

3.3.4 Halo and galaxy selection and comparison

The basic halo selection for the DMO and DMG haloes is the same as for MS and HR1 described in section 3.2.4: we require haloes to have $Q \leq 0.5$, and $N_{\rm p}(\leq r) \geq 300$ for the innermost radius in question. Again, we use slightly different selection criteria for the angular momentum orientation results (see Appendix B).

Having two simulations of the same region, run both with and without baryons, means we can directly compare the properties of individual haloes between the two. We match each dark matter halo in DMG with its counterpart in DMO, by finding the closest DMO halo centre within $100\,h^{-1}$kpc of the DMG halo centre.

3.3.5 Results

Angular momentum profiles

We show the cumulative specific angular momentum profiles of haloes in the DMO and DMG simulations in figure 3.7. The results show the same basic trends as those of the MS and HR1 simulations (figures 3.2 and 3.3; we also plot the same $j \propto r$ trend for comparison). The mass trend of $j(\leq r)$, visible in the top panels, is removed using the circular velocity and radius of each halo, $j(\leq r)/(V_{\rm vir}R_{\rm vir})$ (middle panels). The mass trend is also not present when considering the angular velocity $\omega(r)$. There is also a similar degree of halo-to-halo scatter compared to the MS and HR1 results.

Figure 3.8 plots the median $\omega(r)$ results from all four simulations together: we can

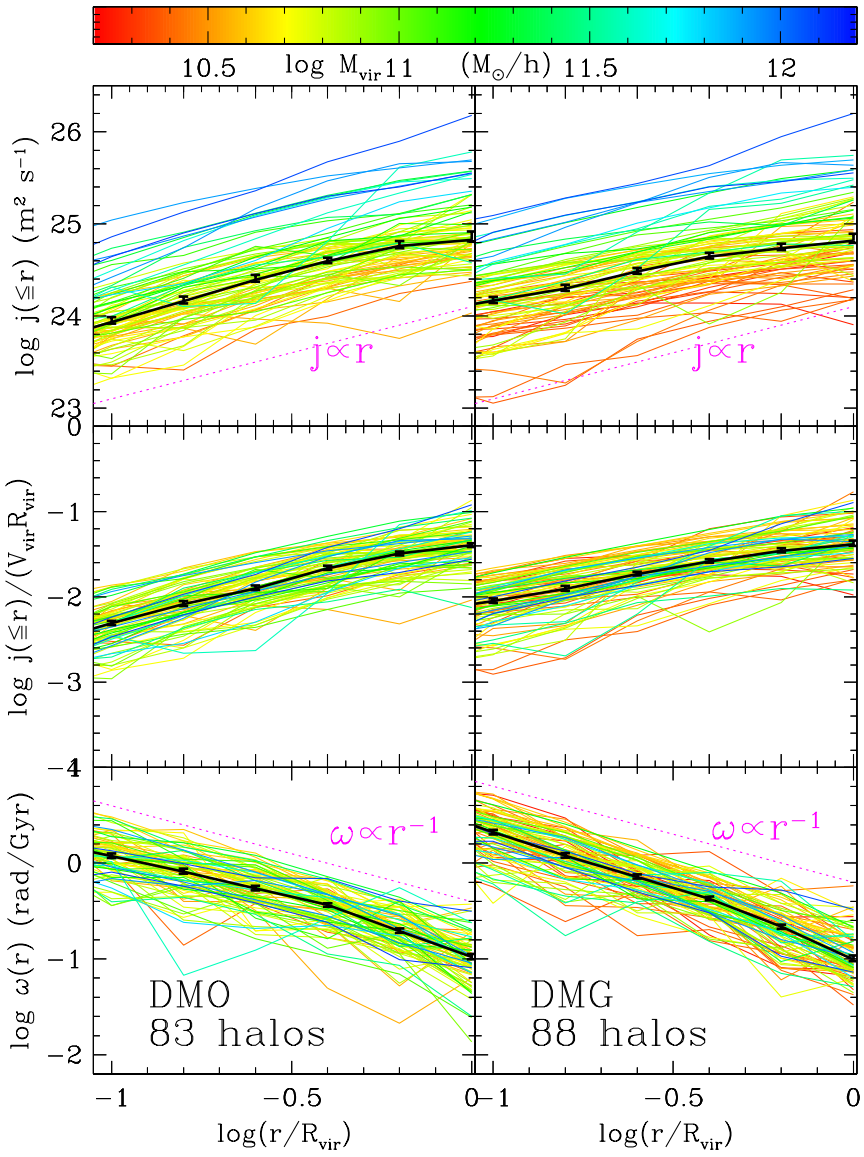

Figure 3.7: Cumulative specific angular momentum profiles (top), scaled angular momentum $j(\leq r)/(V_{\rm vir}R_{\rm vir}) = j(\leq r)/\sqrt{GM_{\rm vir}R_{\rm vir}}$ (middle), and angular velocity profiles (bottom), of the dark matter in haloes in the DMO and DMG simulations (left and right panels respectively). The profile for each halo is plotted, colour-coded by its total mass. The heavy black lines are the median profiles, with error bars calculated using equation 3.9. As a guide, the dotted magenta lines show the radial scaling from simple arguments with constant circular velocity, with arbitrary normalisation (see text). Scaling the angular momentum of each halo by its circular velocity and radius removes the mass-dependence of $j(\leq r)$.

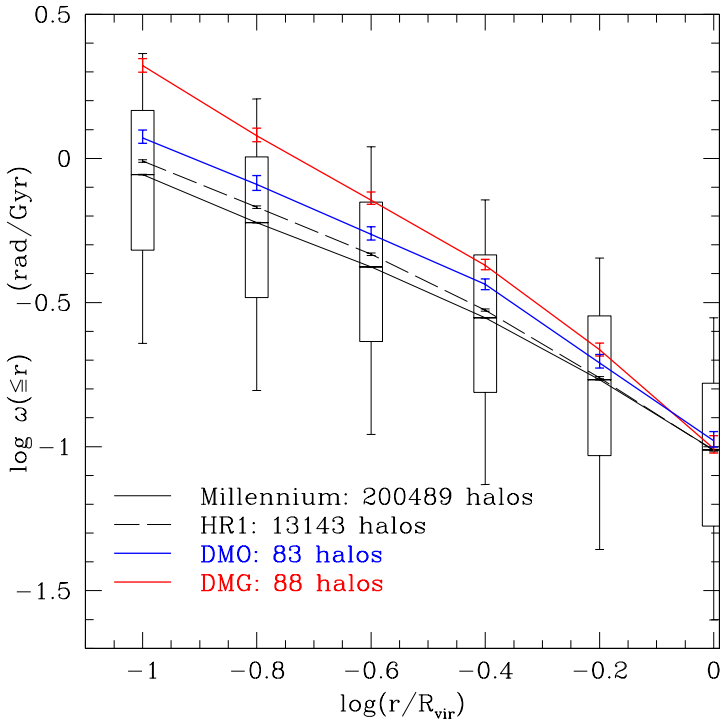

Figure 3.8: The median dark matter angular velocity profiles for haloes in our four simulations. The profiles for haloes containing baryons (DMG) have a significantly greater angular velocity in their inner regions, in the median. As in previous figures, the error bars give the uncertainty in the median (equation 3.9), and the outer bars and boxes on the MS line give the spread of the data (the boxes enclose 68 percent, and the outer bars enclose 95 percent of the data).

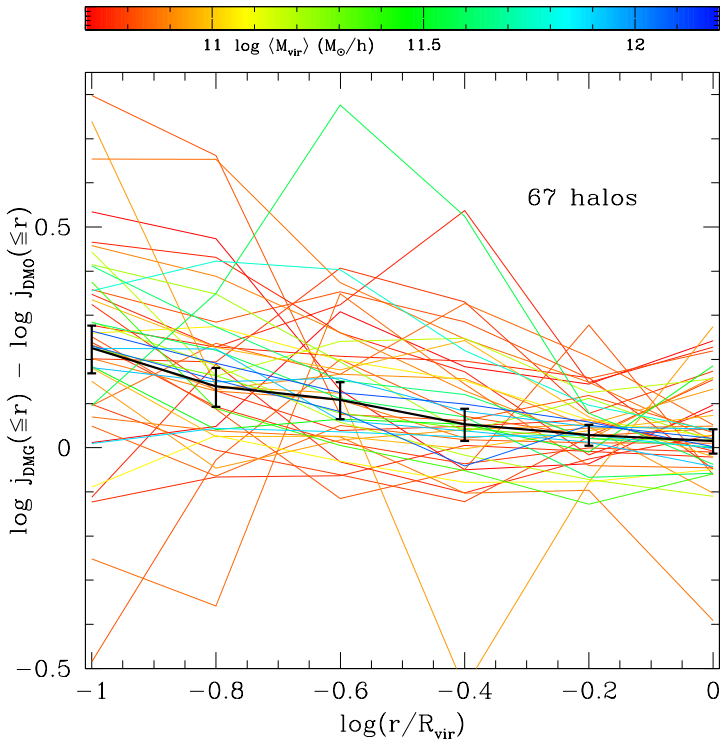

Figure 3.9: Logarithm of the ratio of the cumulative specific dark matter angular momentum profiles of haloes from the DMG simulation to that of the corresponding haloes in the DMO simulation. Each line represents the ratio from a matched DMG-DMO halo pair, colour-coded by the mean mass of the two haloes. The median of the profile ratios is marked by the heavy black line, with error bars given according to equation 3.9.

immediately see that the dark matter in the inner regions of haloes with galaxies spin significantly faster than their dark-matter only counterparts. This can be seen even more clearly in figure 3.9, where we plot the the ratio of $j(\leq r)$ for each DMG halo to that of its DMO counterpart (the equivalent plot for $\omega(r)$ is very similar). Although there is a large halo-to-halo scatter, the median trend is that the angular momentum of the dark matter in the inner 10 percent of a halo is ~ 50 percent greater if that halo is simulated with baryons. It is also important to note that at the virial radius, the dark matter is unaffected by the baryons.

We now look into the difference between the $j_{\rm inner}$ of the DMG and DMO haloes in more detail. As already discussed, semi-analytic models owe much of their success to the fact that they conserve angular momentum of the dark matter and baryons separately, without any transfer between the two components. In the past, hydrodynamical simulations have suffered from transferring large amounts of angular momentum from the

baryons to the dark matter, and the implementation of feedback processes has helped alleviate that by restricting that transfer.

If we consider the dark matter in a single DMG halo and its DMO counterpart, then we would expect it to be more centrally concentrated in the DMG case, due to the baryons dissipating their energy, falling to the halo centre and thus causing a deeper potential well (see e.g. Gnedin et al. 2004, and later discussion in section 4.4.3). If the dark matter conserves its own angular momentum, we would expect that the increase in $j(\leq r)$ would be due to that additional dark matter mass within r spinning up as it fell in. So if the additional angular momentum of the dark matter in the DMG halo is the same as that of the dark matter in the DMO halo at a radius containing the same dark matter mass, then we can say there has been no transfer of angular momentum between the dark matter and the baryons.

We let M_0 be the mass of the dark matter contained within $0.1R_{\rm vir}$ of the DMG halo[2], and let r_0 be the radius in the corresponding DMO halo that contains the same mass, i.e:

$$M_{\rm DMO}(\leq r_0) = M'_{\rm DMG}(\leq 0.1R_{\rm vir}) =: M_0 \tag{3.13}$$

We then compute the ratio between the dark matter $j(\leq 0.1R_{\rm vir})$ of the DMG halo, and $j(\leq r_0)$ of its DMO counterpart. In figure 3.10, we compare this to the ratio of dark matter masses within $0.1R_{\rm vir}$ (note that $R_{\rm vir,DMG} \simeq R_{\rm vir,DMO}$, so we do not distinguish them in this plot).

Figure 3.10 shows us that the increase in angular momentum of dark matter in DMG haloes at a given mass is much more than the corresponding change in mass at that radius (the median point shows it to be about 60 percent change in j compared to 10 percent change in mass). This suggests that the angular momentum of the dark matter is not simply conserved, but instead gains, at least in part, from the baryons. This is consistent with the results of Kaufmann et al. (2007), who performed a detailed investigation of the different ways that angular momentum can be transported away from the cooling gas in a halo, given that current simulations have not yet reached the resolution whereby the final angular momentum of the gas has converged.

[2]When comparing the dark matter mass between the DMO and DMG haloes, we scale each halo's $M_{\rm DMG}$ by $f_{\rm bary}$, the fraction of mass in baryons within $R_{\rm vir}$; i.e. we use $M'(\leq\ r) = M(\leq r)/\left(1 - f_{\rm bary}\right)$.

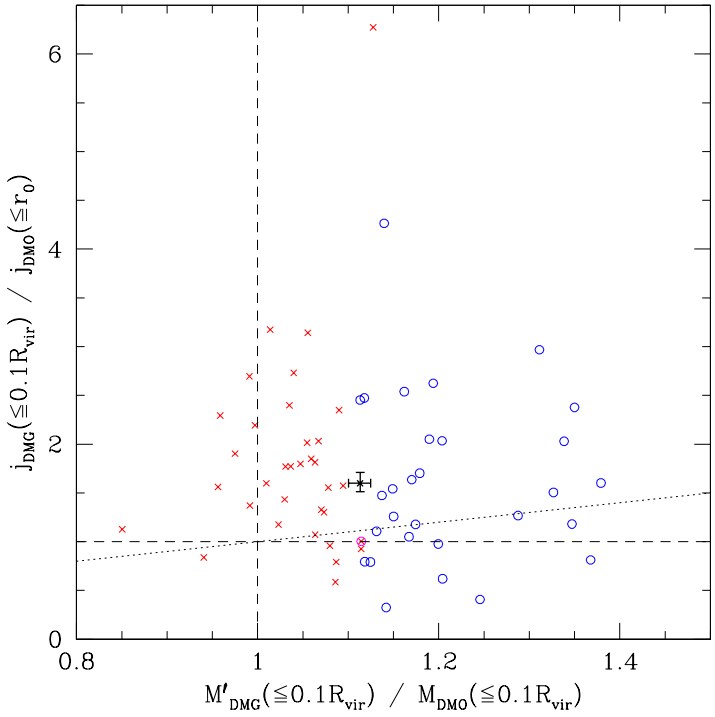

Figure 3.10: Ratio of the specific angular momentum of the dark matter mass within $0.1R_{\rm vir}$ of each DMG halo, to that of the corresponding DMO halo at a radius r_0 that contains the same mass. This is plotted against the ratio of dark matter masses at $0.1R_{\rm vir}$ for each halo pair (the DMG dark matter mass is scaled by the baryon fraction, see text). Dashed lines mark unity for each axis, and the 1:1 line is marked with dots. Haloes are selected according to our usual criteria of $N_{\rm p}(\leq 0.1R_{\rm vir}) \geq 300$ and $Q \leq 0.5$. Blue circles mark the 29 halo-pairs with $r_0 \geq 0.1R_{\rm vir}$; red crosses mark the 34 haloes where $r_0 < 0.1R_{\rm vir}$. In the latter case, the measured $j(\leq r_0)$ could come from fewer than 300 particles, but in practice this only occurs for one halo (marked with a magenta circle around its red cross) since most have $r_0 \approx 0.1R_{\rm vir}$. The median of all the halo-pairs excluding this one is marked with a black cross with error bars.

Spin orientation profiles

We examine the dark matter spin orientation profiles of haloes in the DMO and DMG simulations in the same way as for the MS and HR1 data; note that the 'inner' region is again set at $\approx 0.25R_{\rm vir}$. From the individual halo profiles (figure 3.11) we can see that, as with the MS and HR1 haloes, there is a median trend such that the dark matter angular momentum vector at $R_{\rm vir}$ is 15–30° away from that of the inner dark matter, but also that there is a very large scatter about that trend. There is also no discernible trend with halo mass; given the small mass range of these haloes, this is consistent with the results shown earlier (figure 3.5). When comparing the median trends of DMO to those of DMG (lower panel of figure 3.11), there is a suggestion that the haloes that have experienced baryonic physics have a total spin that is slightly more well-aligned than the dark-matter only haloes. However, the two lines are within each others' error bars, so this result on its own is inconclusive.

In order to examine any difference between the orientation distributions in more detail, we compare the orientation profiles of DMG haloes directly with their counterparts in the DMO simulation. These results are shown in figure 3.12. There is a definite tendency for the baryonic processes inside the DMG haloes to change the orientation of the inner dark matter angular momentum, while the outer regions of the haloes remain well-aligned with their DMO counterparts. In combination with the tentative results from figure 3.11, we find that the baryons tend to cause the inner regions of haloes to become better aligned with their total halo angular momentum vector.

This is in agreement with the similar work of Bailin et al. (2005a), who considered the angle between the minor axis of the haloes simulated with and without galaxy-formation physics. They found that the inclusion of galaxy formation re-orients the inner halo shape axes while leaving the outer halo unchanged.

Dark Matter-Galaxy alignment distributions

For most practical purposes, the orientation of a halo to its galaxy is a more important distribution than the intra-halo orientation profile itself. The alignment of a galaxy with its halo is in principle an observable quantity, since the gravitational lensing of background objects can be used to measure the size and shape of the mass distribution surrounding a galaxy (although in practice this can be extremely difficult). Furthermore, semi-analytic models are used to place the modelled galaxies into pure-ΛCDM simulated haloes. If we

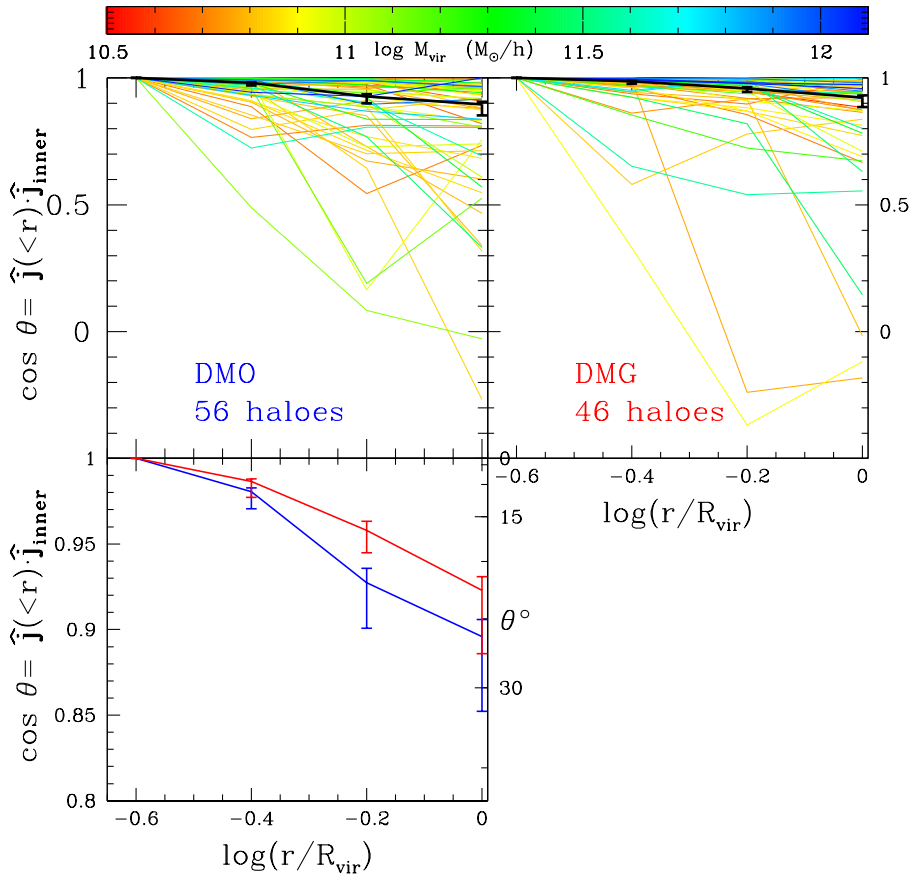

Figure 3.11: Cumulative dark matter angular momentum orientation profiles of haloes in the DMO and DMG simulations (top left and right respectively). Each halo is colour-coded according to its mass, with the median profile shown in heavy black, with error bars plotted according to equation 3.9. The bottom-left panel shows just the two median lines, with DMO and DMG shown in blue and red respectively.

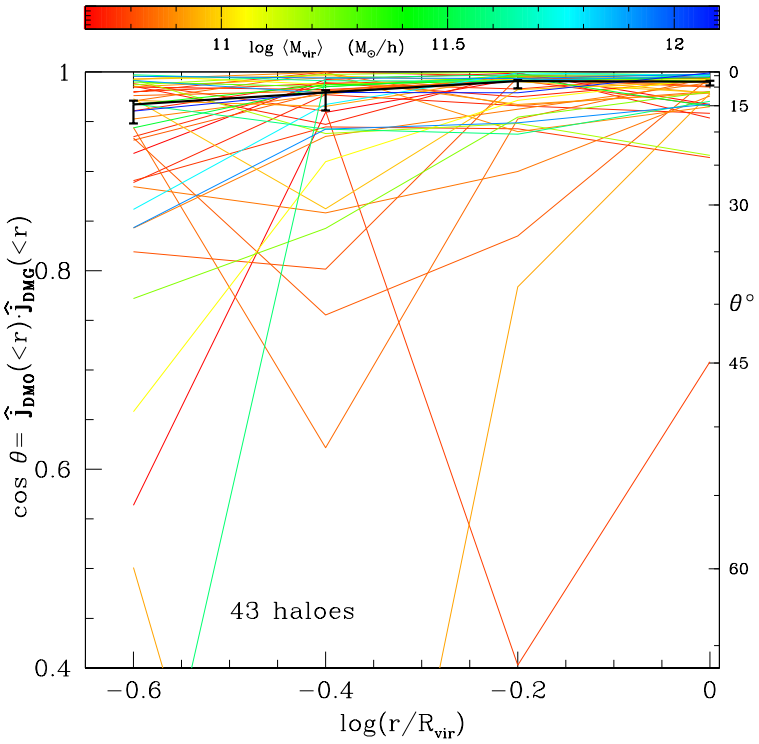

Figure 3.12: Angle between the cumulative specific angular momentum vectors of dark matter in the DMG simulation and their counterparts in the DMO simulation ($\cos\theta = 1$ means the dark matter mass within that radius in the DMG halo is aligned with that from the DMO simulation). Each halo pair is colour-coded according to the mean of the two halo masses, and the median trend with error-bars is marked with the heavy black line.

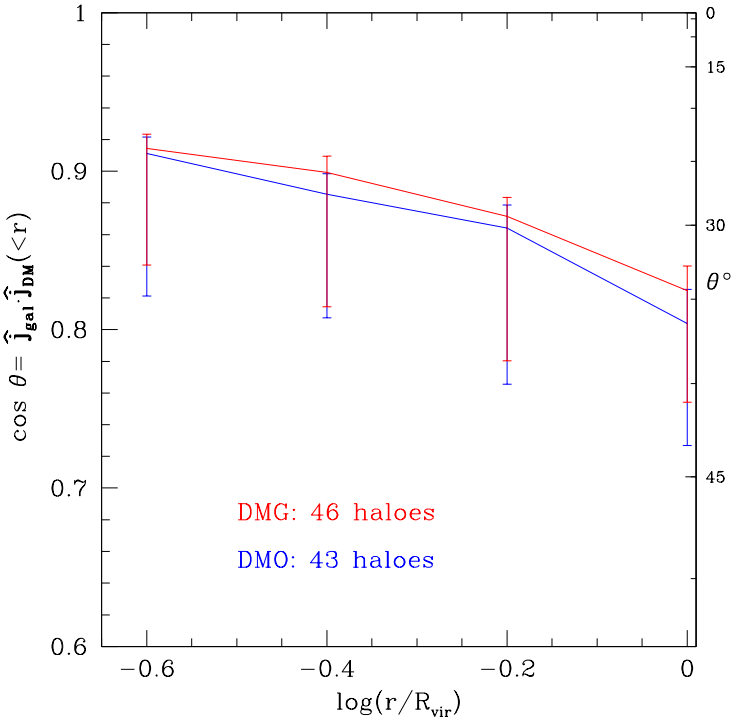

Figure 3.13: Orientation profiles of haloes of the galaxies in the DMG haloes with respect to the cumulative dark matter angular momentum vector of the DMG parent haloes themselves (red), or the corresponding DMO haloes (blue). Just the median profiles are plotted. Note that the error bars are the uncertainties on the median (equation 3.9), *not* the spread of the data, which is much larger.

are also to model galaxy alignments (for example to produce mock galaxy catalogues for lensing), we need to know how a fully-simulated galaxy would compare to the equivalent pure-ΛCDM halo in order to implement the orientation.

Previous work (on these simulations) by Libeskind et al. (2007) showed that the galaxy angular momentum is a very accurate proxy for the orientation of the galaxy itself (i.e. its mass distribution). Therefore, in this work, we shall use the angular momentum of the stellar component of the galaxies to define their orientations.

Figure 3.13 shows the median orientation profiles of the stellar component of galaxies from DMG with respect to the dark matter in either their parent haloes, or in the corresponding DMO haloes. The first thing to note is that there is a very large scatter in the results, to the extent that we do not show the usual boxes and outer bars; the error bars shown give the uncertainty in the median. Only a very weak trend with radius is visible: The median goes from 25° at $\approx 0.25 R_{\rm vir}$ to 35° at the virial radius, but the scatter means

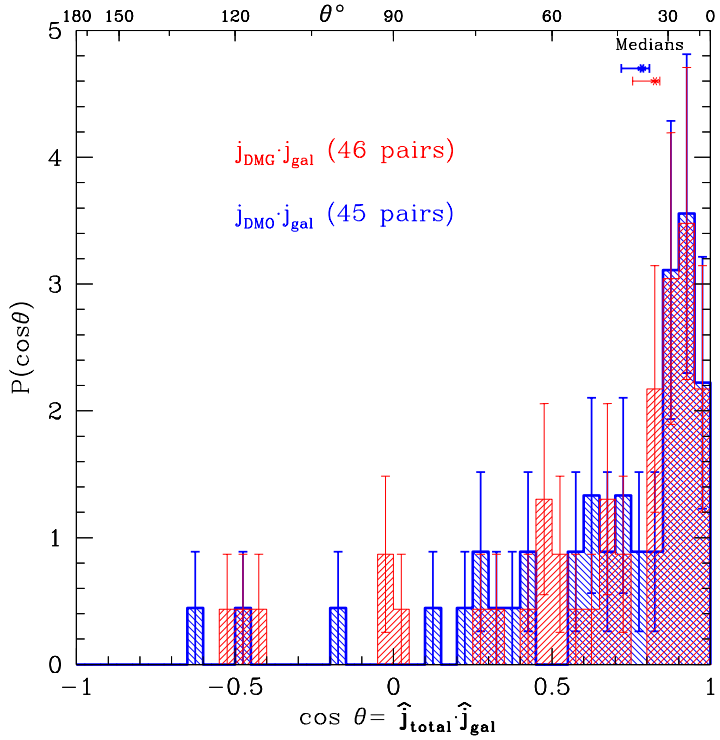

Figure 3.14: Distribution of the angles between the specific angular momentum vector of the stellar components of galaxies in DMG haloes, and the total dark matter specific angular momentum of the DMG halo itself (red) or the corresponding DMO halo (blue). The medians of the distribution are marked (at arbitrary heights) with error bars given by equation 3.9.

that this is of very low significance.

We examine the alignment distributions themselves in figures 3.14 and 3.15, plotting the histograms of cosines between $\boldsymbol{j}_{\rm gal}$ and the dark matter $\boldsymbol{j}_{\rm tot}$ and $\boldsymbol{j}_{\rm inner}$ respectively. The distribution for the inner halo is certainly tighter than at $R_{\rm vir}$, but haloes are present over the same range of values. Furthermore, the distributions remain essentially unchanged if the same region is simulated without the baryons. This galaxy–halo misalignment serves to wash out the subtle changes in the relative orientations of the dark matter from the DMO and DMG simulations seen in the previous section.

We have also examined the alignment distributions given by splitting the galaxy–halo populations according to their disc-to-total ratios. However, because this restricts us to galaxies with at least 5000 star particles, we are left with too few objects in the resulting disc-dominated and bulge-dominated populations to be able to make any reliable conclusions. We cannot measure any significant difference in galaxy–halo alignment due

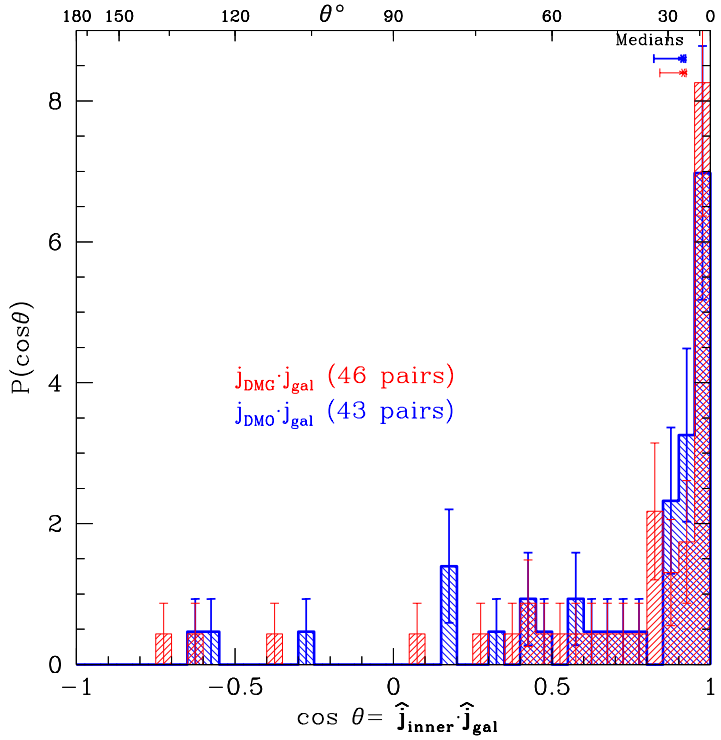

Figure 3.15: As figure 3.14, but this time using the angle between the *inner* halo dark matter angular momentum vector and the stellar component of the central galaxy. The medians and their uncertainties are marked.

to galaxy morphology.

In their analogous work on halo shape axes, Bailin et al. (2005a) found that the presence of baryons caused the inner halo to align itself with the galactic disc. We do not find such a strong correlation in terms of angular momenta, probably due to a combination of a different physical model, a larger mass range, and having more objects; the correspondence would also be affected by the distribution of alignments between the halo angular momentum and shape axes (see Chapter 2). Our results are similarly consistent with those from the four haloes presented in Gustafsson et al. (2006), both in terms of the variability between individual haloes and the overall trend. Croft et al. (2008) looked at the orientations of the shape and angular momenta of the different components of their galaxies (at $z = 1$), defined as the dark matter, gas and stars in the self-bound subhaloes in their simulation. Their results show slightly worse alignment than we see here (a median angle of 43.5° between dark matter and stars in the galaxies; we have 23.9° and 34.4° for the median angles with the inner and total halo respectively). The difference in selection will be significant: we only use the central galaxy in each halo, as we decided

we do not have the resolution to be able to look at subhaloes properly. However, we also take great care to remove objects whose combination of angular momentum magnitude and number of particles results in an uncertain measure of orientation. Not doing this will result in greater scatter in the angle between components. Croft et al. (2008) do perform resolution tests however, which are very informative: in their lower resolution run, the median alignment is significantly poorer. The resolution in our simulations is slightly better, so our results are probably consistent.

Croft et al. (2008) and Gustafsson et al. (2006) used different physical models to form galaxies in their simulations. While we expect this to have a strong impact on the angular momentum *magnitude* of the objects that form (which, according to Kaufmann et al. (2007), has yet to reach convergence in a simulation), it is not clear to what extent different physics will systematically effect the orientation of galaxies.

Kang et al. (2007) used a semi-analytic model to study the central-satellite galaxy alignments. They found that they could match the observed characteristics of the satellite galaxy alignment distributions (e.g. colour and mass dependence) if each central galaxy was perfectly aligned to its halo's spin axis rather than the shape axis. It would be interesting to see how our finding of a broad galaxy–halo alignment distribution affects the results of such a semi-analytic model. (The alignments of satellite galaxies in our DMG simulation has already been investigated in Libeskind et al. 2007.)

Projected Mass Distributions

The misalignment between haloes and their galaxies can have very important consequences for observational efforts to measure halo properties, such as from gravitational lensing. In practice, the lensing signal from individual galaxy-mass haloes is too weak to be useful; it has to be averaged over many objects, by stacking data from appropriately scaled and aligned images (Natarajan and Refregier, 2000). Thus, in order to produce predictions of the observable shapes of dark matter haloes from simulations, we also need to look at aligned, stacked, projected shapes rather than the full 3-D triaxiality/sphericity distribution (as seen in Chapter 2).

The broad distribution of galaxy–halo (mis-)alignments (figure 3.14) will have a significant impact on the observable halo shape from a stacked 2-D mass distribution. We take the population of relaxed, well-resolved DMG haloes containing well-resolved galaxies (i.e. $Q_{\rm lim} = 0.5$, and requiring at least 300 dark matter particles in each halo, as well as at least 300 star particles in each galaxy), and transform their particles' coordinates

such that the x–y 'image' plane corresponds to their galaxy's major–minor axis plane. We then compute the 2-D projected mass distribution matrix M of the halo, which has the components:

$$\mathcal{M}_{\alpha\beta} = \sum_{i=1}^{N_{\rm p}} m_i r_{i,\alpha} r_{i,\beta} \tag{3.14}$$

where the sum is over all particles in the halo (dark matter and baryons), and α, β denote the matrix indices (1 or 2), such that $r_{i,1}$ is the halocentric distance of particle i in the direction parallel to the galaxy's major axis; $r_{i,2}$ is the distance parallel to the galaxy's minor axis. These matrices are then normalised by the halo size, $\mathsf{M}' = \mathsf{M}/\left(M_{\rm vir} R_{\rm vir}^2\right)$, and then summed over all the selected haloes, resulting in a stacked mass distribution matrix. This has eigenvectors and eigenvalues that describe the net shape distribution of the selected haloes, in 2-D projection aligned by their galaxy.

Figure 3.16 shows the ellipse defined by the resulting eigenvectors, along with those from each individual halo. Here we can see that although the projected mass distributions of individual haloes are by no means necessarily circular, the misalignment of the halo with the galaxy means that the stacked mass distribution is almost exactly circular: the axis ratio is $b/a = 0.989$ (so the eccentricity is $\epsilon = \sqrt{1 - b^2/a^2} \simeq 0.1$ and the ellipticity is $e = 1 - b/a \simeq 0.01$); given the uncertainties associated with measuring the angular momentum and shape directions, this is indistinguishable from a circle.

The distribution of the individual and stacked axis ratios themselves is shown in figure 3.17. Even though the distribution peaks significantly away from $b/a = 1$, the stacked result (marked by the arrow) is essentially indistinguishable from unity. We have estimated the error on this stacked halo result, by bootstrap-resampling the projected-halo shape data, and re-computing the stacked result. The point with the percentile boxes and outer bars in figure 3.17 shows the median and spread (68 percent of the data within the boxes, 95 percent within the bars) of the data from 5000 bootstrap resamplings.

There has been some limited observational work to attempt to measure the shapes of dark matter haloes using weak lensing. Hoekstra et al. (2004) claimed to have found a significant detection of halo ellipticity, excluding circular haloes at the 99.5 percent confidence level, and yielding an average axis ratio of ≈ 0.7. However, they lacked redshift data, which limited the accuracy of their results. Parker et al. (2007) found a similar result (an axis ratio of ~ 0.7 at a 2σ level) using the CFHT Legacy Survey, again without redshift data. Mandelbaum et al. (2006) used the very large dataset of the SDSS (including redshifts and morphologies), and performed a very thorough exploration of

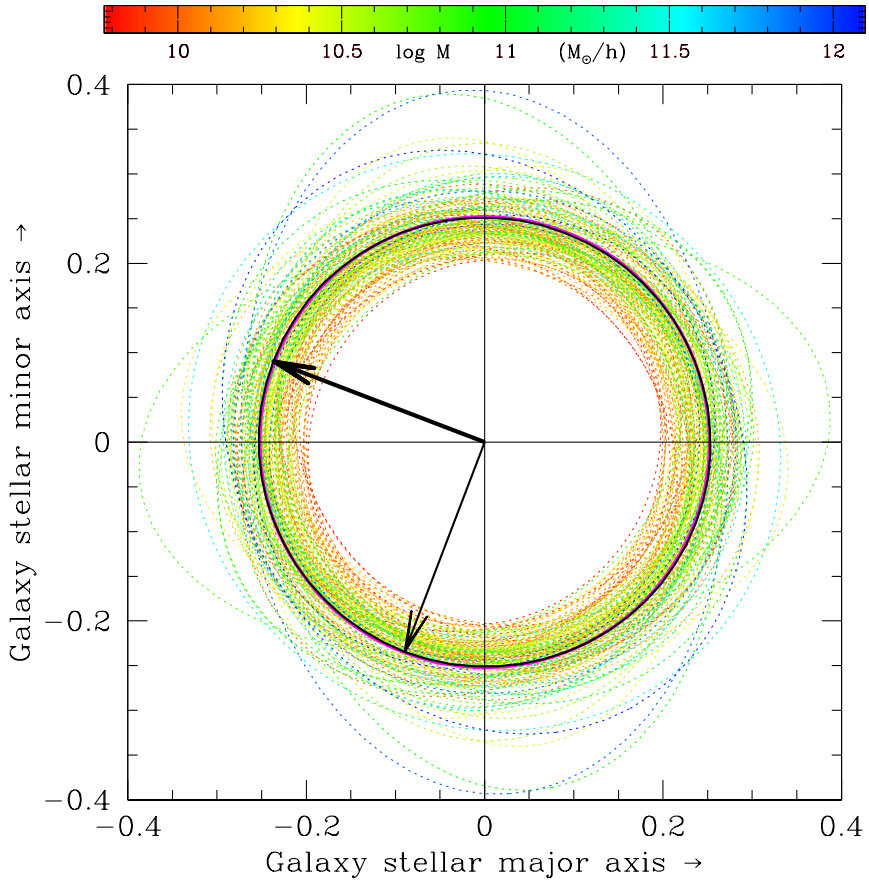

Figure 3.16: The 2-D projected normalised mass distributions of DMG haloes (coloured dotted lines), each having been aligned according to its galaxy's stellar mass distribution. The colouring is by the total halo mass. The net result from stacking each halo is the heavy black ellipse, with arrows marking the semi-major (heavy) and semi-minor (lighter) axes. Plotted beneath the stacked mass distribution ellipse is a circle (heavy magenta) as a visual aid. The axes are labelled in the dimensionless units of the matrix M' (see text).

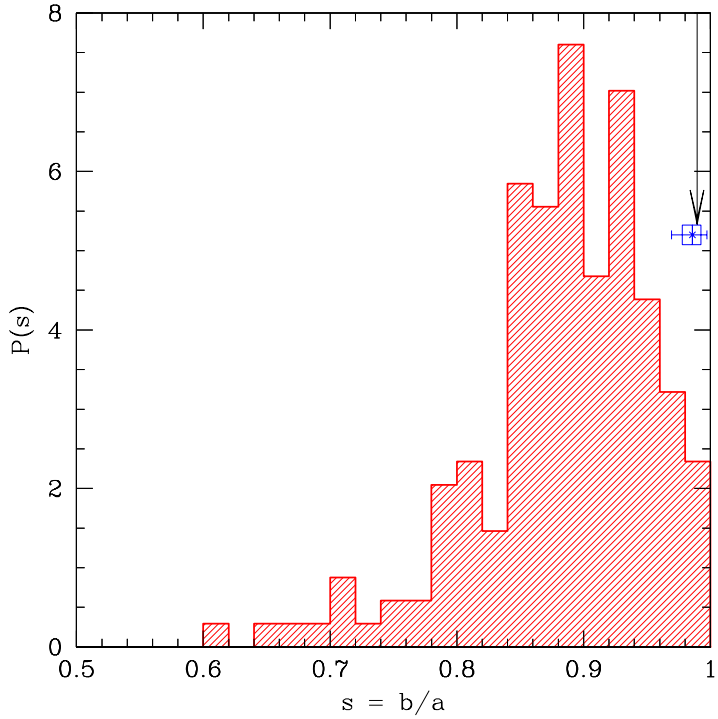

Figure 3.17: Normalised histogram of the axis ratios of the 2-D projected mass distributions of haloes shown in figure 3.16. The axis ratio of the stacked mass distribution is indicated by the arrow at $b/a \simeq 1$. Below the arrow is a point with percentile boxes and outer bars (see figure 3.2), showing the spread of data from bootstrap-resampling the projected halo distribution (see text). This gives an estimate of the uncertainty on the stacked-halo result.

possible systematic effects (see also Mandelbaum et al., 2005). Their results were far less conclusive, not finding definitive detection of halo ellipticity. There was a hint that spiral galaxies are aligned perpendicular to their haloes when averaged over luminosities, and that ellipticals are increasingly well aligned with increasing luminosity. However, these results were not statistically significant. We have checked to see if our results vary with galaxy morphology, as determined by the disc-to-total ratios. However, we do not have enough objects to be able to detect any statistically significant variation (there are just 30 galaxies that pass the additional criterion of having more than 5000 star particles, 10 of which have B-band disc-to-total ratios > 0.7.).

These papers highlight the difficulties in using weak lensing to measure halo properties, and the results we have presented here have shown how small the effect is that they are trying to detect. When interpreting this result, it is important to bear in mind the caveats that come with it, and how they might be answered. Firstly, our use of the SO algorithm for defining the halo boundaries inherently biases the halo mass distributions to be more spherical (see Chapter 2). However, figures 3.16 and 3.17 show that this is not the main cause of the near-spherical stacked halo: rather, it is the mis-alignment between galaxy and halo that smears out the significant projected ellipticities of the haloes.

We have only shown the projected halo ellipticities at the virial radius. Studies have shown that CDM haloes are expected to become increasingly aspherical towards the centre (Hayashi et al., 2007). However, it is not clear that this remains the case for systems with baryons: the limited studies of the shape profiles of CDM haloes with baryons suggest that their sphericity does not vary much with mass, and they could even become *more* spherical towards the centre, depending on their merger histories (Kazantzidis et al., 2004; Bailin et al., 2005a; Gustafsson et al., 2006).

Finally, it is worth noting what constraints might also be possible from strong gravitational lensing. Strong lensing can provide good constraints on the innermost regions of galaxies and clusters, and has been used to measure halo density profiles (see e.g. Hoekstra and Jain, 2008; Chen and McGaugh, 2008, and references therein). Minor and Kaplinghat (2007) modelled the effect of an ellipsoidal mass distribution, with different galaxy–halo alignment distributions, on the strong-lensing signal from haloes with a central elliptical galaxy. In particular, they compared the lensing probability as a function of image separation, for double- and quadruple-image systems, and "naked cusp" systems (strongly-magnified triple-image configurations). They found that the total lensing probability at relatively large separations ($\gtrsim 5''$) is significantly higher for triaxial sustems

compared to spherical systems, due to the additional mass along the line of sight. Furthermore, at relatively small image-separations ($\lesssim 5''$), the lensing probablilties of cusps and quads is increased relative to the probability for double-images, if the major axes of the projected mass and light distributions are aligned (and reduced if they are anti-aligned). This method, of examining the relative image multiplicities of a population of strong-lensing systems, provides a statistical way of measuring the galaxy–halo alignment without having to perform individual lens modelling.

3.4 Conclusions

In this chapter we have investigated the angular momentum structure of dark matter haloes. We have looked at cluster-mass haloes from a pair of very large-scale ΛCDM simulations, containing many well-resolved objects. We then extended our study down to galaxy-mass haloes, simulated both with and without the physics of gas and star-formation. We also compared the orientation of the dark matter angular momentum to that of the galaxies that form within the haloes.

We have found that the cumulative specific angular momentum of the dark matter within a given radius, $j(\leq r)$, in the simulations without baryons, exhibits significant scatter between haloes. However, there is a clear trend in the median, similar to the $j \propto r$ scaling from simple circular motion arguments. The normalisation of this trend scales with halo mass, although the halo-to-halo variation still produces a significant scatter, even at fixed mass. We find an equivalent trend with radius for the angular velocity magnitude $\omega(r)$, which still shows a significant degree of scatter, but does not depend on halo mass. It can clearly be seen that haloes do not rotate like solid bodies, and behave much more like they have constant rotational velocity (i.e. similar to a $\omega \propto r^{-1}$ scaling). These results are consistent over the ~ 5 orders of magnitude in halo mass spanned by our pure-ΛCDM simulations.

We also find a large scatter in the orientation of the dark matter cumulative angular momentum vectors at different radii, compared with that within an 'inner' radius of $\approx 0.25 R_{\rm vir}$, $\boldsymbol{j}_{\rm inner}$. In the median, the total specific angular momentum (i.e. at the virial radius) is directed about 25° away from $\boldsymbol{j}_{\rm inner}$. The data is spread over a wide range of angles, with 95 percent of the haloes having their total angular momenta directed between 5° and 65° away from their $\boldsymbol{j}_{\rm inner}$. There is also a weak trend with mass, with the more massive haloes showing a greater range of alignment angles (hence more misalignment in

the median). We suggest that this is due to the hierarchical nature of structure formation, with the more massive haloes being more likely to have suffered a recent merger event that could have altered the halo angular momentum structure.

Following this work on dark-matter-only simulations, we then moved on to investigate the effects of baryons on the dark matter angular momentum. We used an existing simulation of galaxy formation in a small volume (DMG), in tandem with the same volume re-simulated without baryons (DMO). This enables us not only to compare the distributions of halo properties with and without baryons, but also to compare individual haloes with their counterparts in the other simulation.

We detected a small (about 50%) but significant increase in the median dark matter angular momentum magnitude at $0.1R_{\rm vir}$ in haloes with galaxies, compared to their dark matter-only counterparts (note that, typically, the bulk of the mass of the galaxies themselves is within a significantly smaller scale). This difference decreases with halo radius, such that by $R_{\rm vir}$ the haloes simulated with and without baryons are indistinguishable (although there is a significant scatter between individual haloes). We have shown that this increase is due, at least in part, to transfer of angular momentum away from the baryons and into the dark matter; the baryons do not conserve their own angular momentum.

The process of galaxy formation also affected the orientation of the dark matter angular momentum vectors. Although again there is a large amount of variation between haloes, the median of the distribution suggests that the presence of baryons causes the dark matter in the inner regions of the halo to become better aligned with the total halo spin direction. This is consistent with previous results on changes to the halo shape axes (Bailin et al., 2005a).

Comparing the orientation of the angular momentum of the stellar components of the galaxies with that of the dark matter throughout the haloes, we found that the galaxies exhibit a broad distribution of alignments, ranging from perfectly aligned to over 120° away. There is a slightly greater tendency for alignment in the inner regions of the halo. We find that because of the large amount of scatter between haloes, it is not possible to distinguish between the halo–galaxy alignments when using the haloes from the DMG or DMO simulations; the orientation distributions are the same. We also cannot distinguish between the galaxy–halo alignment distributions of bulge-dominated and disc-dominated galaxies, since protecting against numerical resolution effects in this case leaves us with very few objects.

Gravitational lensing is potentially a very powerful tool for testing theories of ΛCDM

structure formation, and the more complex physics that goes into the galaxies themselves. However, we need concrete predictions from simulations of the projected halo mass distributions, aligned according to the galaxies. We have found that, although individual haloes have aspherical projected mass distributions, when they are aligned by their galaxies and stacked the shape distribution is washed out; the resulting distribution is circular. Thus, our prediction of the ellipticity of the weak lensing signal from ΛCDM haloes is indistinguishable from that of modified gravity theories such as TeVeS. Further work (with more haloes) is required to see if there is any set of selection criteria—such as selecting by morphology or luminosity—that will provide a detectable signal.

So, a consistent picture is emerging from this work and others about the spin and shape structure of ΛCDM haloes, and what happens to them under the influence of gasdynamics, star formation and feedback. Dark matter haloes are triaxial with a preference for prolateness, becoming increasingly prolate towards their centres (Chapter 2, and Hayashi et al. 2007). They have very little coherent rotation, and less angular momentum towards their centres. The halo angular momentum is more consistent with scalings as if it has constant rotational velocity rather than like a solid body (figures 3.2 and 3.8). If they are simulated with baryons and the physics of galaxy formation however, they become more spherical overall, with a tendency towards oblateness (Kazantzidis et al., 2004; Bailin et al., 2005a; Gustafsson et al., 2006). The inner regions of the haloes change the most, increasing in rotation (figures 3.8 and 3.9), and becoming more aligned with the original halo at $R_{\rm vir}$ (figures 3.11 and 3.12), i.e. the halo has become more coherently aligned overall. The baryons have taken information about the halo orientation at $R_{\rm vir}$ into the inner halo as they collapse, resulting in central galaxies that tend to be slightly better aligned with the inner halo than the total halo (figures 3.13, 3.14 and 3.15; Bailin et al. 2005a, Gustafsson et al. 2006)

Although this is an appealing picture, it must be stressed that all the quantities involved (magnitudes and directions of shapes and angular momenta) have very broad distributions due to large variation between individual haloes. One of the most important limitations of this work and others is the small numbers of well-resolved objects available for study. The internal alignment structure of haloes and galaxies is expected to depend on their merger histories, and therefore morphologies. Simulations with many more haloes are required in order to split the distributions according to such properties.

Furthermore, galaxy formation simulations have by no means yet 'converged' on a single recipe for the baryonic physics involved; simulated galaxies, while much more realistic

than a decade ago, are not yet passable for the 'real thing'. We would expect different physical processes to affect the angular momentum structure of haloes differently, since they are known to affect the angular momentum of the baryons (Okamoto et al., 2005). For example, Zavala et al. (2008) showed that differences in galaxy morphology stemming from different feedback processes are related to the galactic angular momentum tracking the evolution of that of the dark matter at different radii (e.g. inner instead of total). Therefore, further studies need to be made of the influence of different physical processes (such as different feedback modes) on the angular momentum and shape profiles of the resulting galaxy–halo systems, and their observational consequences.

Chapter 4

Density profiles of dark matter haloes

The work described in sections 4.2 to 4.3 has been published as Neto et al. (2007, hereafter N07).

4.1 Introduction

A broad consensus is emerging on the properties of dark matter haloes within the ΛCDM paradigm, thanks to modern simulations of the formation of cosmic structures. Properties such as the mass function of haloes (see Tinker et al. 2008, and references therein), the angular momentum and shape (see Chapter 2), and the density profiles and substructure within the virial radius are becoming very well determined over a large range of halo masses.

The spherically-averaged halo mass density profile, $\rho(r)$, is a particularly interesting property. The internal mass distribution of haloes has immediate observational consequences, through gravitational lensing studies of galaxy clusters, or rotation curves of disc galaxies. Furthermore, studies have long shown that the density profiles of relaxed purely dark-matter haloes exhibit remarkably simple, and similar, behaviour over a wide range of objects. The apparently 'universal' behaviour is well-described by the functional form proposed by Navarro et al. (1996, 1997), for the mass density in terms of the cosmological critical density $\rho_{\rm crit}$:

$$\frac{\rho(r)}{\rho_{\rm crit}} = \frac{\delta_{\rm c}}{(r/r_{\rm s})(1+r/r_{\rm s})^2} \tag{4.1}$$

The two free parameters in the NFW profile are the characteristic density $\delta_{\rm c}$, and the scale radius $r_{\rm s}$; the latter is often described in terms of the halo radius R (which we shall define later), as the concentration $c \equiv R/r_{\rm s}$. This density profile behaves like $\rho(r) \propto r^{-3}$ at large radii ($r \gg r_{\rm s}$), but changes smoothly to follow $\rho(r) \propto r^{-1}$ towards the centre of the halo.

In figure 4.1 we show the NFW density profile and corresponding circular velocity profile ($v_{\rm c}(r) = \sqrt{GM(\leq r)r^{-1}}$, where the spherically-averaged mass within r is $M(\leq r) = 4\pi \int_0^r x^2 \rho(x) {\rm d}x$), along with those from other models. The constant-density case $\rho(r) = \rho_0$ is clearly not realistic, but provides a useful fiducial line. The singular isothermal sphere (SIS) has a density $\rho(r) = v_{\rm c}^2/(4\pi G r^2)$, where the circular velocity $v_{\rm c}$ is independent of radius. Most density profiles proposed in the literature for dark haloes are shallower than the r^{-2} trend of the SIS model at small radii, but steeper at large radii. The Burkert (1995) profile,

$$\rho(r) = \frac{\rho_{\rm c}}{(1 + r/r_{\rm c})\left(1 + (r/r_{\rm c})^2\right)} \tag{4.2}$$

exhibits a central core within $r_{\rm c}$, with the density tending to a constant value of $\rho_{\rm c}$, in contrast to the 'cuspy' NFW model that continues to increase towards the centre. Some observations (such as rotation curves of spiral galaxies, which we discuss in section 4.4.4) suggest the need for a density profile with an inner core, although data are not consistent enough for this to be true of all galaxy types (see e.g. Chen and McGaugh, 2008, and later discussion).

Nevertheless, the work of Navarro et al. (1997, hereafter NFW97) and many subsequent studies has showed that the NFW profile is a good fit to well-resolved, relaxed dark matter-only haloes that have formed hierarchically, regardless of their mass or the underlying cosmology[1]. The cosmological information is encoded in the correlations between the parameters in the function, which also in principle allows measurements of the density of haloes to be used to constrain cosmological parameters. These correlations arise because the characteristic density of a system is related to the density of the Universe at the time when the halo forms. This result has been confirmed in many subsequent studies of the NFW model (e.g. Kravtsov et al., 1997; Avila-Reese et al., 1999; Ghigna et al., 2000; Jing, 2000; Bullock et al., 2001b; Eke et al., 2001; Klypin et al., 2001; Dolag et al., 2004).

As a result, many semi-analytic or empirical algorithms have been developed to explain and predict the distributions and correlations of halo structural parameters as measured in N-body simulations. The differences in these procedures however lead to significantly

[1]Recent studies of very high resolutions simulations have shown small but systematic deviations of dark matter haloes away from the NFW profile (Navarro et al., 2004b; Prada et al., 2006; Merritt et al., 2006; Gao et al., 2008). It has been found that a density profile with a smoothly varying logarithmic slope that depends on r (the "Einasto" profile) yields a better fit to simulated haloes. However, the difference is small, and the NFW profile will suffice for the purposes of this chapter.

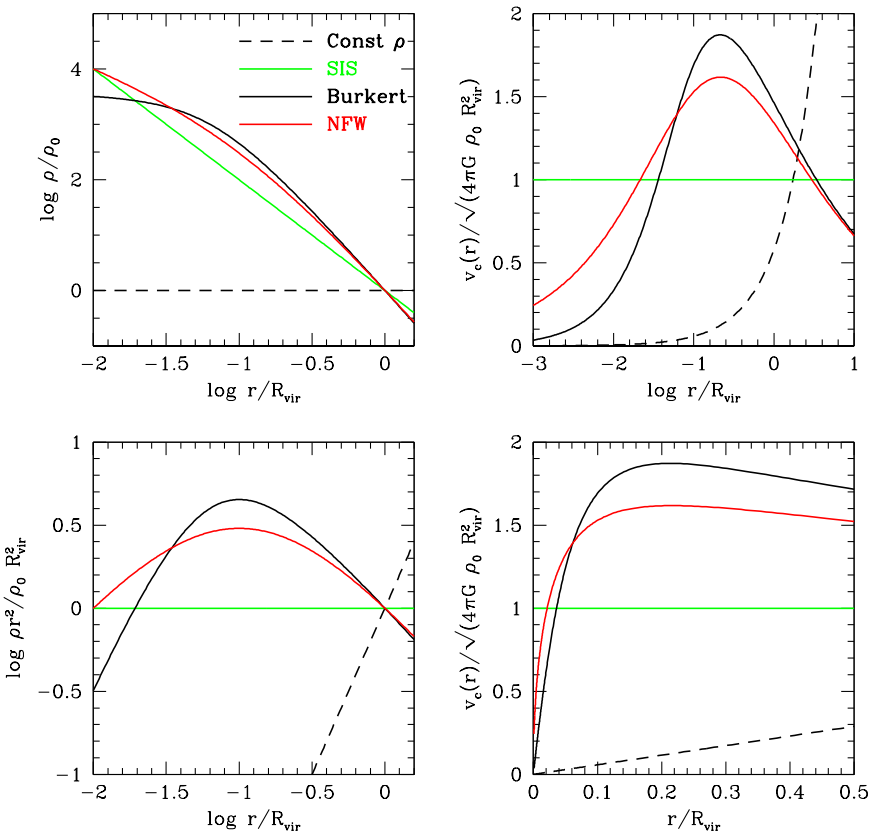

Figure 4.1: Illustrative comparison of density profile models (left) and their corresponding circular velocity profiles (right). The lower panels simply use different axis scales: the lower density plot is normalised by the isothermal scaling $\rho(r) \propto r^{-2}$, and the lower circular velocity plot has a linear x–axis showing the region to $0.5R_{\rm vir}$. The profiles are normalised such that $\rho(R_{\rm vir})/\rho_0 = 1$. The four profiles plotted are for a constant density ρ_0, an isothermal sphere ($\rho(r) \propto r^{-2}$, constant $v_{\rm c}$), and the models of NFW97 (equation 4.1) and Burkert (1995) (equation 4.2). The NFW scale radius is set at $r_{\rm s} = 0.1R_{\rm vir}$, with the Burkert core radius $r_{\rm c}$ set such that $\mathrm{d}\ln\rho/\mathrm{d}\ln r = -2$ occurs at the same place in both models; this yields $r_{\rm c} \simeq 0.066R_{\rm vir}$.

different predictions, especially when their methods are extrapolated beyond the range of the data they were originally devised to fit.

For example, in the original model of NFW97, the characteristic density is set at the redshift (z) when most of the mass that comprises the halo in the present is first contained within non-linear collapsed structures. Bullock et al. (2001b, hereafter B01) on the other hand found that they could fit the data from their simulations better if they assumed that the scale radius at fixed halo mass is independent of redshift. This resulted in significantly different evolution of the resulting structural parameters. Eke et al. (2001, hereafter ENS) confirmed the results of B01, and extended their model for use with a truncated matter power spectrum (e.g. for a warm dark matter model). The differences between the models of NFW97 and B01 are most significant at high masses, where they are most difficult to validate: the most massive objects in a simulation are also the rarest, and the combination of high resolution (so that $\rho(r)$ is accurately measured) and a large simulation volume (to provide enough objects for a statistically meaningful sample) has been very difficult to achieve.

While these models can reproduce reasonably well the measured relationship between concentration, mass and formation redshift, they do not account for the scatter in the relationships (as first discussed in Jing 2000). This has been tackled through the use of semi-analytic models, the most successful of which ascribe the scatter in concentration to variation in the halo mass accretion histories of objects of a given mass. For example, in the model of Wechsler et al. (2002, hereafter W02), the scatter in the concentration-mass relation originates in the variations of the redshift at which the mass accretion rate of the halo's main progenitor peaks. In contrast, the model of Zhao et al. (2003b, hereafter Z03) uses the time when the most massive progenitor stops undergoing rapid mass accretion to set the concentration. This was extended to higher redshifts in Zhao et al. (2003a).

It is very important to test the different predictions of models such as these *outside* the mass and redshift ranges they were originally derived to fit. This is typically around redshift $z = 0$, and at the characteristic mass scale[2] M_*. In order to extend the mass and/or redshift range of the data used to test the models, one requires either a simulation

[2]The characteristic mass M_* is defined as the mass at which the dimensionless 'peak height' $\nu \equiv \delta_c/\sigma(M) = 1$ (e.g. Zentner, 2007), where $\sigma^2(M)$ is the variance of the density field after smoothing with a spherical top hat filter enclosing an average mass M, and δ_c is the overdensity of a spherical perturbation at its collapse redshift. These are calculated using linear theory (see section 1.3) extrapolated to $z = 0$. Gao et al. (2005) use a value of $M_* = 6.15 \times 10^{12}\, h^{-1}\mathrm{M}_\odot$ for the MS, and we also used this value in section 2.4.6.

with an extremely large dynamic range, or a series of specifically designed simulations of single objects (e.g. NFW97). The disadvantage of the latter method is that it results in relatively few haloes, and there is a danger that the way they are selected for simulation could introduce subtle biases in their structural parameters. Macciò et al. (2007, hereafter M07) used a series of simulations of varying box sizes and resolution to extend their results down to much lower halo masses. However, in order to get down to masses $M \lesssim 10^{10}\,h^{-1}\mathrm{M}_{\odot}$, they had to use a very small simulation box size (side length $14.2\,h^{-1}$Mpc), which has the potential problem of bias due to such a simulation missing large-scale power.

The alternate solution is to increase the dynamic range of a simulation, essentially by putting more particles into the box. The work presented in the first part of this chapter makes use of the two large ΛCDM simulations used in Chapter 3, the *Millennium Simulation* (MS) and the smaller higher resolution simulation referred to as HR1 (see section 1.5.5 for details). The combination of large volumes with substantial numbers of particles results in minimal statistical uncertainty when characterising halo properties such as concentration, spin, formation redshift, and the degree of relaxation. Even including the HR1 simulation however, the haloes used here do not go down to masses as low as M07: to prevent biases in the structural parameters measured, the halo mass range used here is limited to 10^{12}–$10^{15}\,h^{-1}\mathrm{M}_{\odot}$.

The large number of haloes available allows deviations from the correlations of concentration and mass to be studied in detail. The analysis presented here uses only the halo population at $z = 0$; an analysis of the structural parameters of haloes in these simulations at higher redshifts was presented in Gao et al. (2008).

The second part of this chapter deals with the question of how baryons affect the density profiles of haloes. Although the MS allows us to charaterise the density profiles of purely dark-matter haloes over a wide range of mass, we expect the internal mass distribution of haloes to be transformed by the baryonic processes of galaxy formation. Just as in Chapter 3, we use a high resolution region simulated both with and without baryons to compare the effect on individual haloes' density profiles.

Although there have been attempts to measure this in the past, previous work has been hampered by incomplete physics (e.g. neglecting star formation, feedback, or radiative cooling of the gas), poor resolution, or by having too few objects. Rudd et al. (2008) found that the galaxy-formation process causes haloes to become significantly more centrally concentrated, but the effect becomes much smaller if the gas is not allowed to cool radiatively and form stars (in agreement with Lin et al. 2006). Gustafsson et al. (2006)

found that the baryons steepened the inner density profiles of their four haloes, causing them to deviate away from the NFW profile shape. The halo simulated with baryons in Romano-Díaz et al. (2008) exhibited a stronger cusp at early times, but this became smoothed out into a small core by $z = 0$. We extend studies such as these by using simulations containing a larger number of galaxy–halo systems. It is not expected that the simulations we use produce perfectly realistic galaxy systems however: we also investigate how the circular velocity profiles of the haloes compare to observed spiral galaxy rotation curves, as characterised by the *Universal Rotation Curve* of Persic et al. (1996) and Salucci et al. (2007).

The outline of this chapter is as follows. We briefly review the simulations used for investigating the dark matter halo concentrations, and detail the methods used for halo definition and selection, in section 4.2. Section 4.3 presents the results of the dark matter halo studies, including the analysis of the halo concentration parameter and its correlations with mass, spin and formation time. We also investigate the ability of different models to predict the trends and scatter in the concentration. We then move on in section 4.4 to analyse how the density profiles change due to the presence of gas and stars, and also how the corresponding circular velocity profiles compare to measured rotation curves from spiral galaxies. Section 4.5 presents my conclusions for this chapter.

4.2 Dark matter concentrations: haloes in the simulations

4.2.1 Halo identification

We use the ten billion particle *Millennium Simulation* (MS), in conjunction with the smaller, higher resolution HR1 simulation (see Springel et al. (2005b) and section 1.5.5 for full details). These both use the same ΛCDM cosmology, and allow the identification of many millions of haloes at $z = 0$. The problem of identifying and selecting dark matter structures appropriate to the physical quantities being studied is a critical stage in the analysis of a cosmological simulation. The simulation code used ran an implementation of the 'friends-of-friends' algorithm (FOF, e.g. Davis et al. 1985) on the fly, with a linking length of $b = 0.2$ in terms of the mean interparticle separation, and a minimum group size of 20 particles. Following completion of the simulation, the SUBFIND code (Springel et al., 2001a) was ran on the particle data. This breaks down each FOF group into self-bound substructures, including the main body of the halo itself (the most massive 'substructure'), and any resolved subhaloes; a FOF group will also contain additional

particles not contained within a self-bound structure. Using this additional information from SUBFIND means that we are able to immediately reject 'haloes' identified in the FOF catalogue, but which do not contain any self-bound component (typically very low-mass objects). The halo definition we use in this chapter is based on the substructure information given by SUBFIND, which is itself based on the simple particle groups returned by FOF.

The centre of each halo is defined to be at the minimum of the gravitational potential of the most-massive substructure in the corresponding FOF group. A spherical outer boundary to each halo is then defined at a radius R_Δ from the centre, using an overdensity criterion, $\rho(\leq R_\Delta) = \Delta_c \rho_{crit}$. The overdensity Δ_c is not unique, but is usually defined with the intention of selecting virialised objects. In an Einstein-de Sitter (i.e. flat, matter-dominated) universe, the spherical collapse model yields a value of $\Delta_c \approx 200$ (see section 1.3). This was the value chosen in NFW97 and it has remained in common usage. In the ΛCDM cosmology however, the overdensity of a virialised sphere is lower (Eke et al., 1996). Using the approximation of $\Delta_c \approx 178\Omega_m^{0.45}$ (Eke et al., 1998), we get $\Delta_c = 95.4$ at $z = 0$. We shall refer to the halo radii derived using this value as the virial radii (R_{vir}), but for ease of comparison with other works, the radii obtained using $\Delta_c = 200$ will also be retained (R_{200}).

We define our haloes to be the total mass within a distance of R_{vir} (or R_{200}) from the potential-minimum centre of the most-massive substructure identified by SUBFIND (itself based on the FOF groups). Note that this definition can include particles not present in either the SUBFIND substructures or the FOF groups. The mass of the haloes thus defined is given by

$$M_\Delta = \frac{4}{3}\pi \Delta_c \rho_{crit} R_\Delta^3 \tag{4.3}$$

This halo definition is equivalent to the 'SO' (Spherical Overdensity) definition used in Chapter 2.

4.2.2 Halo selection

Having defined our haloes, we must then select carefully those that are appropriate for our study. Different halo properties are subject to different numerical biases, and selection criteria appropriate for one quantity are not necessarily sufficient (or even necessary) for another. Furthermore, when a halo is out of equilibrium—for example, when it is in the process of a merger—the halo properties change rapidly, on a timescale much shorter than

the interval between simulation snapshots. The halo boundary radius and mass defined above are designed to select virialised objects, so it is inappropriate to apply them to objects undergoing a merger: in such cases, the definition of the halo itself becomes highly ambiguous. The inclusion of such objects in a halo catalogue leads to increased scatter in measured properties and biases in correlations, as we shall see.

This chapter is primarily concerned with the spherically-averaged density profiles of dark matter haloes. For these to be measured meaningfully, the halo must not be dominated by dense substructures, it must have an unambiguously defined centre, and it must be dynamically relaxed (or nearly so). These requirements are translated into three well-defined selection criteria for our final 'Relaxed' halo catalogue. Haloes excluded by these criteria comprise the 'Unrelaxed' catalogue, and the two taken together are the 'Full' halo catalogue.

The fraction of the total halo mass contained in resolved substructures with centres within $R_{\rm vir}$ (as identified by SUBFIND, and excluding the most-massive substructure), is denoted $f_{\rm sub}$. Haloes selected for the Relaxed catalogue must satisfy $f_{\rm sub} < 0.1$.

The position of the halo centre ($\boldsymbol{c}_{\rm pm}$, as defined by the potential minimum) and the centre of mass of the halo ($\boldsymbol{c}_{\rm cm}$) should be very similar. Following Crone et al. (1996) and Thomas et al. (2001), we define $S \equiv |\boldsymbol{c}_{\rm cm} - \boldsymbol{c}_{\rm pm}|/R_{\rm vir}$, and apply the constraint $S < 0.07$.

Finally, we apply a cut in the (instantaneous) virial ratio, $2T/|U|$. Here, T is the kinetic energy computed from the velocities of the halo particles in the centre-of-momentum frame, and U is the potential energy computed using the positions of all the halo particles (or by taking a random sample of 1000 particles if there are more than that number; see Chapter 2). This ratio should have a value of unity for an isolated, virialised object; to allow for minor variations, the haloes selected for the Relaxed catalogue are constrained to have $2T/|U| < 1.35$. See section 2.3.2 for a more detailed discussion of the use of the virial ratio[3].

It is important to note that $f_{\rm sub}$ and S are complementary measures, and are strongly correlated. For low-mass haloes, the amount of mass in substructures will be underestimated, as the subhaloes will not be sufficiently resolved for SUBFIND to identify them. However, the mass distribution within the halo may still be sufficiently irregular that it can be excluded through the constraint on S. Similarly, the substructures could be arranged, by chance, such that they do not shift the centre of mass significantly away from

[3]The 'virial ratio' used here is defined following N07, and is slightly different to that used in section 4.4 and Chapters 2 and 3, $|2T/U + 1|$.

the gravitational centre; however, $f_{\rm sub}$ could still identify the halo as unrelaxed. Furthermore, the virial ratio means the selection criteria make use of the kinematic information of the particle velocities, allowing the removal of unrelaxed objects that happen to satisfy the other two criteria.

N07 performed a thorough study of the dependence of these selection criteria on the number of particles in the haloes. The strong dependence of $f_{\rm sub}$ on resolution has already been noted; the virial ratio was also found to become increasingly unreliable for haloes with $N_{\rm p} \lesssim 1000$. We defer assigning a formal lower limit on the number of particles, pending an examination of the density profiles themselves. In terms of the relative importance of the three selection criteria already described, it is the limit on S that removes the most haloes. A significant number are also rejected by the $f_{\rm sub}$ criterion, and the virial ratio limit only rejects a few additional haloes. Figure 4.2 shows the relationships between these different criteria and their effect on the halo population.

4.2.3 Density profiles and NFW fits

Each halo is divided into 32 radial bins, spaced logarithmically between $\log r_0/R_{\rm vir} = -2.5$ and the virial radius. The mass density is measured in each bin, yielding the spherically averaged mass profile $\rho(r_i)$. In N07, an NFW profile ($\rho_{\rm NFW}(r)$, see equation 4.1) was fitted to each halo, by varying the two free parameters ($\delta_{\rm c}$ and $r_{\rm s}$) in order to minimise the rms deviation between the measured profile and the NFW function:

$$\sigma^2_{\rm fit} = \frac{1}{N_{\rm bins} - 1} \sum_{i=1}^{N_{\rm bins}} \left[\log \rho(r_i) - \log \rho_{\rm NFW}(r_i|\delta_{\rm c}, r_{\rm s})\right]^2 , \tag{4.4}$$

where r_i is the radial distance to the outer edge of bin i from the halo centre. This definition of $\sigma_{\rm fit}$ assigns equal weight to each bin. An alternative would be to use Poisson weighting in each bin (see equation 4.14); this was tested, and the results were not found to differ significantly.

For NFW profile fitting, the radial range used for the fit is of critical importance. Most haloes of different masses are resolved to different degrees within a single simulation; since we only use two simulations, we have to be particularly careful. N07 performed extensive testing of the biases introduced in the resulting halo structural parameters when fitting over different radial ranges, in particular in the mass range that is common to both simulations. The eventual method chosen was a uniform radial range in terms of $R_{\rm vir}$, ensuring that haloes of different masses are treated equally. It was found that the minimum radius of the fit had to be $r_{\rm min} \geq 0.05$ to prevent introducing bias in the

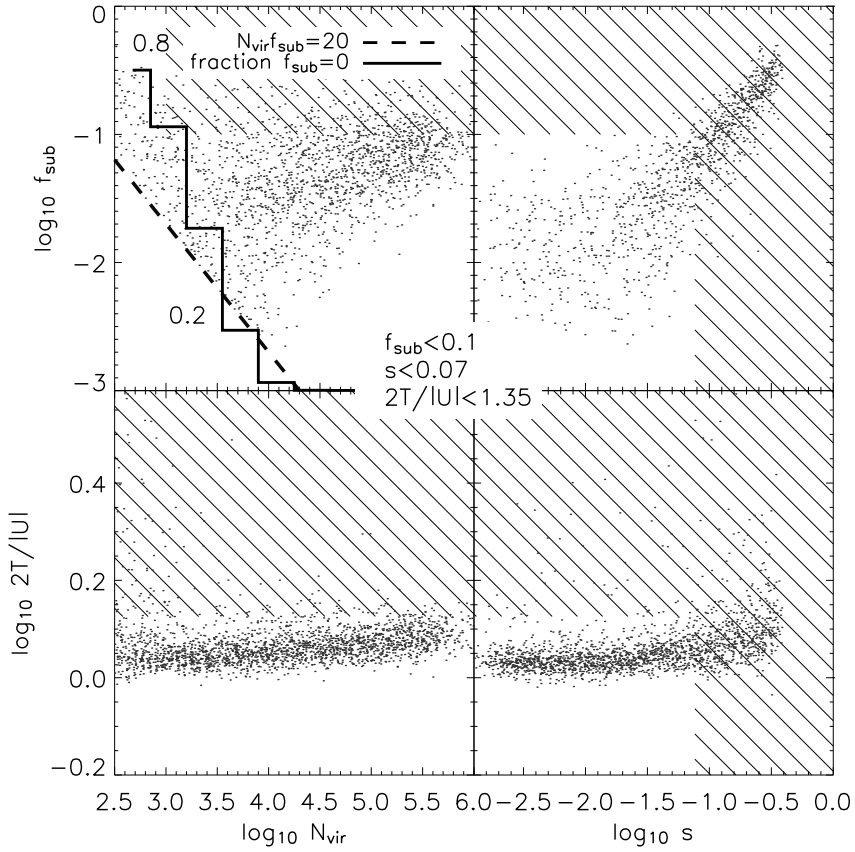

Figure 4.2: The criteria used to define the Relaxed halo sample (see section 4.2.2): the fraction of mass in resolved substructures $f_{\rm sub}$, the virial ratio $2T/|U|$, the centre-shift S, and the number of particles within the virial radius $N_{\rm vir}$ (called $N_{\rm p}$ in the text). The shaded regions indicate areas where haloes are rejected from the Relaxed catalogue. The dots represent a uniform sample of haloes from the MS with $N_{\rm p} > 300$. In the top-left panel, the dashed line shows the detection limit of SUBFIND (20 particles), with the solid histogram showing the fraction of haloes in each mass bin with no resolved substructures (i.e. $f_{\rm sub} = 0$). *This figure has been reproduced from N07.*

correlation between halo concentration ($c_{200} = R_{200}/r_{\rm s}$) and mass. However, a value of $r_{\rm min} = 0.05$ also minimised the scatter in the concentration-mass relationship, so this was the value chosen.

These tests were performed with haloes containing at least 1000 particles. Using this particle-number limit did not introduce significant biases into the correlation of the concentration parameter with halo mass. However, it was found that the quality of the fits, as measured by $\sigma_{\rm fit}$, was significantly poorer for haloes realised with fewer than 10 000 particles. Therefore, this conservative limit was adopted as a minimum number of particles for haloes used as the analysis. This yields a final mass range for the haloes used here of 10^{12}–$10^{15}\,h^{-1}{\rm M}_{\odot}$.

4.3 Dark matter concentrations: results and discussion

4.3.1 Concentration and halo mass

N07 performed a thorough analysis of the relationship between the concentration parameter and halo mass, which we shall summarise in this section.

The relationship between concentration and mass, for both the Relaxed and Full halo catalogues, is shown in figure 4.3. The median $c(M)$ trend is well-defined, but weak. It is well-fitted by a power law, as shown in the figure. The results also agree very well with those of M07, who use a mass range of 2×10^9–$2 \times 10^{13}\,h^{-1}{\rm M}_{\odot}$. The differences are likely to be due to their use of the mean rather than the median, and the differences in selection criteria between M07 and N07. However, the similarity between the two results implies that the median halo concentration is well-described by a single power law over approximately 6 decades in halo mass.

The results are also in reasonably good agreement with the predictions of NFW97 and ENS, although they both underestimate the concentration at lower masses. At higher masses, there is a hint of the median concentration converging to a single value. As a consequence, the NFW97 model performs slightly better than the ENS or B01 models, since constant concentration at high masses is implicitly built in to the NFW97 model. Both the ENS or B01 models predict a strong drop in concentration at high masses (Z03 have already noticed this behaviour, and cautioned against the B01 model at high masses).

M07 claimed that the B01 model fits their data better than the ENS model at low masses. However, the difference only becomes noticeable at masses below $\sim 10^{10}\,h^{-1}{\rm M}_{\odot}$. This mass corresponds to just 700 particles in the highest resolution (smallest volume)

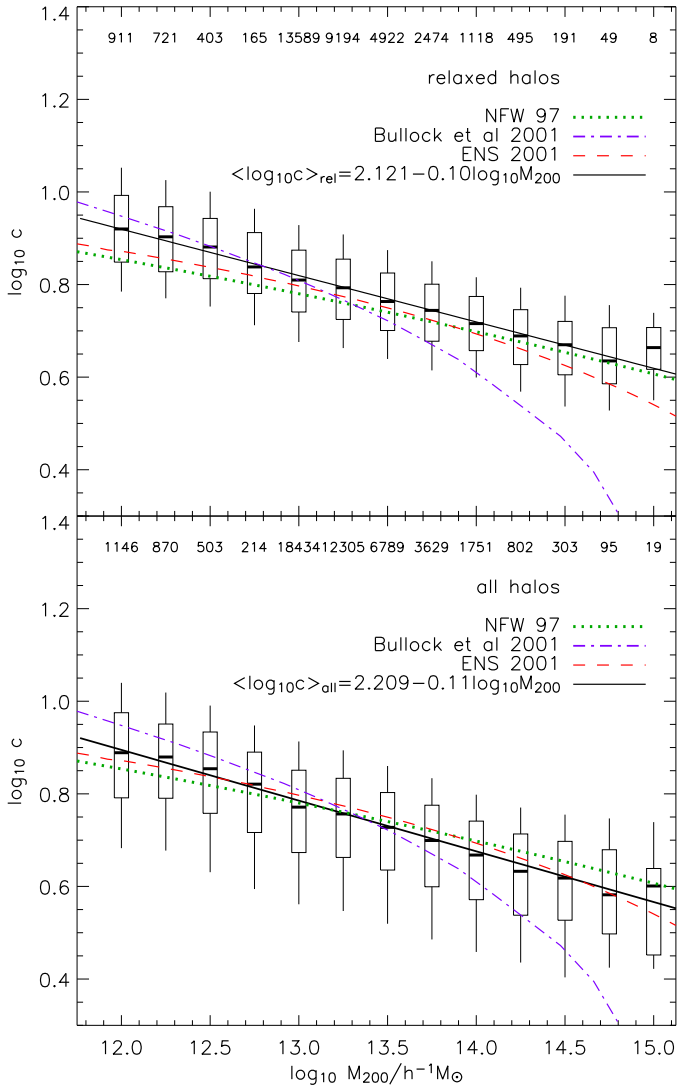

Figure 4.3: Mass-concentration relation for haloes from the Relaxed catalogue (top panel), and for all haloes (bottom panel). The outer bars and boxes show percentiles of the distribution: the inner boxes mark 25 and 75 percent of the data, while the outer bars show the 5 and 95 percent tails. The points in the centres of the boxes are the medians. The numbers along the top of each panel indicate the number of haloes in each mass bin. The best fitting power law relation to the median concentrations is given by the solid line, with the parameters shown in the legend of each panel. The dot-dashed line shows the prediction of the B01 model; the dashed and dotted lines corresponds to the ENS and NFW97 models, respectively, with $\Gamma = 0.15$, as this approximates best the input power spectrum of the MS. See text for further details. *This figure has been reproduced from N07.*

simulation in their suite. We have discussed above the concerns related to the small box size in the highest resolution simulations of M07, and N07 showed that at least ~ 1000 particles are required to produce unbiased concentrations (and 10 000 particles to produce fits that do not depend on particle number); since the correlation also has a large scatter, it was concluded that it is premature to judge conclusively the relative accuracy of the ENS and B01 models at low mass. Further tests are required using higher resolution simulations in larger volumes; or alternatively at higher redshift, where there is a greater difference between the two models (see Gao et al., 2008).

Since the trend with mass is weak, and has a large scatter, the distribution of the halo concentration parameter at fixed mass is also of interest. N07 found that only the haloes in the Relaxed catalogue have concentrations that follow a lognormal distribution at fixed mass. The Full halo catalogue has a tail at low-c that skews the distribution away from a lognormal. In fact, the concentrations from the population of Unrelaxed haloes alone *do* follow a lognormal, and the sum of the two best-fit lognormal distributions (Relaxed and Unrelaxed haloes) describes the concentrations of the Full halo population at fixed mass very well (see N07).

When examining the resulting lognormal distributions as a function of halo mass, the dispersion in c_{200} was found to decrease monotonically with mass. This suggests that the high-mass haloes are a more homogeneous population than the low-mass haloes. The high-mass objects are rare and have collapsed recently; the low-mass haloes will have a much wider distribution of formation times (we shall return to this point later in detail).

4.3.2 Concentration versus spin

The question of the origin of the large scatter in the distribution of concentrations as a function of mass is not addressed in the models of NFW97, B01 or ENS. One possibility is that the variation in concentration in fixed mass may be related to the distribution of halo angular momentum: the spin parameter λ also has a large amount of scatter at fixed mass (see Chapter 2). Both NFW97 and B01 investigated this possibility and did not find a significant correlation between spin and concentration. However, Bailin et al. (2005b) did find a correlation, which they claim might explain why low surface-brightness galaxies appear to inhabit low-density haloes. Using the statistical power of the MS, extended to lower masses using HR1, we can revisit this question.

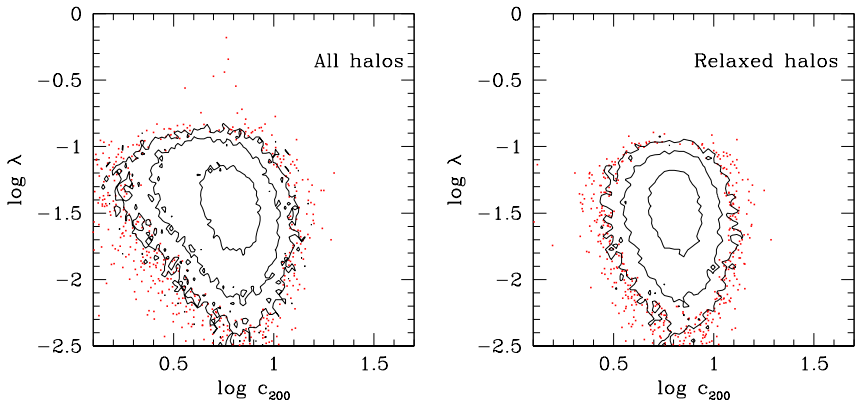

Figure 4.4: The distribution of concentration and spin parameters for the two halo samples. The contours enclose 65, 95 and 99 percent of the data, with individual points plotted for the remaining one per cent of the haloes.

The spin parameter is defined in the same way as in Chapter 2, as

$$\lambda \equiv \frac{J|E|^{1/2}}{GM^{5/2}}, \tag{4.5}$$

where the quantities are described in section 2.2. The data used here are the same as for the 'SO' haloes in Chapter 2. We added to that data the results for λ for haloes from the HR1 simulation, computed in the same way. We show the joint distribution of concentration and spin parameters in figure 4.4.

Although the correlation seen by Bailin et al. (2005b) is clearly visible in the distribution from the Full halo catalogue, for the Relaxed haloes the trend disappears. The low concentrations seen in unrelaxed haloes is a transient feature of the rapid evolution of the mass distribution that occurs during an accretion event: they are a consequence of the ambiguity of the halo definition in such situations, and the profile-fitting procedure, rather than being genuinely indicative of a low-density halo.

The question of why the low-concentration (i.e. unrelaxed) haloes tend to have high spin also needs to be addressed. D'Onghia and Navarro (2007) showed that the halo spin parameter of the mass within their 'virial' boundaries during mergers tends to increase, but that it then decreases during the subsequent process of virialisation. Therefore, haloes from the Relaxed sample here should have lower values of λ, whereas the unrelaxed haloes will have higher spin (albeit temporarily). This change in the angular momentum distribution is partially due to the arbitrariness of the outer boundary of the halo: a large accretion event such as a merger brings in mass and angular momentum, but redistributes

it such that the high-spin material ends up preferentially on weakly-bound orbits. As the halo virialises, the high-spin material can end up lying outside the virial radius, reducing λ for virialised objects (see also Vitvitska et al., 2002).

In conclusion, we found that since there is no significant correlation between λ and c for Relaxed haloes, the distribution of the spin parameter cannot directly be the source of the variation in concentration parameter at fixed mass. This is in agreement with M07. Most of the effect seen in Bailin et al. (2005b) was due to the inclusion of haloes that were not in equilibrium. There is a hint of a very weak correlation remaining, visible in the slant of the contours in the bottom panel of figure 4.4, but this is too small to have observable consequences.

4.3.3 Concentration versus formation time

NFW97 claimed that the halo mass-concentration relationship is a consequence of the relationship between formation time and halo mass. They also showed that most of the scatter in the $c(M)$ relationship is due to the variation of formations times for haloes of fixed mass. We revisit their analysis in this section. To get information about the histories of the haloes identified at $z = 0$, we use the merger trees described in Harker et al. (2006) and Bower et al. (2006). The merger trees identify progenitors of a given halo in preceding snapshots of the simulation. This enables single objects to be tracked over the course of the simulation, for example by tracking the mass accretion history (MAH) of the most-massive progenitor (MMP) of a given halo identified in the present. We shall denote this by $M_{\rm P}(z)$. Alternatively, one can analyse the spectrum of masses from all the progenitors of a halo as a function of redshift.

The details of the algorithm used to identify the merger trees differs slightly from that in Springel et al. (2005b), which was also used for analysis of the MS. However, this difference is in most cases only significant for haloes undergoing major mergers, which are excluded from the Relaxed halo catalogue here. There is an added complication that the merger trees use the 'TREE' halo definition described in Chapter 2, rather than the 'SO' haloes used here (see section 2.3.2). In practice, calculations involving the MAH of haloes (i.e. $M_{\rm P}(z)$) are performed using the masses of the TREE haloes, which are then identified with their counterpart SO haloes at $z = 0$ (where the TREE halo's $M_{\rm P}(0)$ will be similar to the SO halo's $M_{\rm vir}$).

The concept of a 'formation' time (in practice, a redshift $z_{\rm f}$) of a dark matter halo does not have a unique definition. Various definitions have been used in the past (e.g.

Lacey and Cole, 1993; Navarro et al., 1997; Wechsler et al., 2002; Zhao et al., 2003b), but if it is to have important consequences for the halo structural parameters, it is important to test the impact of these definitions. Any method will be somewhat arbitrary however[4].

One of the simplest and most widely used definitions is the redshift at which a halo's most-massive progenitor first exceeds half the halo's final mass: $M_{\rm P}(z_{\rm f}) = \frac{1}{2}M_{\rm P}(0)$. Using this, we show in figure 4.5 the relationship between formation redshift and final halo mass. Each point is colour-coded by concentration: the colour-gradient visible in the plot suggests a strong link between concentration and formation time.

In figure 4.6, we show (for two mass bins) the deviations of haloes away from the median relations of concentration and formation time with mass (as seen in figures 4.3 and 4.5 respectively). This shows that the residuals of the two relations are strongly correlated, and therefore that a significant amount of the scatter in concentration at fixed mass is due to variations in formation redshift at that mass.

We wish to quantify how significant a contribution this is. N07 compared the rms scatter in the (logarithmic) concentration distribution, σ_c, to the rms scatter about the $1:1$ line in figure 4.6, σ_z (for the two mass bins shown in that figure). The fractional reduction in the variance, $|\sigma_c^2 - \sigma_z^2|/\sigma_c^2$, is an estimate of how much of σ_c is due to the variation in $z_{\rm f}$. They found a reduction of 35% for the lowest mass bin, and just 12% for the highest mass bin. This means that the formation time can only account for a small fraction of the variance in c, so there must be other effects at work. Wechsler et al. (2006) suggested that the excess scatter could be due to the effect of the halo environment. However, the effect that they found was limited to the low-mass haloes, and we see additional scatter at high masses too.

An alternative explanation is that the simple definition of formation time used above is not adequate to capture all the relevant information influencing halo structure. After all, the mass within the NFW scale radius $r_{\rm s}$ is much less than the $\frac{1}{2}M_{\rm P}(0)$ used in the definition of $z_{\rm f}$ above. The scatter could come from aspects of the merger tree as a whole, which are neglected when considering the MAH of the most-massive progenitor only. N07 tested four different definitions of $z_{\rm f}$, by comparing them to the characteristic density $\delta_{\rm c}$. This has an expected 'natural' scaling of $\delta_{\rm c} \propto (1+z_{\rm f})^3$. Three of these

[4]It is also important to note that although we will be referring to this characteristic time as a 'formation' redshift, for most definitions one can continue to track the life of the halo's MMP back to earlier times. The fact that the halo exists before it has formed reflects a failing of English rather than the physical definition itself.

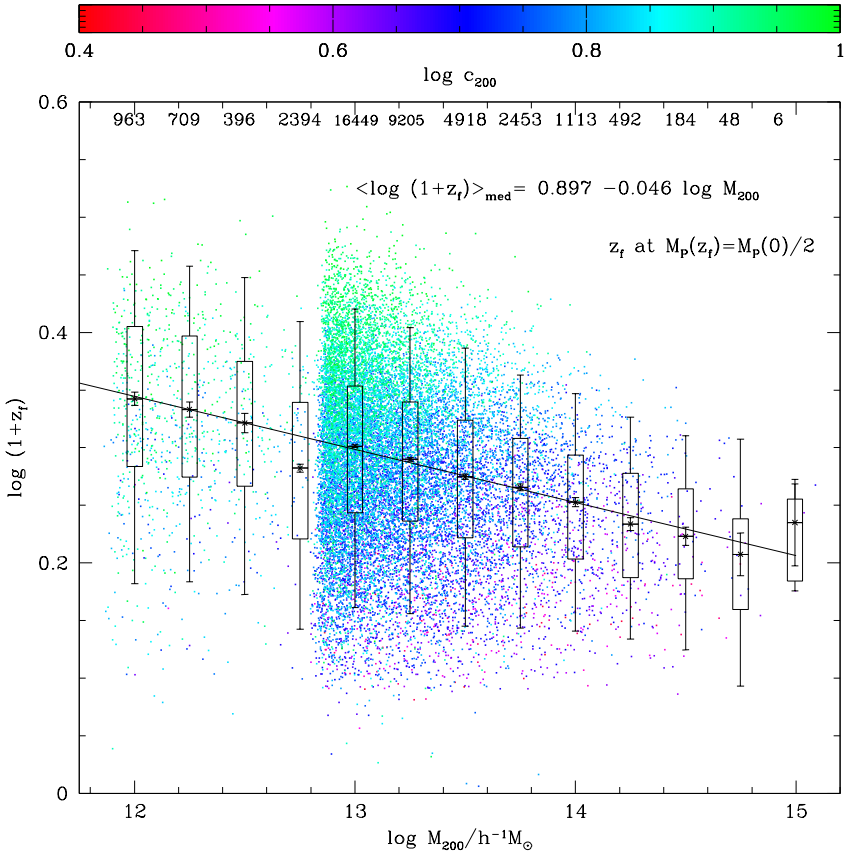

Figure 4.5: Halo formation redshift as a function of final mass for haloes from the Relaxed catalogue. The formation redshift is given by the redshift at which the halo's most-massive progenitor first reaches half the final halo mass. The crosses show the median in the different mass bins, with the error bars on the crosses giving the uncertainty in the median (see equations 2.13 & 3.9). The percentiles of the distribution at that mass are given by the boxes (75 and 25 percent) and the outer bars (5 and 95 percent). The numbers along the top of the main panel indicate the number of haloes in each bin. The straight line is a least square fit to the median z_f. A random sample of half the haloes are plotted as points, colour-coded according to their concentration parameter. A gradient in colour is visible, with bluer points nearer the top and redder points nearer the bottom: this shows qualitatively a correlation between concentration and formation time.

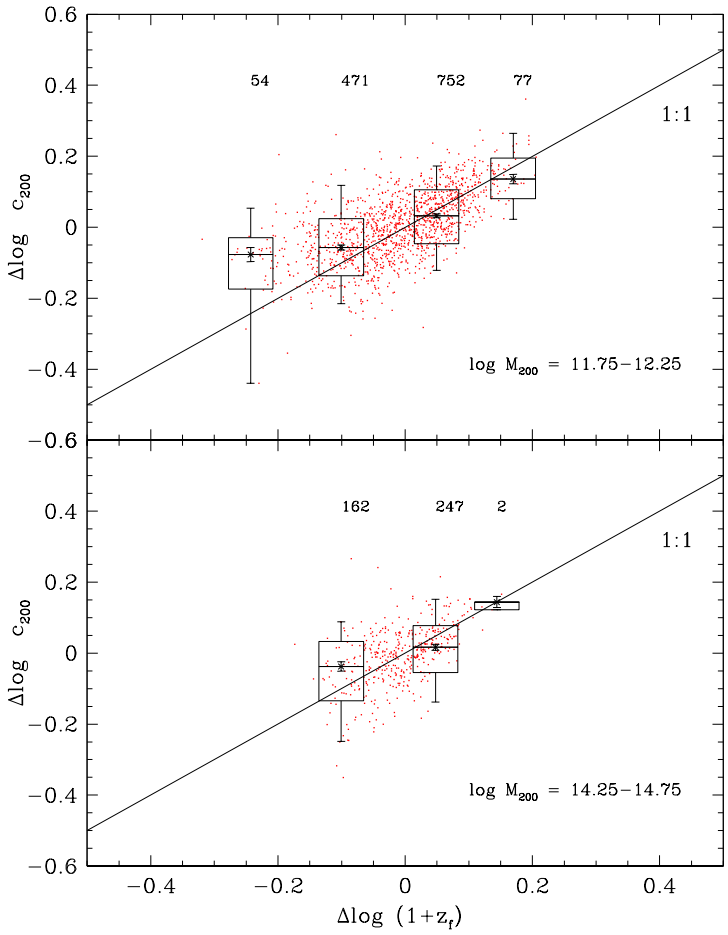

Figure 4.6: Deviations in c_{200} from the median mass-concentration relation (figure 4.3) plotted against deviations in $z_{\rm f}$ from the median mass-formation time relation (figure 4.5), for two mass bins, as labelled in each panel. The residuals are strongly correlated. This suggests that that much of the scatter in the $c(M)$ relation is due to variations in the formation time of haloes of given mass. As before, the points indicate the medians, and percentiles of the distribution are indicated with the outer bars (5th and 95th percentiles) and boxes (25th and 75th percentiles). The number of haloes in each $\Delta \log(1 + z_{\rm f})$ bin is given above each bin. The solid lines show the $1 : 1$ relation.

definitions simply changed the fraction of the final halo mass that the MMP must reach for the halo to be deemed to have 'formed' (1/10 and 1/4 were tested, in addition to the value of 1/2 already investigated). The fourth definition is that described in NFW97: the halo has 'formed' when the combined mass of all progenitors of mass $> fM_{\rm P}(0)$ first exceeds $\frac{1}{2}M_{\rm P}(0)$. NFW97 used $f = 0.01$, to match their results from the Extended Press–Schechter (EPS) formalism (Press and Schechter, 1974; Bond et al., 1991; Lacey and Cole, 1993; Zentner, 2007). This uses just the present-day halo mass to derive the merger history. However, we found that we must use a higher value of $f = 0.1$ when using the actual merger history measured from the N-body simulations. It was found that the NFW97 prescription for $z_{\rm f}$ fitted the 'natural scaling' of $\delta_{\rm c}$ better than the other definitions, implying that the full mass-spectrum of a halo's progenitors is important in determining its structural parameters.

4.3.4 Predictions of the concentration

The results of the previous section show that one must take into account some information about a halo's mass accretion history in order to predict its concentration accurately. Common practice with current semi-analytic models is to take the median $c(M)$ relation, and either ignore the scatter completely or just produce it statistically (Cole et al., 2000). However, since the halo formation time can impact on the clustering of haloes (Gao et al., 2005), making use of the MAH of a halo when computing its structural parameters could significantly affect the semi-analytic predictions of the size and internal structure of a galaxy.

In this section we investigate the accuracy of three models that use different aspects of the MAH to predict a scattered distribution of concentrations.

Wechsler et al. (2002)

In the model described in W02, the MAH of a halo's most-massive progenitor is fitted to a power-law,

$$\log M_{\rm P}(z) = \log M_{\rm P}(0) - \alpha z, \tag{4.6}$$

where the free parameter is related to the formation redshift (and scale factor) through

$$\frac{\alpha}{2\ln 10} = \frac{1}{1+z_{\rm f}} = a_{\rm f}. \tag{4.7}$$

The concentration parameter of the halo is then given by $c_{\rm W} = c_0/a_{\rm f}$. W02 found that $z_{\rm f}$ defined in this way correlated well with the concentration parameters measured by B01.

In the original paper, W02 used a value of $c_0 = 4.1$, as this was the typical concentration of haloes that are forming now ($a_\mathrm{f} = a_0 \equiv 1$). However, due to our different halo definition and virial radius, we take a value of $c_0 = 2.26$ to produce a good match to our measured concentrations. Although this model is very simple to implement, we found that equation 4.6 is a poor approximation to the actual MAH in a significant number of systems.

Zhao et al. (2003)

In Z03, the MAH of the most-massive progenitor is modelled as having two phases. The halo begins life in a period of fast accretion and mergers, before reaching a slower accretion phase at late times. The model works by assuming that the inner properties of the halo (e.g. r_s) are fixed during the early fast accretion phase, and only weakly change thereafter. After identifying the redshift of the turning point in the MAH, z_tp, it is then used to estimate the concentration at $z = 0$.

Z03 found that a good approximation to z_tp is given when the following function reaches its maximum:

$$\mathcal{Z}(z) = \log v(z) - \gamma \log H(z) \tag{4.8}$$

where the constant $\gamma = -1/4$. Using the expressions for circular velocity ($v = \sqrt{GM/R}$) and halo mass[5] ($M = \frac{4}{3}\pi\Delta_\mathrm{h}\bar{\rho}R^3$), and the scaling relations for the mean density of the Universe $\bar{\rho} \propto (1+z)^3$ and the Hubble parameter $H^2(z) \propto \left(\Omega_{\mathrm{m},0}(1+z)^3 + \Omega_\Lambda\right)$, it can be shown that

$$\mathcal{Z}(z) \propto \frac{1}{3}\log M_\mathrm{P}(z) + \frac{1}{2}\log(1+z) + \frac{1}{8}\log\left(\Omega_{\mathrm{m},0}(1+z)^3 + \Omega_\Lambda\right) \tag{4.9}$$

The maximum of this expression can be found (this involves interpolating the MAH between the simulation snapshots), yielding z_tp, and $M_\mathrm{tp} \equiv M_\mathrm{P}(z_\mathrm{tp})$.

The concentration parameter at $z = 0$ is then found by making use of the power-law relationships found in Z03:

$$\frac{M(< r_\mathrm{s}(z))}{M(< r_\mathrm{s}(z_0))} = \left(\frac{r_\mathrm{s}(z)}{r_\mathrm{s}(z_0)}\right)^{3\alpha} \tag{4.10}$$

where z is the redshift we are interested in, z_0 is some fiducial redshift (which we will take to be z_tp) and $M(< r)$ refers to the mass within the radius r of the MMP at the specified redshift. The constant α is found to be 0.48 during the slow (recent) accretion phase, and

[5]The halo identification at $z > 0$ is based on FOF with $b = 0.2$, i.e. using a constant comoving mean interparticle separation. This means we can use the same overdensity value value Δ_h at all redshifts.

0.64 in the fast (older) accretion phase. Using this in conjunction with standard relations for NFW haloes, Z03 derived the following equation:

$$\frac{\left(\ln(1+c(z)) - \frac{c(z)}{1+c(z)}\right) c(z)^{-3\alpha}}{\left(\ln(1+c_{\rm tp}) - \frac{c_{\rm tp}}{1+c_{\rm tp}}\right) c_{\rm tp}^{-3\alpha}} - \left(\frac{M_{\rm P}(z)}{M_{\rm tp}}\right)^{1-\alpha} \left(\frac{1+z}{1+z_{\rm tp}}\right)^{3\alpha} = 0 \tag{4.11}$$

This is solved at $z = 0$, with $\alpha = 0.48$ (since $z < z_{\rm tp}$) and $c_{\rm tp} = 4.0$ (which Z03 found to be the typical value at $z_{\rm tp}$), yielding a prediction for $c(0) =: c_{\rm Z}$.

As with the W02 model, differences in halo definition meant we had to scale the predicted concentrations to match the values that we measure from the MS, multiplying $c_{\rm Z}$ by 0.55. Furthermore, like W02, this method is prone to failing due to the requirement of a specific form for $M_{\rm P}(z)$. A significant fraction of haloes do not have a two-phase MAH, instead having just a single slow phase, or multiple fast phases.

Navarro, Frenk, and White (1997)

As already discussed, the NFW97 model defines the formation time at the redshift when half the mass of the final halo is contained within progenitors more massive than $f M_{\rm P}(0)$. We take a value of $f = 0.1$ here. Having found the formation redshift, this is then related to the predicted characteristic density through

$$\delta_{\rm c} = C\Omega_{\rm m,0}(1+z_{\rm f})^3, \tag{4.12}$$

where the constant C has the value 3×10^3. The predicted concentration $c_{\rm N}$ is then found from the characteristic density by solving the following:

$$\delta_{\rm c} = \frac{\Delta}{3}\left(\frac{c_{\rm N}^3}{\ln(1+c_{\rm N}) - \frac{c_{\rm N}}{1+c_{\rm N}}}\right). \tag{4.13}$$

Comparison of predictions

Figure 4.7 shows the distributions of concentrations predicted by the three models described here against the distribution of measured concentrations. The models use different features of the merger trees to get characteristic redshifts, with different procedures following that to generate a predicted concentration. W02 approximates the MAH of the most-massive progenitor to a power-law. Z03 finds a redshift at which the (same) MAH transitions from an early fast phase to a slower phase at late times. The NFW97 model uses the redshift at which the entire mass spectrum of resolved progenitors has grown above some threshold mass. Despite these differences in method however, the figure

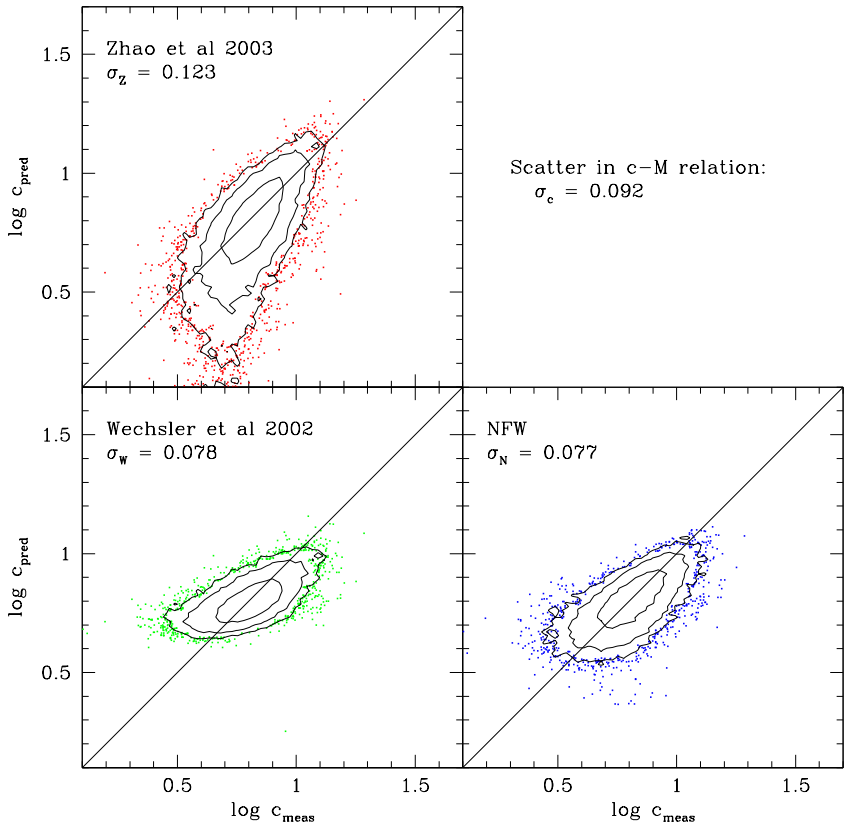

Figure 4.7: Comparisons of the concentrations predicted by the Z03 (top), W02 (bottom left) and NFW97 (bottom right) models with those measured from the simulations. The contours enclose 65%, 95% and 99% of the haloes (from the Relaxed catalogue), with the remaining 1% plotted as points. The σ-values indicated in each panel give the rms scatter in the prediction $\langle \log^2(c_{\rm meas}/c_{\rm pred})\rangle^{1/2}$. Also marked is σ_c, the corresponding rms scatter about the mass-concentration relation for the same set of haloes.

shows that the predicted concentrations all correlate reasonably well with the measurements from the haloes themselves. The contours for the W02 and Z03 models show significant deviations from symmetry about the 1 : 1 line, due to biases in the predicted concentrations. This is due to haloes whose MAHs are poorly described by the prescriptions in those models.

We have measured the rms scatter between the predicted and measured concentrations (marked on each panel). The best (marginally) is the NFW97 model, with $\sigma_{\rm N} = 0.077$. However, this is only slightly less than the measured dispersion in the measured concen-

trations themselves ($\sigma_c = 0.092$). Looking at the fractional change in variance (cf. section 4.3.3), $|\sigma_c^2 - \sigma_{\rm N}^2|/\sigma_c^2$, we find that despite the good correlation between the predicted and measured concentrations, the NFW97 model still only accounts for about 30 percent of the variance in the concentration-mass relationship.

By this measure, the W02 model does similarly well, although the correlation with the measured results has a slope that is slightly too shallow. The Z03 model has more scatter, but this is entirely due to the low-$c_{\rm Z}$ tail, which originates in haloes that do not adequately satisfy its two-phase model of the MAH.

Therefore, although all three models produce predictions that agree well with the measured concentrations, *none* can account for even half of the scatter in the concentration-mass relationship.

4.4 Haloes with baryons

The preceding sections in this chapter used very large simulations to characterise precisely the distribution of the concentration parameters of dark matter haloes, and investigated the source of its variation and the accuracy of models that attempt to predict it. We now proceed to calculate the density profiles of galaxy-scale haloes, simulated with baryonic physics including star formation and feedback. In addition to comparing the density profiles to those from dark matter-only haloes, we use the related circular velocity profiles to assess the realism of the simulated galaxy systems.

4.4.1 The simulations

To analyse the impact of baryons on density profiles in haloes, we used the DMG simulation described in section 1.5.5, and used extensively in Chapter 3. We refer the reader to those sections and Okamoto et al. (2005) for a full description. Very briefly, the simulation consists of a high resolution region of dark matter, gas and star particles, surrounded by a series of lower-resolution (higher mass) boundary particles. The stars can form from the gas either by exceeding a density threshold (the quiescent mode, resulting in a Salpeter (1955) IMF), or due to the presence of shocks from galaxy mergers (the burst mode, resulting in a top-heavy IMF). The IMF from the burst mode results in more supernovae per unit mass of stars formed, which heat the surrounding gas (feeding energy back into it), and which can eject it out of the galaxy. As in Chapter 3, the DMG simulation is used in conjunction with a dark matter-only simulation of the same region ('DMO'), to allow

a direct comparison between haloes. In addition to DMG and DMO, for the purposes of this section we also use the single-halo simulations GDMG and GDMO, also described in section 1.5.5. These use the same physical models as the DMG and DMO simulations, and provide a single additional well-resolved object to study. Since GDMG and GDMO use the same cosmology, physics, and have very similar resolution as the DMG and DMO simulations respectively, most references to either larger simulation should be read as also including the object from the smaller simulation.

Haloes are identified using the same 'spherical overdensity' algorithm as before: a halo centre is identified as the potential minimum of the most massive self-bound substructure found by SUBFIND from the FOF dark-matter particle groups. The halo boundary radius is defined such that it encloses an overdensity calculated using equation 3.1; $\Delta_c = 101.1$ for the cosmology used in these simulations (see table 1.3).

Following the work by N07 on halo selection for studying density profiles, and my previous work using these simulations (Chapter 3), we chose the following criteria to select haloes for analysis:

- The number of dark matter particles: $N_{p,DM} \geq 4000$
- The centre-shift parameter $S \leq 0.07$
- The virial ratio $|2T/U + 1| \leq 0.5$

The particle number-limit of 4000 was chosen to balance the constraints of resolution and halo numbers: requiring very well-resolved haloes reduces the number available for analysis. The value we chose is below the (conservative) minimum of 10 000 particles chosen by N07, which they note was chosen to maximise the quality of their NFW fits. My value will produce slightly poorer fits, but it is well above the minimum for producing unbiased values of the concentration parameter (1000 particles). The virialisation criteria is also slightly different to that used for the MS analysis in this chapter (but the same as that used for the MS in Chapters 2 and 3): The previous criteria ($2T/U + 1 \geq 0.35$, see section 4.2.2) is slightly tighter than the value used here; however, here the criterion applies to both sides of the distribution of virial ratios.

For the DMG simulations, we make use of the central galaxies of each halo, using the definition from Chapter 3 (i.e. running FOF on the star and gas particles within R_{vir}, with a linking length of $b = 0.02$). We have computed for the galaxies' disc-to-total ratios in terms of both mass, $(D/T)_m$, and B-band luminosity, $(D/T)_B$ (see section 3.3.3 for further details).

Applying these selection criteria to the DMO and DMG halo populations yields a catalogue of 20 haloes. Some properties of the four most massive (and best resolved) objects are shown in table 4.1, with a visual comparison in an Appendix (section A.2).

4.4.2 Computing the density profiles

To compute the density profiles of haloes in the DMO and DMG simulations, we use a scheme based on that of N07 (described in section 4.2.3). This means initially setting up 32 radial bins between $R_{\rm vir}$ and $10^{-2.5}R_{\rm vir}$, spaced logarithmically. However, whereas N07 chose to use a uniform radial range over all haloes, here we use an adaptive scheme, and extend the radial binning down towards the halo centres, until there is a core of 50 particles remaining (haloes with fewer than 50 particles are not considered). This means that although the bins are the same width (in terms of $R_{\rm vir}$) for all haloes, the number of bins varies. We do this so that we can make the most out of the relatively few haloes we have available: we want to avoid rejecting any unnecessarily from resolution constraints (there are so many haloes in the MS that this is not a problem, allowing the cleaner choice of the uniform binning scheme). Note that, in practice, the particle-number limit described earlier ($N_{\rm p} \geq 4000$), and the inner radius we describe below, ensure the reliability of the density profiles we analyse, regardless of the choice of binning scheme.

For the DMG haloes, we compute two density profiles: one of the dark matter alone, and one of the total mass including the baryons. As in the preceding sections, we fit an NFW function (equation 4.1) to the density profiles, by varying $\delta_{\rm c}$ and $r_{\rm s}$ such that they minimise the rms deviation ($\sigma_{\rm fit}$) between the measured discrete density profile and the NFW function:

$$\sigma^2_{\rm fit} = \sum_{i=1}^{N_{\rm bins}} N_{\rm p}(r_i) \left[\log \rho(r_i) - \log \rho_{\rm NFW}(r_i|\delta_{\rm c}, r_{\rm s}) \right]^2 \tag{4.14}$$

This implementation assigns Poisson-error weights to each bin through $N_{\rm p}(r_i)$, the number of particles in bin i, whereas N07 assigned equal weights (cf. equation 4.4). In agreement with N07, we also found that this choice did not significantly affect the results. We use the convergence criterion given in Power et al. (2003) to determine the innermost radius for the NFW fit, rather than the empirically-determined uniform range used in N07. The NFW function is fitted to the data over a radial range $r_{\rm conv} < r \leq R_{\rm vir}$, where the convergence radius $r_{\rm conv}$ is the radius that satisfies

$$\frac{\sqrt{200}}{8} \frac{N_{\rm p}(\leq r)}{\ln N_{\rm p}(\leq r)} \left(\frac{\rho(\leq r)}{\rho_{\rm crit}} \right)^{-1/2} \geq 0.6, \tag{4.15}$$

Halo	Sim.	DM Particles	Mass of component $/10^{11}\,h^{-1}\mathrm{M}_\odot$				Halo shape	Galaxy disc/total	
		N_p	Halo Total	Halo DM	Gal. Gas	Gal. Stars	$s = c/a$	Mass	B-band
G	DMO	62 681	12.3	12.3	—	—	0.87	—	—
	DMG	63 589	12.0	10.7	0.15	0.39	0.81	0.49	0.82
A	DMO	66 769	12.9	12.9	—	—	0.86	—	—
	DMG	67 390	12.5	11.1	0.16	0.62	0.83	0.67	0.88
B	DMO	46 418	8.97	8.97	—	—	0.86	—	—
	DMG	46 443	8.45	7.66	0.16	0.35	0.87	0.46	0.71
C	DMO	42 246	8.17	8.17	—	—	0.81	—	—
	DMG	41 944	7.64	6.92	0.03	0.29	0.87	0.46	0.62

Table 4.1: Properties of the four most massive haloes from the selection described in section 4.4.1. Haloes A, B and C are from the DMO and DMG simulations, and halo G is from the GDMO/GDMG simulations. These haloes are marked in figures 4.8 and 4.9. A visual comparison of these haloes and their galaxies is provided in section A.2.

where $\rho(\leq r)$ is the mean density *within* the radius r. Strictly, this limit is only applicable for haloes in the DMO simulation, as the convergence tests of Power et al. (2003) did not use simulations containing gas or stars. Since the baryonic particles will be concentrated in the centres of the haloes, including their number in the calculation of $r_{\rm conv}$ pulls the limit strongly inwards, implying that a much larger radial range can be fitted reliably. However, without thorough convergence tests (beyond the scope of this thesis), it is impossible to assess how reasonable this is. Although an un-converged dark matter profile would have too low a density in the inner regions (Power et al., 2003), the additional physics associated with the baryonic particles means that this cannot be assumed to be true for the DMG simulations.

4.4.3 Results: density profiles with baryons

Figure 4.8 shows the density profiles of *all* the objects that pass the selection criteria (the DMO haloes and their counterpart halo–galaxy systems in DMG *both* have to be selected). As expected, the profiles from the DMO haloes are fitted well by NFW functions (blue and cyan lines). Since we are plotting $\rho(r)r^2$, the location of $r_{\rm s}$ is given by the peak of the fitted curve.

Looking at the density profiles from the DMG simulations (red for the dark matter[6], green for the full mass density), we can see that in the outer regions of the halo, very little changes in most cases: the density tends to drop like r^{-3}, just as the NFW profile does. Furthermore, the DMG haloes' dark matter density profiles match their total-mass density profiles in the outer regions. This means that, as expected, the baryons are mostly in the halo centres with the outer halo being dominated by dark matter. Note that the 'radius' of each galaxy (the distance to the most distant particle in the baryonic FOF group) is $\sim 0.1R_{\rm vir}$ (marked with vertical bars coloured blue for discs, $(D/T)_B \geq 0.7$, and red otherwise). The resolution of the simulations means that for many haloes their galaxy—and hence the majority of their baryons—is mostly in the under-resolved inner region.

The inner radial limit of the NFW fit to the DMO profile, $r_{\rm conv}$, is indicated by the thick vertical line for each halo. We also mark the nominal values of $r_{\rm conv}$ calculated for the DMG profiles by the transitions from solid to dotted lines. As discussed above, without extensive convergence tests, we have no way of judging how reasonable this is, or

[6]For the dark-matter components of the DMG haloes, we scale the profile of each halo by its baryon fraction, $f_{\rm bary}$, i.e. the values plotted are $\rho'(r) = \rho(r)/\left(1 - f_{\rm bary}\right)$.

even if the 'real' convergence radius is outside that of the DMO haloes. In the absence of a more rigorous study, we recommend treating the convergence radius of the DMO haloes as the approximate inner limit of 'believability' for the dark matter and total-mass profiles from the DMG simulations, too.

Given that caveat, there is still evidence from the objects presented here that the density profiles of ΛCDM systems containing stars and gas do not follow NFW profiles. For the best-resolved systems, the profiles of the DMG mass, and to a lesser extent the dark matter, show a clear deviation from the NFW form, with an increase in the steepness of $\rho(r)$ in the inner halo. This trend continues within $r_{\rm conv}$ (whereas most of the DMO haloes continue their NFW trend), and it is visible in that sense for *all* the selected haloes regardless of resolution (although we cannot say if this is a physical effect for the less well-resolved cases).

The divergence of the DMG haloes from NFW profiles is in agreement with the four haloes studied in Gustafsson et al. (2006). Other studies have looked into how the concentration parameter changes when baryons are added to a simulation (e.g. Lin et al., 2006; Rudd et al., 2008); however, since our DMG haloes do not have NFW profiles, it would not be meaningful to find the concentration from an NFW fit.

As already discussed, it is computationally very expensive to run large simulations involving baryons and the additional physics for galaxy formation. Because of this, it has been common to simply use dark matter simulations, and scale the results using the *adiabatic contraction* model when comparing with observed systems (see Blumenthal et al., 1986; Gnedin et al., 2004; Sellwood and McGaugh, 2005, and references therein). If the infall of dissipative baryons occurs adiabatically (e.g. the gas falls into the halo through slow steady accretion), then the angular momenta of the dark matter and baryonic components are conserved separately. This means that the dark matter component can be assumed to simply contract, due to the baryons in the centre deepening the potential well. The dark matter density profile becomes steeper in the centre. However, since we have already shown that in the DMG simulation there is some transfer of angular momentum between the two components (section 3.3.5), we shall not consider this model further. Gnedin et al. (2004) performed a detailed comparison of galaxy–halo systems whose baryons were simulated both with and without cooling and star formation, alongside different implementations of the adiabatic contraction model.

The recent study of Romano-Díaz et al. (2008) found that, for the single halo they simulated, the presence of baryons caused the density profile to flatten, forming a core

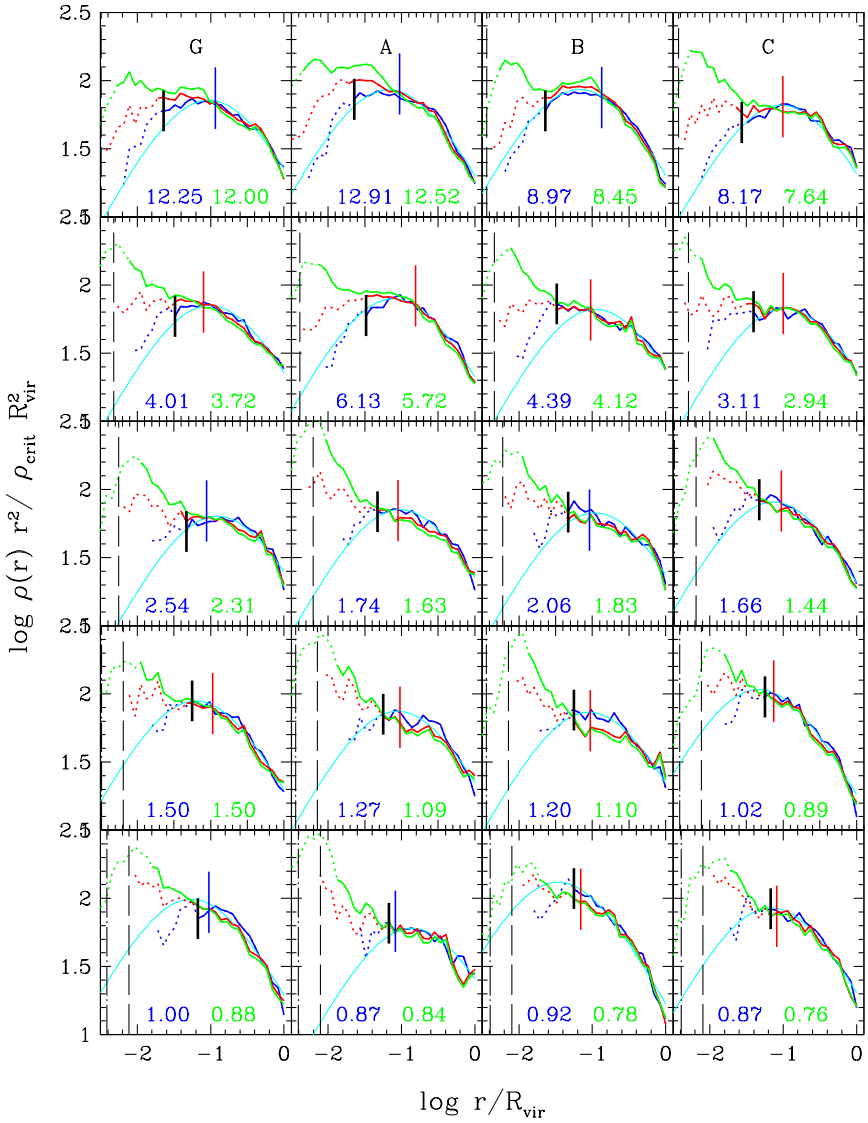

Figure 4.8: The density profiles of all the haloes selected from the DMG and DMO simulations: DMO profiles (blue) have NFW fits (cyan), and for the DMG haloes we show both the dark matter (red, scaled by $f_{\rm bary}$, see text) and total mass profiles (green). The values of $M_{\rm vir}/10^{11}\,h^{-1}{\rm M}_{\odot}$ are marked in each panel, using the same colour scheme. We mark $r_{\rm conv}$ by the transition from solid to dotted lines in the profiles, with that of the DMO haloes emphasized with a vertical black bar (they are only illustrative for the DMG haloes). The galaxy 'radius' (see text) for each DMG halo is marked by a long vertical bar, colour-coded by morphology: blue for discs, $(D/T)_B \geq 0.7$, and red otherwise. The softening lengths η are marked by a long-dashed black line (dark matter), and a dot-dashed line (baryons).

by $z = 0$ (although it initially has a steeper, isothermal cusp, $\rho(r) \propto r^{-2}$, at high-z). Their simulation uses a similar physical model to that used in DMG (see Heller et al., 2007), although they use a different code. The authors claim that the core is produced by the action of subhaloes containing baryons, which heat up the halo centre, causing dark matter to flow out. However, the small size of the observed core ($r \sim 2\,\mathrm{kpc}$) suggests that it is likely to be a numerical artefact. While the authors state that the softening used means that the gravitational forces are sufficiently accurate at these scales, the problem of two-body relaxation will still remain (Power et al., 2003). Okamoto (2008, private communication) analysed a similar-scale simulation, and found that it also formed a small core. Its location well inside the unconverged inner region (i.e. $r_{\mathrm{core}} \ll r_{\mathrm{conv}}$) lends weight to possibility that two-body effects are the source of the effect.

The result that the density profiles in our simulations become *more* cuspy (steeper), rather than shallower, is potentially problematic. Many observations of galactic systems have implied a constant-density core, although it is important to note that this does not seem to be a universal feature: gravitational lensing studies of elliptical galaxies suggests that NFW (or steeper) cusps provide a good fit (e.g. Gavazzi et al., 2007; Chen and McGaugh, 2008), but low surface-brightness galaxies (LSBs, expected to be dominated by dark matter), and some clusters, appear to have cores; see e.g. Sand et al. (2004), Kuzio de Naray et al. (2008), and references therein. On the other hand, Meneghetti et al. (2007) found that failure to take halo shape into account may mean that the central densities from gravitational lensing may be significantly underestimated. The observation of cored haloes is often seen as a threat to the whole ΛCDM paradigm, given how well the NFW profile fits dark matter-only simulations. We shall look at how the density structure of the simulated haloes compares with observational evidence in the next section.

4.4.4 Realism of galactic systems: circular velocity profiles

The galaxy formation model used in the DMG and GDMG simulations was investigated in depth in Okamoto et al. (2005), and we am using use the most successful model from that study. However, our understanding of the galaxy formation process is far from complete, and here we shall look at how the mass distribution in the simulated galaxy–halo systems compares with observational results.

A convenient method is to compare the circular velocity profile of simulated objects with the rotation curves measured from real disc galaxies. The so-called circular velocity profile of a halo is really just its cumulative mass distribution ($v_{\mathrm{c}}(r) = \sqrt{GM(\leq r)r^{-1}}$),

rather than any function of the velocities of the halo particles themselves. However, it can be compared to the rotation curves from velocity measurements of observed galaxies.

Persic et al. (1996) and Salucci et al. (2007) describe an empirical result called the *Universal Rotation Curve* (URC). It uses a simple model of a halo with a baryonic disc, and fits the free parameters of the model such that the resulting rotation curves fit those of a large population of observed spiral galaxies. Regardless of the physical realism of the model, the URC provides a convenient functional form for generating rotation curves that match observations for galaxies of a given luminosity.

In Salucci et al. (2007), the authors used much more observational data to constrain the functional form they use, although it is based on the same principles. They also extrapolate their model out to the virial radius of their model halo. This was done in order to make predictions based on the model that would fit the observed data, but could also be compared directly with simulations. Since we will be using the URC only as a proxy for observational data, we am not interested in the accuracy of their model; we restrict my use of the URC to the unextrapolated version, found just from fitting the model equations to the observed rotation curve data. The basis of the URC is a decomposition of the rotation curve into 'disc' and 'halo' components, which add in quadrature:

$$V^2_{\rm URC}(r) = V^2_{\rm D}(r) + V^2_{\rm H}(r) \tag{4.16}$$

The disc component is modeled as a Freeman (1970) disc, with an exponentially decaying surface density profile:

$$\Sigma_{\rm D}(r) = \frac{M_{\rm D}}{2\pi R^2_{\rm D}} e^{-r/R_{\rm D}} \tag{4.17}$$

where $R_{\rm D}$ and $M_{\rm D}$ are the disc scalelength and mass respectively. The disc size is defined as $R_{\rm opt} = 3.2R_{\rm D}$. The contribution to the rotation curve is then, in terms of the normalised radius $y = r/R_{\rm D}$:

$$V^2_{\rm D}(y|M_{\rm D}, R_{\rm D}) = \frac{1}{2}\frac{GM_{\rm D}}{R_{\rm D}} y^2 \left(I_0K_0 - I_1K_1\right) \tag{4.18}$$

where I_n and K_n are the modified Bessel functions, and are evaluated at $y/2$.

The halo is modeled with a Burkert (1995) density profile, which differs from the NFW profile by having a core of radius $r_{\rm c}$ and density $\rho_{\rm c}$ (see section 4.1, equation 4.2, and figure 4.1). This provides the following contribution to the circular velocity:

$$V^2_{\rm H}(r|r_{\rm c}, \rho_{\rm c}) = \frac{6.4G\rho_{\rm c}r^3_{\rm c}}{r}\left\{\ln\left(1+\frac{r}{r_{\rm c}}\right) - \arctan\left(\frac{r}{r_{\rm c}}\right) + \frac{1}{2}\ln\left[1+\left(\frac{r}{r_{\rm c}}\right)^2\right]\right\} \tag{4.19}$$

Salucci et al. (2007) then use the observational data to constrain the relationship between ρ_c, r_c and M_D:

$$\frac{\rho_c(r_c)}{\mathrm{g\,cm^{-3}}} = 5\times10^{-24}\,(r_c/\mathrm{kpc})^{-2/3}\exp\left(-\left(\frac{r_c/\mathrm{kpc}}{27}\right)^2\right) \quad (4.20)$$

$$\frac{M_D(\rho_c)}{10^{11}\mathrm{M_\odot}} = \left(\frac{\log\frac{\rho_c}{\mathrm{g\,cm^{-3}}}+23.515}{-0.964}\right)^{1/0.31} \quad (4.21)$$

Note that the form of these expressions implicitly constrains the parameters: equation 4.21 means that $\log\rho_c/\mathrm{g\,cm^{-3}} < -23.515$, leading to $r_c > 2.0797\,\mathrm{kpc}$ from equation 4.21. The equations are not without uncertainty; equation 4.21 in particular is derived from an "eyeball fit" to the data, and has an uncertainty $\delta r_c/r_c$ of 30 to 50 percent (Salucci and Burkert, 2000).

These expressions leave r_c and R_D as free parameters in $V_{URC}(r)$. They are valid out to a radius $R_l \approx 6R_D$, the limit of the observed rotation curves. We fit the URC as described here to the $v_c(r)$ profiles of the halo–galaxy systems selected from the DMG simulations[7]. As when fitting NFW curves to the density profiles, we take the value of r_{conv} of the equivalent DMO halo as the inner radius for the fit; we also fix the outer radius at $20\,h^{-1}$kpc. This is much simpler than fitting out to R_l, since in that case the fitting range would depend on the value of one of the free parameters, and given the approximate nature of the URC in the first place, this level of precision was not deemed necessary. Figure 4.9 shows the circular velocity curves and URC fits for the halo–galaxy systems, selected in the same way as before.

The figure shows that, essentially, there are no real disc galaxies that have rotation curves similar to the circular velocity profiles observed in these simulations[8]. The disc-galaxy haloes in the simulations (those with $(D/T)_B \geq 0.7$, marked with an asterisk) are in fact among the worst-matched objects in the sample; some of the more bulge-dominated galaxies appear to be better fits (this does not mean they are more 'realistic' of course, since the URC is defined using observations of spiral galaxies only). Most of

[7]Strictly, the rotation speeds from disc geometries (including the URC with its explicit disc model) should not be compared directly to the spherically-averaged circular velocity profiles. However, the difference is expected to be sufficiently small that it can be neglected for the purposes of this study: Binney and Tremaine (2008, p101–102) show that the rotation curve of an exponential disc peaks about 15% higher and peaks slightly further out than that of a sphere of the same mass.

[8]We have focused here on the later URC paper (Salucci et al., 2007), but we get qualitatively similar results using the first paper (Persic et al., 1996). The fits tend to be slightly worse in that case, due to the different way the URC equations are formulated and the approximations involved.

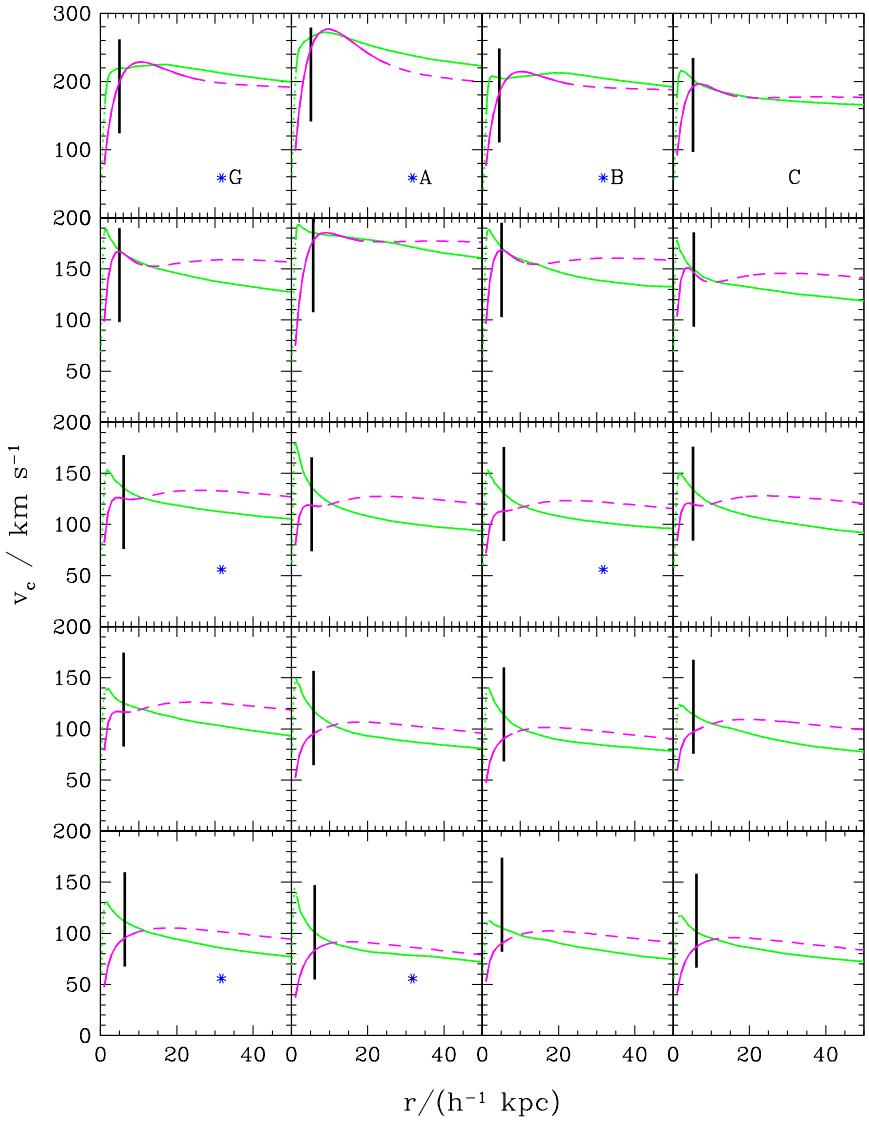

Figure 4.9: Circular velocity profiles for the 20 selected halo–galaxy systems in the DMG simulations. Haloes marked with a blue asterisk have $(D/T)_B \geq 0.7$. The green curves give $v_c(r)$ calculated using all the mass in each DMG halo. The value of $r_{\rm conv}$ for each corresponding DMO halo is marked with a black bar, and the transition from solid to dotted indicates $r_{\rm conv}$ computed using the DMG halo (but see text). The magenta curves show the best-fitting Universal Rotation Curve, with the outer limit for which the URC is reliably defined, $R_l = 6R_{\rm D}$, marked by the transition from the solid to dashed line. The URC fits are performed between $r_{\rm conv}$ and $20\,h^{-1}$kpc. The plots are truncated at $50\,h^{-1}$kpc, although the virial radii of the haloes are much larger.

the lower-mass objects (the lower panels in the figure) have very similar $v_c(r)$ profiles, both in terms of shape and overall magnitude, and thus produce similarly bad best-fit URC curves.

The source of the problem is simple: the haloes have too much mass in their centres. This means that they rise sharply within the first $\sim 3\,h^{-1}$kpc (although this is always within $r_{\rm conv}$). For the most massive objects, they then have a broad peak (with $r > r_{\rm conv}$) and begin a gentle decline. For the less well resolved haloes there is a much sharper peak (with $r < r_{\rm conv}$ still) before the slow decay. For the best-resolved objects, the URC has to fit to a gentle rise towards a broad peak. It can place the peak at roughly the right radius, but this causes it to drop too fast afterwards. For the less well-resolved haloes, the fit starts where the $v_c(r)$ data is already falling away from its peak. The URC cannot reproduce this, yielding curves that are instead either flat or still rising at $r_{\rm conv}$. Furthermore, this results in very little separation between $r_{\rm conv}$ and the URC's own outer limit of R_l.

These results are not atypical for current simulations. Abadi et al. (2003), Gustafsson et al. (2006) and Governato et al. (2007) all exhibit circular velocity profiles with similarly problematic shapes. These results emphasize the need for further studies of the structure of haloes simulated with baryons, using different recipes for star formation and feedback and at high resolution. Preliminary results of a series of such tests have recently been presented by Pedrosa et al. (2008), based on the simulation code of Scannapieco et al. (2008). While their results are similar to ours, it does not seem that varying the supernova feedback parameters alone can solve the problem of the high central density. It seems likely that more detailed physical models, which incorporate additional processes (such as feedback from AGN), will be necessary. Although the simulations we have used here are very successful in alleviating many of the difficulties associated with the galaxy-formation physics in simulations (see Okamoto et al., 2005; Libeskind et al., 2007), the problems are still far from solved definitively.

4.5 Conclusions

In this chapter, we have examined the structural parameters of haloes in a ΛCDM universe, both in large dark matter-only simulations, and later in smaller simulations to study the impact of gas and star formation.

As others have found, the density profile of relaxed dark matter haloes is well-fitted

by the functional form given in Navarro et al. (1997, NFW97). Neto et al. (2007, N07) found that at least 1000 particles are required for the concentration distribution to be free of numerical bias, and investigated various potential pitfalls that can arise from studying poorly-resolved or unrelaxed haloes. They extended previous studies of the concentration-mass relation to much higher masses, and therefore rarer objects. In combination with the results of Macciò et al. (2007), it was found that the concentrations of relaxed haloes follow the same power-law relationship over six decades in halo mass. The results are in reasonable agreement with Eke et al. (2001) and NFW97; however, the model of Bullock et al. (2001b) fails at high masses: the predicted median concentration is a factor of ~ 2 too low for haloes of mass $\sim 10^{15}\,h^{-1}\mathrm{M}_{\odot}$.

The trend in $c(M)$ is weak, and the scatter in concentration at fixed mass is equally important. The distribution of the concentrations of Relaxed haloes at fixed mass is well-fitted by a lognormal function, with a mean and dispersion that decrease with increasing halo mass.

By combining the concentrations measured in N07 with the spin parameters measured in Chapter 2, we found that there was no significant correlation between them. This is in apparent contradiction to Bailin et al. (2005b). A correlation between λ and c can be shown to exist, however, if the unrelaxed haloes are included, as they are systematically biased towards lower concentrations and higher spins. The lack of correlation amongst the relaxed haloes means that the spin distribution cannot be a significant source of the scatter in the $c(M)$ relation.

Instead, a significant amount of the scatter seems to come from variations in the formation times of haloes. After testing various different definitions of formation redshift (z_{f}), it was found that the structural parameters of haloes are best predicted by models that take the full spectrum of progenitor masses into account when finding the formation redshift, rather than just the most massive progenitor.

We compared the predictions of the halo concentration in the models of Wechsler et al. (2002), Zhao et al. (2003b) and a variant of the Navarro et al. (1997) model that uses the merger trees to compute z_{f}. All three models produced concentrations that correlate well with the measured values. However, none of the models can account for more than about 30% of the variance in the measured distribution. This implies that a large fraction of the scatter is likely to depend on a more subtle aspect of the merger histories of the haloes, which is not captured in these relatively simple schemes.

We then used a simulation of a much smaller, high resolution volume, that included

gas and star formation, to investigate how this changes the density profile. We found that the total mass density profiles of these objects do not follow an NFW shape, instead becoming steeper within $\sim 0.1R_{\rm vir}$ (although they do converge onto the $\rho(r) \propto r^{-3}$ trend at larger radii).

Finally, we used the mass density profile information to examine the circular velocity profiles of the haloes simulated with baryons. These were compared to the URC of Salucci et al. (2007), a functional form constrained to match observed rotation curves. We found that the disc galaxy–halo systems in our simulations cannot be matched to any rotation curve described by the URC. Much work therefore remains to be done, in testing the impact of different models of galaxy formation in simulations.

Chapter 5 | *Conclusions*

5.1 Haloes in dark matter-only simulations

We have used the Millennium Simulation (MS) and HR1 simulation to determine structural properties of dark matter haloes with unprecedented precision. In Chapter 2, we examined the distributions of the spin parameters and shapes of the haloes, and their dependence on mass, environment, and halo definition. Chapter 3 built on this and examined the angular momentum profiles of those haloes, considering both their magnitude and orientation. In Chapter 4, we investigated the source of scatter in the concentration parameter of the MS and HR1 haloes, relating it to both the spin parameter and the halo formation time.

The halo definition algorithm is a critical step in the post-simulation analysis of a cosmological model. We have tested the dependence of the spin parameter λ, and the halo sphericity s and triaxiality $\mathcal{T}$, on the algorithm used. In addition to comparing the "friends-of-friends" (FOF) and "spherical overdensity" (SO) methods, we tested a third definition that uses the merger trees together with substructure information (section 2.3). This TREE definition effectively cleans the FOF halo population of objects that have been artificially linked, but are dynamically separate.

The work presented in this thesis has emphasised the importance of choosing a halo definition, and subsequent halo selection criteria, which are appropriate to the quantities being studied. The TREE haloes were ideal for measurements of λ and halo shape, but for the halo profile properties, studied in spherically-averaged radial bins, the SO definition is a more suitable choice. Furthermore, model fits to density profiles are more susceptible to biases caused by the presence of substructure; the selection criteria needed to reflect this by removing the less smooth haloes. Similarly, the angular momentum vector directions were only reliable if the vector magnitudes were not too small.

We found that, for the MS TREE halo population of more than 1.5 million, the spin parameter was poorly described by the traditional lognormal distribution. Instead, we proposed an alternative function (equation 2.15), which is not biased away from $j = 0$ and

thus provides a better description of the data. We have detected a slight but significant trend in the variation of λ with halo mass, such that higher mass haloes have lower median spin values. However, the trend differs significantly for different halo definitions.

The MS haloes exhibit a broad range of shapes, with a tendency for prolateness, consistent with previous results; the particular distribution depends strongly on the halo definition. More massive haloes tend to be less spherical and more prolate. The relationship between spin and shape depends strongly on halo mass: the more spherical haloes have relatively low median spins, independent of mass; whereas the median spin of the most massive haloes is independent of their sphericity. The least massive haloes ($M_{\rm h} = 10^{11.4}$–$10^{12}\,h^{-1}{\rm M}_{\odot}$) have spins that anticorrelate strongly with sphericity.

We examined two-point correlation functions for haloes selected according to their spin or shape, and found that these parameters depend significantly on the halo environment. Haloes with greater spin, or a more spherical shape, tend to reside in more clustered environments. The effect becomes stronger at higher masses.

The cumulative specific angular momentum profiles of haloes, $j(\leq r)$, show a significant amount of scatter. However, the median profiles at fixed mass behave similarly to the $j(\leq r) \propto r$ trend expected from simple circular-motion arguments with constant velocity. The median trend scales with halo mass, with the more massive haloes having more specific angular momentum (in the median) within all radii. This mass trend disappears if one considers the angular velocity $\omega(r)$ instead, but there is still a large amount of halo-to-halo scatter. Haloes do not rotate as solid bodies, but instead behave as if they have a constant circular velocity ($\omega \propto 1/r$), consistently over the five orders of magnitude in halo mass that are studied in Chapter 3.

We have found that both the inner and total angular momentum vectors tend to align perpendicular to the halo major shape axis, and parallel to the minor axis. We also calculate the angular momentum orientation profiles themselves. The median total halo angular momentum $\boldsymbol{j}(\leq R_{\rm vir})$ is directed about 25° away from the inner angular momentum $\boldsymbol{j}(\lesssim 0.25R_{\rm vir})$. However, the data exhibit a large degree of scatter, with the bulk of the angles between haloes' total and inner angular momenta lying between 5° and 65°. A weak mass trend is also visible, with a greater range of values present for the most massive haloes, resulting in a reduced alignment in the median. These massive haloes are more likely to have suffered a recent merger or near-merger event, which could easily change the spin orientation structure.

In Chapter 4 We used the measurements of halo concentration, c, from the NFW fits of

Neto et al. (2007), and investigated the source of their scatter. Although it had been suggested that a correlation between λ and concentration indicated that the scatter in λ was a significant contributor, We showed that relaxed haloes show no such correlation. Instead, we found that a significant amount of the scatter in concentration at fixed mass seems to come from the variation in halo formation time: the variance in c for haloes of a given mass correlates with the variance in their formation redshift. However, the definition of formation time is somewhat arbitrary. We tested three different models that predict halo concentration using different aspects of their merger histories. The most successful model used the full spectrum of progenitor masses, rather than defining a characteristic redshift based on the mass accretion history of the most massive progenitor alone. Nevertheless, all three models succeeded in predicting concentrations that correlated reasonably well with those measured in the simulations. However, none of them could account for more than about 30% of the measured scatter. This means that there is likely to be some other significant aspect of the merger histories that these relatively simple schemes do not take into account.

5.2 Haloes simulated with baryonic physics

We have used a simulation of the formation of galaxies within CDM haloes (DMG, Okamoto et al., 2005), which includes a multiphase ISM model, star formation in quiescent and burst modes, and supernova feedback, to investigate how the structural properties of haloes are transformed by baryonic physics. Using a dark matter-only simulation of the same region (DMO), We were also able to compare individual objects directly.

In Chapter 3, we used these simulations to study the effect of baryons on the dark matter angular momentum. We found that the angular momentum within $0.1R_{\rm vir}$ is about 50% greater in the median for the haloes with baryons, even though typically the bulk of the galaxy mass is within a significantly smaller scale. The difference in angular momentum reduces as we consider the dark matter within larger radii, such that by $R_{\rm vir}$ the median angular momentum of the haloes is the same as in the dark matter-only case. Part of the increase in the inner angular momentum is due to transferral from the baryons as the haloes collapse.

We also examined changes in the orientation of the dark matter angular momentum. Despite the large amount of variation between individual haloes, the median trend is that the baryons cause the inner dark matter to become slightly better aligned with the total

halo angular momentum direction.

The simulated galaxies' angular momenta also exhibited a broad range of orientations, with respect to their parent haloes. The galaxies tend to be slightly better aligned with the inner regions of the haloes, than with all the dark matter within $R_{\rm vir}$. However, there is no significant difference between the galaxy–halo alignment distributions if the parent haloes are replaced by their dark matter-only counterparts. We also attempted to distinguish between the alignment distributions of disc-dominated and bulge-dominated galaxies. However, separating the population into these two samples results in too few well-resolved objects to be able to make any firm conclusions: we did not find any significant difference between the galaxy–halo orientations of the two types of galaxy.

The broad galaxy–halo alignment distributions have implications for future measurements of halo shape using weak gravitational lensing. We measured the halo shape resulting from stacking the projected halo mass distributions, aligned according to their galaxy. The stacked projected mass distribution shape was indistinguishable from circular. If the orientation distributions from this simulation are a faithful sample of the true distribution, then it will be extremely challenging for weak lensing surveys to use halo shape measurements to distinguish between ΛCDM and alternative-gravity theories such as TeVeS.

Finally, in Chapter 4, we used the same simulations to see how the baryons affected the dark-matter and total-mass density profiles. We found that within about $0.1R_{\rm vir}$, the density profiles of the haloes with baryons tend to diverge from the NFW shape, with a steeper central profile. This is also reflected in the halo circular velocity profiles, which we compared to observed objects using the Universal Rotation Curve (URC) formalism. The haloes in the simulations used here do not match any rotation curve that can be modelled by the URC. This demonstrates an important shortcoming in the simulations: there is too much matter in the central regions compared to data from observed disc galaxies.

5.3 Future prospects

The work presented in this thesis can be extended and applied in a variety of directions.

Current semi-analytic models (such as GALFORM, Cole et al. 2000) set the size of galactic discs directly using the spin parameter λ. In practice, this is generated by sampling a lognormal distribution, even when the model is based on the haloes from an N-body simulation (e.g. Helly et al., 2003). An obvious extension is to use the spin parameters

measured from the haloes themselves, or to sample the measured distribution (equation 2.15) for the under-resolved haloes. This will allow for greater continuity when a given galaxy's disc size is re-computed, since halo spin parameters are expected to be correlated in time; resampling from a lognormal will result in uncorrelated spins each time. Furthermore, the environmental dependence of the spin parameter will become encoded into the galaxy properties. In simulations with large numbers of objects (such as the MS), this will allow more realistic measures of statistical properties of galaxy populations in different environments.

The halo angular momentum direction information could also be incorporated into semi-analytic models. Currently, models do not monitor changes to the direction of the halo spin vector, even though events such as halo flybys can cause dramatic changes to a halo's orientation and presumably perturb its internal structure. It would be useful to investigate the significance of spin flips on halo structural parameters, and to consider an additional criterion based on this to trigger the model to re-assess the galaxy properties based on the halo.

In principle, galaxy orientations could be directly incorporated into semi-analytic models using the galaxy–halo alignment distributions from section 3.3.5. In practice however, these would benefit from further study of galaxy-formation simulations. There are two main questions concerning my results from the DMG simulations that remain unresolved: (1) How robust are the measurements of the changes to the angular momentum and density profiles to changes in the physical model used in the simulation, and (2) can relationships be found between halo and galaxy properties when objects are selected by environment, morphology, luminosity, colour, size, etc?

In order to answer the first question, further simulations must be analysed that use significantly different models for the ISM, star formation and feedback processes. We need to investigate under what circumstances the density profiles of haloes can be made to match those from observations, to ensure that we are analysing sufficiently realistic systems. The simulations must have at least the size and resolution of the ones analysed here, although the answer to the second of the above questions is of course to use larger simulations, at higher resolution.

An increase in size (simulation volume) means more objects, which means the ability to discern trends amongst sub-populations of objects: haloes selected by spin, shape, or concentration, galaxies selected by luminosity, colour or morphology, etc. The work on the MS has shown how existing results can be improved when they are re-examined

using a much larger halo population. Chen and McGaugh (2008) have shown the importance of careful object selection when comparing simulations to observations: low surface brightness galaxies appear to have cored mass density profiles, but giant elliptical galaxies suggest a cuspy profile. Simulations and models need to produce many objects, with a range of properties, so that selecting subsets of galaxy–halo systems to match an observed population will result in sufficient numbers of objects to make robust conclusions.

An increase in resolution (i.e. reduced softening lengths and particle masses, for the Lagrangian simulations considered here) means being able to make more definitive statements about the behaviour of the central regions of galaxy–halo systems. The results presented here on the spin orientation profiles in particular would benefit from being able to see down to the central galaxy, since that is where the galaxy–halo misalignment will be most significant.

As an example, consider the study of the projected mass distribution of galaxy-aligned haloes (section 3.3.5), intended to inform weak lensing studies that attempt to measure the shape of the gravitational potential around galaxies. Increased resolution would allow the shape of the projected halo mass distribution to be computed as a function of radius. This could be used to characterise how the strength of any ellipticity signal varies with distance from the central galaxy. With more objects, the distribution could be filtered by galaxy type, and a set of selection criteria could be devised that maximises the chance of detecting an ellipticity signal.

Appendix A | *Examples of haloes*

A.1 Effects of the group-finder algorithm on the Millennium Simulation haloes

The following plots give examples of haloes from the catalogues derived from the Millennium Simulation in Chapter 2. They have been chosen as clear examples of various (usually undesirable) groupfinder effects—they are *not* 'typical' haloes from their respective catalogues. We show them to give some visual intuition as to the problems that can be encountered with different group-finding algorithms, as described in section 2.3.

The first three show FOF haloes with unusual properties in real and velocity space. Figure A.1 shows a halo that is clearly made up of at least two objects joined via a tenuous bridge. We show a more massive halo that nevertheless consists of many linked objects in figure A.2. Figure A.3 shows a very distorted object located near a much larger halo.

The final two figures compare the results of the three different group-finding algorithms used. Figures A.4 and A.5 compare haloes defined using the FOF, SO and TREE algorithms. In both cases, projections of the selected FOF halo (and its neighbours) are shown in the left-hand panels, and the corresponding SO/TREE halo and neighbours are in the right-hand panels. The selected haloes (green) have, again, been chosen to provide a striking illustration of the effects of different algorithms. The more 'normal' haloes in the background (blue) are less strongly affected by the choice of groupfinder.

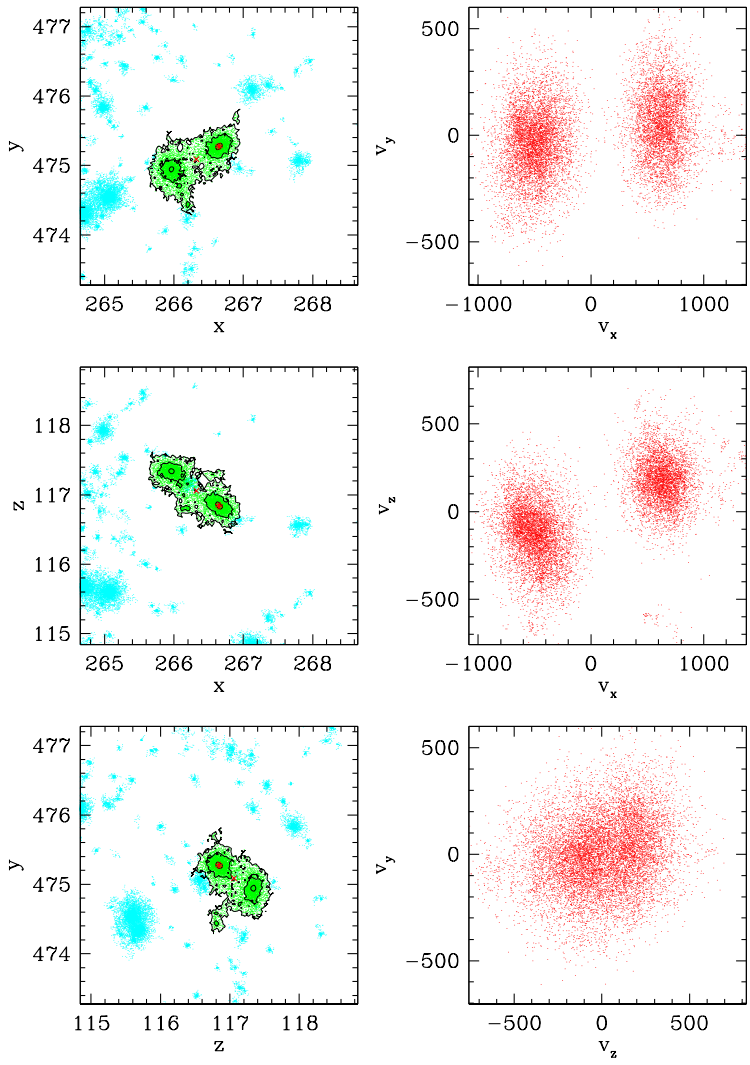

Figure A.1: An example of a FOF halo made of two objects linked by a tenuous bridge. The left-hand panels show projections of the halo (overplotted in green) and its neighbours within $2\,h^{-1}$Mpc (blue) in real space, in units of h^{-1}Mpc. The black contours show projected particle density, at 1, 10 and 100 particles per contouring bin. The potential-minimum centre of the main halo is marked with a red star, and the centre-of-mass is marked with a red cross. The right-hand panels show the particles of the selected halo in velocity space, in $\mathrm{km\,s^{-1}}$. This halo has a mass of $M_\mathrm{h} = 11\,418 m_\mathrm{p} \approx 9.82 \times 10^{12}\,h^{-1}\mathrm{M}_\odot$, and a spin parameter of $\lambda = 1.5712$. Its virial ratio, $\frac{2T}{U} + 1 = -4.23$ means it is excluded from the FOFclean catalogue.

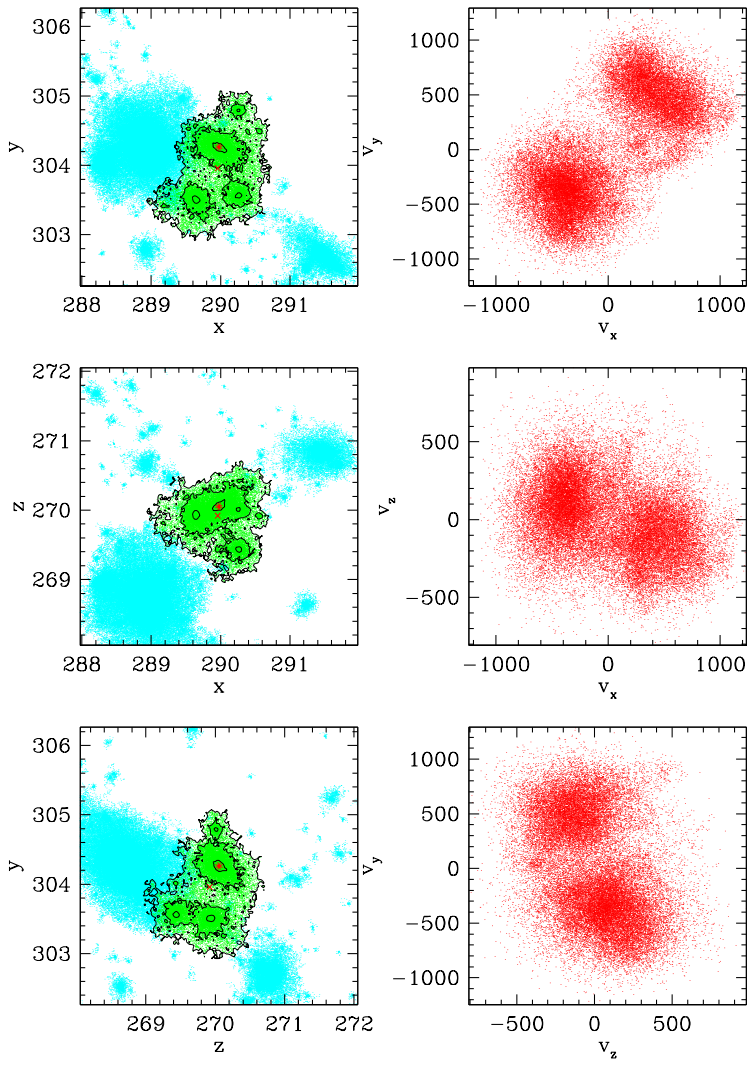

Figure A.2: As figure A.1, but showing an example of a larger multi-object FOF halo. This halo has a mass of $M_{\mathrm{h}} = 38\,741 m_{\mathrm{p}} \approx 3.33 \times 10^{13}\,h^{-1}\mathrm{M}_{\odot}$, and a spin parameter of $\lambda = 0.3295$. Its virial ratio, $\frac{2T}{U} + 1 = -2.05$ means it is excluded from the FOFclean catalogue.

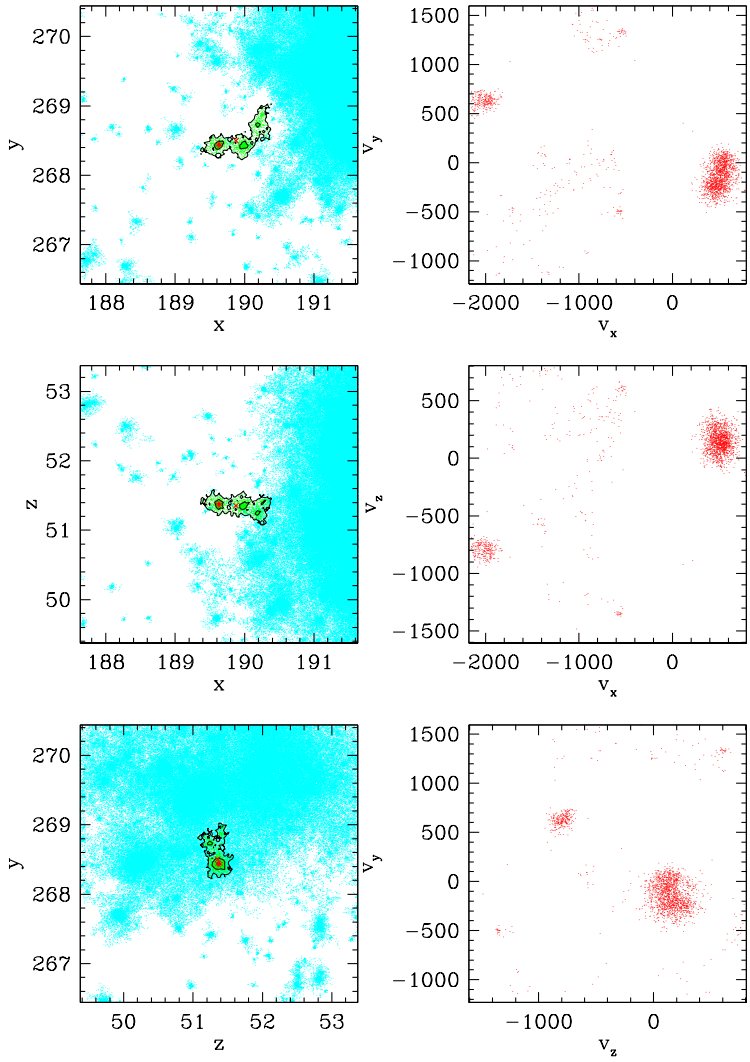

Figure A.3: As figure A.1, but showing an example of a small FOF halo with a large neighbour. The selected halo has a mass of $M_{\rm h} = 1967 m_{\rm p} \approx 1.69 \times 10^{12}\, h^{-1}{\rm M}_{\odot}$, and a spin parameter of $\lambda = 17.60$. Its virial ratio, $\frac{2T}{U} + 1 = -53.8$ means it is excluded from the FOFclean catalogue.

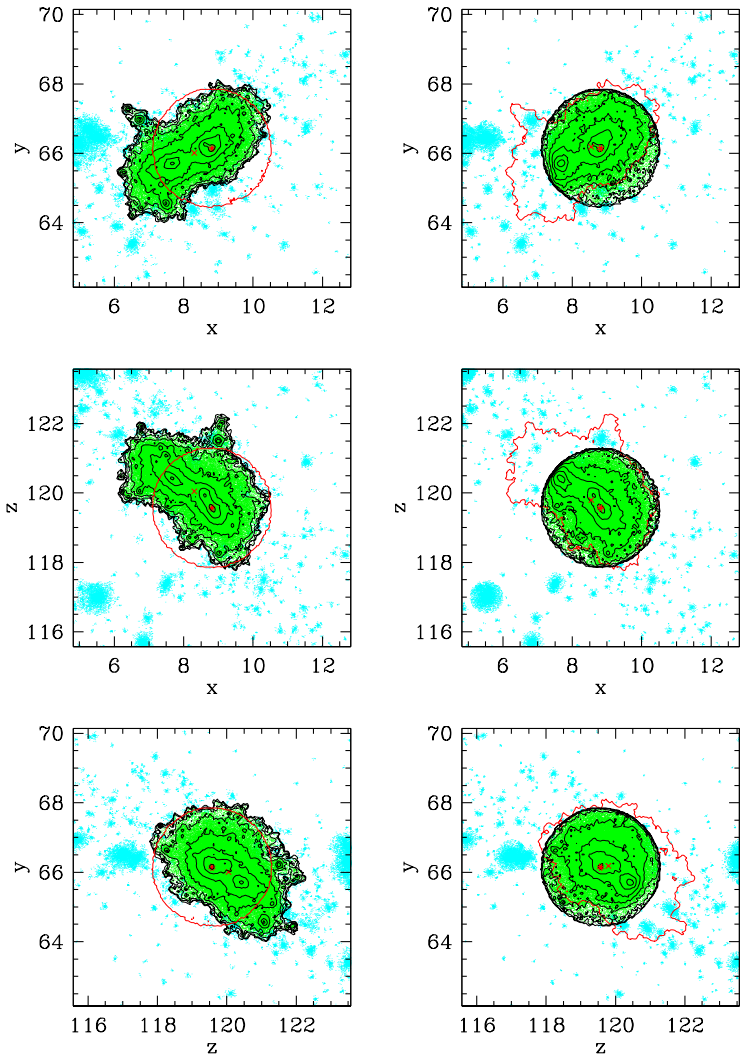

Figure A.4: As figure A.1, but showing a comparison of a massive FOF halo (left) and the corresponding SO halo (right), and their neighbours in each catalogue within $4\,h^{-1}$Mpc. A random sample of 1/4 of the particles are plotted; this does not effect the overall image of the halo. Projected logarithmic density-contours are plotted in black, spaced every factor of $\sqrt{10}$ between 1 and $10^{3.5}$ particles per contouring bin. The outermost contour (the halo boundary) is reproduced on the opposite panel in red. Note how the SO halo includes particles that were not part of the FOF group, and are much less dense than the halo proper. The FOF halo has mass $M_\mathrm{h} = 744\,019 m_\mathrm{p} \approx 6.40 \times 10^{14}\,h^{-1}\mathrm{M}_\odot$, spin $\lambda = 0.05959$, and virial ratio $\frac{2T}{U} + 1 = -0.262$; it is included in the FOFclean catalogue. The SO halo has mass $M_\mathrm{h} = 610\,023 m_\mathrm{p} \approx 5.25 \times 10^{14}\,h^{-1}\mathrm{M}_\odot$, spin $\lambda = 0.04539$ and virial ratio $\frac{2T}{U} + 1 = -0.332$, slightly less relaxed than its FOF counterpart but still included in the SOclean catalogue.

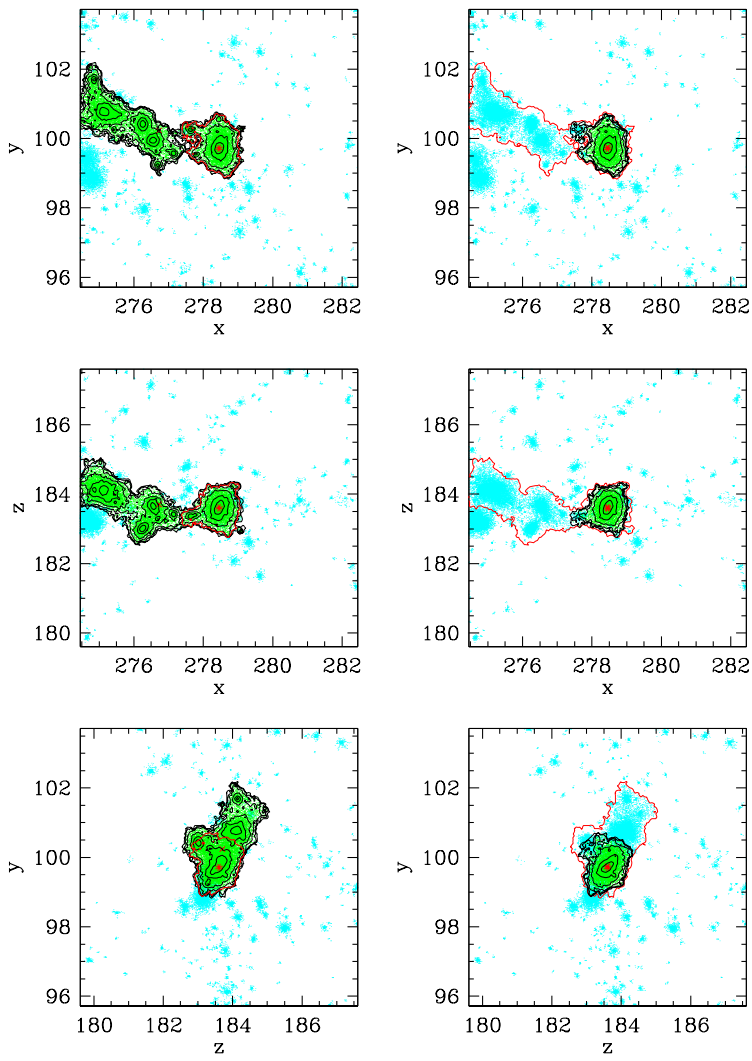

Figure A.5: As figure A.4, but comparing a massive FOF halo (left) and the corresponding TREE haloes (right). Again, a random selection of 1/4 of the points are plotted, and the density contours are spaced every factor of $\sqrt{10}$ up to $10^{2.5}$ particles per contouring bin. Note how the FOF halo is highly extended, with the subhalo housing the potential minimum being linked to a large neighbouring halo. The TREE catalogue splits these into two objects. The FOF halo has a mass of $M_{\rm h} = 126\,033 m_{\rm p} \approx 1.08 \times 10^{14}\,h^{-1}{\rm M}_{\odot}$, and a spin of $\lambda = 0.1953$. It has a virial ratio of $\frac{2T}{U} + 1 = -0.111$, so it is included in the FOFclean catalogue (despite its peculiar structure). The TREE halo has a much lower mass of $M_{\rm h} = 40\,719 m_{\rm p} \approx 3.50 \times 10^{13}\,h^{-1}{\rm M}_{\odot}$, and a spin of $\lambda = 0.05711$. It is slightly less relaxed however, with a virial ratio of $\frac{2T}{U} + 1 = -0.159$; it is included in the TREEclean catalogue.

A.2 Haloes with and without baryons

Here we provide a visual representation of the relationships between halo, galaxy, mass and angular momentum, for the four most massive haloes (G, A, B and C) selected in Chapter 4 from the DMO and DMG simulations . Various properties of these galaxy–halo systems are provided in table 4.1, and their density and circular velocity profiles were shown in the top panels of figures 4.8 and 4.9.

Figure A.6 compares the mass distributions of the four haloes. The left panels show the haloes as simulated with just dark matter. The middle column shows the dark matter from the corresponding haloes simulated with baryons, and the right panels show the mass distribution of the baryons (gas and star particles). The haloes are shown in the 'natural' x–y frame of the simulation, without any additional rotation.

Figures A.7 to A.10 each show one of the four halo-galaxy systems from the DMG simulations in detail. The left panels show the distribution of the galactic star particles, and the right panels show the dark matter halo (note that these are at different scales). The objects in each figure have been rotated such that the galaxy is face-on, i.e. the x–axis in the image corresponds to the major axis of the galaxy (as defined by its inertia tensor), the image y–axis is the galaxy's intermediate axis, and the galaxy's minor axis is directed out of the page. The upper panels show the mass distribution of the galaxy and halo. The lower panels show the angular momentum distribution: each pixel is colour-coded according to the z–component of the total specific angular momentum of the particles projected in that pixel (j_z). This means that, for example, a bright blue pixel has a large positive j_z, indicating anticlockwise rotation in the image plane. Red indicates a negative j_z (into the page), and therefore clockwise rotation. Disc galaxies rotating in the image plane should therefore appear monochromatic. The fact that galaxy "C" is slightly bimodal in image colour implies a misalignment between its mass and angular momentum distributions. This is not too surprising however, since it is the least 'discy' of the four objects (see table 4.1).

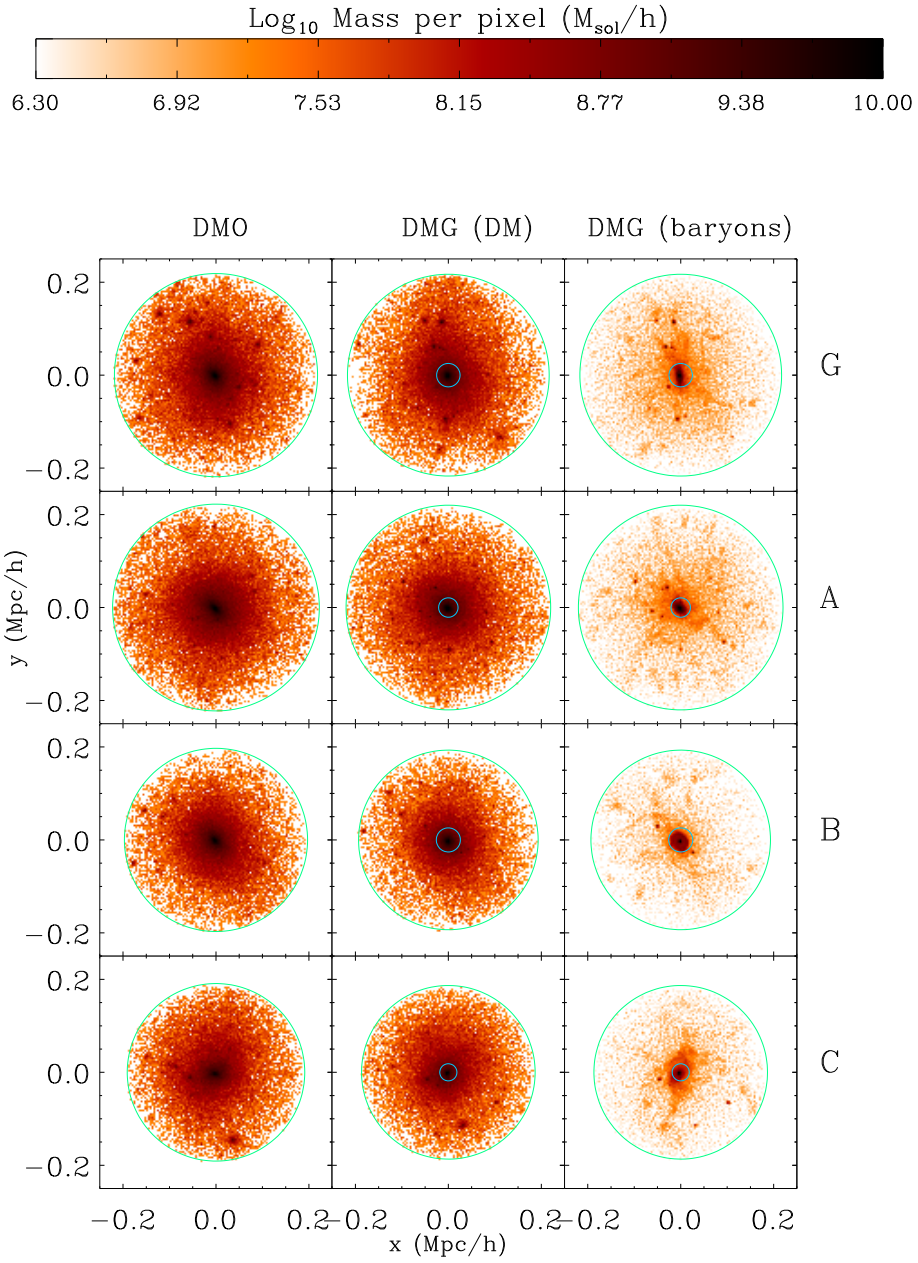

Figure A.6: Comparison of the four large haloes from the DMO and DMG simulations described in table 4.1. Each row is a different halo (G, A, B and C from top to bottom). The left column shows the halo from the DMO simulation. The middle column is the dark matter component of the corresponding DMG halo, and the right column shows its total baryonic component (gas and stars). The colours give the projected mass density in each pixel. Rings are drawn at $R_{\rm vir}$ and the galaxy radius. The extremes of the colourbar are upper and lower limits respectively, for the sake of contrast. Each halo is shown in the simulation x–y frame, without rotation, but centred on the halo centre.

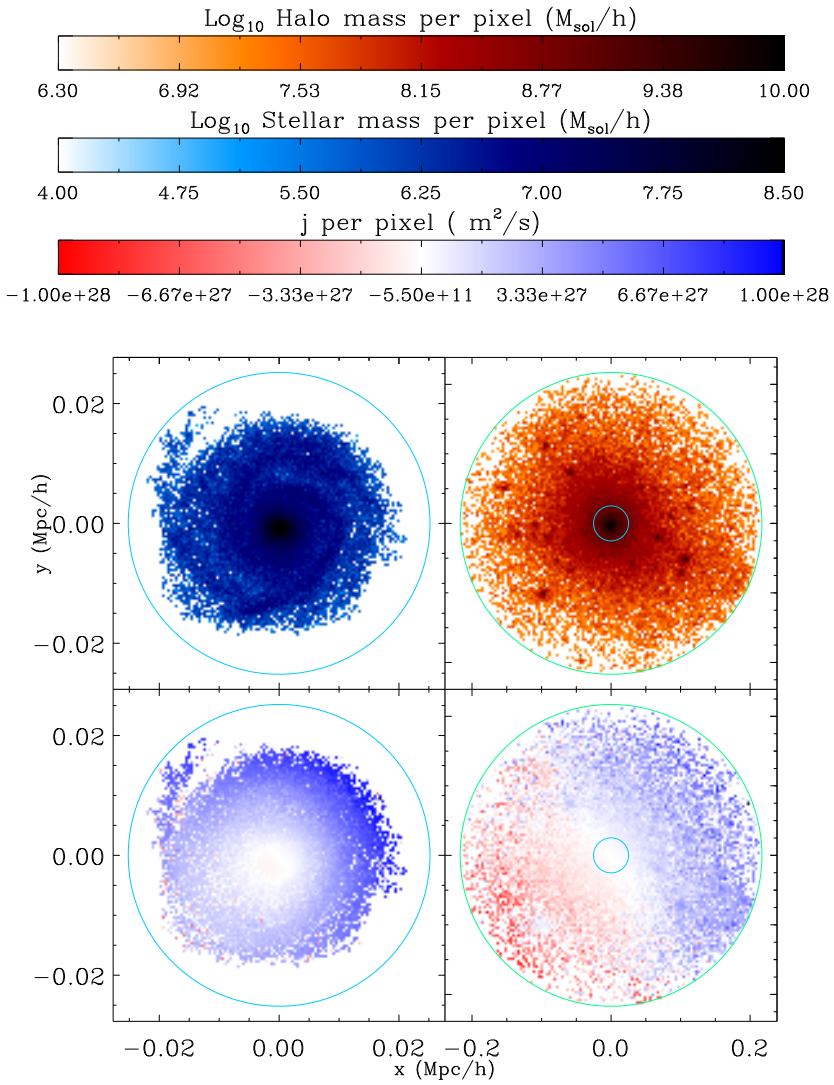

Figure A.7: Mass and angular momentum distributions for halo "G" and its central galaxy. Top: Mass density of (left) stellar component of the galaxy, and (right) the dark matter component of halo (see text). Bottom: specific angular momentum per pixel for (left) the stellar component of the galaxy, and (right) the dark matter component of the halo. In all four panels, the galaxy–halo system is rotated such that the x and y axes correspond to the galaxy's major and intermediate axis directions respectively.

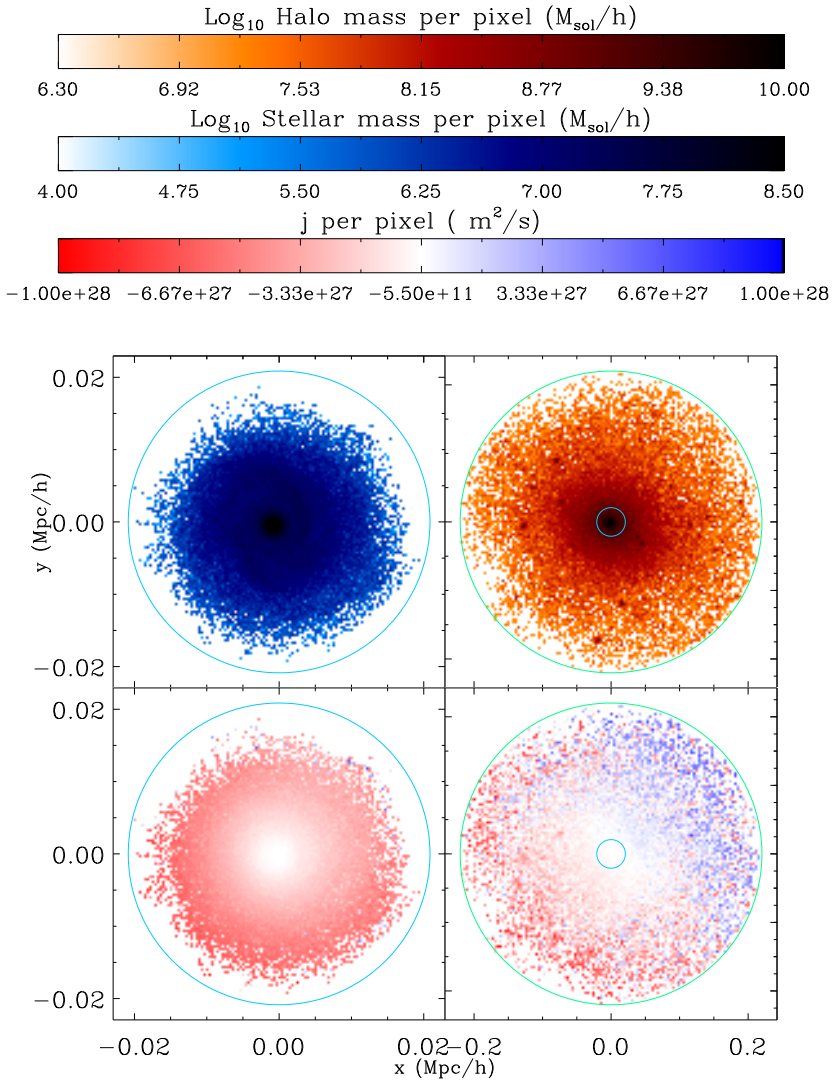

Figure A.8: Mass and angular momentum distributions for halo "A" and its central galaxy. Layout and colour schemes are the same as for figure A.7.

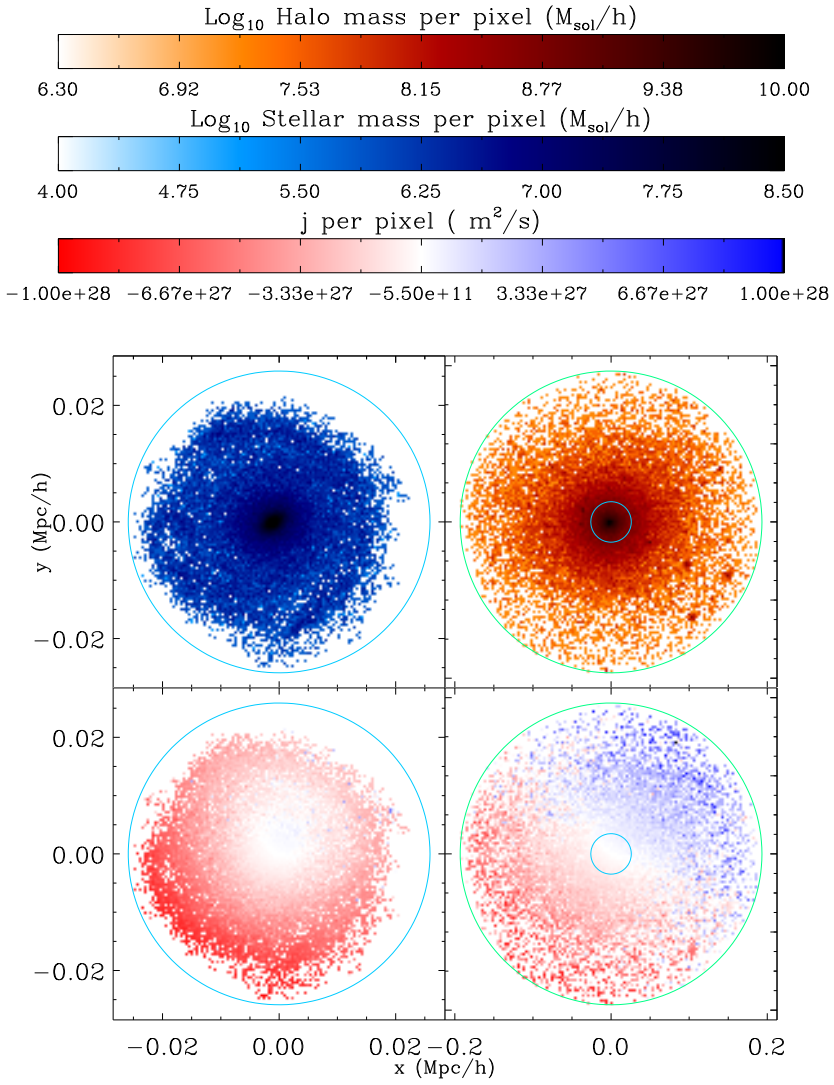

Figure A.9: Mass and angular momentum distributions for halo "B" and its central galaxy. Layout and colour schemes are the same as for figure A.7.

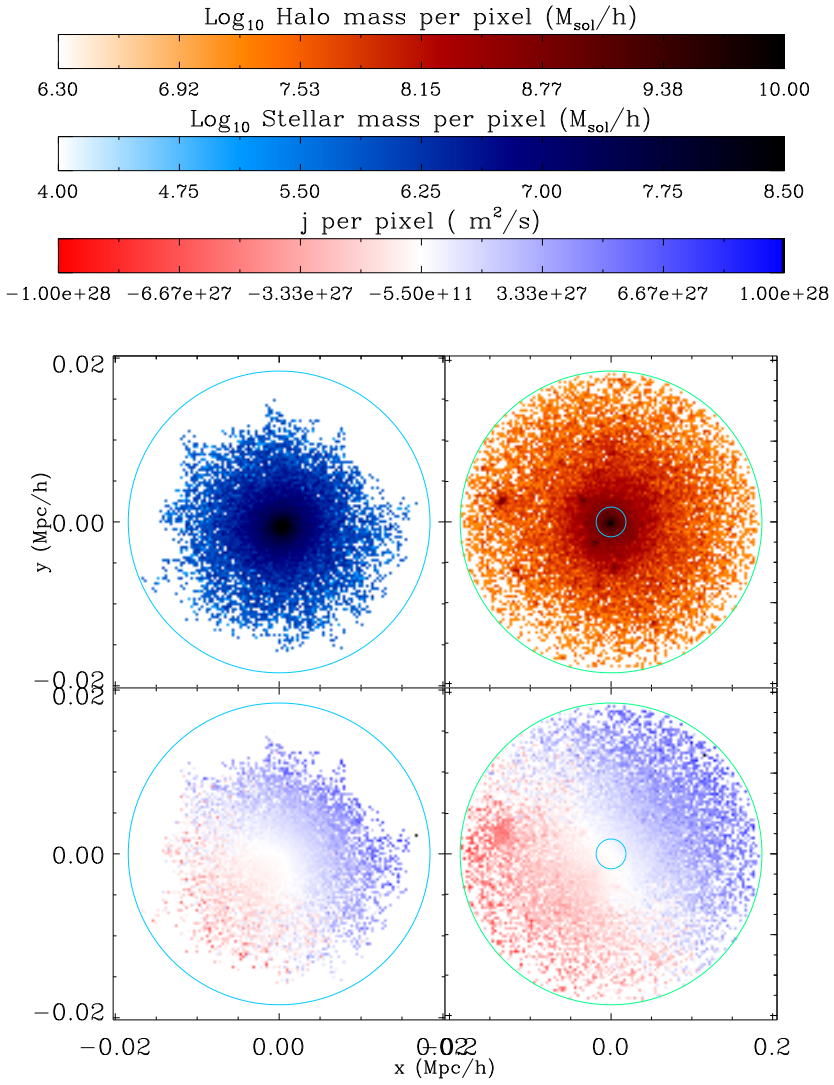

Figure A.10: Mass and angular momentum distributions for halo "C" and its central galaxy. Layout and colour schemes are the same as for figure A.7.

Appendix B | *Orientation resolution tests*

In sections 3.2.5 and 3.3.5 we considered the orientations of halo (or galaxy) angular momentum vectors. These are formed from a vector sum of the contributions from the objects' constituent particles. The vector sum means that the contribution from many particles can be much smaller than that of a single particle. If the summed vector's magnitude is particularly small, then the individual particles' vectors must have been largely in opposite directions, and have mostly cancelled out. In that case, the inclusion of a very few particles with parallel vectors, or even a single particle, can completely dominate the result. Clearly, any property that is dominated by the effects of discreteness in such a way is not reliable. To ensure our results are robust, we have performed extensive Monte Carlo tests using the halo catalogues from the HR1, DMO and DMG simulations. (This problem has been tackled in the past by Bullock et al. (2001a), Bailin and Steinmetz (2004), and Avila-Reese et al. (2005). We re-visit it here to ensure that we can retain as many haloes as possible for our simulations, while rejecting those that are clearly unreliable.)

For each halo, we perform 5000 bootstrap samples (e.g. Heyl et al., 1994) from both the particles from the halo in total, and from just the halo inner region, independently. The cosine of the angle between the original $\boldsymbol{j}_{\rm tot}$ (or $\boldsymbol{j}_{\rm inner}$) and the bootstrap-sampled $\boldsymbol{j}_{\rm tot}$ (or $\boldsymbol{j}_{\rm inner}$) is computed. We take the median of the 5000 samples for each halo and plot it against the magnitude of the original vector, rescaled in such a manner that any halo-to-halo trends are removed: we use the dimensionless quantity $\tilde{j}(\leq r) \equiv j(\leq r)/j_0(\leq r)$, where $j_0(\leq r)$ is the specific angular momentum of a (hypothetical) test-particle in a circular orbit at radius r, $j_0 = v_{\rm c} r$. Since the circular velocity $v_{\rm c}(r) = \sqrt{GM(\leq r) r^{-1}}$, we have:

$$\tilde{j}(\leq r) = \frac{j(\leq r)}{\sqrt{GM(\leq r) r}} \tag{B.1}$$

We have confirmed that this quantity does not vary systematically with either mass or radius.

We wish to find a limiting value of $\tilde{j} = \tilde{j}_{\rm lim}$ such that some given percentage of haloes with $\tilde{j} \geq \tilde{j}_{\rm lim}$ have their median bootstrapped vectors aligned to within a given angle. In particular, we require that 99.5 percent of the selected haloes have $\theta_{\rm med} \leq 15^\circ$, where θ is the angle between the actual halo $\boldsymbol{j}$ and the bootstrap-sampled vector.

In practice, the limits one gets from this process, and the severity of the cut on the resulting halo population depend strongly on the other selection criteria used. We always restrict ourselves to 'virialised' haloes ($Q_{\rm lim} = 0.5$), but the minimum number of particles in the given region (total or inner halo) has a strong impact. To balance the competing restrictions of having a well-resolved inner region, and spin orientations robust against discreteness effects, we decided to move the 'inner' radius outwards: the spin-magnitude results use $r_{\rm inner} = 0.1R_{\rm vir}$, but we chose to move to two bins further out for the orientation profiles, to $r_{\rm inner} = 10^{-0.6}R_{\rm vir} \approx 0.25R_{\rm vir}$. We also use 1000 as the minimum number of particles in the given region (total or inner), rather than the 300 we use for the analysis of the angular momentum magnitudes. Doing this meant that we were left with a large enough sample of haloes to be statistically viable, once the cuts in $N_{\rm p}$ and $\tilde{j}$ had been applied.

Figure B.1 shows the bootstrap results for the angular momentum of dark matter within $R_{\rm vir}$. The median of the bootstrapped angles from each halo are plotted, with a clear increase in scatter visible for haloes with low $\tilde{j}$ (that is, low j compared to that of a typical particle). The same trend applies to haloes from the HR1, DMO and DMG simulations. Our requirement that most haloes should have a median bootstrap angle within 15° produces a selection criterion of approximately $\log_{10}\tilde{j} \geq -1.5$. Figure B.2 shows the results of applying this method to the inner regions of the haloes only. Although the scatter behaves slightly differently, the value of $\tilde{j}_{\rm lim}$ is very similar. It is worth noting that, as long as they are produced with the same selection criteria, the presence of the DMO and DMG haloes does not affect the value of $\tilde{j}_{\rm lim}$ significantly. Including the galaxies (in terms of their stellar components) also does not affect the results greatly, as the galaxies generally have higher angular momentum anyway.

Thus, the halo selection criteria we use for our work on angular momentum orientation

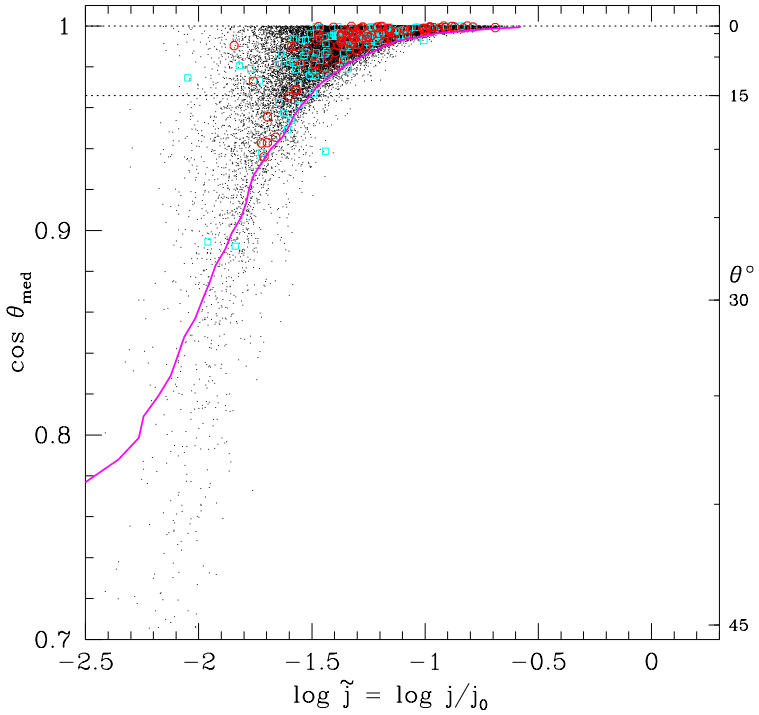

Figure B.1: Bootstrap resampling results for the angular momenta of the dark matter within $R_{\rm vir}$. Each point is the median of the 5000 angles between the $\boldsymbol{j}_{\rm tot}$ of a halo and that of the bootstrap-resamplings of that halo. This angle is plotted against the halo's scaled angular momentum $\tilde{\jmath}$, so that the different simulations can be compared together. The heavy magenta contour joins the series of lower limits on $\tilde{\jmath}$ such that 99.5 percent of the haloes with $\tilde{\jmath} \geq \tilde{\jmath}_{\rm lim}$ are better aligned in the median than that angle. The haloes have been selected to be 'virialised' ($Q \leq 0.5$) and well-resolved (at least 1000 dark matter particles), and have been taken from the HR1 (black dots), DMO (cyan squares) and DMG (red rings) simulations.

are:

$$\begin{aligned} Q &\leq 0.5 \\ N_{\rm p} &\geq 1000 \text{ (inner or total)} \\ \log_{10}\tilde{\jmath} &\geq \begin{cases} -1.44 & \text{(total)} \\ -1.51 & \text{(inner)} \end{cases} \end{aligned}$$

We do not select according to the $\tilde{\jmath}$ of the galaxies.

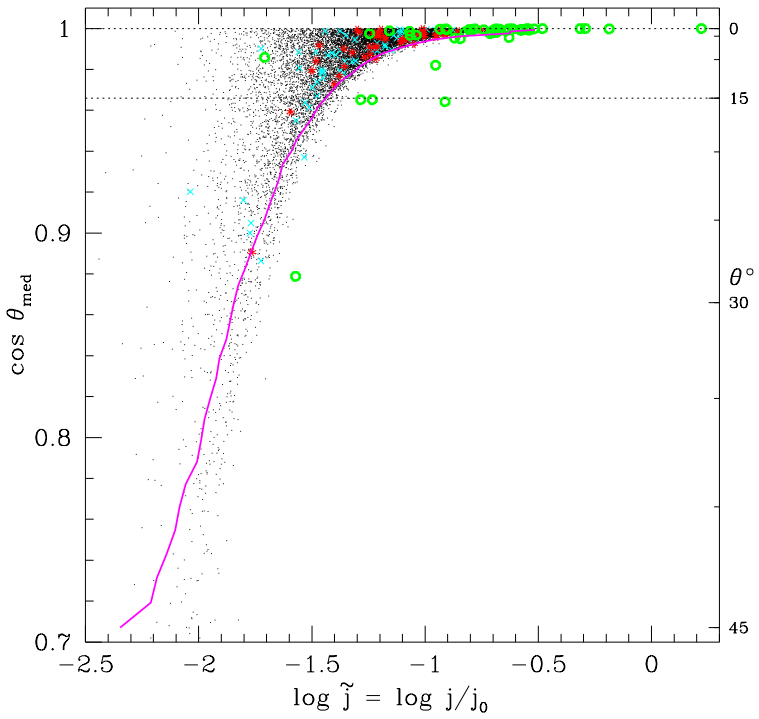

Figure B.2: As for figure B.1, but for the angular momentum of the dark matter within $\approx 0.25R_{\rm vir}$; the $N_{\rm p}$ selection criteria therefore applies to this inner region. HR1 haloes are marked as black dots, DMO haloes as blue crosses, and DMG haloes as red asterisks. Also included are the angular momenta of the stellar components of the central galaxies from the DMG haloes (green rings). To be included, the DMG haloes/galaxies also need to satisfy $N_{\rm p} \geq 1000$ on the star particles. Inclusion of the galaxies does not affect the resulting limit on $\tilde{j}$.

Bibliography

Abadi, M. G., Navarro, J. F., Steinmetz, M., and Eke, V. R.: 2003, *ApJ* **591**, 499

Allgood, B., Flores, R. A., Primack, J. R., Kravtsov, A. V., Wechsler, R. H., Faltenbacher, A., and Bullock, J. S.: 2006, *MNRAS* **367**, 1781

Avila-Reese, V., Colín, P., Gottlöber, S., Firmani, C., and Maulbetsch, C.: 2005, *ApJ* **634**, 51

Avila-Reese, V., Firmani, C., Klypin, A., and Kravtsov, A. V.: 1999, *MNRAS* **310**, 527

Baer, H. and Tata, X.: 2008, *ArXiv e-prints* 0805.1905

Bailin, J., Kawata, D., Gibson, B. K., Steinmetz, M., Navarro, J. F., Brook, C. B., Gill, S. P. D., Ibata, R. A., Knebe, A., Lewis, G. F., and Okamoto, T.: 2005a, *ApJ* **627**, L17

Bailin, J., Power, C., Gibson, B. K., and Steinmetz, M.: 2005b, *ArXiv Astrophysics e-prints* 0502231

Bailin, J. and Steinmetz, M.: 2004, *ApJ* **616**, 27

Bailin, J. and Steinmetz, M.: 2005, *ApJ* **627**, 647

Balsara, D. S.: 1991, *Ph.D. thesis*, Illinois Univ., Urbana-Champaign.

Balsara, D. S.: 1995, *J. Comp. Phys.* **121**, 357

Bardeen, J. M., Bond, J. R., Kaiser, N., and Szalay, A. S.: 1986, *ApJ* **304**, 15

Barnes, J. and Efstathiou, G.: 1987, *ApJ* **319**, 575

Barnes, J. and Hut, P.: 1986, *Nature* **324**, 446

Baugh, C. M.: 2006, *Rep. Prog. Phys.* **69**, 3101

Baugh, C. M., Lacey, C. G., Frenk, C. S., Granato, G. L., Silva, L., Bressan, A., Benson, A. J., and Cole, S.: 2005, *MNRAS* **356**, 1191

Bekenstein, J. D.: 2004, *Phys. Rev. D* **70(8)**, 083509

Bertone, G., Hooper, D., and Silk, J.: 2005, *Phys. Rep.* **405**, 279

Bett, P., Eke, V., Frenk, C. S., Jenkins, A., Helly, J., and Navarro, J.: 2007, *MNRAS* **376**, 215

Binney, J. and Tremaine, S.: 2008, *Galactic Dynamics: Second Edition*, Princeton University Press, Princeton, NJ, USA

Blumenthal, G. R., Faber, S. M., Flores, R., and Primack, J. R.: 1986, *ApJ* **301**, 27

Bond, J. R., Cole, S., Efstathiou, G., and Kaiser, N.: 1991, *ApJ* **379**, 440

Booth, C. M., Theuns, T., and Okamoto, T.: 2007, *MNRAS* **376**, 1588

Bower, R. G., Benson, A. J., Malbon, R., Helly, J. C., Frenk, C. S., Baugh, C. M., Cole, S., and Lacey, C. G.: 2006, *MNRAS* **370**, 645

Bregman, J. N.: 2007, *ARA&A* **45**, 221

Bruzual, G. and Charlot, S.: 2003, *MNRAS* **344**, 1000

Bryan, G. L. and Norman, M. L.: 1997, *ArXiv Astrophysics e-prints* 9710187

Bryan, G. L. and Norman, M. L.: 1998, *ApJ* **495**, 80

Bullock, J. S.: 2002, in P. Natarajan (ed.), *Proceedings of the Yale Cosmology Workshop "The Shapes of Galaxies and Their Dark Matter Halos", New Haven, Connecticut, USA, 28-30 May 2001*, p. 109, Singapore: World Scientific

Bullock, J. S., Dekel, A., Kolatt, T. S., Kravtsov, A. V., Klypin, A. A., Porciani, C., and Primack, J. R.: 2001a, *ApJ* **555**, 240

Bullock, J. S., Kolatt, T. S., Sigad, Y., Somerville, R. S., Kravtsov, A. V., Klypin, A. A., Primack, J. R., and Dekel, A.: 2001b, *MNRAS* **321**, 559

Burkert, A.: 1995, *ApJ* **447**, L25

Carroll, S. M., Press, W. H., and Turner, E. L.: 1992, *ARA&A* **30**, 499

Catelan, P. and Theuns, T.: 1996, *MNRAS* **282**, 436

Chapman, G., Cleese, J., Gilliam, T., Idle, E., Jones, T., and Palin, M.: 1970, in *"Spam"*, Monty Python's Flying Circus, BBC Television, episode 25

Chen, D.-M. and McGaugh, S.: 2008, *ArXiv e-prints* 0808.0225

Chen, D. N., Jing, Y. P., and Yoshikaw, K.: 2003, *ApJ* **597**, 35

Cole, S. and Lacey, C.: 1996, *MNRAS* **281**, 716

Cole, S., Lacey, C. G., Baugh, C. M., and Frenk, C. S.: 2000, *MNRAS* **319**, 168

Colless, M., Dalton, G., Maddox, S., Sutherland, W., Norberg, P., Cole, S., Bland-Hawthorn, J., Bridges, T., Cannon, R., Collins, C., Couch, W., Cross, N., Deeley, K., De Propris, R., Driver, S. P., Efstathiou, G., Ellis, R. S., Frenk, C. S., Glazebrook, K., Jackson, C., Lahav, O., Lewis, I., Lumsden, S., Madgwick, D., Peacock, J. A., Peterson, B. A., Price, I., Seaborne, M., and Taylor, K.: 2001, *MNRAS* **328**, 1039

Colless, M., Peterson, B. A., Jackson, C., Peacock, J. A., Cole, S., Norberg, P., Baldry, I. K., Baugh, C. M., Bland-Hawthorn, J., Bridges, T., Cannon, R., Collins, C., Couch, W., Cross, N., Dalton, G., De Propris, R., Driver, S. P., Efstathiou, G., Ellis, R. S., Frenk, C. S., Glazebrook, K., Lahav, O., Lewis, I., Lumsden, S., Maddox, S., Madgwick, D., Sutherland, W., and Taylor, K.: 2003, *ArXiv Astrophysics e-prints* 0306581

Couchman, H. M. P.: 1991, *ApJ* **368**, L23

Croft, R. A. C., Di Matteo, T., Springel, V., and Hernquist, L.: 2008, *ArXiv e-prints* 0803.4003

Crone, M. M., Evrard, A. E., and Richstone, D. O.: 1996, *ApJ* **467**, 489

Davis, M., Efstathiou, G., Frenk, C. S., and White, S. D. M.: 1985, *ApJ* **292**, 371

Dehnen, W.: 2001, *MNRAS* **324**, 273

Di Matteo, T., Colberg, J., Springel, V., Hernquist, L., and Sijacki, D.: 2008, *ApJ* **676**, 33

Dolag, K., Bartelmann, M., Perrotta, F., Baccigalupi, C., Moscardini, L., Meneghetti, M., and Tormen, G.: 2004, *A&A* **416**, 853

D'Onghia, E. and Navarro, J. F.: 2007, *MNRAS* **380**, L58

Doroshkevich, A. G.: 1970, *Astrophysics* **6**, 320

Dunkley, J., Komatsu, E., Nolta, M. R., Spergel, D. N., Larson, D., Hinshaw, G., Page, L., Bennett, C. L., Gold, B., Jarosik, N., Weiland, J. L., Halpern, M., Hill, R. S., Kogut, A., Limon, M., Meyer, S. S., Tucker, G. S., Wollack, E., and Wright, E. L.: 2008, *ArXiv e-prints* 0803.0586

Efstathiou, G. and Eastwood, J. W.: 1981, *MNRAS* **194**, 503

Efstathiou, G. and Jones, B. J. T.: 1979, *MNRAS* **186**, 133

Einstein, A.: 1916, *Annalen der Physik* **354**, 769

Eisenstein, D. J. and Hu, W.: 1999, *ApJ* **511**, 5

Eke, V. R., Baugh, C. M., Cole, S., Frenk, C. S., King, H. M., and Peacock, J. A.: 2005, *MNRAS* **362**, 1233

Eke, V. R., Cole, S., and Frenk, C. S.: 1996, *MNRAS* **282**, 263

Eke, V. R., Navarro, J. F., and Frenk, C. S.: 1998, *ApJ* **503**, 569

Eke, V. R., Navarro, J. F., and Steinmetz, M.: 2001, *ApJ* **554**, 114

Evans, A. K. D. and Bridle, S.: 2008, *ArXiv e-prints* 0806.2723

Fall, S. M. and Efstathiou, G.: 1980, *MNRAS* **193**, 189

Faltenbacher, A., Gottlöber, S., Kerscher, M., and Müller, V.: 2002, *A&A* **395**, 1

Franx, M., Illingworth, G., and de Zeeuw, T.: 1991, *ApJ* **383**, 112

Freeman, K. C.: 1970, *ApJ* **160**, 811

Frenk, C. S., White, S. D. M., Davis, M., and Efstathiou, G.: 1988, *ApJ* **327**, 507

Frieman, J. A., Turner, M. S., and Huterer, D.: 2008, *ARA&A* **46**, 385

Fryxell, B., Olson, K., Ricker, P., Timmes, F. X., Zingale, M., Lamb, D. Q., MacNeice, P., Rosner, R., Truran, J. W., and Tufo, H.: 2000, *ApJS* **131**, 273

Furman, S.: 1991, in R. Tokar (ed.), *"End of the road!", Transformers #80*, Marvel Comics

Gao, L., Navarro, J. F., Cole, S., Frenk, C. S., White, S. D. M., Springel, V., Jenkins, A., and Neto, A. F.: 2008, *MNRAS* **387**, 536

Gao, L., Springel, V., and White, S. D. M.: 2005, *MNRAS* **363**, L66

Gardner, J. P.: 2001, *ApJ* **557**, 616

Gavazzi, R., Treu, T., Rhodes, J. D., Koopmans, L. V. E., Bolton, A. S., Burles, S., Massey, R. J., and Moustakas, L. A.: 2007, *ApJ* **667**, 176

Gelb, J. M. and Bertschinger, E.: 1994, *ApJ* **436**, 467

Geller, M. J. and Huchra, J. P.: 1989, *Science* **246**, 897

Ghigna, S., Moore, B., Governato, F., Lake, G., Quinn, T., and Stadel, J.: 2000, *ApJ* **544**, 616

Gill, S. P. D., Knebe, A., and Gibson, B. K.: 2004, *MNRAS* **351**, 399

Gingold, R. A. and Monaghan, J. J.: 1977, *MNRAS* **181**, 375

Gnedin, O. Y., Kravtsov, A. V., Klypin, A. A., and Nagai, D.: 2004, *ApJ* **616**, 16

Goldhaber, G. and Perlmutter, S.: 1998, *Phys. Rep.* **307**, 325

Gott, J. R. I., Jurić, M., Schlegel, D., Hoyle, F., Vogeley, M., Tegmark, M., Bahcall, N., and Brinkmann, J.: 2005, *ApJ* **624**, 463

Gottlöber, S. and Turchaninov, V.: 2006, in G. A. Mamon, F. Combes, C. Deffayet, and B. Fort (eds.), *XXIst IAP Colloquium "Mass Profiles and Shapes of Cosmological Structures", Paris, France, July 4-9, 2005*, Vol. 20 of *EAS Publications Series*, pp 25–28

Governato, F., Mayer, L., Wadsley, J., Gardner, J. P., Willman, B., Hayashi, E., Quinn, T., Stadel, J., and Lake, G.: 2004, *ApJ* **607**, 688

Governato, F., Moore, B., Cen, R., Stadel, J., Lake, G., and Quinn, T.: 1997, *New Astronomy* **2**, 91

Governato, F., Willman, B., Mayer, L., Brooks, A., Stinson, G., Valenzuela, O., Wadsley, J., and Quinn, T.: 2007, *MNRAS* **374**, 1479

Gustafsson, M., Fairbairn, M., and Sommer-Larsen, J.: 2006, *Phys. Rev. D* **74(12)**, 12352201

Haardt, F. and Madau, P.: 1996, *ApJ* **461**, 20

Hahn, O., Porciani, C., Carollo, C. M., and Dekel, A.: 2007, *MNRAS* **375**, 489

Harker, G., Cole, S., Helly, J., Frenk, C., and Jenkins, A.: 2006, *MNRAS* **367**, 1039

Hayashi, E., Navarro, J. F., and Springel, V.: 2007, *MNRAS* **377**, 50

Heller, C. H., Shlosman, I., and Athanassoula, E.: 2007, *ApJ* **671**, 226

Helly, J. C., Cole, S., Frenk, C. S., Baugh, C. M., Benson, A., and Lacey, C.: 2003, *MNRAS* **338**, 903

Hernquist, L. and Katz, N.: 1989, *ApJS* **70**, 419

Heyl, J. S., Hernquist, L., and Spergel, D. N.: 1994, *ApJ* **427**, 165

Hockney, R. W. and Eastwood, J. W.: 1988, *Computer simulation using particles*, Bristol: Hilger, 1988

Hoekstra, H. and Jain, B.: 2008, *ArXiv e-prints* 0805.0139

Hoekstra, H., Yee, H. K. C., and Gladders, M. D.: 2004, *ApJ* **606**, 67

Hopkins, P. F., Bahcall, N. A., and Bode, P.: 2005, *ApJ* **618**, 1

Hoyle, F.: 1951, in *"Problems of Cosmical Aerodynamics"; Proceedings of a Symposium on the Motion of Gaseous Masses of Cosmical Dimensions, Paris, France, August 16-19, 1949 (UNESCO, jointly sponsored by the IAU and IUTAM)*, pp 195–197

Hubble, E. P.: 1926, *ApJ* **64**, 321

Iliev, I. T., Ciardi, B., Alvarez, M. A., Maselli, A., Ferrara, A., Gnedin, N. Y., Mellema, G., Nakamoto, T., Norman, M. L., Razoumov, A. O., Rijkhorst, E.-J., Ritzerveld, J., Shapiro, P. R., Susa, H., Umemura, M., and Whalen, D. J.: 2006, *MNRAS* **371**, 1057

Jing, Y. P.: 2000, *ApJ* **535**, 30

Jing, Y. P. and Suto, Y.: 2002, *ApJ* **574**, 538

Kane, G. and Watson, S.: 2008, *Modern Physics Letters A* **23**, 2103

Kang, X., van den Bosch, F. C., Yang, X., Mao, S., Mo, H. J., Li, C., and Jing, Y. P.: 2007, *MNRAS* **378**, 1531

Kasun, S. F. and Evrard, A. E.: 2005, *ApJ* **629**, 781

Katz, N. and Gunn, J. E.: 1991, *ApJ* **377**, 365

Kaufmann, T., Mayer, L., Wadsley, J., Stadel, J., and Moore, B.: 2007, *MNRAS* **375**, 53

Kazantzidis, S., Kravtsov, A. V., Zentner, A. R., Allgood, B., Nagai, D., and Moore, B.: 2004, *ApJ* **611**, L73

Klypin, A., Gottlöber, S., Kravtsov, A. V., and Khokhlov, A. M.: 1999, *ApJ* **516**, 530

Klypin, A. and Holtzman, J.: 1997, *ArXiv Astrophysics e-prints* 9712217

Klypin, A., Kravtsov, A. V., Bullock, J. S., and Primack, J. R.: 2001, *ApJ* **554**, 903

Klypin, A. A. and Shandarin, S. F.: 1983, *MNRAS* **204**, 891

Knebe, A., Green, A., and Binney, J.: 2001, *MNRAS* **325**, 845

Komatsu, E., Dunkley, J., Nolta, M. R., Bennett, C. L., Gold, B., Hinshaw, G., Jarosik, N., Larson, D., Limon, M., Page, L., Spergel, D. N., Halpern, M., Hill, R. S., Kogut, A., Meyer, S. S., Tucker, G. S., Weiland, J. L., Wollack, E., and Wright, E. L.: 2008, *ArXiv e-prints* 0803.0547

Kravtsov, A. V., Klypin, A., and Hoffman, Y.: 2002, *ApJ* **571**, 563

Kravtsov, A. V., Klypin, A. A., and Khokhlov, A. M.: 1997, *ApJS* **111**, 73

Kuzio de Naray, R., McGaugh, S. S., and de Blok, W. J. G.: 2008, *ApJ* **676**, 920

Lacey, C. and Cole, S.: 1993, *MNRAS* **262**, 627

Lacey, C. and Cole, S.: 1994, *MNRAS* **271**, 676

Lahav, O., Lilje, P. B., Primack, J. R., and Rees, M. J.: 1991, *MNRAS* **251**, 128

Le Borgne, D., Rocca-Volmerange, B., Prugniel, P., Lançon, A., Fioc, M., and Soubiran, C.: 2004, *A&A* **425**, 881

Lee, J. and Pen, U.-L.: 2000, *ApJ* **532**, L5

Lemson, G. and Kauffmann, G.: 1999, *MNRAS* **302**, 111

Lemson, G. and Virgo Consortium, t.: 2006, *ArXiv Astrophysics e-prints* 0608019

Libeskind, N. I., Cole, S., Frenk, C. S., Okamoto, T., and Jenkins, A.: 2007, *MNRAS* **374**, 16

Lin, W. P., Jing, Y. P., Mao, S., Gao, L., and McCarthy, I. G.: 2006, *ApJ* **651**, 636

Linehan, G. and Mathews, A.: 1996, in *"Hell"*, Father Ted, Channel 4 Productions, season 2 episode 1, from $11'35''$

Lucy, L. B.: 1977, *AJ* **82**, 1013

Macciò, A. V., Dutton, A. A., and van den Bosch, F. C.: 2008, *ArXiv e-prints* 0805.1926

Macciò, A. V., Dutton, A. A., van den Bosch, F. C., Moore, B., Potter, D., and Stadel, J.: 2007, *MNRAS* **378**, 55

Maller, A. H. and Dekel, A.: 2002, *MNRAS* **335**, 487

Mandelbaum, R., Hirata, C. M., Broderick, T., Seljak, U., and Brinkmann, J.: 2006, *MNRAS* **370**, 1008

Mandelbaum, R., Hirata, C. M., Seljak, U., Guzik, J., Padmanabhan, N., Blake, C., Blanton, M. R., Lupton, R., and Brinkmann, J.: 2005, *MNRAS* **361**, 1287

Mayer, L., Governato, F., and Kaufmann, T.: 2008, *ArXiv e-prints* 0801.3845

McKee, C. F. and Ostriker, J. P.: 1977, *ApJ* **218**, 148

Meneghetti, M., Bartelmann, M., Jenkins, A., and Frenk, C.: 2007, *MNRAS* **381**, 171

Merritt, D., Graham, A. W., Moore, B., Diemand, J., and Terzić, B.: 2006, *AJ* **132**, 2685

Merritt, D. and Sellwood, J. A.: 1994, *ApJ* **425**, 551

Mészáros, P.: 1974, *A&A* **37**, 225

Minor, Q. E. and Kaplinghat, M.: 2007, *ArXiv e-prints* 0711.2537

Mo, H. J., Mao, S., and White, S. D. M.: 1998, *MNRAS* **295**, 319

Monaghan, J. J.: 1988, *Comput. Phys. Comm.* **48**, 89

Monaghan, J. J.: 1992, *ARA&A* **30**, 543

Monaghan, J. J.: 1997, *J. Comp. Phys.* **136**, 298

Monaghan, J. J. and Gingold, R. A.: 1983, *J. Comp. Phys.* **52**, 374

Mortlock, D. J. and Turner, E. L.: 2001, *MNRAS* **327**, 557

Natarajan, P. and Refregier, A.: 2000, *ApJ* **538**, L113

Navarro, J. F., Abadi, M. G., and Steinmetz, M.: 2004a, *ApJ* **613**, L41

Navarro, J. F., Frenk, C. S., and White, S. D. M.: 1996, *ApJ* **462**, 563

Navarro, J. F., Frenk, C. S., and White, S. D. M.: 1997, *ApJ* **490**, 493

Navarro, J. F., Hayashi, E., Power, C., Jenkins, A. R., Frenk, C. S., White, S. D. M., Springel, V., Stadel, J., and Quinn, T. R.: 2004b, *MNRAS* **349**, 1039

Neto, A. F., Gao, L., Bett, P., Cole, S., Navarro, J. F., Frenk, C. S., White, S. D. M., Springel, V., and Jenkins, A.: 2007, *MNRAS* **381**, 1450

Nicastro, F., Mathur, S., and Elvis, M.: 2008, *Science* **319**, 55

Norman, M. L. and Bryan, G. L.: 1999, in S. M. Miyama, K. Tomisaka, and T. Hanawa (eds.), *Proceedings of the International Conference on Numerical Astrophysics (NAP98), Tokyo, Japan, March 10-13, 1998*, Vol. 240 of *Astrophysics and Space Science Library*, p. 19, Kluwer Academic, Boston, Mass., USA

Okamoto, T.: 2008, in A. Frebel, J. R. Maund, J. Shen, and M. H. Siegel (eds.), *"New Horizons in Astronomy: Frank N. Bash Symposium 2007", Austin, Texas, USA, 14-16 October 2007*, Vol. 393 of *Astronomical Society of the Pacific Conference Series*, pp 111–125

Okamoto, T., Eke, V. R., Frenk, C. S., and Jenkins, A.: 2005, *MNRAS* **363**, 1299

Okamoto, T., Nemmen, R. S., and Bower, R. G.: 2008, *MNRAS* **385**, 161

O'Shea, B. W., Bryan, G., Bordner, J., Norman, M. L., Abel, T., Harkness, R., and Kritsuk, A.: 2004, *ArXiv Astrophysics e-prints* 0403044

O'Shea, B. W., Nagamine, K., Springel, V., Hernquist, L., and Norman, M. L.: 2005, *ApJS* **160**, 1

Padmanabhan, T.: 1993, *Structure formation in the Universe*, Cambridge Univ. Press, Cambridge, UK

Parker, L. C., Hoekstra, H., Hudson, M. J., van Waerbeke, L., and Mellier, Y.: 2007, *ApJ* **669**, 21

Pearce, F. R., Jenkins, A., Frenk, C. S., White, S. D. M., Thomas, P. A., Couchman, H. M. P., Peacock, J. A., and Efstathiou, G.: 2001, *MNRAS* **326**, 649

Pedrosa, S. E., Tissera, P. B., and Scannapieco, C.: 2008, *ArXiv e-prints* 0807.2548

Peebles, P. J. E.: 1969, *ApJ* **155**, 393

Peebles, P. J. E.: 1971, *A&A* **11**, 377

Peebles, P. J. E.: 1984, *ApJ* **284**, 439

Peebles, P. J. E.: 1993, *Principles of physical cosmology*, Princeton Series in Physics, Princeton University Press, Princeton, NJ, USA

Percival, W. J. et al.: 2002, *MNRAS* **337**, 1068

Persic, M., Salucci, P., and Stel, F.: 1996, *MNRAS* **281**, 27

Porciani, C., Dekel, A., and Hoffman, Y.: 2002a, *MNRAS* **332**, 325

Porciani, C., Dekel, A., and Hoffman, Y.: 2002b, *MNRAS* **332**, 339

Power, C., Navarro, J. F., Jenkins, A., Frenk, C. S., White, S. D. M., Springel, V., Stadel, J., and Quinn, T.: 2003, *MNRAS* **338**, 14

Prada, F., Klypin, A. A., Simonneau, E., Betancort-Rijo, J., Patiri, S., Gottlöber, S., and Sanchez-Conde, M. A.: 2006, *ApJ* **645**, 1001

Pratchett, T.: 1990, *Wings*, Corgi Childrens

Press, W. H. and Schechter, P.: 1974, *ApJ* **187**, 425

Prochaska, J. X. and Tumlinson, J.: 2008, *ArXiv e-prints* 0805.4635

Reed, D., Governato, F., Quinn, T., Gardner, J., Stadel, J., and Lake, G.: 2005, *MNRAS* **359**, 1537

Riess, A. G., Filippenko, A. V., Challis, P., Clocchiatti, A., Diercks, A., Garnavich, P. M., Gilliland, R. L., Hogan, C. J., Jha, S., Kirshner, R. P., Leibundgut, B., Phillips, M. M., Reiss, D., Schmidt, B. P., Schommer, R. A., Smith, R. C., Spyromilio, J., Stubbs, C., Suntzeff, N. B., and Tonry, J.: 1998, *AJ* **116**, 1009

Romano-Díaz, E., Shlosman, I., Hoffman, Y., and Heller, C.: 2008, *ApJ* **685**, L105

Rozo, E., Nagai, D., Keeton, C., and Kravtsov, A.: 2006, *ArXiv Astrophysics e-prints* 0609621

Rudd, D. H., Zentner, A. R., and Kravtsov, A. V.: 2008, *ApJ* **672**, 19

Salpeter, E. E.: 1955, *ApJ* **121**, 161

Salucci, P. and Burkert, A.: 2000, *ApJ* **537**, L9

Salucci, P., Lapi, A., Tonini, C., Gentile, G., Yegorova, I., and Klein, U.: 2007, *MNRAS* **378**, 41

Sánchez, A. G., Baugh, C. M., Percival, W. J., Peacock, J. A., Padilla, N. D., Cole, S., Frenk, C. S., and Norberg, P.: 2006, *MNRAS* **366**, 189

Sand, D. J., Treu, T., Smith, G. P., and Ellis, R. S.: 2004, *ApJ* **604**, 88

Scannapieco, C., Tissera, P. B., White, S. D. M., and Springel, V.: 2008, *MNRAS* **389**, 1137

Schäfer, B. M.: 2008, *ArXiv e-prints* 0808.0203

Seljak, U. and Zaldarriaga, M.: 1996, *ApJ* **469**, 437

Sellwood, J. A. and McGaugh, S. S.: 2005, *ApJ* **634**, 70

Shapley, H. and Curtis, H.: 1921, *Bull. Nat. Res. Coun.* **2**, 171

Sharma, S. and Steinmetz, M.: 2005, *ApJ* **628**, 21

Shaw, L. D., Weller, J., Ostriker, J. P., and Bode, P.: 2006, *ApJ* **646**, 815

Sijacki, D. and Springel, V.: 2006, *MNRAS* **366**, 397

Sijacki, D., Springel, V., di Matteo, T., and Hernquist, L.: 2007, *MNRAS* **380**, 877

Spergel, D. N., Bean, R., Doré, O., Nolta, M. R., Bennett, C. L., Dunkley, J., Hinshaw, G., Jarosik, N., Komatsu, E., Page, L., Peiris, H. V., Verde, L., Halpern, M., Hill, R. S., Kogut, A., Limon, M., Meyer, S. S., Odegard, N., Tucker, G. S., Weiland, J. L., Wollack, E., and Wright, E. L.: 2007, *ApJS* **170**, 377

Spergel, D. N., Verde, L., Peiris, H. V., Komatsu, E., Nolta, M. R., Bennett, C. L., Halpern, M., Hinshaw, G., Jarosik, N., Kogut, A., Limon, M., Meyer, S. S., Page, L., Tucker, G. S., Weiland, J. L., Wollack, E., and Wright, E. L.: 2003, *ApJS* **148**, 175

Springel, V.: 2005, *MNRAS* **364**, 1105

Springel, V., Di Matteo, T., and Hernquist, L.: 2005a, *MNRAS* **361**, 776

Springel, V., Frenk, C. S., and White, S. D. M.: 2006, *Nature* **440**, 1137

Springel, V. and Hernquist, L.: 2002, *MNRAS* **333**, 649

Springel, V. and Hernquist, L.: 2003, *MNRAS* **339**, 289

Springel, V., White, S. D. M., Jenkins, A., Frenk, C. S., Yoshida, N., Gao, L., Navarro, J., Thacker, R., Croton, D., Helly, J., Peacock, J. A., Cole, S., Thomas, P., Couchman, H., Evrard, A., Colberg, J., and Pearce, F.: 2005b, *Nature* **435**, 629

Springel, V., White, S. D. M., Tormen, G., and Kauffmann, G.: 2001a, *MNRAS* **328**, 726

Springel, V., Yoshida, N., and White, S. D. M.: 2001b, *New Astronomy* **6**, 79

Steinmetz, M.: 1996, *MNRAS* **278**, 1005

Sutherland, R. S. and Dopita, M. A.: 1993, *ApJS* **88**, 253

Tegmark, M. et al.: 2004, *Phys. Rev. D* **69(10)**, 103501

Thomas, P. A., Muanwong, O., Pearce, F. R., Couchman, H. M. P., Edge, A. C., Jenkins, A., and Onuora, L.: 2001, *MNRAS* **324**, 450

Tinker, J. L., Kravtsov, A. V., Klypin, A., Abazajian, K., Warren, M. S., Yepes, G., Gottlober, S., and Holz, D. E.: 2008, *ArXiv e-prints* 0803.2706

Tonini, C., Lapi, A., Shankar, F., and Salucci, P.: 2006, *ApJ* **638**, L13

van den Bosch, F. C.: 1998, *ApJ* **507**, 601

van den Bosch, F. C., Abel, T., Croft, R. A. C., Hernquist, L., and White, S. D. M.: 2002, *ApJ* **576**, 21

Vitvitska, M., Klypin, A. A., Kravtsov, A. V., Wechsler, R. H., Primack, J. R., and Bullock, J. S.: 2002, *ApJ* **581**, 799

Wadsley, J. W., Stadel, J., and Quinn, T.: 2004, *New Astronomy* **9**, 137

Warren, M. S., Quinn, P. J., Salmon, J. K., and Zurek, W. H.: 1992, *ApJ* **399**, 405

Wechsler, R. H., Bullock, J. S., Primack, J. R., Kravtsov, A. V., and Dekel, A.: 2002, *ApJ* **568**, 52

Wechsler, R. H., Zentner, A. R., Bullock, J. S., Kravtsov, A. V., and Allgood, B.: 2006, *ApJ* **652**, 71

Weinberg, D.: 1997, in M. Persic and P. Salucci (eds.), *"Dark and Visible Matter in Galaxies and Cosmological Implications", Sesto Pusteria, BZ, Italy, 2-5 July 1996*, Vol. 117 of *Astronomical Society of the Pacific Conference Series*, pp 578–597, See appendix A. Further details available from `http://www.astronomy.ohio-state.edu/~dhw/Silliness/silliness.html`

Weinberg, D. H., Hernquist, L., and Katz, N.: 1997, *ApJ* **477**, 8

Wetzel, A. R., Cohn, J. D., White, M., Holz, D. E., and Warren, M. S.: 2007, *ApJ* **656**, 139

White, S. D. M.: 1984, *ApJ* **286**, 38

White, S. D. M., Davis, M., and Frenk, C. S.: 1984, *MNRAS* **209**, 27P

White, S. D. M. and Frenk, C. S.: 1991, *ApJ* **379**, 52

White, S. D. M., Frenk, C. S., and Davis, M.: 1983, *ApJ* **274**, L1

White, S. D. M. and Rees, M. J.: 1978, *MNRAS* **183**, 341

Williams, K. E.: 2007, *"A Relaxed Halo"*, sketch, pencil on paper

Yadav, J., Bharadwaj, S., Pandey, B., and Seshadri, T. R.: 2005, *MNRAS* **364**, 601

Yepes, G., Kates, R., Khokhlov, A., and Klypin, A.: 1997, *MNRAS* **284**, 235

Zavala, J., Okamoto, T., and Frenk, C. S.: 2008, *MNRAS* **387**, 364

Zentner, A. R.: 2007, *IJMPD* **16**, 763

Zhao, D. H., Jing, Y. P., Mo, H. J., and Börner, G.: 2003a, *ApJ* **597**, L9

Zhao, D. H., Mo, H. J., Jing, Y. P., and Börner, G.: 2003b, *MNRAS* **339**, 12

It's over – FINISHED!

Furman (1991), etc.